



Technical University of Crete

School of Electrical and Computer Engineering  
Digital Image and Signal Processing Laboratory  
Telecommunications Division

***Functional connectivity analysis of cerebellum's network  
during resting-state using functional Magnetic Resonance  
Imaging (fMRI) data***

Master Thesis

Vasileios C. Pezoulas

**Thesis committee:** Professor Michael Zervakis (**Supervisor**)  
Professor Costas Balas  
Associate Professor Aikaterini Mania

**Chania, July 2017**



## Credits

*I would like to thank:*

*First and foremost, my **family** for the valuable support they have provided me all these years not only as an undergraduate but also as a postgraduate student, despite all the difficulties and challenges of our era.*

*From the bottom of my heart **Professor Sifis Micheloyannis** from the Medical School of University of Crete who recently passed away. It was an honor to work with this remarkable person and I will never forget his contribution not only to this thesis but also to my personal improvement as a young scientist and a human being.*

***Professor Michalis Zervakis** for the confidence he showed me through all these years, his decisive guidance as well as his valuable support for conducting this thesis and finally for giving me the opportunity to explore the field of neuroscience.*

***Professor Costas Balas** and **Associate Professor Aikaterini Mania** for accepting to evaluate the work presented in this thesis as members of my thesis committee.*

*The **Max Planck Society** for the financial support of the publication that is described in the first part of this thesis and especially **Dr. Manousos A. Klados** as well as the Society of Applied Neuroscience for hosting the international biennial conference, under the *Frontiers in Human Neuroscience* journal, where the first part of this thesis was presented in Corfu, Greece, at October 2016. **Dr. Manousos A. Klados** was a member of the Max Planck Society that time and has been a great mentor of mine throughout this thesis.*

*The **Bodossaki Foundation** for the 4-month scholarship I received during my 3<sup>rd</sup> semester as a master student.*

*The **Pancretan Endowment Fund** for the scholarship of excellence I received during my 4<sup>th</sup> semester as a master student. The second part of this thesis focuses on the methodology and the outcomes of the related research work which has been prepared for submission in the *IEEE journal of Biomedical Health and Informatics*.*

***Dr. Kostantinos Michalopoulos** for his valuable contribution and guidance in the second part of this thesis.*

*To my mother Vasiliki, a living hero*

## Abstract

During the last years, it has been established that the prefrontal and posterior parietal brain lobes, which are mostly related to intelligence, have many connections to cerebellum. However, there is a limited research exploring cerebellum's relationship with cognitive processes and gender as well. The current thesis consists of two fundamental parts. In the first part of this thesis, a lobular network analysis of cerebellum was conducted with the purpose of investigating its overall organization in individuals with low and high crystallized Intelligence Quotient (IQ). In order to do so, resting-state fMRI (rs-fMRI) data were collected from 136 healthy subjects from the well-known Human Connectome Project (HCP) database. Cerebellum was anatomically parcellated, in the Montreal Neurological Institute (MNI) coordinate space, into 28 lobules-Regions of Interest (ROIs) and thereafter correlation matrices were constructed by computing Pearson's correlation coefficients between the average BOLD timeseries for each pair of ROIs. Afterwards, Minimum Spanning Trees (MSTs) were constructed in order to retain only the strongest connections within each network. Subsequently, six global and three local metrics were calculated in order to retrieve features concerning the functional and structural characteristics of each MST. Moreover, a hub analysis was conducted in order to identify nodes with high importance. The computed set of metrics gave rise to extensive statistical analysis in order to examine differences between low and high-IQ groups, as well as between all possible gender-based group combinations. Our results suggest that both male and female networks have small-world properties with significant differences only in females (especially in higher IQ females) indicative of higher neural efficiency in cerebellum. In addition, an increased effort dedicated by the low-IQ population is detected in three specific lobules. In the final part of this study, instead of performing a lobular analysis of cerebellum, a voxel-wise clustering analysis approach was adopted based on Spectral Graph Theory. The main goal of this venture is to define a larger number of functional cerebellar regions and thus provide a much more accurate and data-driven gender-based network analysis of cerebellum's activity. The recruited clustering approach was based on a spatially constrained version of the conventional spectral clustering algorithm by combining the average correlation matrix across 100 subjects with an appropriately thresholded Euclidean distance matrix. The procedure was first tested on synthetic data prior to any application on the original data. In order to find the most stable threshold as well as the optimal number of clusters, a repeated cross-validation procedure was executed on randomly defined subsets of the original population by assessing two basic clustering evaluation indices. The estimated parameters were then used to apply the SCSC procedure on the original data and extract a resting-state network atlas which was combined with the anatomical one, to define a functional atlas of cerebellum with 46 ROIs. To our knowledge, this atlas is the first resting-state functional cerebellar atlas based on the HCP data. This atlas was finally used to perform a gender-based network analysis of cerebellum, similar to the one described previously. Our results suggest the existence of significant differences in the optimal organization of the MSTs between the two genders. Finally, the dominant hub that was found in functional region 10 supports the dominance of the Left VI lobule in cerebellum's functional connectivity as it was already reported in the first part of this study.

**Keywords:** cerebellum; rs-fMRI; functional connectivity; crystallized IQ; gender; network analysis; minimum spanning trees; spectral graph theory

## Περίληψη

Τα τελευταία χρόνια, είναι πλέον γνωστό ότι οι προ-μετωπιαίοι και οπίσθιοι βρεγματικοί λοβοί του ανθρώπινου εγκεφάλου, που σχετίζονται κατά κόρον με την νοημοσύνη, έχουν πολλαπλές συνδέσεις με την παρεγκεφαλίδα. Ωστόσο, η σχετική βιβλιογραφία γύρω από την μελέτη της σχέσης της παρεγκεφαλίδας με τις γνωστικές διεργασίες αλλά και με το φύλο είναι αρκετά περιορισμένη. Η τρέχουσα διατριβή αποτελείται από δύο βασικούς πυλώνες. Στο πρώτο μέρος της διατριβής, διεξάγεται μια ανατομική ανάλυση του δικτύου της παρεγκεφαλίδας, σε επίπεδο λοβίων, με αμφότερο σκοπό την διερεύνηση της συνολικής δραστηριότητας της παρεγκεφαλίδας σε άτομα με χαμηλό και υψηλό (κρυσταλλικό) δείκτη νοημοσύνης (IQ). Για τον σκοπό αυτό συγκεντρώθηκαν δεδομένα fMRI, σε κατάσταση ηρεμίας, από 136 υγιή υποκείμενα, μέσω της ευρέως γνωστής βάσης δεδομένων του Human Connectome Project (HCP). Η παρεγκεφαλίδα απομονώθηκε ανατομικά από τον υπόλοιπο εγκέφαλο, στον MNI (Montreal Neurological Institute) χώρο συντεταγμένων, σε συνολικά 28 λοβία-περιοχές ενδιαφέροντος (ROIs) και εν συνεχεία κατασκευάστηκαν πίνακες συσχέτισης υπολογίζοντας τον συντελεστή συσχέτισης για κάθε πιθανό ζεύγος μέσω των BOLD (Blood Oxygen Level Dependent) χρονοσειρών, ανά περιοχή ενδιαφέροντος. Κατόπιν, δομήθηκαν ελάχιστα συνδεδεμένα δέντρα (MSTs) με αμφότερο σκοπό την διατήρηση των ισχυρότερων συνδέσεων ανά δίκτυο. Εν συνεχεία, υπολογίστηκαν έξι καθολικές και τρεις τοπικές μετρικές δικτύων με στόχο την εξαγωγή χρήσιμων τοπολογικών και λειτουργικών χαρακτηριστικών των MSTs. Επιπλέον, διεξήχθη μια πλήρης hub ανάλυση προκειμένου να εντοπιστούν οι σημαντικότεροι κόμβοι (hubs). Το σύνολο των εξαγόμενων μετρικών πυροδότησε την δυνατότητα εκτεταμένης στατιστικής ανάλυσης προκειμένου να εξεταστούν διαφορές μεταξύ των ομάδων χαμηλής και υψηλής νοημοσύνης καθώς και μεταξύ όλων των πιθανών συνδυασμών ομάδων βάσει του φύλου. Τα αποτελέσματά μας προτείνουν ότι τόσο τα δίκτυα των ανδρών όσο και των γυναικών εκδηλώνουν την χαρακτηριστική small-worldness ιδιότητα με σημαντικές διαφορές μόνο στις γυναίκες (ειδικά στις γυναίκες με υψηλό IQ), γεγονός που υποδεικνύει μια υψηλότερη νευρονική απόδοση στην παρεγκεφαλίδα. Επίσης, εντοπίζεται μια αυξημένη προσπάθεια που αφιερώνεται από τα άτομα με χαμηλή νοημοσύνη, σε τρεις συγκεκριμένους λοβούς της παρεγκεφαλίδας. Στο δεύτερο και τελευταίο μέρος της διατριβής, πραγματοποιείται μια πλήρης ανάλυση των voxels της παρεγκεφαλίδας, έναντι της κλασσικής ανατομικής ανάλυσης σε λοβία, βασισμένη σε πτυχές της φασματικής θεωρίας γράφων. Ο στόχος αυτού του εγχειρήματος είναι να οριστούν περισσότερες λειτουργικές περιοχές της παρεγκεφαλίδας και συνεπώς να διεξαχθεί μια πιο ακριβής και στοχευμένη ανάλυση του δικτύου της παρεγκεφαλίδας σε άντρες και γυναίκες. Η μέθοδος ομαδοποίησης βασίστηκε σε μια χωρικά περιορισμένη εκδοχή του κλασσικού spectral clustering αλγόριθμου (SCSC) συνδυάζοντας την μέση μήτρα συντελεστών συσχέτισης από 100 υποκείμενα με μια κατάλληλα κατωφλιωμένη μήτρα Ευκλείδειων αποστάσεων. Η διαδικασία εφαρμόστηκε πρώτα σε συνθετικά δεδομένα πριν την τελική εφαρμογή του στα αρχικά δεδομένα. Εν συνεχεία, διεξήχθη μια επαναλαμβανόμενη διαδικασία διασταυρούμενης επικύρωσης, πάνω σε τυχαία επιλεγμένα σετ υποκειμένων, με σκοπό την εύρεση του πιο σταθερού κατωφλίου καθώς και του βέλτιστου πλήθους των clusters, αξιολογώντας δύο βασικούς δείκτες ομαδοποίησης. Έπειτα, οι εκτιμημένες παράμετροι χρησιμοποιήθηκαν για την εφαρμογή του προτεινόμενου αλγόριθμου στα αρχικά δεδομένα με στόχο την εξαγωγή ενός χάρτη της παρεγκεφαλίδας, σε κατάσταση ηρεμίας, ο οποίος συνδυάστηκε με τον ανατομικό χάρτη ώστε να οριστεί ένας λειτουργικός χάρτης της παρεγκεφαλίδας με 46 περιοχές ενδιαφέροντος. Απ' όσο γνωρίζουμε, ο χάρτης αυτός είναι ο πρώτος λειτουργικός χάρτης της παρεγκεφαλίδας, σε κατάσταση ηρεμίας, βασισμένος στα δεδομένα της βάσης του HCP. Βάσει αυτού, πραγματοποιήθηκε μια παρόμοια ανάλυση του δικτύου της παρεγκεφαλίδας, όπως προηγουμένως, βάσει του φύλου. Τα αποτελέσματά μας υποδηλώνουν σημαντικές διαφορές στη βέλτιστη οργάνωση των MSTs μεταξύ των δύο φύλων. Τέλος, ο κυρίαρχος κόμβος που εντοπίστηκε στην λειτουργική περιοχή 10, υποστηρίζει την κυριαρχία του αριστερού λοβίου VI της παρεγκεφαλίδας στην λειτουργική συνδεσιμότητα αυτής, όπως αναφέρθηκε ήδη στο πρώτο μέρος της μελέτης.

**Λέξεις-κλειδιά:** παρεγκεφαλίδα, fMRI σε κατάσταση ηρεμίας, λειτουργική συνδεσιμότητα, κρυσταλλικός δείκτης νοημοσύνης, φύλο, ανάλυση δικτύου με ελάχιστα συνδεδεμένα δέντρα, φασματική θεωρία γράφων

# Table of Contents

<b>1. Introduction</b> .....	<b>17</b>
1.1 The human cerebellum .....	17
1.1.1 Neuronal structure and action potentials .....	17
1.1.2 The cerebellar cortex .....	20
1.1.3 Cerebellum's anatomy and its relationship with the cerebrum .....	22
1.1.4 Cerebellum and intelligence .....	26
1.1.5 Clinical abnormalities.....	26
1.1.6 The anatomical atlas used in this thesis .....	27
1.2 The fMRI dataset .....	28
1.2.1 The Human Connectome Project.....	28
1.2.2 HCP scanning parameters and pre-processing pipelines .....	29
1.2.3 Additional information related to subjects history .....	29
1.3 Modern network analysis and Spectral Graph Theory in neuroscience .....	30
1.4 Related studies in cerebellar and cerebral hemispheres .....	31
1.5 Scope and contribution to the existing literature .....	32
1.6 Thesis outline .....	33
<b>2. Functional magnetic resonance imaging (fMRI)</b> .....	<b>36</b>
2.1 History .....	36
2.2 Magnetic resonance imaging (MRI) .....	38
2.2.1 Physiological basis.....	38
2.2.2 Resonance and Larmor (or precessional) frequency .....	39
2.2.3 Basic MRI pulse sequences and parameters .....	41
2.2.4 Relaxation times and tissue contrast .....	43
2.2.5 Image reconstruction .....	45
2.3 The BOLD contrast mechanism .....	47
2.4 From MRI to fMRI activation maps .....	49
2.5 Spatial and temporal resolution.....	50
2.6 Basic pre-processing techniques .....	52
2.7 Clinical applications.....	53
2.8 Conclusions and future challenges.....	54
<b>3. Lobular analysis of cerebellum's network with respect to IQ and gender</b> .....	<b>56</b>
3.1 Overview .....	56
3.2 IQ groups formation .....	57
3.3 BOLD time-series extraction per anatomical lobule .....	59
3.4 Network construction .....	61
3.4.1 Graph modeling .....	61
3.4.2 Common network models .....	62
3.4.3 Small-worldness property evaluation.....	63
3.5 Minimum Spanning Trees .....	65

3.5.1	Basic concept .....	65
3.5.2	MST formation .....	65
3.5.3	Local MST features.....	66
3.5.4	Global MST features .....	68
3.6	Hub(s) detection.....	69
3.7	Correlation between hub metrics and Median Response Times .....	72
3.8	Statistical analysis per group combination .....	75
3.8.1	One-way ANOVA.....	75
3.8.2	Statistical analysis application procedure .....	76
3.8.3	Results for each group combination .....	77
3.9	Acknowledgements.....	80
<b>4.</b>	<b>Voxel-wise analysis of cerebellum .....</b>	<b>81</b>
4.1	Overview .....	81
4.2	Population of interest .....	82
4.3	BOLD time-series extraction from the cerebellar voxels .....	82
4.4	Further pre-processing.....	82
4.5	Voxel-wise functional graphs construction.....	83
4.6	Spectral graph theory concepts for clustering .....	84
4.6.1	Fundamental basis .....	84
4.6.2	Eigenvalue decomposition (EVD) .....	84
4.6.3	The Laplacian of a graph .....	85
4.6.4	Spectral clustering .....	87
4.6.5	The Normalized-cut (N-cut) algorithm .....	89
4.6.6	Spatially constrained spectral clustering .....	90
4.7	Clustering evaluation .....	91
4.7.1	Silhouette index .....	91
4.7.2	Davies-Bouldin index .....	92
4.8	Clustering homogeneity evaluation .....	93
4.9	Application on synthetic time-series.....	93
4.10	Application on cerebellum's data .....	97
4.11	Cross-validation for performance evaluation .....	99
4.12	Resting-state network atlas .....	103
4.13	Final cerebellar atlas .....	105
4.14	Gender-based functional connectivity analysis .....	110
4.14.1	Functional parcellation of cerebellum .....	111
4.14.2	Network construction and Minimum Spanning Trees formation .....	111
4.14.3	Statistical analysis and hubs .....	112
4.15	Acknowledgements.....	114
<b>5.</b>	<b>Discussion and future work .....</b>	<b>115</b>
5.1	Discussion.....	115
5.2	Future work .....	119
5.3	Cerebellum's atlases availability .....	121
<b>6.</b>	<b>References .....</b>	<b>122</b>

<b>Ethics statement .....</b>	<b>135</b>
<b>Acknowledgements .....</b>	<b>136</b>
<b>Publications .....</b>	<b>137</b>
<b>Appendix .....</b>	<b>138</b>

## List of Figures

<b>Figure 1.1.</b> The structure of a typical neuron. (Adapted from wikipedia.org). .....	18
<b>Figure 1.2.</b> A schematic representation which describes the way that information travels to the dendrites-receptors of a neighboring neuron, through the synaptic gap. (Adapted from wikipedia.org). .....	19
<b>Figure 1.3.</b> The action potential of a typical neuron. (Adapted from wikipedia.org). .....	20
<b>Figure 1.4.</b> Detailed organization of the cerebellar cortex in sagittal plane along with the cerebellar circuitry. <b>Abbreviations:</b> GL (granular layer), PCL (Purkinje cell layer), ML (molecular layer), PF (parallel fibers), PC (Purkinje cells), Gr (Granule cells), MF (mossy fibers), DCN (deep cerebellar nuclei), CF (climbing fibers), Go (Golgi cells), UB (unipolar brush cells), Lg (Lugaro cells). (Adapted from Hampson and Blatt, 2015). .....	22
<b>Figure 1.5. (A)</b> A sagittal view of cerebellum’s location along with its connections to the brainstem. <b>(B)</b> The three fundamental cerebellar peduncles. (Adapted from wikipedia.org). .....	23
<b>Figure 1.6.</b> A flattened version of cerebellum’s anatomy showing the main fissures, lobes and lobules with labelling and appropriate color coding. (Adapted from D’Mello and Stoodley, 2015). .....	25
<b>Figure 1.7.</b> The anatomical atlas of cerebellum used in this study. <b>(A)</b> A complete 3D view of the regions of interest, using BrainNet Viewer (Xia et al., 2013). <b>(B)</b> The corresponding flatmap (unfolded) representation of the same atlas based on SUIT’s toolbox. .....	28
<b>Figure 2.1.</b> The fMRI Connectome scanner which is located at the Athinoula A. Martinos Center for Biomedical Imaging, Massachusetts General Hospital (MGH). (Adapted from <a href="http://www.humanconnectomeproject.org/about/scanner/">http://www.humanconnectomeproject.org/about/scanner/</a> ). .....	37
<b>Figure 2.2.</b> In an external magnetic field, protons spin around their own axis and wobble about the axis of the magnetic field (precession). Usually the $z$ direction is up, i.e., the direction of external magnetic field is in the head-foot direction in the scanner. .....	38
<b>Figure 2.3.</b> When a $90^\circ$ RF pulse is applied, the NMV of the protons ( $M_o$ ) is flipped from the vertical ( $z$ ) plane to the horizontal ( $xy$ ) plane (green dashed arc). .....	39
<b>Figure 2.4.</b> A magnetic field ( $B_o$ ) is applied along the $z$ -axis, causing the spinning nucleus to precess around the applied magnetic field. .....	40
<b>Figure 2.5.</b> Splitting of energy levels of a nucleus with spin $m = \frac{1}{2}$ , into two states (E2; spin down and E1; spin up). .....	41

**Figure 2.6.** The timing diagram of a spin-echo pulse sequence. **Abbreviations;**  $n_{PE}$  is equal to the number of times the whole sequence is repeated,  $n_{FE}$  is the number of samples taken during FE. (Adapted from wikipedia.org). .....42

**Figure 2.7. (A)** T1 and **(B)** T2 relaxation times. ....44

**Figure 2.8.** Contrast differences between T2-W, T1-W and FLAIR imaging sequences from a patient with Pick’s disease ` a neurogenerative disease. (Adapted from wikipedia.org). ....45

**Figure 2.9.** Visual representation of the mapping procedure from **(A)**  $k$ -space to **(B)** image space and backwards using IFT and FT, respectively. (The MRI axial slice in **(B)** was adapted and adjusted from wikipedia.org). .....46

**Figure 2.10. (A)** Oxygenated and deoxygenated consumption before/after neuronal activation. **(B)** The relative concentration distribution of the oxygenated and deoxygenated hemoglobin before and after neuronal firing. (Adapted and adjusted from Saka et al., 2010). .....48

**Figure 2.11.** The standard canonical HRF model used in various task fMRI studies. (Adapted and adjusted from wikipedia.org). .....49

**Figure 2.12. (A)** Example of an fMRI 4D dataset where an extra BOLD signal is recorded for each voxel (here one is shown for simplicity). **(B)** An fMRI scan (on sagittal and axial slices) showing activations on regions that belong to the well-known Default Mode Network (DMN) which is usually activated during resting-state. (Adapted and adjusted from wikipedia.org). .....50

**Figure 3.1.** Schematic representation of the basic methodology for executing the lobular analysis of cerebellum. ....57

**Figure 3.2.** IQ scores distribution where the black dashed line represents the median and the red lines correspond to the upper (median plus one quartile) and lower (median minus one quartile) IQ boundaries. ....58

**Figure 3.3.** Cerebellum parcellation procedure (coronal view, **A:** front, **B:** back) followed by its flat surface representation in **(C)**. Color coding is based on each lobule's volumetric size. Presentations **(A)** and **(B)** were created using BrainNet Viewer (Xia et al., 2013) and the flatmap presentation in **(C)** was based on the work of Diedrichsen and Zotow, 2015. ....59

**Figure 3.4.** The three common brain network architectures (Watts and Strogatz, 1998). ....62

**Figure 3.5.** Average weighted and undirected graphs per IQ group (left panel, **A:** low-IQ and **B:** high-IQ) and their corresponding MSTs (right panel, **C:** low-IQ and **D:** high-IQ). On the latter representation, each node's size depends linearly on its average BC value. ....66

**Figure 3.6.** Average DEG, BC, ECC values per ROI for both IQ groups on the left panel and the corresponding distributions on the right panel. ....68

**Figure 3.7.** Hub locations on cerebellum for low (green) and high (yellow) IQ groups based on BC **(A)** and DEG **(B)**. The size of each node depends on the percentage of low/high-IQ subjects with the highest BC **(C)** and DEG **(D)** values. .... 70

**Figure 3.8.** Hub locations on cerebellum for low-IQ males (light blue) and females (orange) IQ groups based on BC **(A)** and DEG **(B)**. The size of each node depends on the percentage of low-IQ males/females with the highest BC **(C)** and DEG **(D)** values. .... 71

**Figure 3.9.** Hub locations on cerebellum for high-IQ males (navy blue) and females (red) IQ groups based on BC **(A)** and DEG **(B)**. The size of each node depends on the percentage of high-IQ males/females with the highest BC **(C)** and DEG **(D)** values. .... 72

**Figure 3.10.** Regions with the maximum correlation between average DEG or BC measure and median response times (MRTs) for low and high-IQ groups. .... 73

**Figure 3.11.** Regions with the maximum correlation between average DEG or BC measure and median response times (MRTs) for low and high-IQ males. .... 74

**Figure 3.12.** Regions with the maximum correlation between average DEG or BC measure and median response times (MRTs) for low and high-IQ females. .... 75

**Figure 4.1.** Application of a 50<sup>th</sup> order FIR filter on the BOLD signal of voxel #19658 of subject 64 in both time (upper panel) and frequency (lower panel) domains. .... 83

**Figure 4.2.** Example of a simple weighted and undirected graph with normalized weights. 86

**Figure 4.3.** A simple visual representation of the spectral clustering steps. **(A)** A concentric distribution of data points on the input space where the data points with the same color have higher similarity (i.e., data points are separated into 3 groups/clusters). **(B)** The Laplacian matrix of the adjacency matrix that corresponds to **(A)**. **(C)** The first (largest) 3 eigenvectors of the Laplacian matrix. **(D)** The first 3 eigenvectors are used to project the original data points onto the eigen-space, where the data separation is much easier for *k*-means. .... 88

**Figure 4.4.** A simple demonstration of the superiority of spectral clustering. **(A)** The original pattern. **(B)** Spectral clustering successfully separates the data points based on the concentric formation. **(B)** The direct application of the *k*-means procedure on the input space is not able to distinguish the pattern. (Adapted and adjusted from [rpubs.com/sandipan/199446](http://rpubs.com/sandipan/199446)). .... 88

**Figure 4.5.** A simple undirected graph which can be partitioned into two disjoint subsets **A** and **B** by minimizing the cut cost (removing edges with red color). .... 89

**Figure 4.6.** An example which demonstrates that minimizing a simple cut cost function is not able to provide an ideal segmentation and apparently results to single-voxel clusters. On the other hand, minimizing the Ncut cost can provide an ideal cut by making sure to provide a “balanced” number of data points per segment. .... 90

**Figure 4.7.** The 1<sup>st</sup> run of the simulation experiment using *k* = 4 patterns. **(A)** The generated seed signals for each pattern. **(B)** The 4 randomly placed patterns on a 128x128 noisy block. Recall that each point in **(B)** is a synthetic time-course. **(C)** The 16534x16534 non-negative

correlation matrix with a 200x200 block for zooming purposes. **(D)** The 16534x16534 distance matrix using  $rc = 2$ , with a 200x200 block for zooming purposes. .... 94

**Figure 4.8.** Simulation results for the 1<sup>st</sup> run after the application of the **(A)** Spectral, **(B)** N-cut and **(C)** Spatially Constrained Spectral clustering procedures, respectively, alongside with the corresponding clustermap's entropy distributions **(D)**, **(E)**, **(F)**, using various radius values. 94

**Figure 4.9.** The 2<sup>nd</sup> run of the simulation experiment using  $k = 6$  patterns. **(A)** The generated seed signals for each pattern. **(B)** The 6 randomly placed patterns on a 128x128 noisy block. Recall that each point in **(B)** is a synthetic time-course. **(C)** The 16534x16534 non-negative correlation matrix with a 200x200 block for zooming purposes. **(D)** The 16534x16534 distance matrix using  $rc = 2$ , with a 200x200 block for zooming purposes. .... 95

**Figure 4.10.** Simulation results for the 2<sup>nd</sup> run after the application of the **(A)** Spectral, **(B)** N-cut and **(C)** Spatially Constrained Spectral clustering procedures, respectively, alongside with the corresponding clustermap's entropy distributions **(D)**, **(E)**, **(F)**, using various radius values. .... 95

**Figure 4.11.** The 3<sup>rd</sup> run of the simulation experiment using  $k = 8$  patterns. **(A)** The generated seed signals for each pattern. **(B)** The 8 randomly placed patterns on a 128x128 noisy block. Recall that each point in **(B)** is a synthetic time-course. **(C)** The 16534x16534 non-negative correlation matrix with a 200x200 block for zooming purposes. **(D)** The 16534x16534 distance matrix using  $rc = 2$ , with a 200x200 block for zooming purposes. .... 96

**Figure 4.12.** Simulation results for the 3<sup>rd</sup> run after the application of the **(A)** Spectral, **(B)** N-cut and **(C)** Spatially Constrained Spectral clustering procedures, respectively, alongside with the corresponding clustermap's entropy distributions **(D)**, **(E)**, **(F)**, using various radius values. .... 96

**Figure 4.13.** The formation of the spatially constrained correlation matrix. **(A)** The average 21522x21522 non-negative correlation (adjacency) matrix with an additional 200x200 block for zooming purposes. **(B)** The average 21522x21522 Euclidean distance matrix with an additional 200x200 block for zooming purposes. **(C)** The spatially constrained correlation matrix which is the result of the element-wise multiplication between matrices in **(A)** and **(B)**. .... 98

**Figure 4.14.** Clustering evaluation results for 30 clusters under examination, on the average correlation matrix. **(A)** The first 30 eigenvalues. **(B)** The average silhouette and **(C)** Davies-Bouldin values computed across 30 clusters for various thresholds (i.e.,  $rc = 2, 3, 5, 8, 10$ , and 12) on the distance matrix  $S$ . .... 98

**Figure 4.15.** The optimal number of clusters across each  $rc$  value for all validation runs, as indicated by the largest gap on each run's average silhouette plot across 30 clusters. .... 99

**Figure 4.16.** The optimal number of clusters across each  $rc$  value for all validation runs, as indicated by the largest gap on each run's Davies-Bouldin plot across 30 clusters. .... 99

**Figure 4.17.** Consistency evaluation results for each  $rc$  value across all runs for cluster 1. The black dashed line indicates a clustering consistency of 0.9 (90%). .... 101

<b>Figure 4.18.</b> Consistency evaluation results for each $rc$ value across all runs for cluster 2. The black dashed line indicates a clustering consistency of 0.9 (90%).	101
<b>Figure 4.19.</b> Consistency evaluation results for each $rc$ value across all runs for cluster 3. The black dashed line indicates a clustering consistency of 0.9 (90%).	102
<b>Figure 4.20.</b> Consistency evaluation results for each $rc$ value across all runs for cluster 4. The black dashed line indicates a clustering consistency of 0.9 (90%).	102
<b>Figure 4.21.</b> The resulting clustermap after the application of the SCSC approach for $k = 4$ , in 2D form with slice indices $P = 46$ , $C = 31$ , $A = 15$ .	103
<b>Figure 4.22.</b> The resulting clustermap after the application of the SC approach for $k = 4$ , in 2D form with slice indices $P = 46$ , $C = 31$ , $A = 15$ .	104
<b>Figure 4.23.</b> The resulting clustermap after the application of the Ncut approach for $k = 4$ , in 2D form with slice indices $P = 46$ , $C = 31$ , $A = 15$ .	104
<b>Figure 4.24.</b> The resulting clustermaps along with the corresponding voxel-wise entropy distributions for each clustering approach.	104
<b>Figure 4.25.</b> The construction steps of cerebellum's functional atlas. <b>(A)</b> The anatomical atlas is projected on <b>(B)</b> the RSN atlas leading to a new <b>(C)</b> functional atlas with 46 functional ROIs.	105
<b>Figure 4.26.</b> The location of the 46 functional nodes in 3D coronal view using BrainNet Viewer (Xia et al., 2013).	110
<b>Figure 4.27.</b> The location of the 46 functional nodes in 3D complete view (without labels for better visualization) using BrainNet Viewer (Xia et al., 2013).	110
<b>Figure 4.28.</b> Network analysis strategy using the functional atlas of cerebellum. The 46x46 correlation matrixes are first constructed after parcellating the functional atlas individually for both genders and then the corresponding Minimum Spanning Trees (MSTs) are formed. On the latter, various local and global metrics are extracted for statistical and hub analysis.	111
<b>Figure 4.29.</b> The average correlation networks of both males and females projected on cerebellum's surface using BrainNet Viewer (Xia et al., 2013).	112
<b>Figure 4.30.</b> The MSTs of the corresponding average correlation networks for both males and females projected on cerebellum's surface using BrainNet Viewer (Xia et al., 2013). Each node's size linearly depends on its corresponding average BC value across each population.	112
<b>Figure 4.31.</b> Nodes with the highest DEG across males and females.	113
<b>Figure 4.32.</b> Nodes with the highest BC across males and females.	114

## List of Tables

<b>Table 2.1.</b> Typical T1 and T2 values for various tissues under a 1.5 Tesla MRI scanner. ....	45
<b>Table 2.2.</b> Spatiotemporal resolution and physiological basis of fundamental non-invasive brain mapping methods (Johnsrude and Hauk, 2005; Nicolas-Alonso and Gomez-Gil, 2013). .....	51
<b>Table 3.1.</b> Demographic information (part 1). ....	58
<b>Table 3.2.</b> Cerebellum's anatomical ROIs information. ....	60
<b>Table 3.3.</b> Small-world properties information. ....	65
<b>Table 3.4.</b> ROI(s) with the maximum correlation coefficient between MRT and DEG or BC measure for both IQ groups and gender. ....	74
<b>Table 3.5.</b> Statistical analysis results based on IQ for the main network metrics. ....	77
<b>Table 3.6.</b> Statistical analysis results based on males IQ for the main network metrics. ....	78
<b>Table 3.7.</b> Statistical analysis results per female IQ group for the main network metrics. ...	78
<b>Table 3.8.</b> Statistical analysis results per low-IQ males and females for the main network metrics. ....	79
<b>Table 3.9.</b> Statistical analysis results between high-IQ males and females for the main network metrics. ....	79
<b>Table 4.1.</b> Demographic information (part 2). ....	82
<b>Table 4.2.</b> Number of anatomically overlaid voxels for each functional ROI. ....	106
<b>Table 4.3.</b> Percentage of anatomically overlaid voxels for each functional ROI. ....	107
<b>Table 4.4.</b> The anatomical locations of the identified functional regions. ....	108
<b>Table 4.5.</b> MNI coordinates of each functional region's node. ....	109
<b>Table 4.6.</b> Statistical analysis results based on gender for the main network metrics. ....	113
<b>Table A1.</b> Mean $\pm$ SD values based on IQ, for the normalized degree. ....	137
<b>Table A2.</b> Mean $\pm$ SD values based on IQ, for the normalized betweenness centrality. ....	138
<b>Table A3.</b> Mean $\pm$ SD values based on IQ, for the normalized eccentricity. ....	139
<b>Table A4.</b> Statistical analysis results based on gender, for degree. ....	140
<b>Table A5.</b> Statistical analysis results based on gender, for betweenness centrality. ....	141
<b>Table A6.</b> Statistical analysis results based on gender, for degree. ....	142



# 1. Introduction

---

## 1.1. The human cerebellum

The human cerebellum, also known as “little brain”, constitutes about 10% of the total brain weight but contains more neurons than all of the rest of the brain due to the small granule cells of the cerebral cortex which are densely distributed (Glickstein, 2007). It is composed of neuronal units which share a common cerebellar microcircuitry (Roostaei et al., 2014). Cerebellum has been always recognized as a distinct subdivision of the human brain with the majority of cerebellum’s network being involved in a wide range of tasks such as cognition, motor function and learning, language, reflex adaptation, spatial and executive functions (Glickstein, 2007; Stoodley and Schmahmann, 2009; Stoodley et al., 2012; Koziol et al., 2014; Styliadis et al., 2015; Van Overwalle and Mariën, 2016). Several deficits resulting from cerebellar lesions include motor dysmetria, ataxia, the cerebellar cognitive affective syndrome (CCAS), also known as the Schmahmann’s syndrome, which includes visual-spatial, emotional and linguistic deficits (Schmahmann and Sherman, 1998; Schmahmann 2004) and psychosis (Stoodley and Schmahmann, 2009). The cerebellum forms closed-loop circuits with the majority of the cerebral cortex, with the cerebellar hemispheres projecting to the contralateral cerebral cortex (Schmahmann, 1991). This closed-loop circuitry, suggests that the cerebellum contains repeating modules, such that the function of a given region of the cerebellum depends on its inputs and outputs (Stoodley, 2014). Nowadays, it has been established that the links between the cerebrum and cerebellum show a topographical organization (Stoodley and Schmahmann, 2009; Buckner et al., 2011). Many fMRI studies attempt to tie the cerebellum with various human tasks but the local cerebellar activations, without the combination of the cerebral hemispheres, have not been extensively studied (Voogd, 2003; Bernard et al., 2012).

### 1.1.1. Neuronal structure and action potentials

Prior to the examination of cerebellum’s anatomy it is important to comprehend the structural and functional characteristics of the cells that constitute the nervous system as well as the signals that travel through them and carry the processing information. These cells are called neurons and are mostly located on the neocortex, the part of the brain that is involved in cognition and thinking. There are approximately 20 billion neurons in the neocortex each

of which is interconnected with 10000 other neurons, so the number of neuronal connections is vast (O'Reily et al., 2012). Neurons are mainly arranged in the form of networks providing information and feedback to each other through information processing (Sternberg and Sternberg, 2012). A typical neuron consists of four basic parts; soma (cell body), dendrites, axon and axon terminals (also referred to as terminal buttons). The following description of the neuronal structure is based on [the author's undergraduate diploma thesis](#).

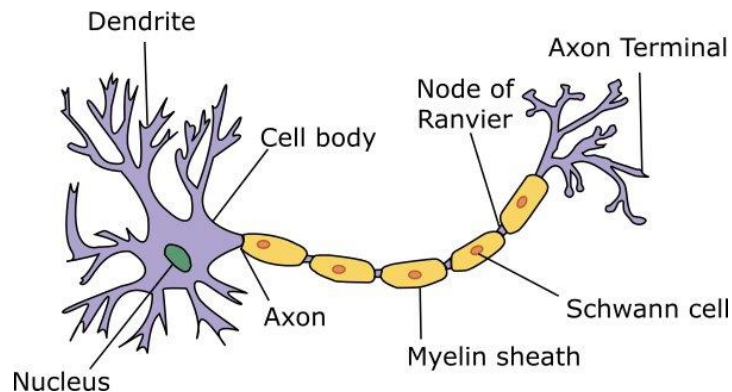


**Figure 1.1.** The structure of a typical neuron. (Adapted from wikipedia.org).

The soma (or cell body) of a neuron contains the nucleus of the cell and connects the dendrites to the axon (O'Reily et al., 2012; Sternberg and Sternberg, 2012; Barnes, 2013). Soma is responsible for the life of a cell. Moreover, the integration of information takes place in the soma which is able to activate multiple dendrites but never more than one axon.

The axon (Feldman, 2011; Sternberg and Sternberg, 2012; Barnes, 2013) is a long, thick tube that extends from the soma and is able to respond to the information by transmitting an electrochemical signal which travels to the axon terminal from where the signal is able to travel to other neurons. The axon begins from the axon hillock and is able to connect with other neuronal cells of different types of cells like the muscle. Its length can be equal to one meter or even more.

The dendrites (Feldman, 2011; O'Reily et al., 2012; Sternberg and Sternberg, 2012) are branch-like structures that receive information from other neurons and transfer them to the soma where the integration of information takes place. Usually there are many dendrites per cell, each one with many branches. The length of a dendrite is small than that of an axon. The ability of learning is strongly related with the formation of new neuronal connections. These connections occur in combination with the increased number of dendrites in the human brain.

Myelin (Sternberg and Sternberg, 2012; Barnes, 2013) is a white fatty substance that surrounds some of the axons. The whiteness of the myelin is related with white matter. The myelin sheath insulates and protects longer axons from electrical interference by other neighboring neurons. It also accelerates information transfer. Myelin is not continuously distributed along the axon but distributed in segments which are broken up by the Nodes of

Ranvier (Sternberg and Sternberg, 2012; Barnes, 2013). These nodes are small gaps in the myelin sheath which are able to increase the information transferring even more by creating electrical signals known as action potentials which travel down the axon. Deficits in myelin sheaths is associated with multiple sclerosis. It is important to note that unmyelinated axons are shorter than the myelinated ones since the latter usually correspond to longer axons. The Schwann cells (Barnes, 2013) are special types of neuroglial cells that provide insulation to one discrete axon. These cells provide the myelin insulation to the axons of the peripheral nervous system (PNS). The unmyelinated Schwann cells play an important role in the maintenance of the axons and their contribution is crucial for the neurons life.

The axon terminals (also known as terminal buttons) are small knobs which are found at the ends of the branches of an axon and do not directly connect with other dendrites of other neurons (Sternberg and Sternberg, 2012). More precisely, there is a small gap which serves as a juncture between the axon terminals of one or more neurons and the dendrites of one or more neurons. This juncture is known as synapse (Sternberg and Sternberg, 2012; Barnes, 2013). Synapses are related with cognition. Decreased cognitive function is associated with reduced efficiency of synaptic transmission (Sternberg and Sternberg, 2012). Synapses are able to establish interconnected neuronal networks from the neural cells of the nervous system (O'Reilly et al., 2012).

Signal transmission between neurons occurs when the axon terminals release one or more neurotransmitters (Feldman, 2011; Sternberg and Sternberg, 2012; Barnes, 2013) at the synapse (**Fig. 1.2**). These neurotransmitters are chemical compounds used for transmission of information across the synaptic gap to the receiving dendrites of the next neuron, etc. The presynaptic ending or synaptic terminal contains cellular organs like the neurotransmitters. When a neuron fires, a pulse is sent which releases the synaptic vesicles that contain the neurotransmitters, through the synaptic cleft (gap), to the receptors, which stimulate or inhibit electrical stimuli. The synaptic area where neurotransmitters are released, is called the active zone (Barnes, 2013).

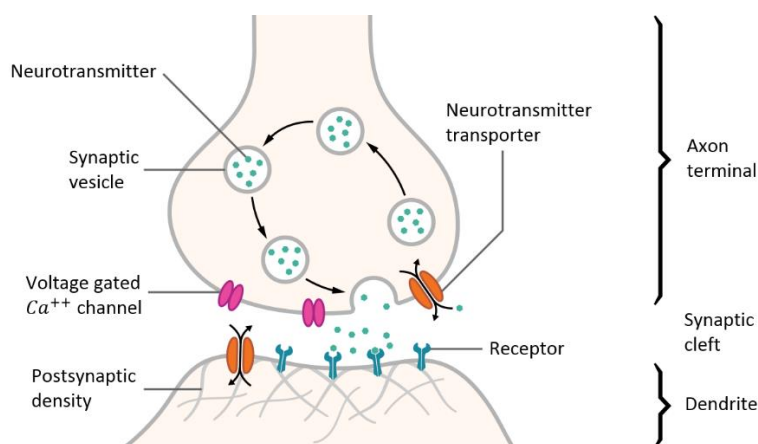


**Figure 1.2.** A schematic representation which describes the way that information travels to the dendrites-receptors of a neighboring neuron, through the synaptic gap. (Adapted from wikipedia.org).

During resting-state, a typical neuron exhibits a resting-state potential with a membrane magnitude being approximately equal to -70 mV (**Fig. 1.3**) (Feldman, 2011; Guyton and Hall, 2012; Barnes, 2013). At this state, a neuron contains  $K^+$  ions (Caldwell, 2009; Barnes, 2013). When a neuron fires (receives a signal/stimulus), its synaptic membrane opens thus activating the  $Na^+$  channels. Due to the fact that the  $Na^+$  ions are more outside the neuron than inside (mostly  $K^+$  ions), this allows the  $Na^+$  ions to pass through the neuron with rates of 100 million ions per second (Caldwell, 2009; Feldman, 2011; Barnes, 2013). The sudden arrival of  $Na^+$  ions alters the charge of the nearby parts of the cell from negative to positive and therefore the number of  $K^+$  ions is greatly reduced. This phenomenon is known as depolarization (da Silva, 2010; Guyton and Hall, 2012; Barnes, 2013). When the positive charge exceeds a certain threshold (typically at -55 mV), an electrical pulse known as action potential, travels along the axon. The action potential is a short-term event which increases fast and then returns back its original (resting) state (negative membrane potential) in approximately 1-2 msec (da Silva, 2010; Feldman, 2011) (**Fig. 1.3**). Afterwards, the  $Na^+$  ions disperse within the neuron and the  $K^+$  ions flow outside the neuron, which causes the membrane potential to return back to -70 mV and repolarization occurs (Guyton and Hall, 2012; Barnes, 2013) (**Fig. 1.3**). In fact, the membrane potential reduces from -70 mV to -80 mV before reaching rest-state because the  $K^+$  ion gates (or channels) remain open a bit more before they permanently close and hyperpolarization occurs (Feldman, 2011; Barnes, 2013). During this period, the neuron is not able to trigger a new action potential and it is known as the refraction period (Barnes, 2013). The action potential is the signal that travels through the brain's neuronal networks.

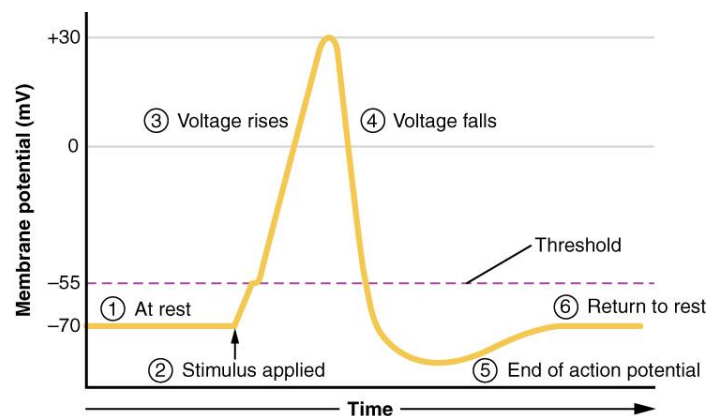


**Figure 1.3.** The action potential of a typical neuron. (Adapted from wikipedia.org).

### 1.1.2. The cerebellar cortex

Cerebellum lies inside the cerebellar cortex, an outer layer of highly convoluted gray matter surrounding the deep nuclei of cerebellum which consists of white matter known as arbor vitae (Roostaei, 2014). The cerebellar cortex is composed of three fundamental layers; the molecular layer, the ganglionic or Purkinje layer and the granular layer (**Fig. 1.4**).

The molecular layer is the most superficial layer and consists of flattened dendritic trees of Purkinje cells (Roostaei, 2014; Fletcher, 2016). The molecular layer also contains stellate

cells and basket cells – the two main types of interneurons that are scattered along dendritic ramifications (**Fig. 1.4**). The basket cells are named after the basket that their axon forms on the input of a Purkinje cell (Fletcher, 2016). Stellate and basket cells form inhibitory synapses onto Purkinje cell dendrites and cell bodies, respectively.

The ganglionic or Purkinje layer (Voogd, 2003; Roostaei, 2014; Fletcher, 2016) lies in the middle and serves as the output layer of the cerebellar cortex (**Fig. 1.4**). It is mainly composed of Purkinje cells which are stacked on the Purkinje layer. The axons of the Purkinje cells provide the only efferent pathway to the deep cerebellar nuclei, and thus Purkinje cells constitute the sole output of all motor coordination in the cerebellar cortex (Roostaei, 2014; Fletcher, 2016). Purkinje cells are one of the largest cells in the human brain and belong to the GABAergic (gamma-Aminobutyric acid) type of neurons. Both basket and stellate cells provide inhibitory (GABAergic) input to the Purkinje cell, with basket cells synapsing on the Purkinje cell axon initial segment and stellate cells onto the dendrites (Roostaei, 2014). In addition, another type of cells known as Lugaro cells, lie just beneath the Purkinje layer and contain long horizontal dendrites that can contact up to 10-15 Purkinje cells, hypothesized to monitor the environment around these cells (Hampson and Blatt, 2015).

The granular layer (Roostaei, 2014; Fletcher 2016) is the deepest layer and is densely packed with a large number of granule cells, mainly Golgi cells, next to white matter (**Fig. 1.4**). These cells synapse onto the dendrite of granule cells. They receive excitatory input from mossy fibers, also synapsing on granule cells, and parallel fibers, which are long granule cell axons. Golgi cells also synapse on excitatory local circuit neurons, known as the unipolar brush cells which have a round nucleus and a short tuft of dendrites with large synaptic junctions and are thought to be involved in cell signaling (Hampson and Blatt, 2015). These cells are mostly found in the vestibulocerebellum (**Section 1.1.3**). The granular layer is thick and serves as the input layer for the cerebellar cortex. In addition, the axons of the granule cells ascend to the molecular layer, where they split into two parallel fibers which form synaptic contacts with the dendritic tree of the Purkinje cells as they move horizontally in the molecular layer (Roostaei, 2014). Granule cells target Golgi cells and the stellate cells as well as basket cells.

Cerebellum receives its main excitatory inputs through two fundamental pathways; the climbing fibers and the mossy fibers (**Fig. 1.4**). The climbing fibers arise mainly from the olivary nucleus of the caudal medulla and excite the Purkinje cells as well as other cerebellar nuclei neurons using chemical compounds such as aspartate and glutamate (Fletcher, 2016). The climbing fibers are named like this because they “climb” the dendritic tree of the Purkinje cells in the Purkinje cell layer, creating hundreds of synaptic connections where each climbing fiber innervates up to approximately 10 Purkinje cells (Roostaei, 2014). The climbing fibers input is delivered directly to the Purkinje cells and it is so strong that a single climbing fiber’s action potential can generate a depolarization waveform in the Purkinje cell (Roostaei, 2014).

The mossy fibers form another major cerebellar input. These fibers arise mainly from (i) the pontine nuclei through the cerebropontocerebellar fibers which are involved in altering

cerebellum for anticipated movements, **(ii)** the spinal cord through the spinocerebellar fibers which are involved in ongoing movements, **(iii)** the vestibular nuclei (and vestibular nerve) through the vestibulocerebellar fibers which are mainly involved in head coordination and eye movement and **(iv)** other similar cerebellar structures mainly through the inferior and middle cerebellar peduncles (Voogd, 2003; Roostaei, 2014; Fletcher, 2016). The mossy fibers deliver the input indirectly to the granule cells which are located on the granular cell layer. Golgi cells send inhibitory input to the mossy fiber glomeruli and have dendrites extending into the lower molecular layer where it contacts parallel fibers. Purkinje cells send inhibitory input to the granule cells and have dendrites extending into the molecular layer where they contact parallel fibers. Climbing fibers ascend from the deep cerebellar nuclei to the molecular layer where they contact Purkinje cells.

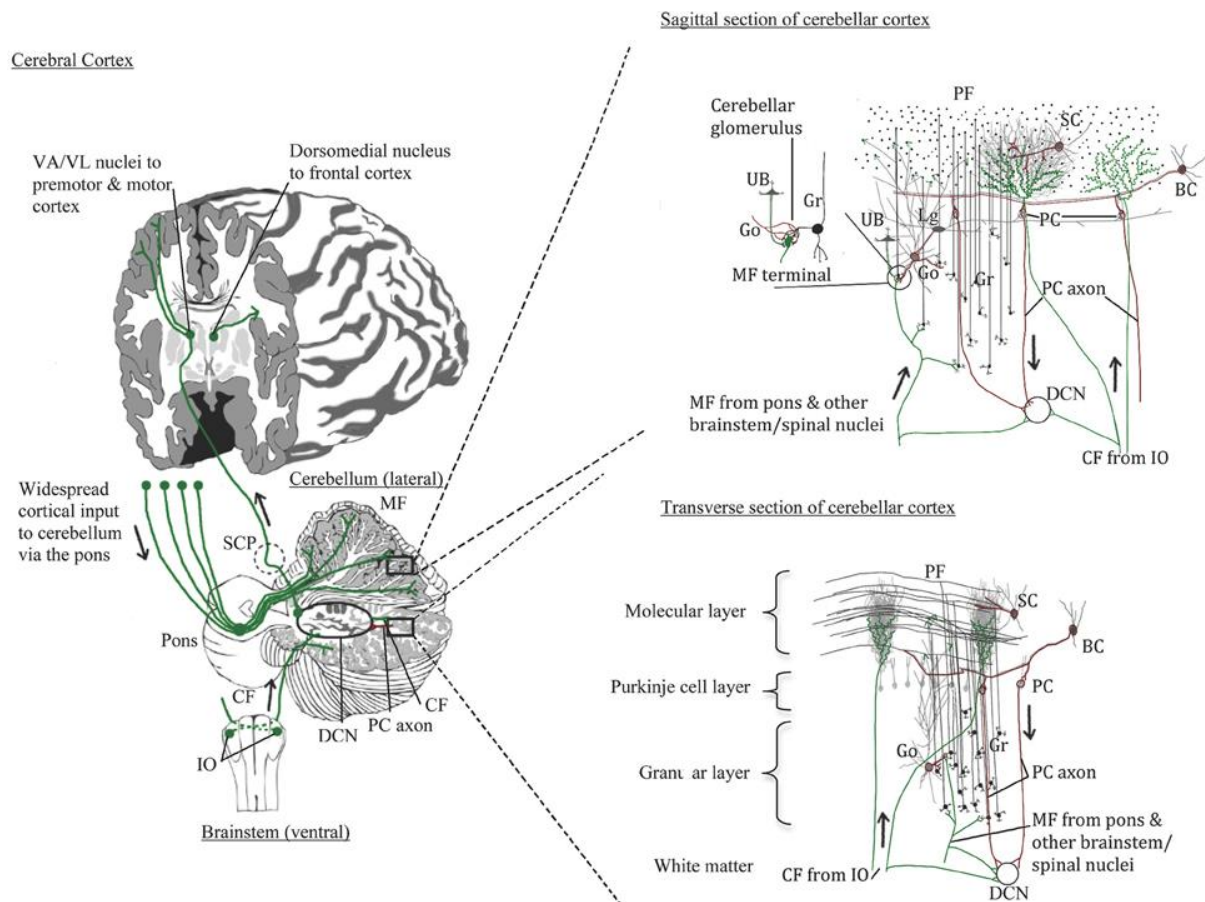


**Figure 1.4.** Detailed organization of the cerebellar cortex in sagittal plane along with the cerebellar circuitry. **Abbreviations:** GL (granular layer), PCL (Purkinje cell layer), ML (molecular layer), PF (parallel fibers), PC (Purkinje cells), Gr (Granule cells), MF (mossy fibers), DCN (deep cerebellar nuclei), CF (climbing fibers), Go (Golgi cells), UB (unipolar brush cells), Lg (Lugaro cells). (Adapted from [Hampson and Blatt, 2015](#)).

### 1.1.3. Cerebellum's anatomy and its relationship with the cerebrum

The cerebellum is located in the posterior fossa (posterior to the brainstem and the fourth ventricle) under the occipital cortex of the human cerebrum (**Fig. 1.5(A)**). It is estimated to contain 101 billion neurons whereas the cerebral cortex is estimated to contain

21-26 billion neurons (Andersen et al., 1992; Pelvig et al., 2008) with the total number of neurons in the human brain going far beyond 120 billion. Cerebellum is connected with the pons which is a fundamental part of the brainstem and consists of neural (fiber) tracts through which the neuronal signals travel from the brain to cerebellum as well as into the thalamus.

Cerebellum is connected to the brainstem via 3 pairs of cerebellar peduncles (**Fig. 1.5(B)**) which are known as the superior, middle and inferior peduncles (Schmahmann, 1991; Fletcher, 2016; Stoodley and Limperopoulos, 2016). These peduncles are named after their position in cerebellum. All of these peduncles emerge from the cerebellar nuclei and connect the cerebellum to the brainstem through the pons. In fact, there are six cerebellar peduncles, three on each side of cerebellum. The superior (or caudal) cerebellar peduncle contains efferent and afferent axons which carry information from the cerebellum to the cerebral cortex via the thalamus (Fletcher, 2016; Stoodley and Limperopoulos, 2016). The middle cerebellar peduncle contains only afferent axons that travel from the cerebral cortex to the cerebellum via the pontine nuclei which lies inside the pons (Fletcher, 2016; Stoodley and Limperopoulos, 2016). Finally, the inferior (or rostral) cerebellar peduncle carries incoming and outgoing axons that connect the cerebellum with the vestibular system and spinal cord or the midbrain (Fletcher, 2016; Stoodley and Limperopoulos, 2016).

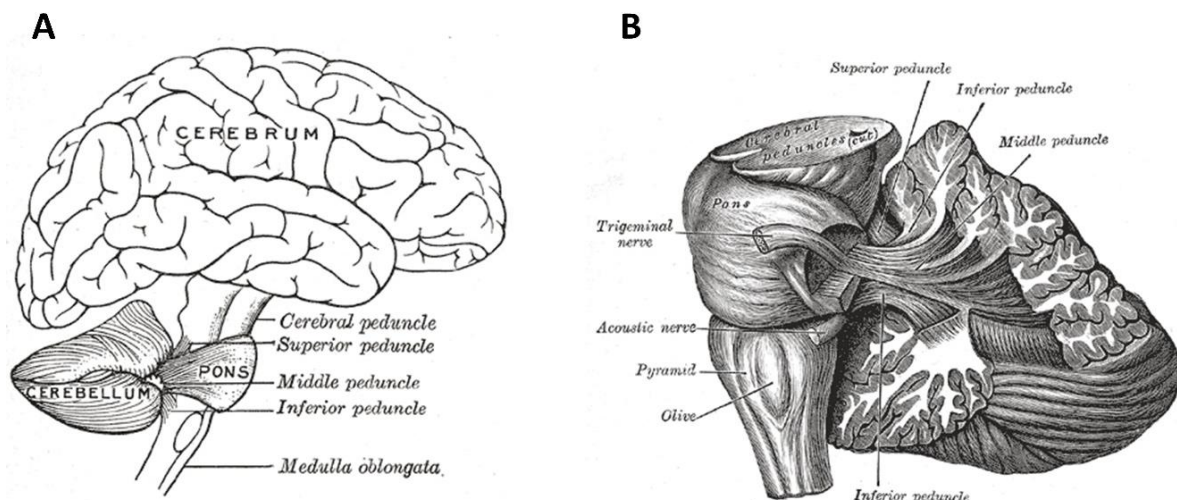


**Figure 1.5. (A)** A sagittal view of cerebellum's location along with its connections to the brainstem. **(B)** The three fundamental cerebellar peduncles. (Adapted from wikipedia.org).

The superior peduncle is connected to the cerebral cortex through the cerebral peduncle where the midbrain is located. The pons, medulla oblongata (also known as medulla) and midbrain (or mesencephalon) form the three major parts of the brainstem. Pons carries the sensory signals up into the thalamus which lies on the diencephalon of the brain and relays the sensor and motor signals to the rest of the cerebrum. The midbrain is an important part of the central nervous system which associated with vision, arousal and motor control. Finally, the medulla oblongata is responsible for fundamental human autonomic functions like breathing, heart rate and blood pressure regulation.

Cerebellum lies within the cerebellar cortex which is divided into 10 transverse lobules marked by Roman numerals (i.e., lobules I-X) (**Fig. 1.6**). Each lobule maintains a central portion in the vermis along with two adjacent lateral segments in the hemispheres (**Fig. 1.6**). Lobules I-V define the anterior lobe, lobules VI-IX the posterior lobe and lobule X the flocculonodular lobe of cerebellum. The latter lobe is known as the vestibulocerebellum (or archicerebellum) because it is associated with the vestibular system (i.e., eye movement, image stabilization on the retina, head and eye tracking; vestibulo-ocular reflex) (Roostaei, 2014; Fletcher, 2016; Stoodley and Limperopoulos, 2016). It receives inputs from the vestibular nuclei as well as visual inputs from the midbrain and sends outputs directly to the vestibular nuclei.

The vermis as well as the intermediate parts of the cerebellar hemispheres form the spinocerebellum, which is also known as paleocerebellum or rostral lobe, and is involved in motor movement, adjustment and coordination (Roostaei, 2014; Fletcher, 2016; Stoodley and Limperopoulos, 2016). Finally, the lateral parts of the hemispheres form the largest part of cerebellum, the neocerebellum, which is also known as cerebrocerebellum or caudal lobe, and is mainly involved in sensorymotor tasks and recently in various cognitive functions (Roostaei, 2014; Fletcher, 2016; Stoodley and Limperopoulos, 2016). It receives input from the parietal lobe through the pontine nuclei, forming pathways that terminate in areas of the premotor cortex and primary motor areas of the frontal lobe (Roostaei, 2014).

Cerebellum is anatomically divided into the 3 major lobes (i.e., anterior, posterior and flocculonodular) by 2 major transverse fissures, known as the primary and the horizontal or posterolateral fissures (Stoodley and Limperopoulos, 2016). The primary fissure separates the anterior from the posterior lobe, the horizontal fissure lies between the posterior and the flocculonodular lobe and the posterolateral fissure separates the flocculonodular lobe from the rest of the cerebellum (**Fig. 1.6**). In addition, there are several secondary fissures; the precentral fissure which is located between lobules I and II, the preculminate fissure which is located between lobules III and IV, the intraculminate fissure which is found between lobules IV and V, the ansoparamedian fissure which separates lobules VIIa and Crus II from lobule VIIb, the prepyramidal fissure which separates lobules VIIb and VIIIa and the intrapyramidal (or intraviventer) which is located between the folium (refers to one of two subdivisions of lobule VII of the cerebellar vermis) and lobule VIIIb.

Cerebellum's structure has been compartmentalized using anatomic, molecular, and physiologic approaches to longitudinal zones (vertical incisions) (Apps and Hawks, 2009). A longitudinal zone is a narrow, rostrocaudally extended sagittal region of the cerebellar cortex in which Purkinje cells receive climbing fiber inputs from specific subregions of inferior olive and project to specific cell groups of the deep cerebellar nuclei (Roostaei, 2014). For example, imagine that the vermis and cerebellar hemispheres on **Fig. 1.6** can each be divided into 3 to 5 longitudinal zones from midline to lateral. In fact, each longitudinal zone can be further subdivided to even narrower compartments which are known in the literature as microzones (Roostaei, 2014). The microzones within the inferior olivary and deep cerebellar nuclei could be regarded as the functional units (or modules) of the human cerebellum. This longitudinal



#### **1.1.4. Cerebellum and intelligence**

The organized network activity at rest could be viewed as the idle state of the brain functions engaged during different tasks in cognition, also influenced by personalized characteristics as lifestyle, demographics and psychometric measures including intelligence (Smith et al., 2015). The human intelligence, which is a general cognitive mental ability, depends on structural and functional properties of the brain, as well as on the interaction among different brain regions (Jung et al., 1999; Duncan et al., 2000; Shaw et al., 2006). Findings support the importance of prefrontal cortex and regions of parietal lobes for intelligence (Duncan, 1995; Jung and Haier, 2007; Song et al., 2008; Deary et al., 2010; Ryman et al., 2016). Prefrontal and posterior parietal brain lobes, which are mostly related to intelligence (Basten et al., 2015; Ryman et al., 2016), have many connections to cerebellum (Koziol et al., 2014; Styliadis et al., 2015). Gray and white-matter characteristics have been used to study the correlation between structural findings and intellectual abilities (Mechelli et al., 2005; Hulshoff Pol et al., 2006; Choi et al., 2008; Malpas et al., 2016), while studies associating anatomical and functional connectivity with intelligence have been also reported (Haier et al., 2005; Song et al., 2008; Chiang et al., 2009; Ryman et al., 2016; Tsvetanov et al., 2016), with indicative biomarkers involving the total brain volume and the concentration of the N-acetyl aspartate (McDaniel, 2005; Paul et al., 2016). Furthermore, there are many factors involved in cognitive processes justifying the examination of various brain areas in relation to IQ aspects, like the basal ganglia implicated in cognitive task processing.

It is worth mentioning that the human cerebellum receives multiple inputs from contra- and ipsilateral hemispheres (Suzuki et al., 2012; Sokolov et al., 2014). There is evident functional connectivity among mentalizing areas of the cerebrum (mainly medial prefrontal cortex, medial parietal cortex, and bilateral temporo-parietal region) and mentalizing areas of the cerebellum (mainly the posterior lateral cerebellar lobules) (Van Overwalle et al., 2015; Van Overwalle and Mariën, 2016). Recently, functional and structural networks have been extensively used to study the correlation between brain organization and intelligence. These studies revealed important correlations of local and widespread brain properties related to the cognitive functions and intelligence (Li et al., 2009; Douw et al., 2011). Global efficiency of functional brain networks and rich club organization appear to be important factors in intelligence (Van den Heuvel et al., 2009; Kim et al., 2016; Yeo et al., 2016). Even though it is known that the cerebellum is actively involved in cognitive processes (Koziol et al., 2014; Styliadis et al., 2015), there is a limited research investigating its relationship with IQ. The relationship between cerebellum and intelligence constitutes the first of the two fundamental tasks of this thesis.

#### **1.1.5. Clinical abnormalities**

Deficits resulting from cerebellar lesions include motor dysmetria, ataxia, and intention tremor, but also the cerebellar cognitive affective syndrome (Schmahmann and Sherman,

1998) including executive, visual–spatial, linguistic and emotional deficits, and even mutism and psychosis (Stoodley and Schmahmann, 2009). Damage in the superior peduncle results in hypotonia, hypermetria and intention tremor (Fletcher, 2016). Lesions in the cerebellar hemispheres could lead to deficits in motor planning, delays in the onset of movements, loss of muscular coordination and irregularities in timings of movement components (Roostaei, 2014; Fletcher, 2016). Lesions on the vermis lobules result in truncal tremor and gait ataxia (Fletcher, 2016). Lesions on spinocerebellum could lead to saccadic dysmetria and/or vergence abnormalities (Roostaei, 2014). These disorders in cerebellum usually result from tumors, genetic disorders and heavy metal poisoning (Fletcher, 2016). Furthermore, structural abnormalities in cerebellum have been linked with Attention Deficit Hyperactivity Disorder (ADHD), Autism Spectrum Disorder (ASD) and developmental dyslexia. Reports from ASD studies reveal reduced gray matter concentration in lobule IX, left lobule VIIIb, and Right Crus I (Stoodley, 2014). In ADHD, significantly decreased gray matter has been discovered bilaterally in lobule IX, whereas subjects with developmental dyslexia exhibit decreased gray matter concentration in left lobule VI (Stoodley, 2014).

#### **1.1.6. The anatomical atlas used in this thesis**

The probabilistic anatomical atlas used in this study (**Fig. 1.7(A)**) was obtained from the [spatially unbiased infratentorial template \(SUIT\) toolbox](#) (Diedrichsen et al., 2009; Diedrichsen et al., 2011; Diedrichsen and Zotow, 2015), which is already normalized with the fast nonlinear image registration (FNIRT) normalization method in the Montreal Neurological Institute (MNI152) template. SUIT's probabilistic atlas of cerebellar anatomy (Diedrichsen et al., 2009) was based on the hand segmentation of the cerebellar lobules in 20 healthy participants (10 males, 10 females; average age 23.7 years). These anatomical data were used to create an atlas template of the human cerebellum. Lobules I-IV, V, VI, VIIa (Crus I and Crus II), VIIb, VIIIa, VIIIb, IX and X were separated on T1-weighted MRI scans, where lobules I-IV were added on the same mask and the rest on separate masks using FSL view (Diedrichsen et al., 2009). More specifically, SUIT's cerebellum parcellation procedure was based on Schmahmann's proposal (Schmahmann et al., 1999), with the left and right hemispheres being labeled as separate compartments for all cerebellum lobules (the term lobule is used to denote both hemispheric and vermal compartments). However, the vermal compartments (Vermis VI-X) were defined separately only for the posterior cerebellum (lobules VI-X), due to the clear anatomical boundary between vermis and hemisphere (Schmahmann et al., 1999). In total, 28 regions of interest (ROIs) were defined (see Diedrichsen, 2006; Diedrichsen et al., 2009; Diedrichsen and Zotow, 2015, for further info). A straightforward approach often employed for effective visualization of the cerebellar anatomical areas, as well as their inner compartments, is to construct a flat-surface representation by means of a 2D projection (Diedrichsen and Zotow, 2015) (**Fig. 1.7(B)**).

The aforementioned anatomical atlas is used in order to extract the cerebellar voxels from the fMRI scans (a procedure known as parcellation) prior to the network analysis and

voxel-wise clustering procedures that are described later on, in **Chapters 3 and 4** respectively. It is important to note that both the atlas and the fMRI data are registered on the same coordinate space, i.e., the MNI space, and therefore the parcellation procedure is valid.

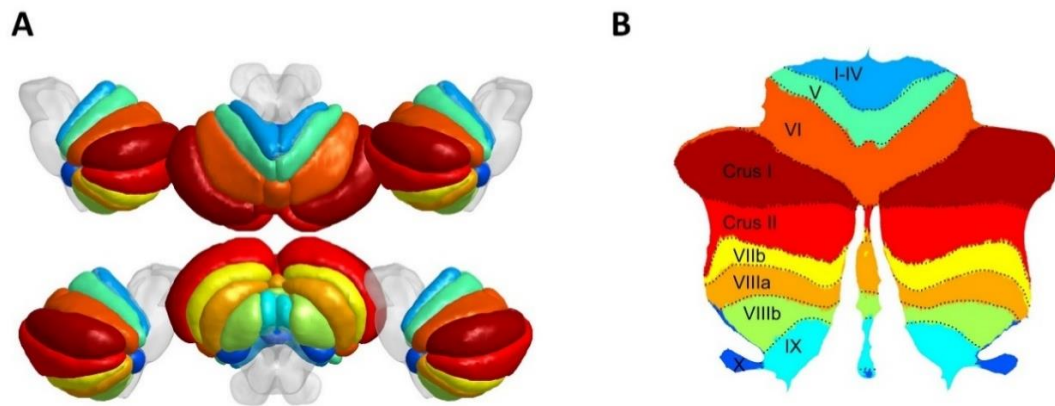


**Figure 1.7.** The anatomical atlas of cerebellum used in this study. **(A)** A complete 3D view of the regions of interest, using BrainNet Viewer (Xia et al., 2013). **(B)** The corresponding flatmap (unfolded) representation of the same atlas based on SUI’s toolbox.

## 1.2. The fMRI dataset

The dataset used in this thesis was collected from the Human Connectome Project (HCP) database, an open-source database aiming to provide deep examination of the human brain connectome (Van Essen et al., 2013).

### 1.2.1. The Human Connectome Project

The Human Connectome Project (HCP) is the result of efforts of co-investigators from the University of California, Los Angeles, Martinos Center for Biomedical Imaging at Massachusetts General Hospital (MGH), Washington University, and the University of Minnesota. The major goal of the HCP is to acquire and share data concerning the structural and functional connectivity of the human brain. More specifically, the project aims to collect resting-state and task fMRI data from hundreds of subjects including twin pairs, develop straightforward tools for providing a detailed mapping of the human connectome as well as a robust and web-based infrastructure for data access and analysis pipelines. HCP is a five-year project sponsored by sixteen components of the National Institutes of Health (NIH), split between two consortia of research institutions. [Funding for the Harvard/MGH-USC consortium is provided through the grant award U01-MH93765.](#)

The present study analyzes resting-state fMRI (rs-fMRI) data that were collected from the HCP database after the HCP S500 + MEG2 data release, between the first six quarterly releases (Q1–Q6), with few cases also collected in Q7 and later. Functional magnetic resonance imaging (fMRI) data was initially acquired from 492 healthy subjects at rest with eyes open

with relaxed fixation on a projected bright cross-hair on a dark background (and presented in a darkened room) (Van Essen et al., 2013). The pre-processed (cleaned) volumetric signals corresponding to the BOLD fMRI time-series were collected from all 492 subjects and were prepared for further analysis using Matlab (The Mathworks Inc., version R2014). Subsets of this huge dataset have been used in **Chapters 3 and 4**. At this point, it is worth mentioning that the latest HCP dataset release includes data from 1100 young healthy adults.

### **1.2.2. HCP scanning parameters and pre-processing pipelines**

The resting-state BOLD signals were obtained through a gradient-echo, EPI sequence using a specifically customized 3T scanner (Van Essen et al., 2012, 2013). In total, 91 volumes were collected with the following parameters: TR = 720 ms, TE = 33.1 ms, FA = 52°, FOV = 208x180 mm, matrix size of 104x90, slice thickness = 2.0 mm; 72 slices; 2.0 mm isotropic voxels, multiband factor = 8, echo spacing = 0.58 ms, bandwidth = 2290 Hz/Px. Descriptions of these scanning parameters are provided in **Chapter 2**. Denoised BOLD time-series consisting of 1200 frames with approximately 15 min duration were extracted from the first resting state session (REST1) of the HCP data management platform, i.e., [connectomeDB](https://connectomeDB.org/), where the oblique axial acquisitions alternated between phase encoding in a left-to-right (LR) direction.

HCP investigators have already performed two basic preprocessing pipelines (Glasser et al., 2013; Van Essen et al., 2013). The first volume-based pipeline removes spatial distortions, realigns volumes using FSL's FLIRT-based motion correction, normalizes the intensity of 4D images to a global mean, registers data into MNI space and finally masks the data with the final brain mask derived from FreeSurfer segmentation. The second surface-based pipeline aims at transforming the time series from volume space to CIFTI gray-ordinates standard space with 2 mm average surface vertex and subcortical volume spacing. Surface data was smoothed using a 2 mm FWHM (Full Width at Half Maximum) kernel and ICA (Independent Component Analysis) was used to isolate independent components from the data based on FSL's MELODIC tool developed by Beckmann and Smith (Beckmann and Smith, 2004), with automatic dimensionality reduction to a maximum of 250 independent components, typically preserving 230 components (Van Essen et al., 2013). The resulting artifactual components were classified into two groups using the FIX algorithm (i.e., FMRIB's ICA-based X-noisefier) developed by Salimi-Khorshidi and colleagues (Salimi-Khorshidi et al., 2014) and finally were removed from the data. Further details on the aforementioned preprocessing pipelines are provided in (Glasser et al., 2013; Van Essen et al., 2013) and some of them are described in **Chapter 2, Section 2.6**.

### **1.2.3. Additional information related to subjects history**

We further requested and received access to sensitive data by signing all necessary consent forms. Subjects with psychiatric history, extensive substance use and hard alcohol history have been completely removed since the cerebellum is heavily impacted by alcohol

abuse/dependence (Sullivan et al., 2010) and there is also evidence to suggest that the cerebellum is impacted by marijuana as well (Block et al., 2000; Lopez-Larson et al., 2011; Solowij et al., 2011). Additional information related to siblings and twins have been obtained. The population has been restricted to only one member of a sibling/twin pair so as to overcome shared variance issues. In addition, crystallized IQ scores were obtained per subject prior to scanning procedure for the needs of **Chapter 3**. Gender information and age intervals per subject are publicly available and did not require any further access to sensitive data.

### **1.3. Modern network analysis and Spectral Graph Theory in neuroscience**

Graph models have been used to represent activity interaction networks, which are often characterized as regular, random, or small-world networks (Boccaletti et al., 2006). The latter class combines high clustering (like regular networks) with short path lengths (like random networks) (Watts and Strogatz, 1998; van den Heuvel et al., 2008a; Messé et al., 2012; Stam and van Straaten, 2012; Stam et al., 2016; Miraglia et al., 2016). Thus, small-world networks are characterized by optimum local segregation and global integration (Stam et al., 2014a; Tewarie et al., 2015b) and form appropriate models for the neural systems including the brain (Watts and Strogatz, 1998; Stam and van Straaten, 2012; Stoodley et al., 2012; Muller et al., 2014). Modern network analysis using graph theoretical tools has become essential in studying the topology of the brain networks. Examples of such studies explore aspects of small-world networks, scale free networks, their hubs and modularity in functional brain networks. Their different parameters are extracted after the construction of a binary (a connection either exists or does not exist) or weighted graph (the connections have strengths) depicting the strength of synchronization and other measures of connectivity among all pairs of the nodes (Stam and van Straaten, 2012; Stam, 2014b). During the last years, the concept of the minimum spanning tree (MST) has been used as an unbiased method for brain networks. MST representations allow comparisons of graphs in different situations or between different individuals avoiding methodological biases. Additionally, the MST is a subnetwork providing similar information with the conventional graph parameters about network topology (Tewarie et al., 2015b). The MST parameters give information related to node characteristics and the diffuse organization (Stam, 2014b; Tewarie et al., 2015b). These parameters are used for hub analysis in order to determine the nodes with high importance during information transfer. Furthermore, they can be used for statistical analysis application with the purpose of discovering significant differences among populations of interest.

Spectral graph theory is based on the eigenvalues and eigenvectors of the Laplacian of a graph in order to solve complex graph partitioning problems based on common linear algebra aspects. The Laplacian of a graph works like the differential operator and therefore provides information about the density of each node within a network. Such a representation combined with the eigenvectors provides a mapping of the original graph onto the eigen-space, where clustering is much easier to be dealt with using a simple  $k$ -means procedure.

The Normalized-cut and spectral clustering algorithms are the two major algorithms of the spectral graph theory (Shi and Malik, 2000). Of course, these algorithms are non-supervised and therefore repeated cross-validation procedures are necessary in order to determine the correct number of clusters prior to the final application on the data. Spectral graph theory has been employed as an accurate clustering method in a variety of resting-state functional connectivity studies of the human brain (van den Heuvel et al., 2009; Craddock et al., 2012; Sato et al., 2013). More specifically, in the study of van den Heuvel et al., 2008b, the Normalized-cut algorithm was applied so as to identify the whole brain's resting-state networks on individual and group levels as well, with an optimal group clustering fit. In the work of Craddock et al., 2012, a spatially constrained version of the Normalized cut (N-cut) algorithm was used in order to generate a whole brain fMRI atlas. In addition, the silhouette width was used as a functional homogeneity quantifier of the ROIs and the dice index was used to measure the similarity between group and individual level clustering. Finally, in the work of Sato et al., 2013, the spectral clustering concept was applied in order to investigate the topological organization of brain's subnetworks modules in ADHD subjects combined with the network's entropy, where the silhouette method was used for determining the correct number of clusters. In the second part of this thesis (**Chapter 4**), Spectral Graph Theory was employed to construct a resting-state functional network atlas of the human cerebellum.

#### **1.4. Related studies in cerebellar and cerebral hemispheres**

Studies on cerebral hemispheres using MRI revealed several differences between men and women, using for instance correlation analysis of MRI data of the cerebral hemispheres (Biswal et al., 2010). In another study, functional connectivity differences between men and women were detected for local and widespread connections, with women showing higher local connectivity density (Tomasi and Volkow, 2012). Studies using fMRI have been performed during several motor or cognitive activations, where the involved regions in the cerebrum and cerebellum become visible. Prefrontal and posterior parietal brain lobes, which are mostly related to intelligence (Basten et al., 2015; Ryman et al., 2016), have many connections to cerebellum (Koziol et al., 2014; Styliadis et al., 2015). Furthermore, there are many factors involved in cognitive processes justifying the examination of various brain areas in relation to IQ aspects, like the basal ganglia implicated in cognitive task processing. Even though it is known that the cerebellum is actively involved in cognitive processes (Koziol et al., 2014; Styliadis et al., 2015), there is a limited research investigating its relationship with IQ. Overall, several tasks such as motor, language, emotional tasks, working memory, music and timing tasks have been also used. The links between cerebrum and cerebellum show a topographical organization (Stoodley and Schmahmann, 2009; Buckner et al., 2011). Functional connectivity studies in brain hemispheres have shown sex differences most commonly reported for the Default Mode Network (DMN), where females show greater connectivity (Allen et al., 2011; Tomasi and Volkow, 2012). Szalkai and colleagues (Szalkai et

al., 2015) using material from the HCP discovered that the average female connectome has more edges and forms a better expander graph, with minimal bisection width as well as more spanning trees than the average male connectome.

Concerning the cerebellum, its lobules are co-activated mainly with regions of the opposite cerebral hemisphere (Apps and Hawkes, 2009; O'Reilly et al., 2010). Additionally, co-activations occur in several cerebellar lobules as well as the lobules of vermis (Bernard et al., 2012; Stoodley et al., 2012). In a recent study (Apps and Hawkes, 2009), the authors explored interactions within the cerebellum and with other cortical and subcortical structures of the brain. They used resting-state functional connectivity in MRI and the cerebellar anatomy (lobules) to estimate co-activations. They found that functional organization of the human cerebellum does not map onto lobular anatomy, a fact that had been noticed before. To extract more detailed information related to the synchrony in the cerebellum and the hemispheres, they used a self-organizing map approach to parcellate the cerebellum. This helped identifying networks with functional similarities independent of the anatomically identified cerebellar networks (Bernard et al., 2012). The organization of cerebellum lobules forms an exploratory issue of the first part of this thesis. Intrinsic connections in cerebellum can give information related to lobules activations or network organization at rest and/or several activations. The local cerebellar activations without the combination to the cerebral hemispheres have not been extensively studied in the literature (Bernard et al., 2012) and this constitutes a fundamental motivation of the current thesis.

## **1.5. Scope and contribution to the existing literature**

The main goal of this thesis is to investigate the functional connectivity of the cerebellar network and its organization during rest, based on fundamental concepts of graph theory for brain network analysis. Concepts like the spectral clustering scheme, which is based on graph partitioning in order to cluster the voxels with similar activation patterns as well as the Minimum Spanning Trees (MSTs) concept, which facilitates consistent and quantitative graph comparisons that are able to overcome methodological biases in graph comparisons as well as disconnected syndromes. Through the computation of various MST metrics, reliable estimations are extracted concerning the local and widespread characteristics of cerebellum's connectivity. In addition, hubs that signify regions with the highest activity across the network can be also detected. Statistical analysis on the extracted measures is able to reveal potential significant differences between low and high-IQ groups as well between males and females.

The author strongly believes that the current results can enhance relevant knowledge to the existing literature and provide good impact in the neuroscientific community. The first part of this thesis aims to investigate the relationship between cerebellum and intelligence using resting-state fMRI data. A classic lobular anatomical analysis of cerebellum on low and high-IQ groups is able to model the functional connectivity networks. The corresponding

MSTs are able to reveal the backbone of these networks along with the extracted features which can be used to describe the functional and structural characteristics of the trees as well as identify the critical nodes within the original networks. More importantly, they can be used for statistical analysis among these two populations by taking into consideration the gender factor. As far as the second part of this thesis is concerned, an attempt to provide a deeper investigation of the cerebellar network is performed by considering each voxel as a single unit or node, thus ignoring lobules. The goal of this procedure is to extract a resting-state network atlas of cerebellum where each region will contain voxels with similar activations. This atlas can be combined with the anatomical atlas in order to form a much more detailed atlas, called functional atlas. The functional atlas can be used for repeating the network analysis procedure described previously, focusing on the gender factor only. The results of this part are data-driven and therefore more accurate. Finally, the extracted atlases will be freely available for reinforcing the neuroscientific community as well as to encourage future cerebellar studies.

The author is proud to mention that the results of the first part of this thesis have been published under the frontiers in Human Neuroscience journal (Pezoulas et al., 2017) as part of the research topic Applied neuroscience: Methodology, Modeling, Theory, Applications and Reviews. The frontiers in Human Neuroscience is the **#1** most cited journal in psychology and the **#1** largest open-access publisher in the category of neuroscience (IF: 3.209, 2017). The same work has been also presented in the form of a conference abstract at the Society of Applied Neuroscience (SAN) biennial meeting (organized by the same journal) in Corfu, 2016. The results of the second and largest part of this thesis are being prepared for submission in the IEEE Journal of Biomedical and Health Informatics journal (IF: 3.451, 2017).

## 1.6. Thesis outline

In this study, the cerebellar network was explored by executing a lobular and a voxel-wise analysis approach, based on tools from modern graph theory.

In **Chapter 2 – Functional Magnetic Resonance Imaging (fMRI)**, the historical background and the basic functionality of fMRI is described. Prior to the description of fMRI's mechanism, fundamental information about the basic concepts of Magnetic Resonance Imaging (MRI) are provided in **Section 2.2** (i.e., the Larmor frequency, resonance, repetition and relaxation times, basic MRI pulse sequences and image reconstruction). The BOLD contrast mechanism is described in **Section 2.3** along with the leap from MRI to fMRI (**Section 2.4**). The spatiotemporal resolution of fMRI is discussed in **Section 2.5** which constitutes a fundamental advantage of fMRI over conventional non-invasive approaches. Basic fMRI pre-processing techniques, including those mentioned in **Section 1.2.2**, are further described in **Section 2.6**. Clinical applications of fMRI including a wide range of pathologies are described in **Section 2.7**, with an overall assessment of fMRI being depicted at **Section 2.8**.

**Chapter 3 – Lobular analysis of cerebellum’s network with respect to IQ and gender**, constitutes the first part of cerebellum’s network analysis. The fundamental hypothesis of the first part of this study is that the local and global characteristics of the cerebellar network exhibit significant differences which are related to gender and IQ. The driving question of the first part of this thesis concerns the extent to which the cerebellum is related to intelligence, in men and women, beyond the cognitive processes (**Section 3.1**). The network organization in individual groups of different gender and IQ levels is examined. The population of interest consists of 69 low-IQ (25/44; males/females) and 67 high-IQ (29/38; males/females) subjects (**Section 3.2**). Cerebellum’s anatomical parcellation procedure is described in **Section 3.3** and the network construction in **Section 3.4** along with the small-worldness property evaluation process. Then, the corresponding Minimum Spanning Trees (MSTs) were computed in order to extract valuable local (degree, betweenness centrality and eccentricity) and global (diameter, radius, leaf fraction, tree-hierarchy, kappa or degree divergence) MST measures (**Section 3.5**). Additional local (i.e., clustering coefficient, characteristic path length or lambda, small-worldness) and global (a proposed connectivity measure) features were extracted from the original networks. The local MST measures of degree and betweenness centrality were then used in order to identify the nodes with the highest importance in the networks of low and high-IQ groups, i.e., hubs (**Section 3.6**). In addition, correlations between the hub metrics and the Median Response Times (MRTs) were computed for each IQ group and for both genders (**Section 3.7**). The computed set of metrics gave rise to extensive statistical analysis in order to examine differences between low and high-IQ groups, as well as between all possible gender-based group combinations (**Section 3.8**). Finally, the acknowledgements in **Section 3.9** state the HCP’s policy and the authors related publications.

**Chapter 4 – Voxel-wise analysis of cerebellum**, constitutes that second and final part of cerebellum’s network analysis. The goal of this chapter is to extract a data-driven resting-state network (RSN) atlas of cerebellum which will be combined with the anatomical atlas in order to construct a detailed functional atlas that will be used for gender-based functional connectivity analysis (**Section 4.1**). The population of interest has been restricted to equally numbered males and females (50/50; males/females) this time (**Section 4.2**). The anatomical parcellation procedure overcomes the lobular boundaries of cerebellum and considers each voxel as a single unit (or node) thus increasing the memory requirements (**Section 4.3**). An extra filtering is applied in the BOLD time-series of each voxel, per subject, in order to eliminate low-frequency noise (e.g., respiratory noise) since averaging is not an option in this part of the analysis (**Section 4.4**). Then, voxel-wise graphs are constructed per subject using correlation coefficient as a functional connectivity measure (**Section 4.5**). **Section 4.6** describes the theoretical basis of spectral graph theory, mainly focusing on the Laplacian of a graph and the spectral clustering and Normalized-cut algorithms for providing solutions to the graph partitioning problem along with a spatially constrained version of the spectral clustering approach, similar with the one described in Craddock et al., 2012 and requires an extra computation of a voxel-wise distance matrix which is multiwise multiplied with the similarity matrix. In fact, a spatially constrained version of the original spectral clustering

algorithm (SCSC) along with a complete cross-validation procedure is proposed and applied on the HCP data. The clustering evaluation (i.e., the average silhouette and Davies-Bouldin indices) along with the clustering homogeneity (i.e., Shannon's entropy) measures are described in **Sections 4.7 and 4.8**, respectively. The spectral clustering and Ncut approaches are first applied on synthetic data (**Section 4.9**) in order to reveal their (crucial) weakness to background noise and how the SCSC procedure is able to overcome this issue. Afterwards, the aforementioned clustering methods are applied on the average correlation matrix across all subjects where the SCSC approach is tested for various thresholds on the distance matrix and then the clustering evaluation measures are computed (**Section 4.10**). A repeated cross-validation (i.e., 10 times) is applied to seek for the threshold (on the distance matrix) that exhibits the most stable performance, i.e., the optimal number of clusters across all runs of the validation procedure (**Section 4.11**). In addition, that threshold must be able to provide maps with highly consistent clusters across all runs – a fact that is evaluated using the Dice similarity coefficient measure. The SCSC algorithm is then applied on the original data using the estimated parameters from **Section 4.11**, leading to the resting-state network (RSN) atlas of cerebellum (**Section 4.12**). This atlas is combined with the anatomical atlas of cerebellum to construct a (detailed) functional atlas with more regions (**Section 4.13**). The latter atlas is used for executing a gender-based functional connectivity analysis of cerebellum similar to the procedure described in **Chapter 3** along with the hub(s) and statistical analysis (**Section 4.14**). Finally, the acknowledgements in **Section 4.15** state the HCP's policy and the authors related publication under preparation.

In **Chapter 5 – Discussion and future work**, an overall discussion and assessment of the results from **Chapters 3 and 4** is provided. Future studies are necessary in order to further address these results in cerebellar-cerebral studies. Finally, the atlases computed in **Chapter 4** will be made publicly available by the author for encouraging future cerebellar studies.

## 2. Functional magnetic resonance imaging

---

### 2.1. History

In the field of neuroscience and specifically in brain functional connectivity analysis, there are two fundamental non-invasive methods that have been developed over the past years which aim to map brain's functional connectivity: **(a)** those that are able to localize the underlying neural electromagnetic activity of the brain and **(b)** those that reflect the local neuronal signaling by mapping the local physiological or metabolic consequences of the altered brain electrical activity (Mathews and Jezzard, 2017). Electroencephalography (EEG) and magnetoencephalography (MEG) are the most common techniques that belong to the first category which examine the electrical and magnetic activity of the brain providing high temporal but poor spatial resolution. The second category evolves modern in-vivo imaging techniques such as magnetic resonance imaging (MRI), positron emission tomography (PET), functional magnetic resonance imaging (fMRI), etc. In this work, emphasis will be placed on fMRI, a non-invasive straightforward approach which is based on the increase in blood flow (or blood oxygenation) to the local vasculature that accompanies neural activity in the brain and provides excellent spatial resolution with an uncertain temporal resolution (Chen and Li, 2011; Glover, 2011; Matthews and Jezzard, 2017).

Over a few decades ago, it has been known that changes in blood flow and blood oxygenation are closely linked to neural activities in the brain. According to the study of Ogawa in 1990 (Ogawa et al., 1990; Ogawa and Lee, 1990), a relationship between de-oxygenated blood flow and distortions on magnetic resonance images was noticed during brain studies on rats using strong magnetic fields (7 and 8.4 Tesla<sup>1</sup>). Ogawa's fundamental observation was that the blood oxygenation level was able to control these distortions, a fact that later led to the development of the well-known Blood Oxygen Level Dependent (BOLD) contrast mechanism. In addition, the first successful fMRI study was conducted at the MGH-NMR (Massachusetts General Hospital - Nuclear Magnetic Resonance) Center under the research leadership of Dr. John Belliveau (Belliveau et al., 1991). Belliveau proposed a breakthrough magnetic resonance technique for quantitative imaging of cerebral hemodynamics, allowing for measurement of regional cerebral blood volume during resting and activated cognitive states (Belliveau et al., 1991). The aforementioned brain imaging

---

<sup>1</sup>1 Tesla = 10.000 Gauss, Earth's magnetic field = 0.5 Gauss.

mechanism was based on the well-known dynamic susceptibility contrast (DSC) using injected Gd-DTPA (gadolinium-diethylenetriamine pentaacetic acid) as an MRI contrast agent (Carr et al., 1984; Belliveau et al. in 1991). This technique was used to generate the first ever functional magnetic resonance maps of human task activation, by using a visual stimulus paradigm (Belliveau et al. in 1991; Kwong et al., 2012). That experiment was the first to explore the power of the intrinsic blood contrast.

One of the most challenging processes in the field of neuroscience is to comprehend the relationship between the BOLD signal and the neural activation. What the BOLD fMRI mechanism does it to detect the local increases in relative blood oxygenation that are most probably a direct consequence of neurotransmitter action and thus reflect local neuronal signaling (Matthews and Jezzard, 2017). As a matter of fact, this method allows localization to volumes of the order of a few to several cubic millimeters ( $mm^3$ ) and can be used in serial studies of individual subjects. It is now known that the BOLD signal does not correlate perfectly with neuronal action potentials but measures a mix of continuous membrane potentials and action potentials (Logothetis and Wandell, 2004). This fact might well complicate the interpretation of the neural activity within a small unit but on the other hand makes us wonder whether the neural information processing might extend beyond action potentials or not (Logothetis and Wandell, 2004).

Nowadays, fMRI dominates in the human brain mapping field due to its relatively low invasiveness, absence of radiation exposure, and relatively wide availability (Chen and Li, 2012). It has been established that fMRI has been used in a large number of studies like in cognitive and affective neuroscience, clinical psychiatry/psychology as well as pre-surgical planning (it has been estimated that where exist between 100.000 and 250.000 entries in PubMed, depending on keywords, according to the paper of Glover, 2011). Functional magnetic resonance imaging has provided researchers with unprecedented access to the brain in action and, in the past decade, has provided countless new insights into the inner workings of the human brain (Lindquist, 2008).

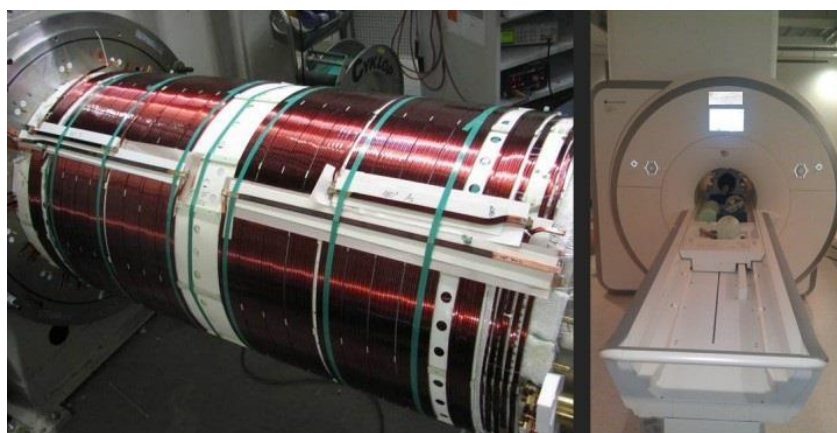


**Figure 2.1.** The fMRI Connectome scanner which is located at the Athinoula A. Martinos Center for Biomedical Imaging, Massachusetts General Hospital (MGH). (Adapted from <http://www.humanconnectomeproject.org/about/scanner/>).

## 2.2. Magnetic Resonance Imaging

In order to comprehend the complex nature of fMRI data and how these images are used to investigate the neuronal activity, it is crucial to understand some basic MRI principles.

### 2.2.1. Physiological basis

Magnetic resonance imaging (MRI) is a modern imaging technique which uses the body's natural magnetic properties to produce detailed images from any part of the body. MRI uses the magnetic characteristics inherent to the protons of hydrogen nuclei in the tissue, mostly in the form of water but to a significant extent in fat as well. The protons spin about their own axes, which creates a magnetic dipole moment for each proton (**Fig. 2.2**). In the absence of an external magnetic field, the axes of these dipoles are arranged randomly, and therefore, the vectors depicting the dipole moments cancel each other out, resulting in a zero net magnetization vector (NMV) and a zero net magnetic field (NMF) for the tissue.

In clinical practice, the hydrogen nucleus (a single proton) is used due to its abundance in water and fat. When the human body is placed in a strong magnetic field generated by a primary superconducting magnet, the protons' axes behave like magnetic dipoles and are all aligned upwards. In fact, some protons will point in the direction of the external field (i.e., north), some will point in the opposite direction (i.e., south), but the net magnetization vector of the dipoles (the sum of individual spins) will point in the direction of the external field. This uniform alignment creates a magnetic vector which is oriented along the axis of the MRI scanner's applied magnetic field. A small proportion of the protons (and therefore the NMV of the tissue) is aligned along the external field (longitudinal magnetization), and the protons precess with a certain frequency (**Fig. 2.2**). The term precession means that a proton spinning about its own axis is simultaneously wobbling about the axis of the external field.

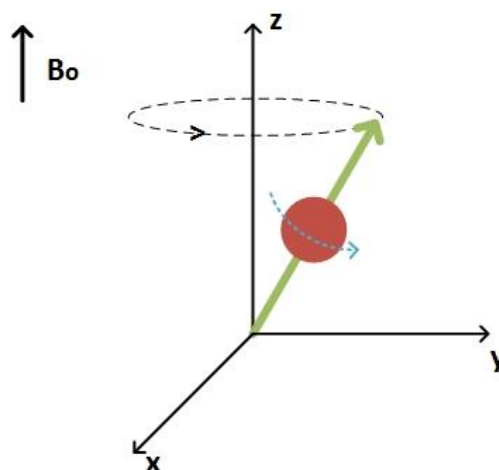


**Figure 2.2.** In an external magnetic field, protons spin around their own axis and wobble about the axis of the magnetic field (precession). Usually the z direction is up, i.e., the direction of external magnetic field is in the head-foot direction in the scanner.

With the purpose of acquiring an MR image, a radio-frequency (RF) pulse is generated by a secondary magnetic field and applied to the part of the body being scanned. When the frequency of this RF pulse matches the Larmor or precession frequency of the protons, the latter receive energy and resonance occurs. The protons flip and the NMV of the tissue ceases transiently to be aligned with that of the external field but flips into another plane, thereby transverse magnetization is produced. When the RF pulse is switched off, the magnetic vector returns to its initial (or resting) state and this causes a radio wave to be emitted. This emitted signal, which is the result of the transverse magnetization, is used to construct the magnetic resonance images and is detected using receiver coils placed around the body part under examination. Varying the magnetic field gradient along the  $x$  ( $M_x$ ) and  $y$  ( $M_y$ ) axes, known as phase and frequency encoding, is able to provide sufficient information to decode the spatial coordinates of the signal emitted by each tissue voxel (volumetric pixel in 3D space). This is accomplished using Fourier transform. The final image is produced by applying a gray scale to the intensity values calculated by the Fourier transform for each voxel within the imaging plane, corresponding to the signal intensity of individual tissue elements.

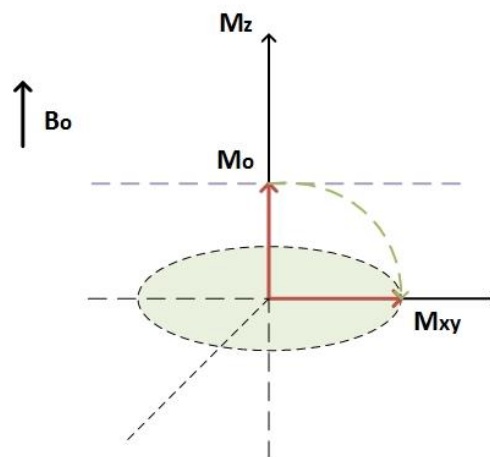


**Figure 2.3.** When a  $90^\circ$  RF pulse is applied, the NMV of the protons ( $M_o$ ) is flipped from the vertical ( $z$ ) plane to the horizontal ( $xy$ ) plane (green dashed arc).

MRI scanners come in different field strengths, usually between 1.5 and 3 Tesla. The strength of the magnetic field can be altered electronically using a series of gradient electric coils and by altering the local magnetic field by these small increments, different slices of the body will resonate as different frequencies are applied. The electrical coils are usually held in zero temperature (using liquid nitrogen or helium), minimizing their resistance and allowing for the strong currents needed to generate the magnetic field.

### 2.2.2. Resonance and Larmor (or precessional) frequency

To determine the spin of a nucleus, one can use the following rules (Zhang et al., 2009):

1. If the number of neutrons and protons are both even, the nucleus has no spin.

2. If the number of neutrons plus the number of protons is odd, then the nucleus has a half-integer spin (i.e.,  $1/2$ ,  $3/2$ ,  $5/2$ ).
3. If the number of neutrons and the number of protons are both odd, then the nucleus has an integer spin (i.e.,  $1$ ,  $2$ ,  $3$ ).

The nuclear magnetic moment ( $m$  or  $\mu$ ) of a nucleus can align with an externally applied magnetic field of strength  $B_o$  in only  $(2I + 1)$  ways, either with or against the applied field  $B_o$ , where  $I$  is the nuclear spin given by **(1)**, **(2)** and **(3)** above. For example, for a single nucleus with  $I = 1/2$ , only one transition is possible between the two energy levels. According to **Fig. 2.2.**, the energetically preferred orientation has the magnetic moment aligned parallel with the applied field (spin  $m = +1/2$ ), whereas the higher energy anti-parallel orientation (spin  $m = -1/2$ ). The rotational axis of the spinning nucleus cannot be orientated exactly parallel (or anti-parallel) with the direction of the applied field  $B_o$  (aligned along the  $z$  axis) but must precess (motion similar to a gyroscope) about this field at an angle, with an angular velocity,  $\omega_L$ , given by **(2.1)**. If we irradiate the sample with radio waves (MHz), then the proton can absorb the energy and be promoted to the higher energy state (**Fig. 2.5**). This absorption is known as resonance because the frequencies of the applied radiation and the precession coincide at that frequency (Zhang et al., 2009).

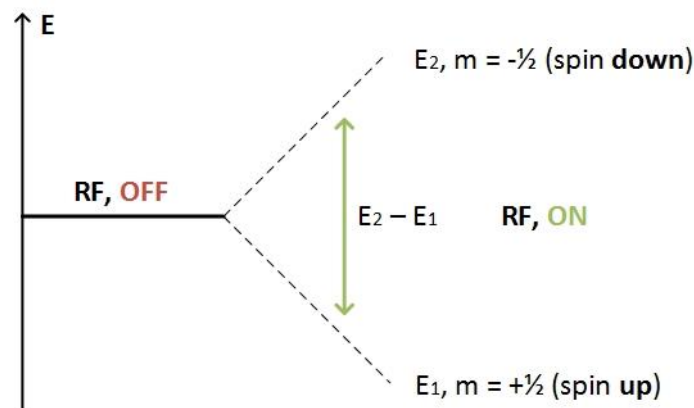


**Figure 2.4.** Splitting of energy levels of a nucleus with spin  $m = 1/2$ , into two states ( $E_2$ ; spin down and  $E_1$ ; spin up).

As it was mentioned in **Section 2.2.1**, in order to construct an MRI image the subject is placed into a strong electromagnetic field (i.e., 1.5-3 Tesla) that is generated by a primary magnet which aligns the magnetization of hydrogen ( $^1\text{H}$ ) atoms within the brain. Then a radiofrequency (RF) pulse with a pre-specified frequency, known as the Larmor frequency or precessional frequency,  $\omega_L$ , is generated by a secondary magnet in order to tip over the aligned hydrogen nuclei. The precessional path around the magnetic field is circular like a spinning top (**Fig. 2.4**). In fact, the Larmor frequency in MRI refers to the rate of precession of the magnetic moment of the proton around the external magnetic field where the frequency of precession is related to the strength of the magnetic field,  $B_o$ , through the following fundamental equation:

$$\omega_L = \gamma \cdot B_o \quad (2.1)$$

where  $\omega_L$  is the Larmor frequency measured in MHz,  $\gamma$  is the gyromagnetic ratio (MHz/Tesla) a parameter that determines how fast the hydrogen will spin around the axis of the magnetic field and  $B_o$  is the strength of the static magnetic field (Tesla). Note that the precession frequency of a hydrogen proton is directly proportional to the strength of the applied magnetic field. The gyromagnetic ratio of the hydrogen isotope is equal to 42.58 MHz/Tesla. Thus the precessional frequency of an 1.5 Tesla MRI scanner should be equal to 63.87MHz.

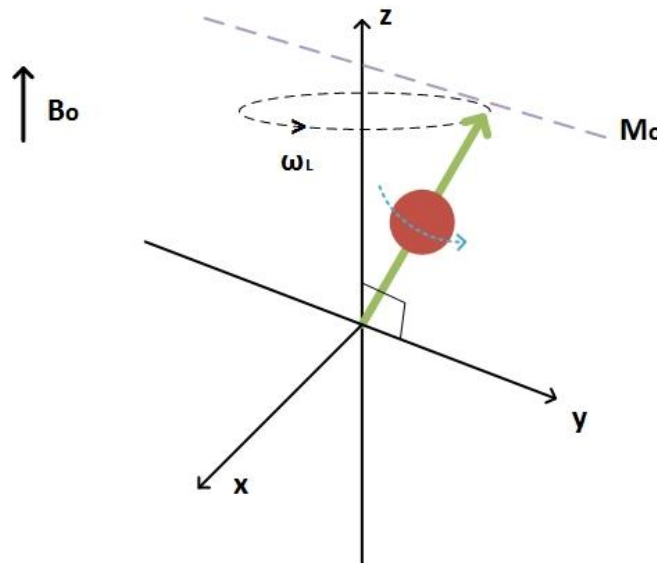


**Figure 2.5.** A magnetic field ( $B_o$ ) is applied along the z-axis, causing the spinning nucleus to precess around the applied magnetic field.

### 2.2.3. Basic MRI pulse sequences and parameters

The repetition time (TR) and echo time (TE) constitute the two fundamental MRI pulse sequence parameters and are typically measured in milliseconds (ms). The echo time (TE) represents the time from the center of the RF-pulse to the center of the echo whereas the repetition time (TR) is the length of time between corresponding consecutive points on a repeating series of pulses and echoes. These times are being presented in the time diagram of a spin echo sequence (**Fig. 2.6**). The parameters  $G_x, G_y, G_z$  are the gradients of the applied magnetic field which correspond to patient's left-to-right, front-to-back and head-to-toe directions, respectively. The first part of the sequence achieves slice selection (SS) through a  $90^\circ$  RF pulse (typically a 'sinc' pulse) thus creating transverse magnetization. The second part of the sequence achieves phase encoding by phase shifting the magnetization in the y direction and finally the third part consists of another pulse which rotates the transverse nuclear magnetization by  $180^\circ$  within the slice. The transverse magnetization refocuses at time TE and forms the spin echo. During that time frequency encoding (FE) takes place.

The spin-echo (SE) pulse sequence is one of the most widely used MRI pulse sequences (Fig. 2.6). The SE pulse sequence timing can be adjusted to give T1-weighted, FLAIR and T2-weighted images (these are described later on Section 2.2.4). The spin echo sequence consists of three fundamental phases (Fig. 2.6):

- a 90° RF pulse followed by phase encoding,
- a 180° RF pulse followed by re-phasing,
- the echo that occurs at TE where frequency encoding takes place.

The SE sequence needs to be repeated many times in order to acquire the entire image. The time between each repetition of the sequence is the TR and is equal to the time that is necessary to allow the longitudinal magnetization to recover in order to generate a transverse magnetization in the next repetition. After the TE ends, the protons will continue to de-phase and the echo vanishes. However, during that time another 180° RF pulse can be sent in order to re-phase the protons again. This 180° RF pulse can be repeated as many times as necessary, each time generating an echo. This method is referred in the literature as Fast Spin Echo (FSE). At this point, it is important to note that at some point the echo will be so weak that it will not be clearly distinguished from the background noise.

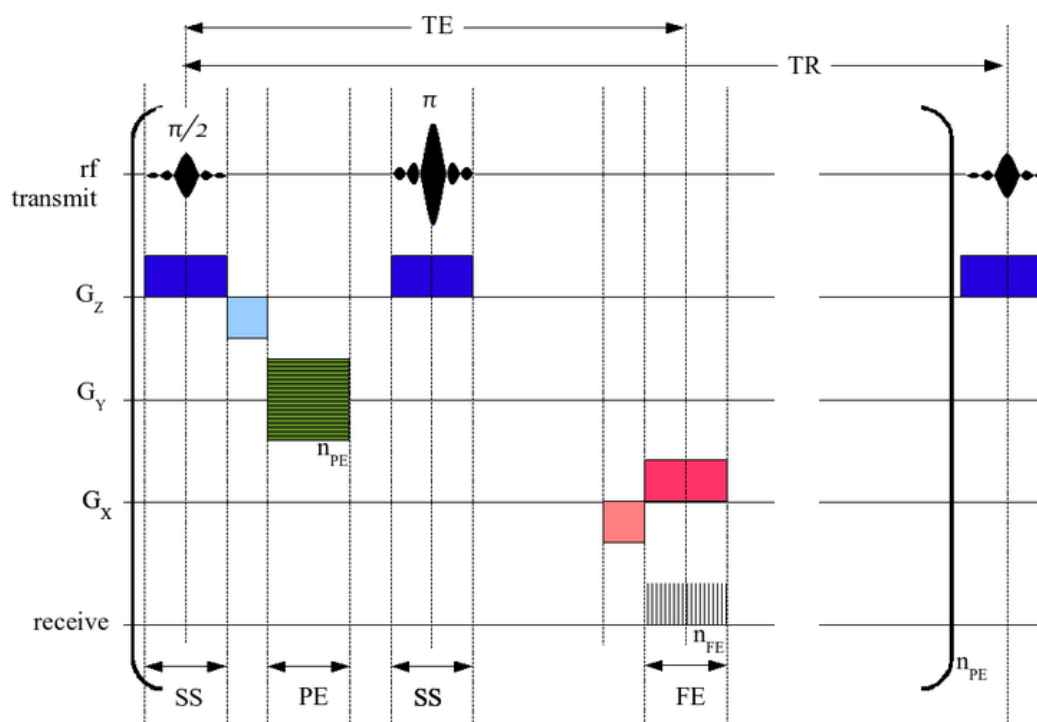


**Figure 2.6.** The timing diagram of a spin-echo pulse sequence. **Abbreviations;**  $n_{PE}$  is equal to the number of times the whole sequence is repeated,  $n_{FE}$  is the number of samples taken during FE. (Adapted from wikipedia.org).

Gradient (refocused) echo (GRE) sequences are an alternative technique to spin echo sequences. A GRE sequence does not use a  $180^\circ$  RF pulse but it is based on the precession of the proton (see **Sections 2.2.1** and **2.2.2** for a quick revision) through a process that is often referred to as free induction decay (FID). Most GRE sequences use an initial excitation RF pulse of less than  $90^\circ$ . The flip angle of the proton is what affects the amount of longitudinal magnetization that is rotated into the  $xy$ -plane. A small flip angle usually leads to a large amount of longitudinal magnetization which makes it available for another repetition. This is important in GRE sequences which are typically used with very short TRs for rapid repetition instead of long TRs which would result to a sequence with very poor signal-to-noise ratio (SNR). However, the main disadvantage of small flip angles is that they decrease the T1 contrast of the sequence. Larger flip angles give more T1 weighting to the image and the smaller flip angle gives more T2 or T2\* weighting.

At this point, it is interesting to note that instead of using repeated  $180^\circ$  RF pulses after  $90^\circ/180^\circ$  RF pulses, like in a SE sequence, a pulse sequence with multiple echoes acquired from different phase steps using re-phasing gradients can be generated. This pulse sequence is known as Echo Planar Imaging (EPI). The EPI sequence can be generated by rapidly reversing (alternating) the FE gradient and this alternation is exactly what creates the gradient echoes. In fact, it utilizes rapidly switching gradients to acquire the entirety of  $k$ -space within one spin echo (the  $k$ -space is used for MR image reconstruction and is described in **Section 2.2.5**). The major advantage of the EPI sequence is that it can generate multiple gradient echoes within a single spin echo and can be performed based on GRE sequences. The EPI sequence is also used in diffusion weighed imaging (DWI).

#### **2.2.4. Relaxation times and tissue contrast**

The T1 relaxation time (also known as longitudinal or "spin-lattice" relaxation time) reflects the length of time it takes for the re-growth of the  $M_z$  component back towards its initial maximum value ( $M_0$ ), i.e., for the  $M_z$  component to recover as shown in **Fig. 2.7(A)**. Alternatively, the T1 relaxation time refers to the time required by protons, within a given tissue, to recover at 63% of their original net magnetization vector along the vertical or longitudinal plane immediately after the completion of the  $90^\circ$  RF pulse. Tissues with short T1 times recover more quickly than those with longer T1 times since their  $M_z$  values are larger and therefore produce a stronger signal which exhibits a brighter spot on the MR image. For example, fat quickly realigns its longitudinal magnetization, and therefore appears brighter than water which has much slower longitudinal magnetization realignment and therefore exhibits less transverse magnetization.

On the other hand, the T2 relaxation time (also known as transverse or "spin-spin" relaxation time) reflects the length of time it takes for the MR signal to decay in the transverse plane, i.e., for the  $M_{xy}$  component to decay, as shown in **Fig. 2.7(B)**. Small T2 constant results to a rapid signal decay and therefore tissues with short T2 times appear darker than those

with longer T2 values. More specifically, the T2 relaxation time is the time it takes for the tissue to lose 63% of its original transverse or horizontal magnetization. The decay of the NMV in the horizontal plane is due to dephasing of the individual proton spins as they precess at slightly different rates due to the local inhomogeneities of the magnetic field (including those that are caused by the tissue itself) leading to a more rapid transverse relaxation time (Logothetis and Wandell, 2004).

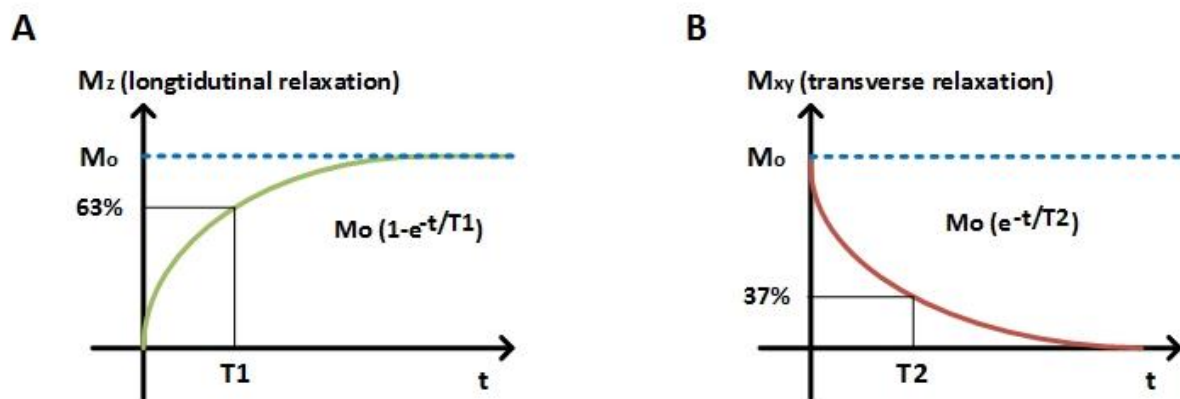


**Figure 2.7. (A) T1 and (B) T2 relaxation times.**

When inhomogeneities are present in a physiological tissue, the decay constant is usually referred to as  $T_2^*$ . In fact,  $T_2^*$  can be considered as an "effective" T2. Note that  $T_2^*$  is always less than or equal to T2 and can sometimes be defined as  $1/T_2^* = 1/T_2 + 1/T_{2i}$ , where  $1/T_{2i} = \gamma \Delta B_i$  and  $\Delta B_i$  represents the local field inhomogeneities across a voxel (Elster, 2017).

According to the literature, the most common MRI scans are referred to as T1-weighted (T1-W) and T2-weighted (T2-W) images. A T1-weighted image relies upon the longitudinal relaxation of a tissue's NMV and is produced by using short TE (i.e., 14 ms) and TR (i.e., 500 ms) constants. Conversely, a T2-weighted image relies upon the transverse relaxation of the net magnetization vector and is produced by using longer TE (i.e., 90 ms) and TR (i.e., 4000 ms) times. Tissues with high water content (like fat, fatty bone marrow, edemas) will appear brighter (signal intensity) in a T1-WI than in a T2-WI. On the other hand, tissues with lower water content (like bones, CSF, blood products) will appear brighter in a T2-WI than in a T1-WI. Grey matter areas appear with intermediate brightness in both T1 and T2 weighted images whereas white matter appears hyperintense (white-ish) compared to gray matter in T1-WI and hypointense (dark-ish) compared to gray matter in T2-WI. In general, the contrast and brightness of the T1-WI and T2-WI are determined by the T1 and T2 properties of the tissue of interest (see **Table 2.1**).

Certain MR sequences using relatively long TE values are called  $T_2^*$ -weighted and are used to accentuate local magnetic homogeneity effects for the detection of hemorrhage or calcifications (Elster, 2017).  $T_2^*$ -sensitive sequences also form the basis for functional MRI using the BOLD contrast mechanism (see **Section 2.3**).

**Table 2.1.** Typical T1 and T2 values for various tissues under a 1.5 Tesla MRI scanner.

Tissue	T1 (ms)	T2 (ms)
Water/CSF	4000	2000
White matter	790	92
Gray matter	900	90
Muscle	900	50
Lung	830	80
Liver	500	40
Fat	250	70
Tendon	400	5
Proteins	250	0.1-1.0

Another widely-used MRI sequence is the Fluid Attenuated Inversion Recovery (FLAIR). This sequence is similar to a T2-weighted image except that the TE and TR times are very long (i.e., TE = 114 ms, TR = 9000 ms). As a matter of fact, abnormalities remain bright but normal CSF is attenuated and made dark. FLAIR is very sensitive to pathology and makes the differentiation between CSF and an abnormality much easier. Another MRI sequence that has been largely replaced by FLAIR, is the Proton Density (PD) weighted imaging which produces contrast by minimizing the impact of T1 and T2 differences with long TR (2000-5000 ms) and short TE (10-20 ms). In PD weighted images, the fluids normally appear as grayish white, almost with similar appearance as the fat in the body. Dual echo and multi-echo sequences can be used to obtain both proton density and T2-weighted images simultaneously.

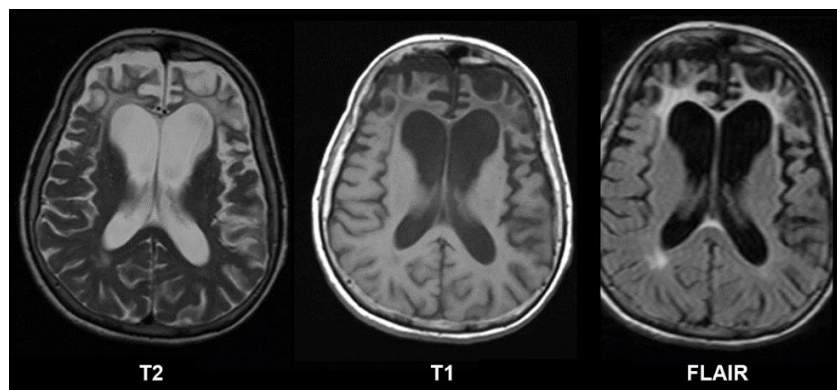


**Figure 2.8.** Contrast differences between T2-W, T1-W and FLAIR imaging sequences from a patient with Pick's disease - a neurodegenerative disease. (Adapted from wikipedia.org).

### 2.2.5. Image reconstruction

When the RF pulse is removed, the excited nuclei returns back to its original aligned position (precession) which causes the inductance of a current in the receiver coil. This current is used to generate the MR signal which is expressed as the Fourier transform of the

spin density at a single point in the frequency space or  $k$ -space. The measurement of the MR signal at the  $j$ -th time-point,  $S(t_j)$ , in a readout period, is defined as (Lindquist, 2008):

$$S(t_j) = \int_x \int_y M(x, y) \cdot e^{-2\pi i(k_x(t_j)x + k_y(t_j)y)} dx dy \quad (2.2)$$

where  $M(x, y)$  is the spin density at point  $(x, y)$  on a Cartesian grid,  $t_j$  is the time at which a data sample and is defined as  $t_j = j\Delta t$ , where  $\Delta t$  depends on the sampling bandwidth of the scanner, with typical values ranging from 250 to 1000  $\mu\text{sec}$  (Lindquist, 2008). Finally,  $(k_x(t_j), k_y(t_j))$  is the point in the  $k$ -space (frequency domain) at which Fourier transform is measured at time  $t_j$  (Paschal and Morris, 2004):

$$k_x(t_j) = \int_0^{t_j} \gamma G_x(t) dt \quad \text{and} \quad k_y(t_j) = \int_0^{t_j} \gamma G_y(t) dt \quad (2.3)$$

where  $\gamma$  is the gyromagnetic ratio (see **Section 2.2.2** for further information),  $G_x(t)$  and  $G_y(t)$  is the strength of the gradient along axes  $x$  (frequency encoding) and  $y$  (phase encoding) respectively, at time  $t$ .

The raw data are typically interpolated onto a Cartesian grid in the frequency domain or  $k$ -space (**Fig. 2.9(A)**) and then IFFT is applied to reconstruct the original image (**Fig. 2.9(B)**). Designing new  $k$ -space sampling trajectories instead of the Cartesian standard grid is of great interest. At this point, it is important to note that the individual points  $(k_x, k_y)$  in  $k$ -space do not correspond one-to-one with individual pixels  $(x, y)$  in the image space. Each  $k$ -space point contains spatial frequency and phase information about every pixel in the final image. However, each pixel in the image space maps to every point in the  $k$ -space and that's exactly the importance of the  $k$ -space in image reconstruction.

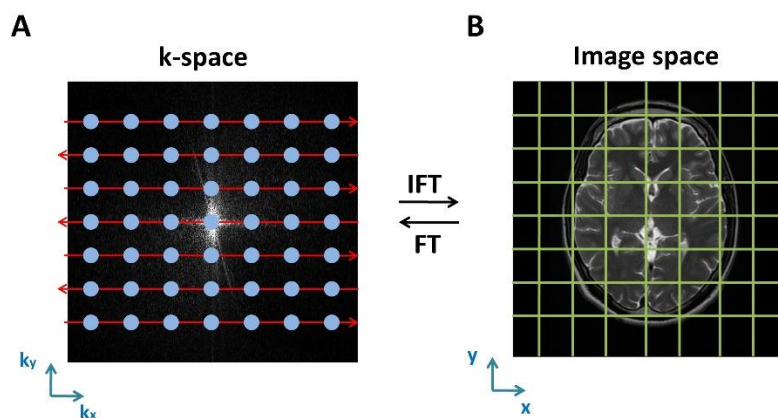


**Figure 2.9.** Visual representation of the mapping procedure from **(A)**  $k$ -space to **(B)** image space and backwards using IFT and FT, respectively. (The MRI axial slice in **(B)** was adapted and adjusted from wikipedia.org).

### 2.3. The BOLD contrast mechanism

Functional magnetic resonance imaging is most commonly performed using the blood oxygenation level dependent (BOLD) contrast mechanism. The BOLD contrast mechanism was first mentioned in the work of Ogawa and colleagues (Ogawa et al., 1990) using strong magnetic fields in rat brain studies through gradient echo pulse sequences. What Ogawa discovered was the existence of a contrast mechanism that could be able to reflect the blood oxygen level on the gradient-echo images by accentuating the susceptibility effects of the deoxygenated hemoglobin in the blood vessels (Ogawa et al., 1990; Logothetis, 2002). More specifically, Ogawa noticed that these effects created local distortions (alterations) on the magnetic field that could be projected on magnetic resonance images with the aims of providing accurate measurements related to neural activity. This combination is now known as functional magnetic resonance imaging (fMRI).

The BOLD contrast mechanism results from the change in magnetic field surrounding the red blood cells depending on the oxygen state of the hemoglobin ( $\text{HbO}_2$ ). It was already known before even the development of the MRI, that fully oxygenated  $\text{HbO}_2$  is diamagnetic whereas fully deoxygenated Hb (dHb) is highly paramagnetic (hemoglobin properties; Brooks, 1937). Hemoglobin (or haemoglobin) consists of two pairs of polypeptide chains (globin), each of which is attached to a complex of protoporphyrin and iron (heme group) (Logothetis, 2002). In dHb the iron ( $\text{Fe}^{2+}$ ) is in a paramagnetic high-spin state, as four of its six outer electrons are unpaired. When oxygenated, the heme iron changes to a low-spin state by receiving the oxygen's electrons. BOLD imaging is based on the aforementioned magnetic differences between the oxygenated and deoxygenated hemoglobin which result to the generation of local gradients in the magnetic field whose strength depends on the  $\text{HbO}_2$  concentration. These gradients alter the intra- and extra-vascular blood's  $T_2$  and  $T_2^*$  relaxation times by generating tiny magnetic field inhomogeneities that are associated with the presence of dHb, which in turn lead to destructive interference from signal within the tissue voxel that shortens the  $T_2^*$  relaxation time (Glover, 2011). The cerebral blood flow (CBF) refreshes with oxygenated blood areas of the brain that are activated during resting-state or during a task performance (Lindquist, 2008). This modulates the susceptibility of the  $\text{HbO}_2$  that flows within the involved areas, thus changing the measured MR signal in these areas. As oxygen extraction falls with enhanced local blood flow in a region of greater neuronal activity, the  $T_2^*$  relaxation time becomes longer and the MR signal intensity increases relative to the baseline state (Mathhews and Jezzard, 2017).

When a neuron fires, it draws oxygen from the blood stream leading to an increase in the concentration of dHb in the blood (**Fig 2.10**). Right after the neuronal firing, the active neurons consume the oxygen available in the local blood stream and thus the relative level of dHb increases more which leads to an initial decrease in the BOLD signal. After the increase in the dHb concentration, the blood flow increases locally in response to the neuronal activity by providing a large amount of oxygenated blood so as to preserve the oxygen consumption.

This in turn results in a local decrease of the dHb consumption. By taking into consideration the fact that dHb is paramagnetic, a reduction in its concentration results in an increase in the homogeneity of the static magnetic field which in turn yields an increase in the BOLD signal. Finally, the concentration of dHb slowly returns to its normal level and the BOLD signal decays till reaching its original baseline level.

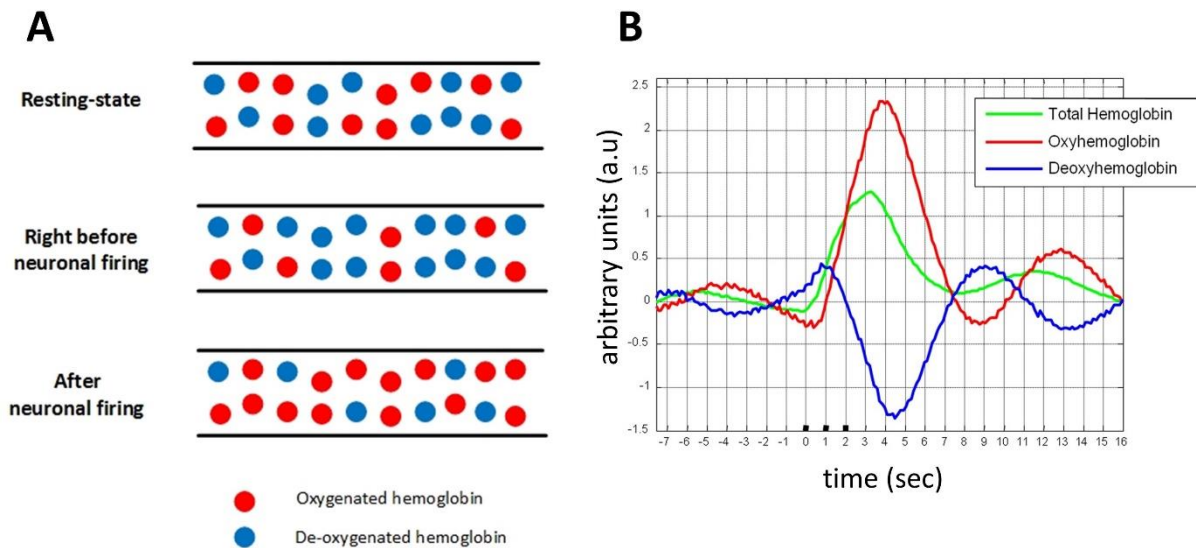


**Figure 2.10.** (A) Oxygenated and deoxygenated consumption before/after neuronal activation. (B) The relative concentration distribution of the oxygenated and deoxygenated hemoglobin before and after neuronal firing. (Adapted and adjusted from [Saka et al., 2010](#)).

The underlying evoked hemodynamic response to a neural event is known as the hemodynamic response function (HRF) (Logothetis, 2004; Lindquist, 2008; Chen and Li, 2012). The hemodynamic response rises to a peak over 4-8 seconds, before falling back to its baseline (**Figs 2.10-2.11**). This leads to changes in local cerebral blood volume and local changes in the concentration of oxygenated hemoglobin, which are detectable through the paramagnetic effects (Chen and Li, 2012). The standard shape used to model the HRF is sometimes called the canonical HRF (**Fig. 2.11**). The increased metabolic demands due to neuronal activity lead to an increase in the inflow of oxygenated blood to active regions of the brain. Since more oxygen is supplied than actually consumed, this leads to a decrease in the concentration of deoxygenated hemoglobin which, in turn, leads to an increase in signal. This positive rise has an onset approximately 2 seconds after the onset of neural activity and peaks 5-8 seconds after that neural activity has peaked (Aquirre et al., 1998). Several studies have shown evidence of a decrease in oxygenation levels in the time immediately following neural activity, giving rise to a decrease in the BOLD signal in the first 1-2 seconds following activation. This decrease is called the initial negative BOLD response or the negative dip (Menon et al., 1995; Malonek and Grinvald, 1996). All the aforementioned aspects are described in the following figure.

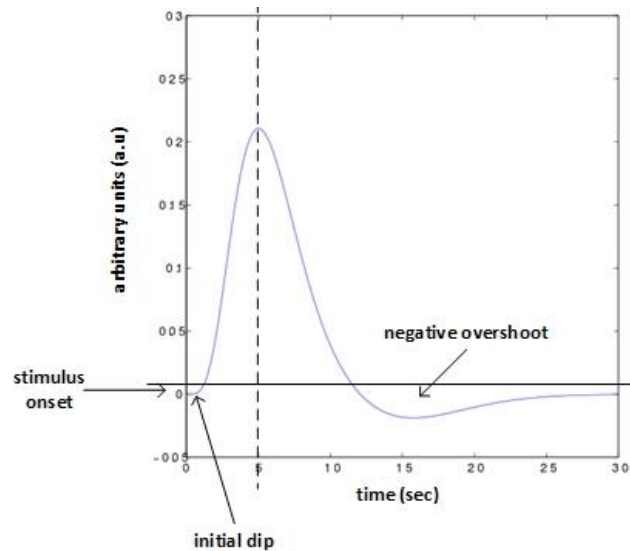


**Figure 2.11.** The standard canonical HRF model used in various task fMRI studies. (Adapted and adjusted from wikipedia.org).

The BOLD contrast mechanism appears best using a gradient echo (GE) pulse sequence where the acquisition is made sensitive to  $T_2^*$  and  $T_2$  relaxation times. The  $T_2^*$  contrast is predominant and is largest in venules at magnetic fields of 1.5T and 3T where most fMRI scanners operate (Glover, 2011). At higher field strengths, the diffusion-weighted contrast of  $T_2$  relaxation time dominates and provides greater spatial specificity (Glover, 2011). In task-fMRI studies the HRF model is used for statistical modeling. In fact, the BOLD signal can be modelled as the convolution of a stimulus function (a series of event spikes) and the HRF. In this work however, resting-state fMRI data are employed for analysis. For further information about task fMRI activity prediction models, see the study of Perrachione and Ghosh, 2013.

## 2.4. From MRI to fMRI activation maps

A typical MRI study consists of a series of 2D brain volumes (slices) collected within a quick succession, leading to a 3D dataset. A pixel in 3D space is referred to as volumetric pixel or voxel for short. During fMRI, an extra (4<sup>th</sup>) dimension is recorded for each voxel, which corresponds to the time space (**Fig. 2.12**). Therefore, the fMRI dataset is a 4D dataset. The temporal resolution of the acquired dataset depends on the time between acquisitions of each individual volume. Once the  $k$ -space has been sampled, the procedure is repeated and a new volume can be acquired alongside with an extra voxel-wise BOLD signal. Therefore, the efficiency of the  $k$ -space sampling is of great importance. In the current thesis, the (resting-state) fMRI data were acquired from the Human Connectome Project (HCP) as it was already mentioned in **Chapter 1**. The HCP database consists of brain volumes of dimensions  $91 \times 109 \times 91$  (i.e., 902629 voxels) where the BOLD signals are collected at  $T$  separate time points throughout the recording time. In resting-state HCP fMRI BOLD data, the number of samples

was equal to 1200 across each run (approximately 15 minutes of resting-state recording). Hence, the resulting data consists of roughly 902629 time series of length  $T$ . Since the recording was repeated for  $M$  subjects, where  $M$  was equal to 500, or even 1100 as in the latest HCP release, it is obvious that the fMRI analysis is in fact a time series analysis problem of massive proportions (Lindquist, 2008).

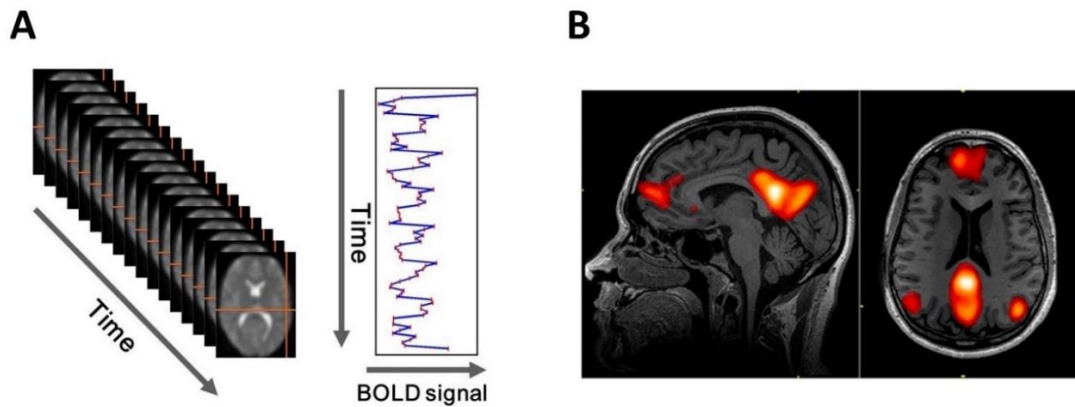


**Figure 2.12.** (A) Example of an fMRI 4D dataset where an extra BOLD signal is recorded for each voxel (here one is shown for simplicity). (B) An fMRI scan (on sagittal and axial slices) showing activations on regions that belong to the well-known Default Mode Network (DMN) which is usually activated during resting-state. (Adapted and adjusted from wikipedia.org).

## 2.5. Spatial and temporal resolution

BOLD fMRI provides detailed anatomical images of the gray and white matter with a spatial resolution well below  $1 \text{ mm}^3$  but with a temporal resolution of a few seconds which is limited by the hemodynamic response itself (Lindquist, 2008; Matthews and Jezzard, 2017). The spatial specificity increases with increasing magnetic field and, for a given magnetic field, can be limited by the signal-to-noise ratio (SNR) and well optimized by using pulse sequences that are less sensitive to signals from within and around large vessels. In general, for MRI, the SNR can be approximately defined as:

$$SNR \approx p^2 w \sqrt{TN} \quad (2.4)$$

where  $p$  is the pixel size,  $w$  is the slice thickness,  $T$  is the acquisition time, i.e., the  $k$ -space readout time and  $N$  is the number of frames. It is obvious that as  $T$  reduces the pixel size ( $p$ ) must be increased in order to retain an acceptable SNR. A typical fMRI pixel size is 3-4 mm and can reach 500  $\mu\text{m}$ , or even less, under a strong 7T magnetic field. fMRI's spatiotemporal resolution can be mainly enhanced by (i) optimizing the MRI pulse sequences, (ii) using higher magnetic fields, (iii) employing intelligent strategies for parallel imaging (Logothetis, 2008). The following table summarizes the spatiotemporal resolution of fundamental non-invasive methods for mapping brain's functional connectivity.

**Table 2.2.** Spatiotemporal resolution and physiological basis of fundamental non-invasive brain mapping methods (Johnsrude and Hauk, 2005; Nicolas-Alonso and Gomez-Gil, 2013).

Method	Activity measured	Spatial resolution	Temporal resolution	Physiological basis
EEG	Electrical	~ 10 mm	~ 0.05 sec	electrical activity across a large number of neurons
MEG	Magnetic	~5 mm	~ 0.05 sec	magnetic fields produced from the electrical activity across neurons
PET	Metabolic	5 - 20 mm	10 sec - mins	radioactive decay resulted from the accumulation of a compound
fMRI		~ 1 mm	~ 1 sec	local magnetic field fluctuations produced by the alteration of HbO <sub>2</sub> magnetic properties
NIRS		~ 5mm	~ 1 sec	focal magnetic field produced by transiently disrupted activity over a large number of neurons

The spatial resolution of EEG/MEG is limited to 5-10 mm due to the fact that the inverse problem (i.e., the ill-posed source localization problem) does not have a unique solution, i.e., the dipole reconstruction is not unique. The EEG appears with a smaller spatial resolution than MEG due to the fact that EEG might be spatially distorted by electrical conduction (Glover, 2011). On the other hand, EEG/MEG can easily capture the dynamics of brain activity and thus offer excellent temporal resolution, i.e., close to 0.05 sec. BOLD fMRI provides excellent spatial resolution but small temporal resolution which is mainly related to the hemodynamic activity. Near Infrared Spectroscopy (NIRS) offers a similar to EEG spatial resolution (close to 5 mm) and is limited by the problem of reconstructing HbO<sub>2</sub> 3D maps from scalp recordings as well as the scattering and attenuation of the infrared photons which limits deeper brain penetration. NIRS's temporal resolution is similar to fMRI's due to blood oxygenation temporal limitations. As far as Positron Emission Tomography (PET) is concerned, its' spatial resolution varies between 5 and 20 mm because it is limited by the size of gamma ray detectors as well as the positron-electron annihilation range (Glover, 2011). PET has the largest temporal resolution than all the aforementioned methods due to the low count rates of the injected nuclide (Glover, 2011), thus requiring further scans.

In the near future, fMRI can provide us with routine-based images of a fraction of a millimeter, e.g.,  $300 \times 300 \mu\text{m}^2$ , with approximately 2 or 3 orders of magnitude smaller voxel volumes than those currently used in human brain imaging (Logothetis, 2008). This enhanced resolution combined with a large number of acquisition channels, can provide scans with excellent spatial detail and with a normal temporal resolution of almost a second or two.

## 2.6. Basic pre-processing techniques

Pre-processing is mandatory prior to any resting-state or task analysis involving fMRI data in order for example to attenuate physiological artifacts such as those originated from head motion or data acquisition artifacts like magnetic field deformations. The major steps involved in fMRI pre-processing are realignment (short-duration motion correction), co-registration of functional images, slice timing correction, normalization, smoothing and separation of spatial or temporal independent components of brain activity. These fundamental steps are briefly described in the sequel.

During the scanning procedure, subject's movement often leads to signal contamination, i.e., the signal from a voxel of interest is mixed with its neighboring voxels signals and thus the recorded data represent false brain activation. This type of artifact is crucial and an incorrect treatment leads to useless studies. A widely used motion correction approach is known as rigid body transformation and is composed by two steps. In the first step, each obtained slice is compared with a target slice which is usually the average slice (or the first slice) and then the image is (translated) shifted across all dimensions and rotated in order to match the target. The matching process is performed by minimizing a cost function, usually the sums of squared differences between the pixels of the input and target images. The image is finally resampled based on the estimated translation and rotation parameters using interpolation, resulting to new motion-free voxel coordinates.

A fundamental hypothesis in fMRI processing is that the voxels within the whole brain are measured simultaneously. Of course this is not true since the 3D fMRI data consist of a large number of slices sampled in a sequential manner. As a matter of fact, at different time-points, similar BOLD signals will be temporally shifted relative to each other. Slice timing correction shifts each voxel's BOLD signal appropriately either by using interpolation in time-space or the Fourier shift transform theorem in spectrum in order to treat these acquisition differences (Lindquist, 2008).

Smoothing is performed in order to solve the blurring of anatomical differences between different brain regions which constitutes a main spatial normalization limitation. Moreover, smoothing may suppress random noise and increase the signal-to-noise ration within a region only if that the spatial extent of that region is larger than the spatial resolution (Lindquist, 2008). Smoothing is usually applied using the full width at half maximum (FWHM) kernel with widths typically being 3 times the voxel size. Spatial smoothing is equivalent to applying a low-pass filter on the sampled  $k$ -space data.

Co-registration is the process of aligning functional images in order to improve the spatial resolution of the fMRI by mapping the acquired data to an image with high spatial anatomical detail. This process is applied through typical rigid body or affine transformations (Lindquist, 2008). Normalization is another crucial pre-processing technique that aims to register each subject's voxel coordinates into a common brain template that lies within the well-known

Montreal Neurological Institute (MNI) or the Talairach coordinate space (for comparing the disparity between these two spaces, see Laird et al., 2010). This step is highly important in studies where statistical comparisons between populations (i.e., normal subjects and subjects with a specific pathology) are performed. Comparing subjects whose voxels are registered in different coordinate spaces results to inaccurate and false results. Normalization is commonly performed using non-linear transformations in order to wrap the input image (i.e., a slice) onto the target/template image using smoothing (Lindquist, 2008).

Generative models like Independent Component Analysis (which is a special case of the Blind Source Separation problem), are mostly used for extracting the components of brain (and non-brain) activity by separating a multivariate signal into independent components through the maximization of the mutual dependence of the source signals, assuming that none or only one of them is Gaussian and the rest are non-Gaussian (Chen and Li, 2012). ICA has been extensively applied on EEG/MEG studies for separating temporally independent components. Nowadays, it has been also extended to fMRI in the form of spatial ICA with the purpose of separating spatiotemporally independent components for revealing the distinct co-activation patterns during resting-state which represent spatially coherent fluctuations of the BOLD signal (Chen and Li, 2012). At this point, it is important to note that a special form of the ICA, known as the ICA-FIX ("fMRIB's ICA-based X-noiseifier") algorithm (Salimi-Khorsidi et al., 2014), has been recently proposed based on multi-level classifiers for subtracting the noisy components of brain activity with a 99% accuracy on the HCP data. For this reason, the ICA-FIX algorithm is the default rs-fMRI denoising method in the HCP pre-processing pipelines.

## **2.7. Clinical applications**

Functional magnetic resonance imaging is a straightforward and non-invasive method for mapping human brain activity based on the local hemodynamic fluctuations that appear as a result of the neuronal activation within a region. fMRI is a widely used approach since it is non-invasive and records the metabolic activity of the brain without the use of exogenous contrast agents as in MRI or nuclides as in PET. Over the last decade, fMRI has been extensively used to map brain activity in subjects during resting-state or during a cognitive, emotional or sensory-motor task. Nowadays, fMRI has been employed as a valuable tool in comprehending various pathological disorders such as brain tumors, epilepsy, Alzheimer's disease, multiple sclerosis, etc. Moreover, fMRI can be combined with diffusion tensor imaging (DTI) to provide accurate white and gray matter probabilistic tractography maps (Glover, 2011; Mathhews and Jezzard, 2017).

The role of fMRI in brain tumor surgery is valuable since it can be used as a pre-surgical tool for investigating the relationship between the tumor and different brain areas involved in cognition, motor, speech, language, etc. A large number of studies examine whether fMRI can accurately estimate the location of cortical areas involved in speech, cognition and

language in relationship to brain tumors (Signorelli et al., 2001, 2003). Understanding the relationship between a lesion and an eloquent region can determine whether a resection is safe or not (Orringer et al., 2012). An alternative is the electrocorticogram (ECoG) which is an invasive method and is not able to provide 3D activation maps. In addition, fMRI can be also combined with direct cortical stimulation for accurately mapping the relationship of a lesion with the identified somatosensory, motor, and language regions of the human brain (Logothetis, 2002; Orringer et al., 2012).

fMRI's contribution to epilepsy treatment is also of great importance. It can be combined with the WADA test (i.e., an international test that establishes cerebral language and memory representation of each hemisphere) for successfully planning and executing an epilepsy surgery (Orringer et al., 2012; Matthews and Jezzard, 2017). For example, in the study of Sabsevitz et al., 2003, fMRI was found to predict positive significant language outcomes (i.e., naming decline) with an accuracy of 81% across 24 patients that underwent left anterior temporal lobectomy (ATL). As a result, fMRI can be used to predict the risk for language function decline and memory deficits following ATL (Orringer et al., 2012). That is exactly the role of an efficient biomarker.

Another application focuses in the diagnosis and management of Alzheimer's disease (AD). Studies suggest that it is possible to demonstrate impairments in hippocampus and parahippocampal gyrus during memory encoding tasks in patients with Alzheimer's disease, using fMRI (Sperling et al., 2003; Golby et al., 2005). This means that fMRI can be used as a biomarker for predicting the decline in cognitive functions, understand the basis of memory loss in patients with AD and evaluate pharmacological treatments by examining the alterations in brain's physiology (Orringer et al., 2012).

## **2.8. Conclusions and future challenges**

The main advantage of fMRI lies on its excellent spatial resolution which provides high resolution anatomical scans combined with a slightly good temporal information obtained from the hemodynamic activity following neural activation. In addition, the fact that it is a non-invasive method which is able to provide highly detailed and accurate 3D maps of brain activity distribution (e.g., human connectomes) during resting-state or task studies (i.e., motor task), place fMRI on the top of non-invasive brain mapping methods. Since the BOLD response is affected by various factors like age, attention, brain pathology, substance use, etc., fMRI can be used as a reliable and effective biomarker for pathological diseases and pre-surgical planning. Of course, many difficulties still exist and need to be further addressed. The images produced must be interpreted carefully, since correlation does not imply causality and brain processes are complex and often non-localized (Chen and Li, 2012). Important tradeoffs between acquisition speed, resolution and SNR should be taken into consideration for providing high quality images with an acceptable temporal resolution. BOLD contrast is an indirect measure of neural activation and the weakness of the neural signal often results to

noise. In addition, the BOLD signal is also influenced by non-neural changes in the body and it is possible to extract a BOLD signal from a non-activated area (Chen and Li, 2012). However, strong magnetic fields (i.e., 7 Tesla) are able to overcome these issues but on the other hand dramatically increase the cost of an fMRI scanner.

Statistical methods must be carefully evaluated since they can easily produce false positives and misinterpretations of brain activation in different areas of the brain during resting-state or under various task experiments (i.e., sensorymotor, cognition). The recent advances in clinical fMRI healthcare are able to provide reliable, non-invasive functional images that can be easily interpreted by physicists and are often employed for pre-surgical planning as well as extracting biomarkers for pathological diseases, more recently for Alzheimer's disease. fMRI remains at the top of neuroimaging methods with an exponential growth in neuroscientific publications since its inception in 90's.

### 3. Lobular analysis of cerebellum's network with respect to IQ and gender

---

#### 3.1. Overview

This chapter comprises a first attempt to the analysis of cerebellum's anatomical network (i.e., lobular analysis) by taking into consideration the effects of the following two factors on cerebellum's functional connectivity: **(a)** crystallized Intelligence Quotient and **(b)** gender. In order to do so, we collect rs-fMRI data for 492 subjects from the HCP database. Prior to the data analysis procedure, we first discard all subjects with hard substance use/alcoholism, psychiatric history and afterwards separate them into two main categories based on their IQ level (low/high-IQ). Thereafter, graphs are constructed per subject by computing Pearson's correlation coefficients between the average BOLD time-series for each pair of ROIs (i.e., lobules), inside the cerebellum. Through the computation of conventional graph metrics, small-world network properties were investigated using the weighted clustering coefficient and the characteristic path length for estimating the trade-off between segregation and integration. The Minimum Spanning Tree (MST) concept was implemented in order to preserve only the strongest connections per network (i.e., extract its backbone structure) as well as avoid any methodological biases in graph comparisons. An additional individual correlation analysis was conducted in order to examine the relationship between the hub indicators (i.e., local MST measures) and the Median Response Time (MRT), per subject. The computed set of local and global graph/MST parameters gave rise to extensive statistical analysis in order to test for differences between low and high-IQ males/females.

The lobular analysis process is presented in **Fig. 3.1**. Cerebellum's anatomical parcellation procedure was executed using a probabilistic cerebellum atlas registered on the MNI space, where the 27 cerebellar ROIs are displayed on the surface using color coding **(A)**. Pearson's correlation coefficient was employed as a functional connectivity metric for each pair of ROIs leading to a 27x27 weighted and undirected graph **(B)**. A weighted graph is a dense graph as it can be visualized through its projection on cerebellum's surface by treating ROIs as nodes **(C)**. In order to preserve only the strongest connections within the network the concept of the Minimum Spanning Tree was applied using Kruskal's algorithm **(D)**. The MST is a loopless subgraph of the original weighted graph and is projected on cerebellum's surface where each node's size linearly depends on its betweenness centrality (BC) value **(E)**.

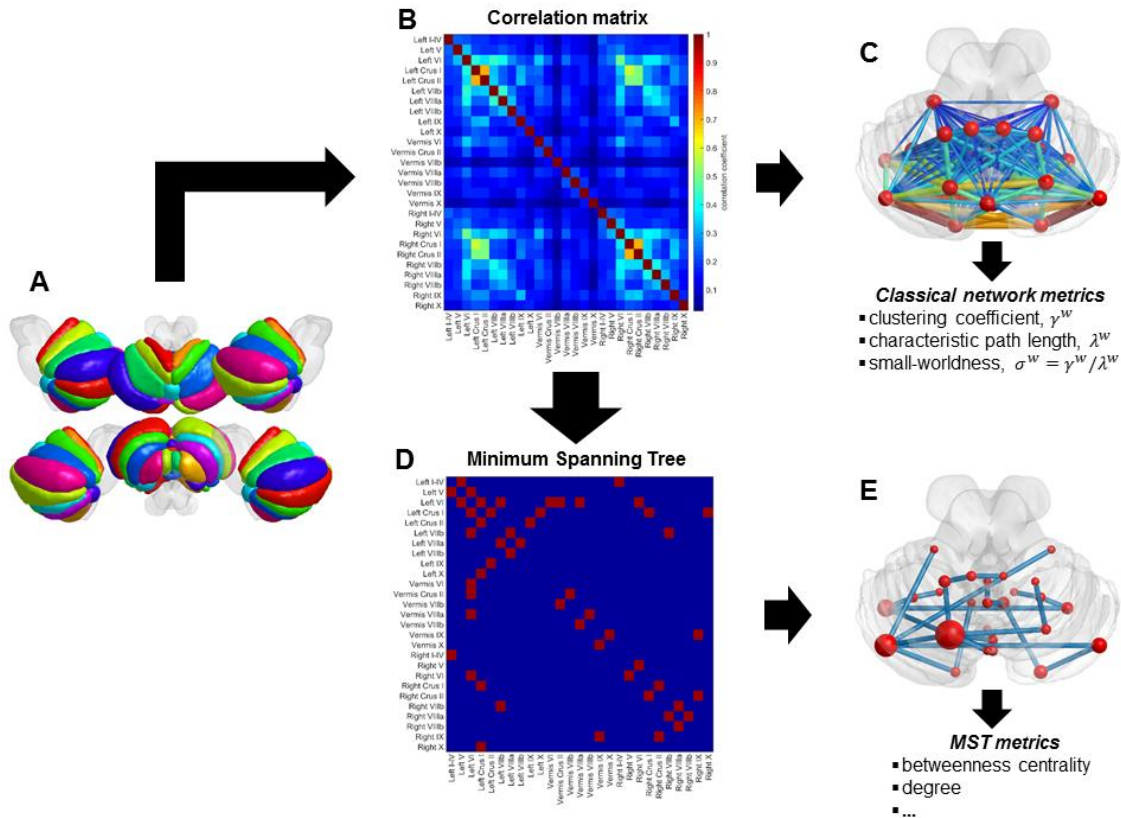


**Figure 3.1.** Schematic representation of the basic methodology for executing the lobular analysis of cerebellum.

### 3.2. IQ groups formation

Crystallized IQ is a measure that involves both educational experience and executive functioning, giving more emphasis to knowledge (Barch et al., 2013; Schipolowski et al., 2014). The HCP database provides crystallized IQ measures obtained using a Form-A of an abbreviated version of the Raven's patterns, developed by Gur and colleagues (Bilker et al., 2012; Barch et al., 2013). More specifically, participants were presented with patterns made up of  $2 \times 2$ ,  $3 \times 3$ , or  $5 \times 5$  arrangements of squares, with one of the squares missing. Each participant must pick one of five response choices that best fits the missing square on the pattern. The task has 24 items and 3 bonus items, arranged in order of increasing difficulty. However, the task discontinues if the participant makes 5 incorrect responses in a row. Median response times (MRTs) were also collected per subject in order to study associations with brain measures.

In this study, the IQ score is defined as the number of correct responses per subject. The score distribution was found to be left-skewed (skewness =  $-0.49$ ), implying that most of the subjects tend to answer correctly most of the items (**Fig. 3.2**). In order to define the low and high-IQ groups, we first find the median of the IQ score distribution from all 492 subjects

(approximately 16), as well as the lower quartile (approximately 6). The minimum score is 3 and the maximum score is 24. An IQ score of 3 is considered very low in practice and since only two subjects responded in this range, they were removed from further analysis without affecting the overall IQ distribution. We define the low-IQ score within the interval from 4 to 10 (median minus one quartile), whereas the upper IQ interval defines scores from 22 (median plus one quartile) to the maximum score of 24. As a result, the low-IQ group includes 69 subjects, whereas the high-IQ group is composed of 67 subjects in total.

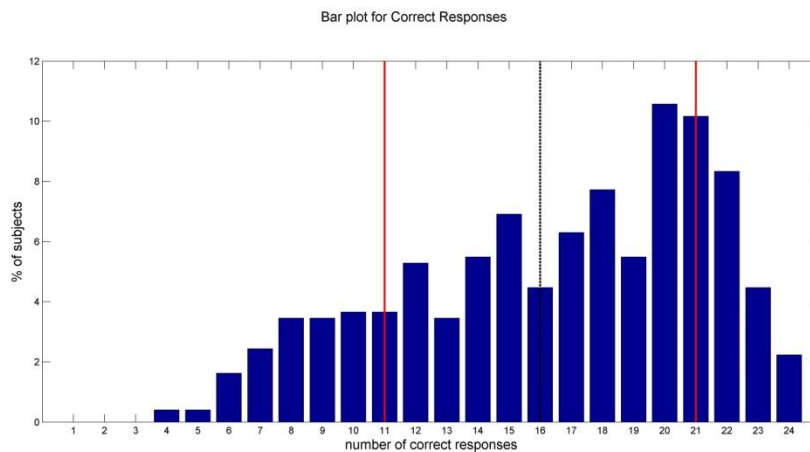


**Figure 3.2.** IQ scores distribution where the black dashed line represents the median and the red lines correspond to the upper (median plus one quartile) and lower (median minus one quartile) IQ boundaries.

The mid-IQ subjects are discarded, so that our population of interest consists of 136 well-separated subjects (69/67; low/high-IQ). More specifically, there are 25 males and 44 females in the low-IQ group, while 29 males and 38 females are involved in the high-IQ group. As far as the educational experience is concerned, both the low-IQ and the high-IQ subjects had an average of approximately 10 years of educational experience although 12 low-IQ subjects and 8 high-IQ subjects were still respondent in school for degree courses. Ages are provided by the HCP database in 4 and 5-year intervals. Only 1 subject was older than 36 years (in high-IQ group), 26 subjects were between 22 and 25 years old (low/high-IQ; 17/9), 56 subjects were between 26 and 30 years old (low/high-IQ; 24/32) and finally 53 subjects were in the age range between 31 and 35 years (low/high-IQ; 28/25). Notice that these age intervals are not wide enough to support the consideration of age influences to intelligence (Li et al., 2004). It is worth mentioning that our population of interest consists of young and healthy adults that underwent several clinical examinations and the large number of estimated network parameters are satisfactory for subsequent statistical analyses.

Group	Scores	Males	Females	Total
Low-IQ	4-10	25	44	69
High-IQ	22-24	29	38	67

### 3.3. BOLD time-series extraction per anatomical lobule

Based on SUI's anatomical atlas of cerebellum (**Section 1.1.6**), the latter was initially parcellated into 28 lobules or regions of interest (ROIs), which are classified as motor related (I–IV, V, VI), cognitive and emotional related (Crus I, Crus II, VIIb, VIIIa, VIIIb, IX, X) according to Stoodley and Schmahmann, 2009; Stoodley et al., 2012; E et al., 2014; Koziol et al., 2014, as shown in **Fig. 3.2**. In order to avoid influences of intracranial volume differences among gender and IQ groups, all MRI structures were matched to the same model through the aforementioned parcellation procedure which was based on the standard (normalized) SUI anatomical cerebellum atlas. The volume of each ROI was defined as the number of its voxels and was calculated from the standard SUI cerebellum atlas (Diedrichsen et al., 2009; Diedrichsen and Zotow, 2015). In addition, a straightforward approach often employed for visualization of the cerebellar anatomical areas, as well as their inner compartments, is to construct a flat-surface representation by means of a 2D projection (Diedrichsen and Zotow, 2015). The flatmap display of the human cerebellum (**Fig. 3.3**) was obtained using the original SUI's probabilistic lobular atlas (Diedrichsen and Zotow, 2015) (in GIFTI format), where borders between lobules were retained and labels were assigned for every lobule based on the symbol coding of Diedrichsen and Zotow, 2015; except for the “H” symbol, which is ignored for simplification.

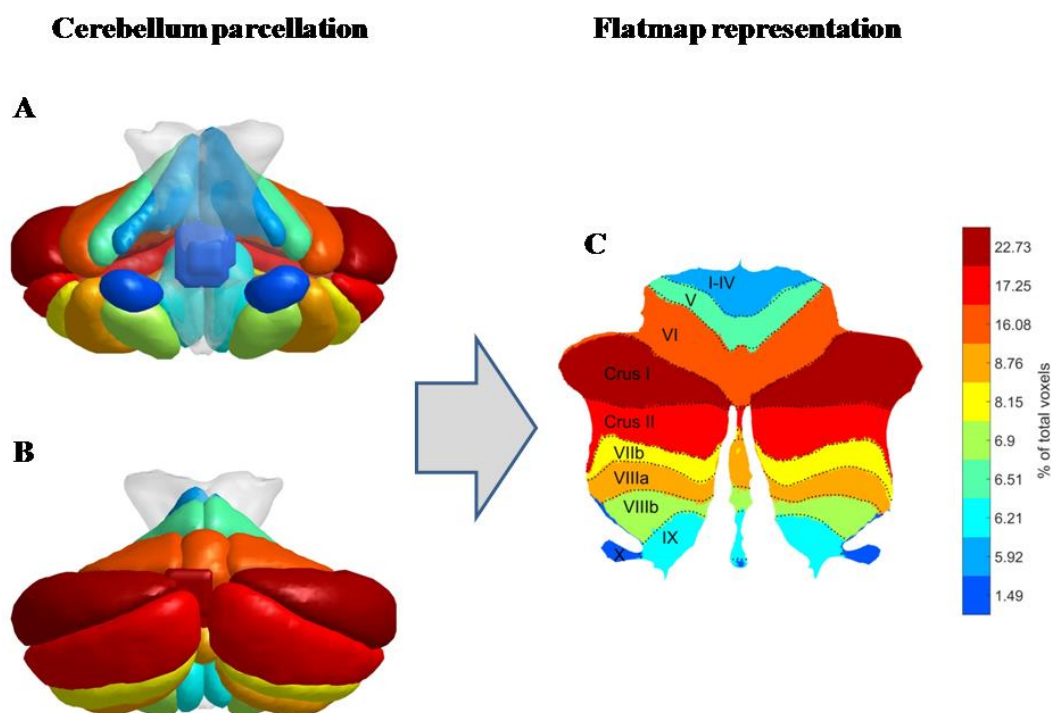


**Figure 3.3.** Cerebellum parcellation procedure (coronal view, **A**: front, **B**: back) followed by its flat surface representation in **(C)**. Color coding is based on each lobule's volumetric size. Presentations **(A)** and **(B)** were created using BrainNet Viewer (Xia et al., 2013) and the flatmap presentation in **(C)** was based on the work of Diedrichsen and Zotow, 2015.

According to **Fig.3.3** and **Table 3.2**, Lobule Crus I was found to be the largest one, occupying approximately 23% of the total cerebellar voxels, comprising almost half of the estimated gray matter volume of the human cerebellum (Diedrichsen et al., 2009). In contrast, one specific region (Vermis Crus I) was found to occupy less than 0.005% of the total volume space and was excluded from subsequent analysis as in previous studies (Riedel et al., 2015). This region is probably the result of a misclassification during the probabilistic atlas formation by Diedrichsen and colleagues. Overall, 27 ROIs were recruited for further analysis, with the number of voxels per ROI and their total contribution to cerebellum's area being presented in **Table 3.2**. The anatomical parcellation of cerebellum was performed for all 136 subjects separately, in order to extract the average BOLD signals from the remaining 27 ROIs, based on SUIT's standard cerebellum atlas.

**Table 3.2.** Cerebellum's anatomical ROIs information.

ROI	Location (Name)	MNI space coordinates			Number of voxels	% of total
		X	Y	Z		
1	Left I-IV	-6	-46	-18	622	2.8901
2	Left V	-16	-48	-20	724	3.3640
3	Left VI	-14	-68	-22	1582	7.3506
4	Left Crus I	-38	-72	-32	2392	11.1142
5	Left Crus II	-12	-82	-40	1866	8.6702
6	Left VIIb	-38	-58	-54	848	3.9402
7	Left VIIIa	-28	-54	-54	812	3.7729
8	Left VIIIb	-18	-52	-56	657	3.0527
9	Left IX	-6	-56	-52	555	2.5788
10	Left X	-20	-36	-46	133	0.6180
11	Vermis VI	0	-74	-22	380	1.7656
12	Vermis Crus II	2	-74	-32	81	0.3764
13	Vermis VIIb	2	-70	-32	27	0.1255
14	Vermis VIIIa	2	-70	-42	221	1.0269
15	Vermis VIIIb	0	-66	-46	110	0.5111
16	Vermis IX	0	-56	-36	130	0.6040
17	Vermis X	0	-48	-36	47	0.2184
18	Right I-IV	6	-46	-16	652	3.0295
19	Right V	18	-50	-20	676	3.1410
20	Right VI	22	-66	-24	1498	6.9603
21	Right Crus I	42	-72	-32	2501	11.6207
22	Right Crus II	20	-80	-22	1765	8.2009
23	Right VIIb	30	-70	-54	878	4.0795
24	Right VIIIa	26	-62	-56	853	3.9634
25	Right VIIIb	20	-54	-56	719	3.3408
26	Right IX	6	-56	-52	652	3.0295
27	Right X	24	-36	-46	140	0.6505

### 3.4. Network construction

#### 3.4.1. Graph modeling

Graph theory forms a graphical approach for the mathematical modeling of complex networks. A graph  $G$  can be defined as a pair  $(V, E)$  where  $V$  is a set of vertices and  $E$  is a set of edges. Graphs can be categorized according to the edge's direction as directed or undirected, and according to edge's weight as weighted or unweighted (binary). In this study, we work with undirected and weighted graphs, where the nodes are placed in the center of the mass of each ROI and the weight connecting two nodes is defined by the correlation of the average BOLD signals of the specified ROIs. Weighted graphs have been characterized as more accurate models of real networks (Reijneveld et al., 2007) with a fixed number of edges (Stam et al., 2014a), unlike unweighted graphs where much of the information is lost due to arbitrary thresholding (van Diessen et al., 2014; Stam et al., 2016) and the introduction of biases (Fornito et al., 2013). Moreover, the lack of connections in unweighted graphs often leads to the well-known disconnection syndrome (Stam and van Straaten, 2012) with negative implications on the computation of useful graph-theory metrics (Reijneveld et al., 2007) and the overall cohesion of the network (Goulas et al., 2015).

The acquired denoised BOLD time-series from 136 subjects in resting-state, were parcellated into 27 regions using the reference atlas that was described in **Section 3.3**. After the extraction of the BOLD time-series from cerebellum's parcellation procedure, the average BOLD time-series were computed per ROI and for every subject separately. Cerebellum's functional connectivity was then assessed by computing Pearson's correlation coefficients between each pair of the 27 ROIs inside the cerebellum, leading to a  $27 \times 27$  correlation (adjacency) matrix per subject in both IQ groups. Negative correlations have been excluded from further analysis (Bohr et al., 2013), with the elimination of the corresponding edge. Pearson's correlation coefficient has been used widely as a connectivity measure among different brain regions in fMRI studies (Smith et al., 2011; Messé et al., 2012; Bohr et al., 2013; Hosseini and Kesler, 2013; Vuksanović and Hövel, 2015; Ye et al., 2015; Yi et al., 2015; Yu et al., 2015; Stam et al., 2016).

Finally, we recruit a proposed global metric so as to describe the effective connectivity of every weighted and undirected graph by means of the average cost in the network. More specifically, connectivity is defined as the sum of the edge weights over the maximum number of edges in (average number of edges), as a special form of the definition in (Klados et al., 2016):

$$conn = \frac{1}{n-1} \cdot \sum_{w_{ij} \in G, i \neq j} w_{ij} \quad (3.1)$$

where  $w_{ij}$  is the weight of the path (edge) that connects nodes  $i$  and  $j$ . This global measure has been computed for each individual's weighted and undirected graph.

### 3.4.2. Common network models

The first Graph Theory applications concerned the study of small and deterministic networks (Stam et al., 2014). However, there are three types of networks that are of great interest nowadays; random, regular and small-world networks (**Fig. 3.4**).

The mathematical properties of random graphs were first developed by Erdos and Renyi in 1960 who successfully revealed the emergence of certain structural properties of them (Erdos and Renyi, 1960). Random networks are non-realistic networks and often used as null models for benchmarking real networks (Stam and van Straaten, 2012). Moreover, random graphs are characterized by low clustering coefficient (local connectedness) and short characteristic path length (average path length) (Stam and van Straaten, 2012; Stam et al., 2014; Miraglia et al., 2016). Random graphs are homogeneous networks (like regular or lattice networks) cause they are formed by topologically equivalent nodes having a Poisson degree distribution (Boccaletti et al., 2006). However, most of the real networks tend to follow a degree distribution that is well localized around an average value (Boccaletti et al., 2006; Stam et al., 2014) such as a power law shaped degree distribution  $P(k) \sim Ak^{-\gamma}$ , where  $A$  is a normalization constant and the exponents vary in the range  $2 < \gamma < 3$  (Boccaletti et al., 2006; van den Heuvel et al., 2008a; Stam and van Straaten, 2012). These type of networks are known as scale-free networks and were firstly introduced by Barabasi and Albert (Barabasi and Albert, 1999). Scale-free networks are mainly characterized by the existence of a few nodes with high degree (hubs) thus preserving the high global connectivity (Barabasi and Albert, 1999; van den Heuvel et al., 2008a; Stam et al., 2012; Stam and van Straaten, 2012).

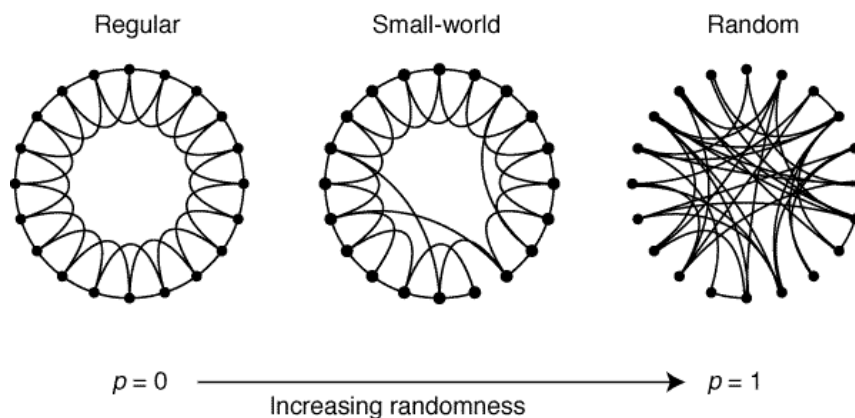


**Figure 3.4.** The three common brain network architectures (Watts and Strogatz, 1998).

The last and most dominant aspect of network science was the small-world model introduced by Watts and Strogatz (Watts and Strogatz, 1998). According to their proposed model (Watts and Strogatz, 1998), vertices are firstly circularly placed on a ring pattern, where each vertex is connected to its neighbors. Then, a random edge was chosen with a rewiring probability  $p$  and afterwards rewired to another random vertex. By testing different values for  $p$  it came out that for  $p = 0$  (no edge rewiring) the resulting model was a lattice (or regular

graph). On the other hand, if every edge was rewired ( $p = 1$ ) the resulting graph was a random one (i.e., ER graph). More importantly, it should be noted that for small  $p$  (i.e., 0.05), the resulting graph combined high clustering (like regular networks) with short path lengths (like random networks) (C.J. Stam, E.C.W. van Straaten, 2012; Watts and Strogatz, 1998; M.P. van den Heuvel et al., 2008; Stam et al., 2015; F. Miraglia et al., 2015; A. Messe et al., 2012). These intermediate networks are called small-world networks and are characterized by both local segregation and global integration (Stam et al., 2014; Tewarie et al., 2015a).

### 3.4.3. Small-worldness property evaluation

A small-world network (Watts and Strogatz, 1998) can be described by high local clustering, characterized by a high clustering coefficient,  $C_p$ , and low minimum path length between any pair of nodes, expressed by a low characteristic path length,  $L_p$  (Watts and Strogatz, 1998). The clustering coefficient quantifies the extent of local cliquishness of a network, or the likelihood that neighbors of a vertex will still be connected (Reijneveld et al., 2007; Stam et al., 2009), whereas the characteristic path length reflects the mean distance or routing efficiency between any given pair of nodes (Yi et al., 2015).

The weighted clustering coefficient of a node  $i$  can be expressed as the average intensity of triangles around that node (Onnela et al., 2005; Rubinov and Sporns, 2010):

$$C^w_i = \sum_{i \in G} \frac{2t^w_i}{k_i(k_i - 1)} \quad (3.2)$$

where  $k_i$  is the degree of node  $i$  and  $t^w_i$  is the weighted geometric mean of the triangles around that node:

$$t^w_i = \frac{1}{2} \cdot \sum_{j,k \in V} (w_{ij}w_{jk}w_{kl})^{1/3} \quad (3.3)$$

where  $w_{ij}, w_{jk}, w_{kl}$  are the weights between node pairs  $(i, j)$ ,  $(j, k)$  and  $(k, l)$ , respectively. The average weighted clustering coefficient can then be expressed as the global metric computing the average nodal clustering coefficient (Watts and Strogatz, 1998; Rubinov and Sporns, 2010):

$$C^w = \frac{1}{n} \cdot \sum_{i \in G} C^w_i \quad (3.4)$$

with  $n$  denoting the total number of nodes.

The weighted characteristic path length is given by:

$$L^w = \frac{1}{n} \cdot \sum_{i \in G} \frac{d^w_{ij}}{(n-1)} \quad (3.5)$$

with  $d_{ij}^w$  denoting the shortest weighted path between nodes and (Rubinov and Sporns, 2010). Notice that the shortest path length is a basis for measuring integration while the number of triangles is for measuring segregation (Rubinov and Sporns, 2010).

Based on the notions of weighted clustering coefficient and characteristic path length, the small-worldness property has been examined by means of the metric defined as (Rubinov and Sporns, 2010):

$$\sigma^w = \frac{\gamma^w}{\lambda^w} = \frac{C^w/C^w_{rand}}{L^w/L^w_{rand}} \quad (3.6)$$

where  $C^w_{rand}$ ,  $L^w_{rand}$  refer to randomly generated networks.

With the aim of investigating the small-worldness property of cerebellum's network associated with the IQ groups, we should compare them to a null model. In order to do so, a total number of 100 random (edge and weight preserving) weighted and undirected graphs (Hosseini and Kesler, 2013) were constructed for computing  $C^w_{rand}$  and  $L^w_{rand}$ , using the [Brain Connectivity Toolbox](#) (Rubinov and Sporns, 2010). In a small-world network,  $C^w$  is significantly larger than  $C^w_{rand}$  ( $\gamma^w > 1$ ) whereas  $L^w$  is comparable to  $L^w_{rand}$  ( $\lambda^w > 1$ ) and, therefore,  $\sigma^w > 1$  (Sporns, 2006; Rubinov and Sporns, 2010). As a result, a small-world network can successfully describe complex brain networks by combining high levels of local clustering among nodes and short paths that are globally linking all nodes of the network, therefore maximizing the efficiency of information transfer at low wiring cost (Bullmore and Sporns, 2009; Wang et. al, 2010).

Cerebellum manifests a small-world network structure in both low and high-IQ populations (low-IQ:  $1.2644 \pm 0.1765$ ; high-IQ:  $1.2126 \pm 0.1010$ ), implying that cerebellum network works efficiently at low wiring cost for both IQ groups. The same evidence stands for males/females comparisons (low-IQ males:  $1.2334 \pm 0.1243$ ; high-IQ males:  $1.2287 \pm 0.1243$ ; low-IQ females:  $1.2821 \pm 0.1994$ ; high-IQ females:  $1.2002 \pm 0.0783$ ). Low-IQ subjects tend to have higher average clustering coefficient ( $1.1939 \pm 0.0857$ ) but smaller characteristic path length ( $0.9548 \pm 0.0917$ ) than their high-IQ peers (avg. clustering coefficient:  $1.1634 \pm 0.0564$ ; characteristic path length:  $0.9640 \pm 0.0689$ ). Moreover, low-IQ males and females have similar characteristic path lengths (low-IQ males:  $0.9523 \pm 0.0774$ ; low-IQ females:  $0.9562 \pm 0.0997$ ) but females have higher average clustering coefficient (low-IQ males:  $1.1671 \pm 0.0661$ ; low-IQ females:  $1.2092 \pm 0.0923$ ). In addition, high-IQ females have higher average clustering coefficient than high-IQ males (high-IQ males:  $1.1520 \pm 0.0396$ ; high-IQ females:  $1.1720 \pm 0.0657$ ), as well as characteristic path-length (high-IQ males:  $0.9454 \pm 0.0878$ ; high-IQ females:  $0.9781 \pm 0.0466$ ). The above results are summarized on **Table 3.3**. Statistical analysis results on these measures as well as on the rest MST measures are presented later on, in **Section 3.8**.

<b>Table 3.3.</b> Small-world properties information.			
<b>Groups</b>	<b>Avg. clustering coefficient</b>	<b>Characteristic path length</b>	<b>Small-worldness</b>
	Mean±SD	Mean±SD	Mean±SD
<b>Low-IQ</b>	1.1939±0.0857	0.9548±0.0917	1.2644±0.1765
<b>High-IQ</b>	1.1634±0.0564	0.9640±0.0689	1.2126±0.1010
<b>Males, low-IQ</b>	1.1671±0.0661	0.9523±0.0774	1.2334±0.1243
<b>Males, high-IQ</b>	1.1520±0.0396	0.9454±0.0878	1.2287±0.1243
<b>Females, low-IQ</b>	1.2092±0.0923	0.9562±0.0997	1.2821±0.1994
<b>Females, high-IQ</b>	1.1720±0.0657	0.9781±0.0466	1.2002±0.0783

### 3.5. Minimum Spanning Trees

#### 3.5.1. Basic concept

An alternative way of modeling a weighted graph  $G$  is based on the notion of the Minimum Spanning Tree (MST), which is an acyclic (loopless) subgraph connecting all nodes of  $G$  (Laskaris and Ioannides, 2001). A spanning tree is a connected subgraph of the original graph with  $n$ -nodes and exactly  $n - 1$  edges (Stam et al., 2014; Tewarie et al., 2015b). A MST is a spanning tree that manages to preserve only the edges that minimize the total cost defined as the sum of the weights of the edges. The minimum spanning tree of a graph is unique if and only if the weights in  $G$  are also unique (Stam et al., 2014a). The MST is a straightforward method that overcomes biases introduced by comparing networks with different number of edges and eliminates any disconnected syndromes within the network (Stam and van Straaten, 2012; van Diessen et al., 2015). This property renders MST a reliable method for the effective interpretation of functional effects and functional connectivity analysis of complex networks in EEG (Boersma et al., 2013; van Diessen et al., 2014; Vourkas et al., 2014; Engels et al., 2015; van Dellen et al., 2015) and MEG (Olde Dubbelink et al., 2014; Tewarie et al., 2014; Tewarie et al., 2015a), as well as in fMRI studies (Lin et al., 2014; Song et al., 2015; Tewarie et al., 2015a). The MST provides a graph representation that absorbs population characteristics into a compact form and facilitates the distinction of different populations through the computation of various metrics or descriptors.

#### 3.5.2. MST formation

In our study, MSTs were constructed using Kruskal's scheme (Kruskal, 1956), which first orders the weights of all edges in ascending order and constructs the MST by sequentially adding the edge with the smallest weight until all nodes are connected in an acyclic subgraph. Nevertheless, since we are only interested in evaluating the strongest connections, e.g., the edges with the largest weights (Boersma et al., 2013; Engels et al., 2015; Tewarie et al., 2015b), the edge weights were defined as the inverse of functional connectivity estimates,

e.g.,  $1/\text{correlation coefficient}$ . The outcome forms an acyclic subgraph that maximizes the total weight and thus includes the strongest connections with the edges of MST having a value of one. In total, 136 MSTs were computed with 27 nodes and 26 edges each, based on the above procedure. In order to model and assess the functionality of each MST, three nodal and six global metrics were recruited, as described in the sequel. The MSTs were finally categorized into two groups based on the IQ level (69/67; low/high-IQ) with the purpose of detecting and characterizing hubs within all 27 ROIs as well as testing for IQ and gender differences. Recall that such MST comparisons assess the effects of only the strongest connections within the original network topology and therefore the MST can be suitably used to examine the IQ's (and gender's) effect in cerebellum.

The average weighted and undirected graphs and the resulting MSTs are presented in **Fig. 3.5** for illustration purposes only, using [BrainNet viewer](#) (Xia et al., 2013). Although the networks in low and high-IQ populations seem similar, their differences are revealed by the corresponding features that quantify the network's topological structure.

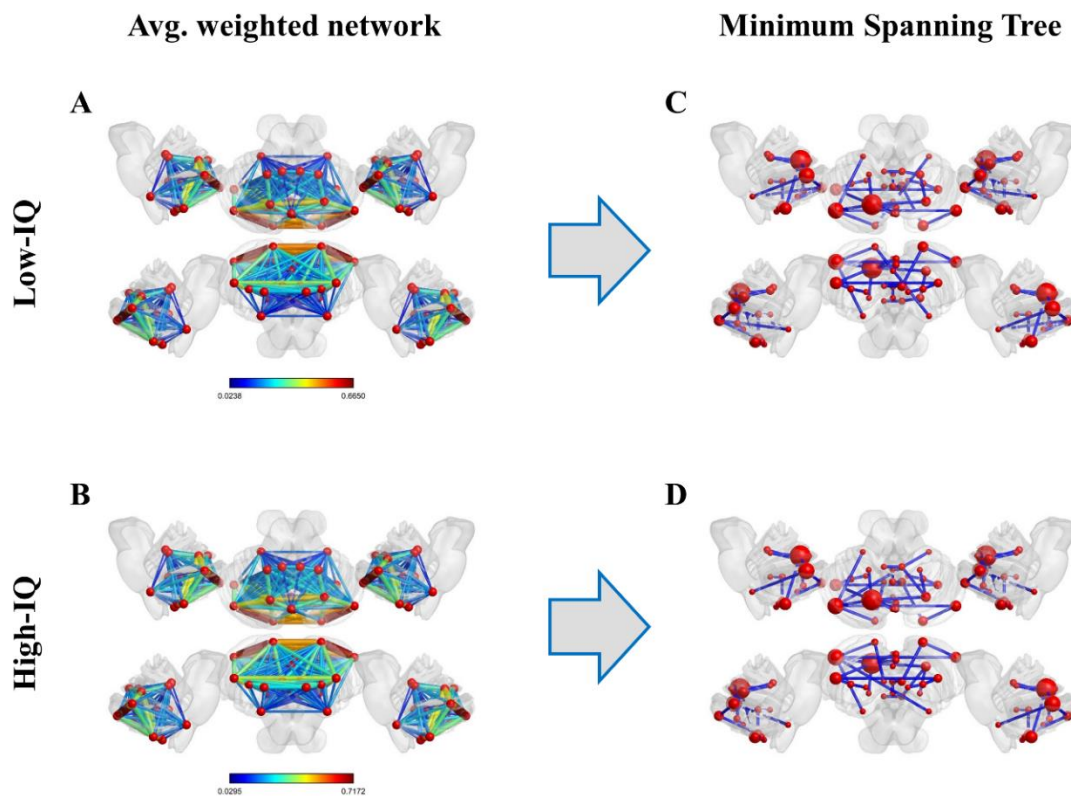


**Figure 3.5.** Average weighted and undirected graphs per IQ group (left panel, **A**: low-IQ and **B**: high-IQ) and their corresponding MSTs (right panel, **C**: low-IQ and **D**: high-IQ). On the latter representation, each node's size depends linearly on its average BC value.

### 3.5.3. Local MST features

For a given node  $i \in V$ , where  $V$  is the set of nodes and  $n$  is the number of nodes, the ensuing local MST metrics are estimated as features of hubs (Stam et al., 2014a).

- **Degree**,  $k_i$ , is the number of neighbors connected to  $i$ :

$$k_i = \sum_{j \in V} a_{ij} \quad (3.7)$$

where  $a_{ij}$  is one if there exists a link between nodes  $i$  and  $j$  and zero otherwise. Nodes with high degree can be considered as hubs. Degree quantifies the significance of a region and is normalized with the corresponding  $DEG_{max}$  in order to be comparable with other local metrics.

- **Betweenness centrality**,  $BC_i$ , defines the number of shortest paths between any two nodes  $k$  and  $l$  in the network passing through  $i$ , divided by the total number of shortest paths between these two nodes (Olaf and Sporns, 2010). More specifically:

$$BC_i = \sum_{\substack{k, l \in V \\ k \neq l, k \neq i, l \neq i}} \frac{p_{kl}^i}{p_{kl}} \quad (3.8)$$

where  $p_{kl}$  is the number of shortest paths between  $k$  and  $l$  and  $p_{kl}^i$  is the number of shortest paths between  $k$  and  $l$  but passing through  $i$ . A BC value of zero indicates a leaf node whereas a BC value of one indicates a central node in a star-like topology. The node with the highest BC plays an important role in the overall network's communication (van Dellen et al., 2015), since it has the highest load and reflects the highest number of shortest paths between any two nodes that run through this node (Boersma et al., 2013; Tewarie et al., 2014). We further normalize BC with the corresponding  $BC_{max}$  in order to maintain a specific normalization pattern with the other local metrics.

- **Eccentricity** of node  $i$ , is the longest shortest path from node  $i$  to any other node in the MST. A node with low eccentricity is more central in a tree and therefore eccentricity acts as a measure of the central topological organization of a network (Otte et al., 2015; van Dellen et al., 2015). For consistency, ECC has been normalized by the corresponding  $ECC_{max}$ , which reflects the graph diameter.

The average DEG, BC, ECC values for low and high-IQ groups are displayed in **Fig. 3.6** and analyzed in more detail in the **Appendix (Tables A1-A4)**, alongside with the average MST local metrics for low/high-IQ males and females. According to **Fig. 3.6**, the DEG and BC metrics tend to have similar distributions since the number of connections that pass through a specific node is related with the overload-ness within the network and vice versa. The number of nodes with the highest BC and DEG values (hubs) is small. On the other hand, ECC values exhibit a much more homogeneous diffuse. Nodes with small eccentricity values are much closer to the center of the network and are characterized by higher BC and DEG values.

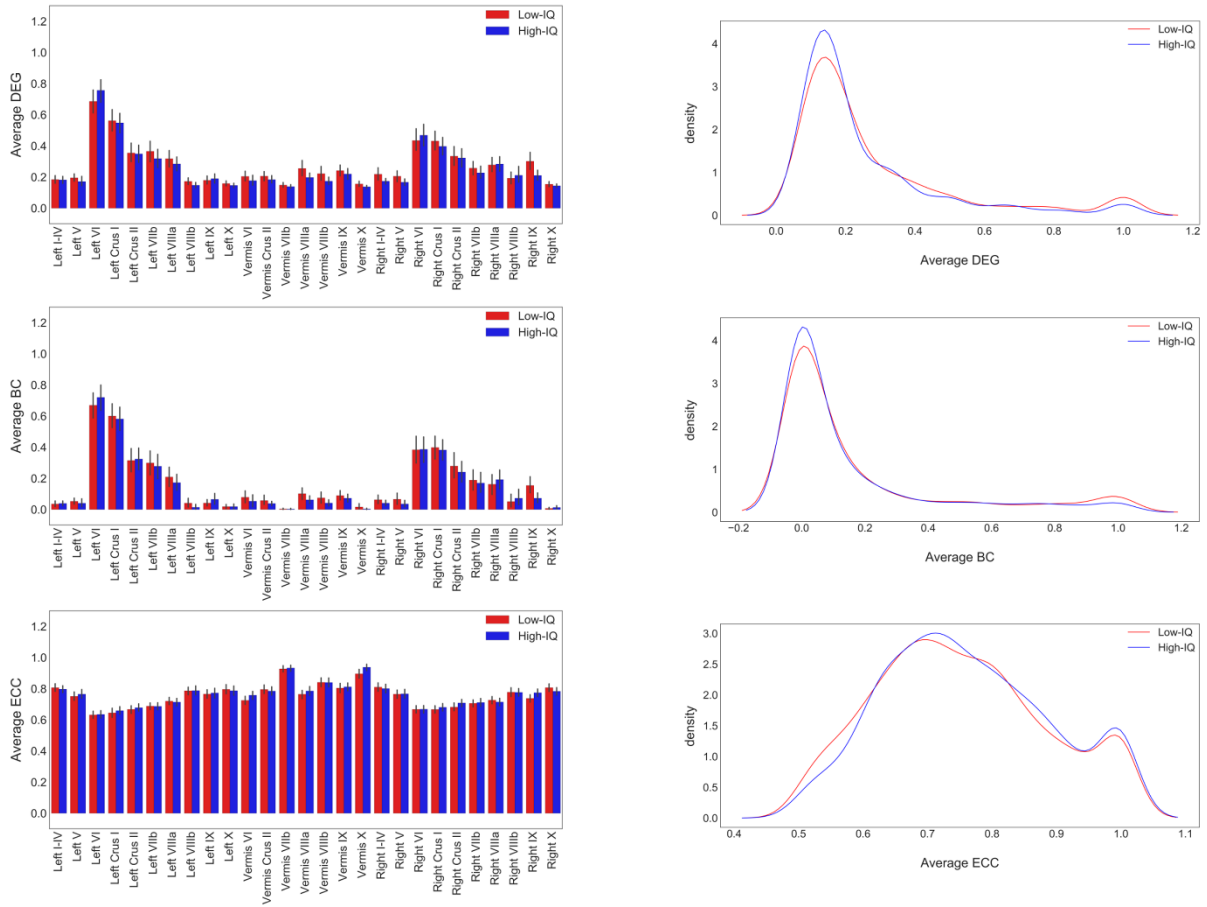


**Figure 3.6.** Average DEG, BC, ECC values per ROI for both IQ groups on the left panel and the corresponding distributions on the right panel.

### 3.5.4. Global MST features

For a given MST with  $n$  nodes and  $n - 1$  edges, we define the following MST global metrics:

- **Leaf number**,  $N_{leaf}$ , is the number of nodes with degree equal to one. It has a lower bound of 2 and an upper bound of  $n - 1$ . However, it's often useful to compute the fraction of leaf nodes,  $L_f = N_{leaf}/n - 1$ , in the MST (Tewarie et al., 2014; Tewarie et al., 2015a, b).
- **Degree correlation**,  $r_{deg}$ , is an index of whether the degree of a node is influenced by the degree of its neighboring connected vertices (Boersma et al., 2013) and is equal to the Pearson correlation coefficient of the MST's degree sequence (known as Pearson degree correlation). Most biological networks tend to be disassortative with negative degree correlation (Boersma et al., 2013).

- **Diameter**,  $d$ , is the maximum eccentricity (longest shortest path) of the nodes and has an upper bound of  $n - N_{leaf} + 1$ . A small diameter leads to better global communication between remote nodes (van Dellen et al., 2015).
- **Radius**,  $r$ , is defined as the node with the smallest eccentricity in the tree, with small radius reflecting more central topology.
- **Kappa or degree divergence**,  $\kappa$ , is a measure of the broadness of the degree distribution (Stam et al., 2014a; Tewarie et al., 2014):

$$\kappa = \frac{\langle k^2 \rangle}{\langle k \rangle} \quad (3.9)$$

where  $k$  is the degree sequence and  $\langle \ \rangle$  denotes the average operator. Degree divergence is related to resilience against attacks, epidemic spreading and the synchronizability (i.e., information flow) of tree nodes (Otte et al., 2015; Tewarie et al., 2015b). High  $\kappa$  values suggest the existence of high degree nodes in the tree, mostly related to scale-free networks (Otte et al., 2015).

- **Tree hierarchy**,  $T_h$ , is an hierarchical metric that quantifies the balance between diameter reduction and overload prevention (Boersma et al., 2013). It is defined as:

$$T_h = \frac{N_{leaf}}{2(n-1)BC_{max}} \quad (3.10)$$

where the denominator is multiplied by 2 to assure that  $T_h$  varies in the interval [0,1].  $T_h$  is equal to  $2/(n-1)$  for a line-like topology and for a star-like topology  $T_h$  approaches 0.5 whereas for intermediate network topologies  $T_h$  can vary between  $2/(n-1)$  and 1 (Stam et al., 2014a). An optimal tree configuration is characterized by a combination of small diameter (i.e., short distances as in a star-like topology) and prevention of the overload of the central tree nodes (hubs). The latter corresponds to  $T_h$  values around 0.5.

### 3.6. Hub(s) detection

Nodes with high BC and DEG values are characterized as critical nodes (hubs) and are used to determine the information flow within the network. In order to detect the most important nodes (hubs), we computed the total number of low/high-IQ males and females exhibiting the maximum DEG, BC values, divided by the total number of subjects per IQ and gender combination, respectively. The cerebellum's surface template was common in all figures for visualization purposes. The size of each node depends linearly on the percentage of the corresponding population with the highest BC or DEG value, according to the case

under examination. With the term “highest BC or DEG value” we refer to nodes that exhibited normalized BC or DEG values close to (or equal to) one.

Hub analysis reveals that lobule Left VI is a critical node having the highest BC value in almost 36% of the low-IQ population and 49% of the high-IQ population, as well as the highest DEG value in 41% of the low-IQ population and 52% of the high-IQ population (**Fig. 3.7**). Thus, lobule Left VI is responsible for “traffic” monitoring in the cerebellum network for both IQ groups. This Left VI's significance in information transfer is of the same importance for low and high-IQ subjects, but with a higher manifestation in the high-IQ population. Moreover, lobules Left Crus I and Right VI can also be characterized as hubs, but with a smaller dominance than Left VI. The Left Crus I lobule activates more in the low-IQ population, as indicated by DEG and almost equally activated for both groups as indicated by BC. Alternatively, the Right VI lobule is more active in the high-IQ population, even though to a smaller extent than other lobules.

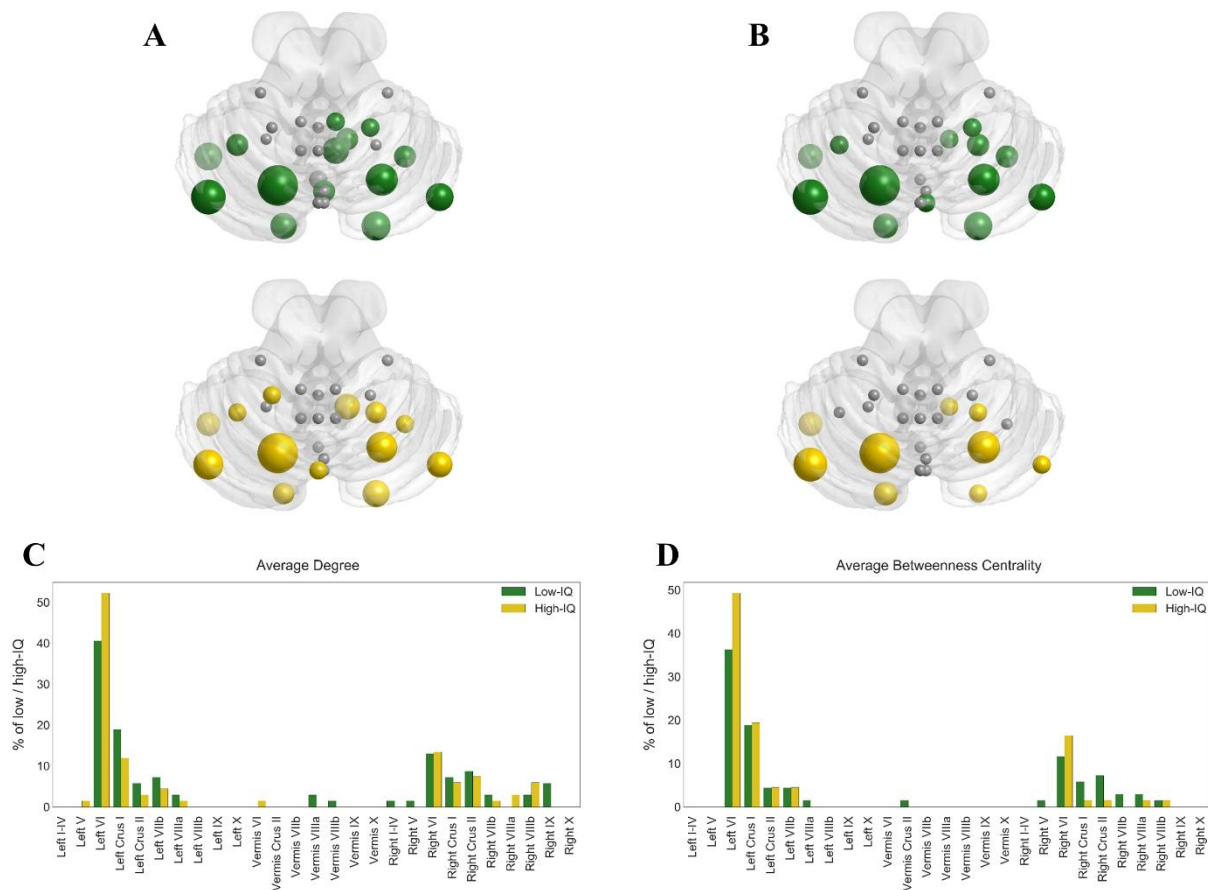


**Figure 3.7.** Hub locations on cerebellum for low (green) and high (yellow) IQ groups based on BC (**A**) and DEG (**B**). The size of each node depends on the percentage of low/high-IQ subjects with the highest BC (**C**) and DEG (**D**) values.

These hub indications have also been validated for the low and high-IQ male/female populations. Region Left VI is indeed a critical node for all groups, having the highest BC value in 40% of low-IQ males and 34% of low-IQ females, as well as the highest DEG value in 48% of low-IQ males and 36% of low-IQ females (**Fig. 3.8**).

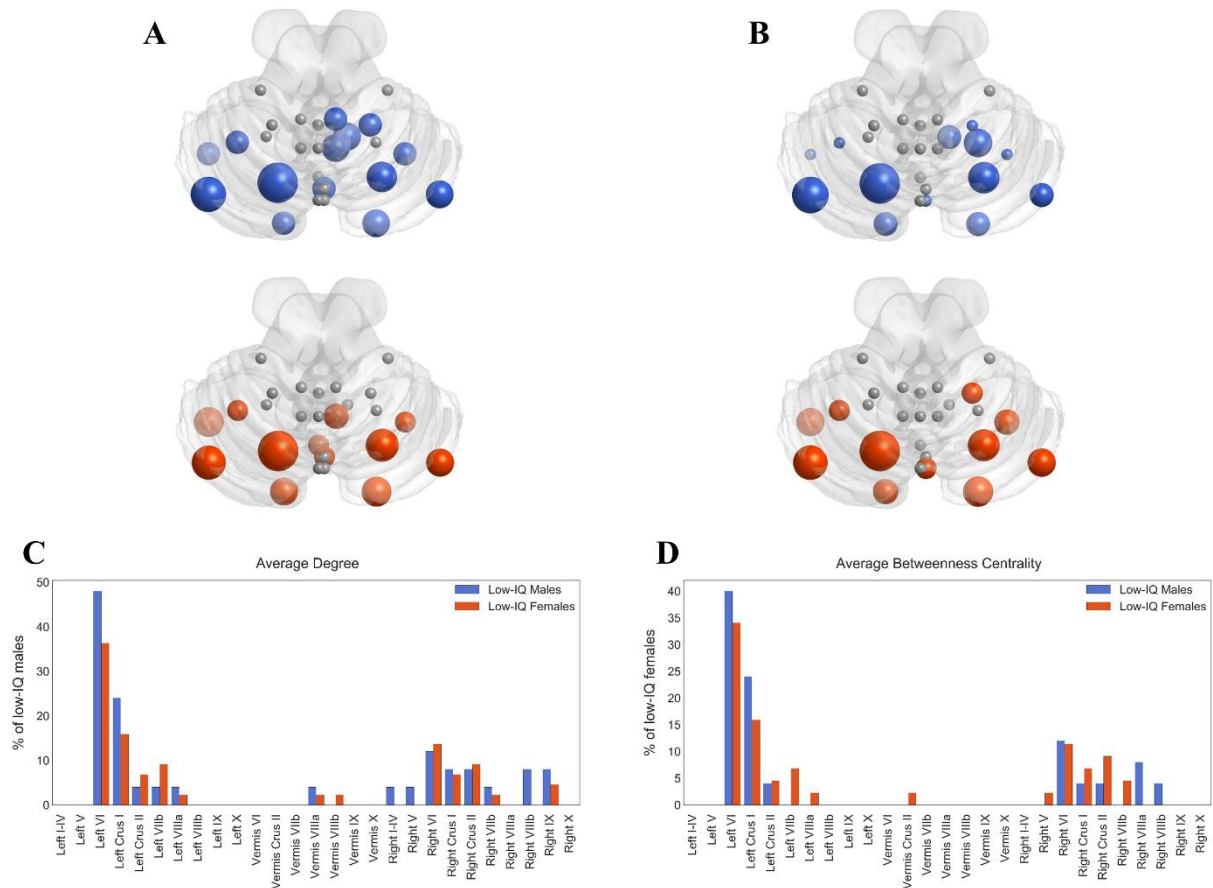


**Figure 3.8.** Hub locations on cerebellum for low-IQ males (light blue) and females (orange) IQ groups based on BC (**A**) and DEG (**B**). The size of each node depends on the percentage of low-IQ males/females with the highest BC (**C**) and DEG (**D**) values.

In the high-IQ population, Left VI demonstrates the highest BC value in 48% of high-IQ males and 50% of high-IQ females, as well as the highest DEG value in 52% of high-IQ males and 53% of high-IQ females (**Fig. 3.9**). In addition, the Left VI hub appears stronger in high-IQ females than high-IQ males. Left Crus I is more activated in low/high-IQ males as indicated by both BC and DEG measures whereas the opposite stands for Right VI which appears to be more activated in low/high-IQ females. In each individual figure we can compare the size and the number of nodes that participate in hub analysis. The bar plots (on the lower panel) and the cerebellar anatomical plots (on the upper panel) encode the same information but offer additional visual interpretation on the cerebellar surface, thus providing the anatomical location for each hub. These figures offer a clear representation concerning the hub locations for the different populations of interest.

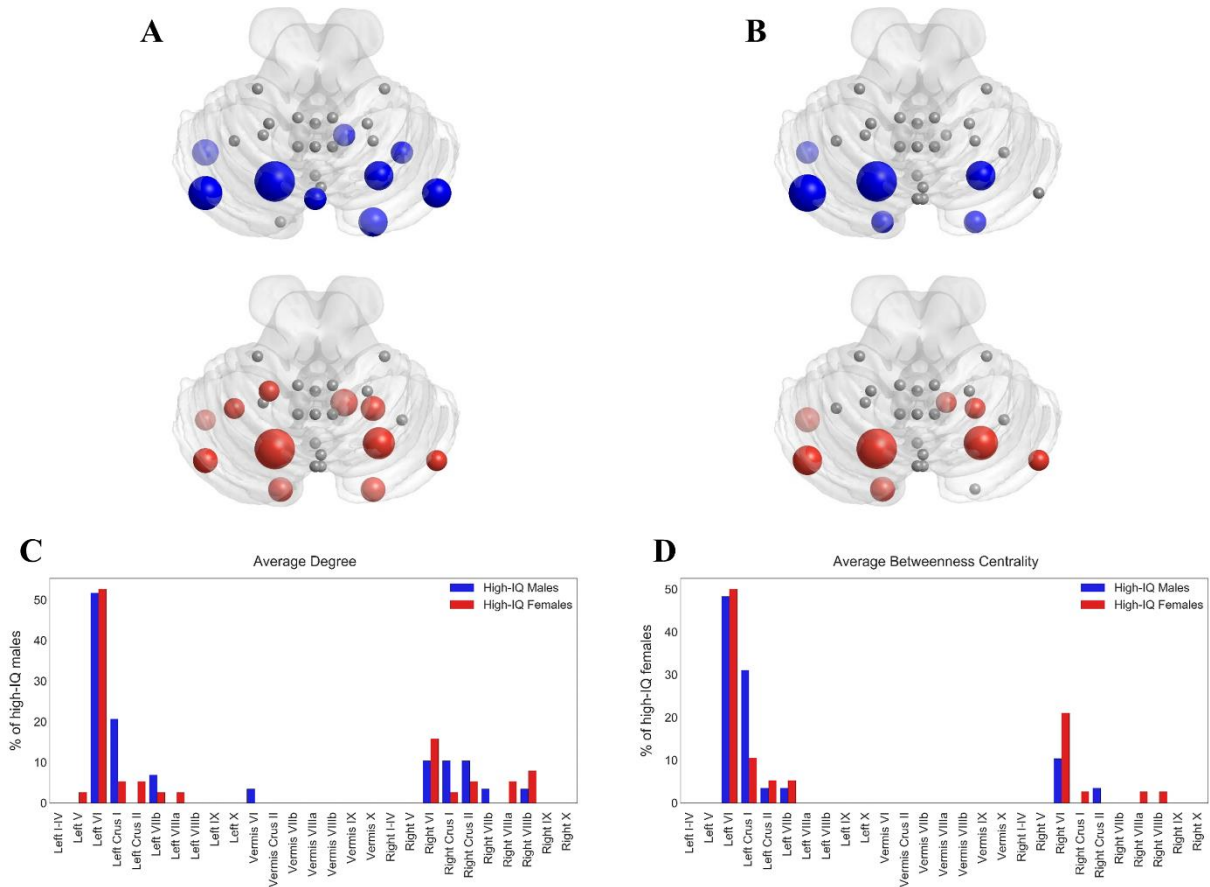


**Figure 3.9.** Hub locations on cerebellum for high-IQ males (navy blue) and females (red) IQ groups based on BC (A) and DEG (B). The size of each node depends on the percentage of high-IQ males/females with the highest BC (C) and DEG (D) values.

### 3.7. Correlation between hub metrics and Median Response Times

Another goal of this study is to seek for the region of cerebellum that is mostly related with the Median Response Times (MRTs) across all individuals. In order to do so, we computed Pearson's correlation coefficients between each ROI's hub indicators (DEG, BC values) and subjects' MRT values, by taking into consideration the IQ factor, respectively. As a final step, the region with the highest (significant or non-significant) correlation value was selected. Alongside with the correlation value, a p-value is also returned which indicates whether there is a significant relationship between the values under examination (i.e.,  $<0.05$ ) or a non-significant one (i.e.,  $>0.05$ ), using lower and upper bounds for a 95% confidence interval for each coefficient. The statistical test uses a standard Student's t distribution for transforming the correlation value. The MRT values were obtained per individual through our Level 1 - HCP access (non-sensitive information). Please note that the MRT values are expressed in seconds (sec). **Figures 3.10 – 3.12** were produced using [Python's Seaborn statistical data visualization library](#). The precision of the r and p-values has been reduced to only two digits after the decimal point, only in the figures, for visualization purposes.

Region Left X exhibited the highest positive significant correlation between DEG and MRT for the low-IQ group ( $r = 0.42$ ,  $p = 0.0004$ ) as well as between BC and MRT ( $r = 0.43$ ,  $p = 0.0003$ ). On the other hand, region Vermis VIIIb indicated the highest positive correlation between DEG and MRT for the high-IQ group ( $r = 0.14$ ,  $p = 0.27$ ) as well as between BC and MRT ( $r = 0.19$ ,  $p = 0.14$ ), without however any statistical significance at all (**Fig. 3.10, Table 3.4**). The distributions of the metrics under examination are displayed on the upper and left panels of each individual subplot opposite to the corresponding label.

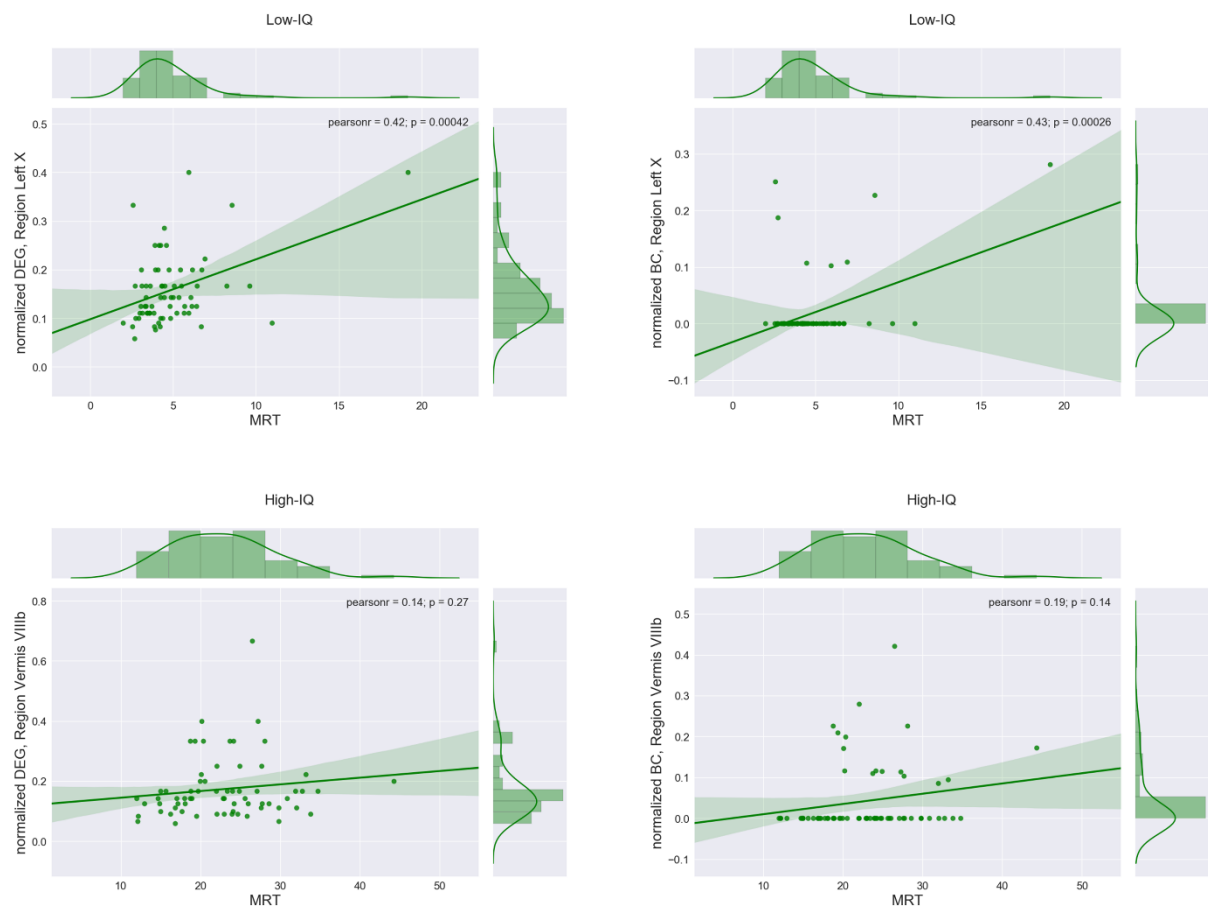


**Figure 3.10.** Regions with the maximum correlation between average DEG or BC measure and median response times (MRTs) for low and high-IQ groups.

The exact same procedure was repeated for males and females in both IQ groups. In the male population, region Left Crus II exhibited the highest positive significant correlation between DEG and MRT for the low-IQ group ( $r = 0.57$ ,  $p = 0.0034$ ), whereas region Left VI was the one for the high-IQ group ( $r = 0.21$ ,  $p = 0.29$ ) but without any significance. Alternatively, the lobule with the highest positive significant correlation between BC and MRT was Vermis VIIIb ( $r = 0.54$ ,  $p = 0.006$ ) for the low-IQ group while Right X was selected for the high-IQ group ( $r = 0.25$ ,  $p = 0.2$ ) without again any significance (**Fig. 3.11, Table 3.4**).

**Table 3.4.** ROI(s) with the maximum correlation coefficient between MRT and DEG or BC measure for both IQ groups and gender.

Group		DEG			BC		
		maximum corrcoef	p	ROI	maximum corrcoef	p	ROI
Low IQ	Total	0.42	<b>0.0004</b>	Left X	0.43	<b>0.0003</b>	Left X
	Males	0.57	<b>0.0034</b>	Left Crus II	0.54	<b>0.006</b>	Vermis VIIIb
	Females	0.47	<b>0.0014</b>	Left X	0.46	<b>0.002</b>	Left X
High IQ	Total	0.14	0.27	Vermis VIIIb	0.19	0.14	Vermis VIIIb
	Males	0.21	0.29	Left VI	0.25	0.2	Right X
	Females	0.23	0.18	Vermis VIIIb	0.2	0.24	Vermis VIIIb

with **bold** highlight: statistical significant results ( $p < 0.05$ ).

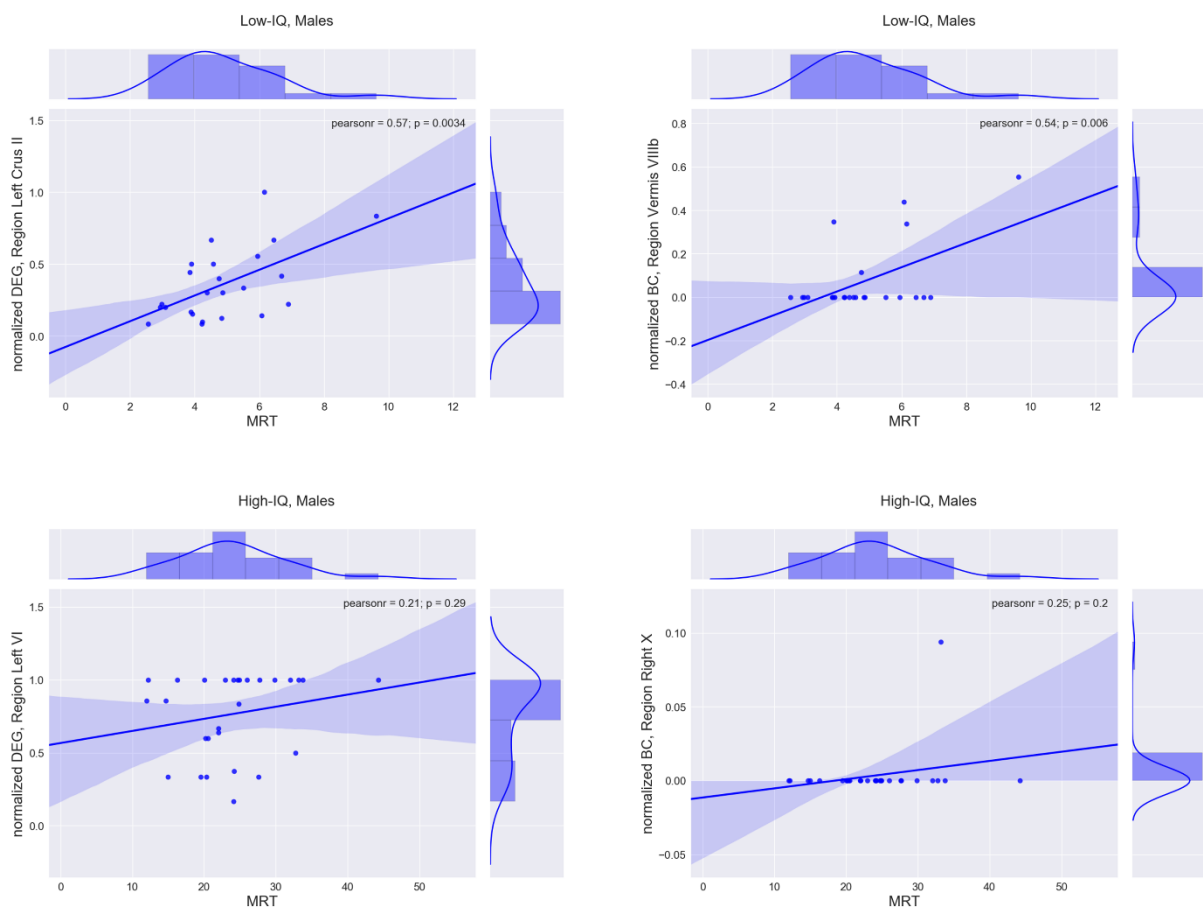


**Figure 3.11.** Regions with the maximum correlation between average DEG or BC measure and median response times (MRTs) for low and high-IQ males.

Focusing now on females, region Left X exhibited the highest positive significant correlation between DEG and MRT for the low-IQ group ( $r = 0.47$ ,  $p = 0.0014$ ). On the other hand, region Vermis VIIIb was the one with the highest positive (non-significant) correlation for the high-IQ group ( $r = 0.23$ ,  $p = 0.18$ ). Finally, the region with the highest correlation between BC and MRT was again Left X ( $r = 0.46$ ,  $p = 0.002$ ) for the low-IQ group and Vermis VIIIb for the high-IQ group ( $r = 0.2$ ,  $p = 0.24$ ) but without any significance (**Fig. 3.12, Table 3.4**). In general, all regions that exhibited the highest correlations between DEG/BC and MRT, in the high-IQ group, were non-significant.

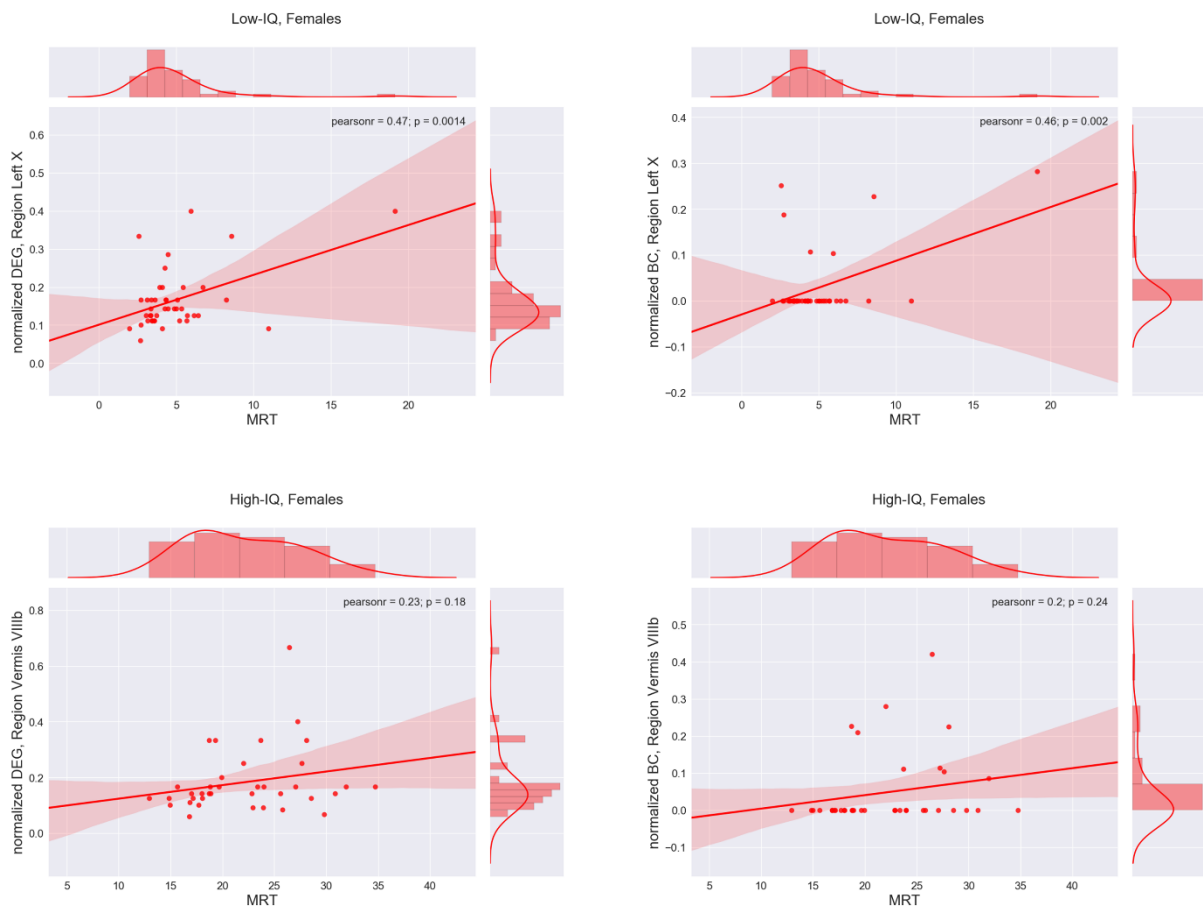


**Figure 3.12.** Regions with the maximum correlation between average DEG or BC measure and median response times (MRTs) for low and high-IQ females.

### 3.8. Statistical analysis per group combination

#### 3.8.1. One-way ANOVA

The purpose of one-way ANOVA is to determine whether data from several groups (levels) of a factor have a common mean. Therefore, one-way ANOVA manages to find out whether different groups of an independent variable have different effects on the response variable, assume  $y$ . One-way ANOVA is a simple special case of the linear regression model.

The one-way ANOVA form of the model is:

$$y_{ij} = \alpha_j + \varepsilon_{ij} \quad (3.11)$$

with the following assumptions:

- $y_{ij}$  is an observation, in which  $i$  represents the observation number, and  $j$  represents a different group (level) of the predictor variable  $y$ . All  $y_{ij}$  are independent.
- $\alpha_j$  represents the population mean for the  $j$ -th group.
- $\varepsilon_{ij}$  is the random error, independent and normally distributed, with zero mean and constant variance, i.e.,  $\varepsilon_{ij} \in N(0, \sigma^2)$ .

This model is also called the “**means model**”. The model assumes that the columns of  $\mathbf{y}$  are the constant  $\alpha_j$  plus the error component  $\varepsilon_{ij}$ . ANOVA helps determine if the constants are all the same. ANOVA tests the hypothesis that all group means are equal (known as null hypothesis) versus the alternative hypothesis that at least one group is different from the others, that is:

- $H_0 = \alpha_1 = \alpha_2 = \dots = \alpha_k$  (null hypothesis).
- $H_1$ : not all group means are equal (alternative hypothesis).

In this work, we used MATLAB’s **`anova1(y, group)`** command where  $\mathbf{y}$  is an individual feature vector containing a local/global MST metric every time (the dimension of vector  $\mathbf{y}$  is equal to  $3672 \times 1$  if we examine a local feature or  $136 \times 1$  if we examine a global one). Each value in  $\mathbf{y}$  belongs to one of the five different group combinations (i.e., low/high-IQ, low/high-IQ males, low/high-IQ females, low-IQ males/females, high-IQ males/females) and has a non-equal number of observations (i.e., an un-balanced design). The input **`group`** is a string vector with the same dimension as  $\mathbf{y}$ , containing the appropriate group label for each element in  $\mathbf{y}$ . As a matter of fact, through this command we can test the equality of group means, specified in **`group`**, for the data in vector  $\mathbf{y}$ .

### 3.8.2. Statistical analysis application procedure

Small-world properties were investigated for all weighted and undirected graphs and, afterwards, the corresponding MSTs were constructed. Subsequently, three local (BC, ECC, DEG) and six global (diameter, degree correlation, radius, kappa, leaf fraction, tree hierarchy) metrics were computed in order to examine the topological and functional characteristics of every MST. Moreover, several global weighted graph metrics, including average weighted clustering coefficient, characteristic path length, small-worldness and connectivity, were also examined in our procedure. The feature datasets are non-normally distributed, in general, so that natural log-transformation was applied in order to approximate normal distribution properties, with the addition of a very small constant ( $1 \cdot e^{-24}$ ) for avoiding zero-value

transforms. Statistical analysis was performed using 1-way unbalanced ANOVA. In total, five cases were investigated in order to test for differences between:

- low and high-IQ groups (low/high-IQ; 69/67),
- males in low and high-IQ groups (low/high-IQ; 25/29),
- females in low and high-IQ groups (low/high-IQ; 44/38),
- males and females in low-IQ group (males/females; 25/44),
- males and females in high-IQ group (males/females; 29/38).

All p-values were corrected based on False Discovery Rate (FDR) using the Benjamini-Hochberg procedure (Benjamini and Hochberg, 1995) with the significance level set to 0.05.

### 3.8.3. Results for each group combination

Below are presented the statistical analysis results for all five group combinations which were stated in the previous section. It is important to note that all three local MST metrics (i.e., DEG, BC and ECC) did not exhibit any significant differences among low/high-IQ groups as well as between the four possible gender-based group combinations (low/high-IQ males, low/high-IQ females, low-IQ males/females, high-IQ males/females). As a matter of fact, the statistical analysis results will be presented only for the global metrics per group combination.

#### ▪ Results for Low/High-IQ population

Between the low/high-IQ groups, significant differences were found only in four global metrics (**Table 3.5**). In particular, these differences are reflected for the metrics of average clustering coefficient (low-IQ:  $1.1939 \pm 0.0857$ ; high-IQ:  $1.1634 \pm 0.0564$ ) ( $F = 5.8769$ ,  $p = 0.0167$ ), connectivity (low-IQ:  $0.1784 \pm 0.0763$ ; high-IQ:  $0.2073 \pm 0.0878$ ) ( $F = 5.1324$ ,  $p = 0.0251$ ), diameter (low-IQ:  $0.4002 \pm 0.1632$ ; high-IQ:  $0.3376 \pm 0.1215$ ) ( $F = 5.2927$ ,  $p = 0.0230$ ) and radius (low-IQ:  $0.4101 \pm 0.1641$ ; high-IQ:  $0.3540 \pm 0.1400$ ) ( $F = 4.3788$ ,  $p = 0.0383$ ).

<b>Table 3.5.</b> Statistical analysis results based on IQ for the main network metrics.				
<b>Metric</b>	<b>Low-IQ</b>	<b>High-IQ</b>	<b>F</b>	<b>p-values</b>
	Mean±SD	Mean±SD		
avg. clustering coefficient	1.1939±0.0857	1.1634±0.0564	5.8769	<b>0.0167</b>
characteristic path length	0.9548±0.0917	0.9640±0.0689	0.6234	0.4312
small-worldness	1.2644±0.1765	1.2126±0.1010	3.6449	0.0584
connectivity	0.1784±0.0763	0.2073±0.0878	5.1324	<b>0.0251</b>
diameter	0.4002±0.1632	0.3376±0.1215	5.2927	<b>0.0230</b>
radius	0.4101±0.1641	0.3540±0.1400	4.3788	<b>0.0383</b>
leaf fraction	0.5920±0.0943	0.6171±0.0872	2.7130	0.1019
tree-hierarchy	0.2960±0.0471	0.3086±0.0436	2.7130	0.1019
kappa	2.2800±0.3344	2.3192±0.2833	0.7636	0.3838
degree correlation	-0.3438±0.1262	-0.3742±0.1233	2.5276	0.1142
with <b>bold</b> highlight: statistical significant results ( $p < 0.05$ ).				

▪ **Results for Low/High-IQ males**

As far as the low/high-IQ males are concerned, no significant differences were found on any global metrics at all (**Table 3.6**).

**Table 3.6.** Statistical analysis results based on males IQ for the main network metrics.

Metric	Low-IQ Males	High-IQ Males	F	p-values
	Mean±SD	Mean±SD		
avg. clustering coefficient	1.1671±0.0661	1.1520±0.0396	0.9639	0.3308
characteristic path length	0.9523±0.0774	0.9454±0.0878	0.1237	0.7265
small-worldness	1.2334±0.1243	1.2287±0.1243	0.0191	0.8907
connectivity	0.2058±0.0822	0.2151±0.0916	0.2060	0.6518
diameter	0.5227±0.2231	0.4906±0.1740	0.0973	0.7563
radius	0.5403±0.2298	0.5161±0.1895	0.0452	0.8325
leaf fraction	0.5892±0.0775	0.6313±0.0766	4.0361	0.0515
tree-hierarchy	0.2946±0.0387	0.3156±0.0383	4.0361	0.0515
kappa	2.3391±0.4098	2.3229±0.3085	0.0001	0.9912
degree correlation	-0.3374±0.1138	-0.3709±0.1213	0.8741	0.3541

▪ **Results for Low/High-IQ females**

On the other hand, significant differences were identified between low and high-IQ females by five global metrics (**Table 3.7**), specifically for average clustering coefficient (low-IQ females:  $1.2092 \pm 0.0923$ ; high-IQ females:  $1.1720 \pm 0.0657$ ) ( $F = 4.2866$ ,  $p = 0.0416$ ), small-worldness (low-IQ females:  $1.2821 \pm 0.1994$ ; high-IQ females:  $1.2002 \pm 0.0783$ ) ( $F = 4.8060$ ,  $p = 0.0313$ ), connectivity (low-IQ females:  $0.1629 \pm 0.0689$ ; high-IQ females:  $0.2014 \pm 0.0856$ ) ( $F = 5.8085$ ,  $p = 0.0182$ ), diameter (low-IQ females:  $0.4291 \pm 0.1654$ ; high-IQ:  $0.3450 \pm 0.1263$ ) ( $F = 6.8101$ ,  $p = 0.0108$ ) and radius (low-IQ females:  $0.4394 \pm 0.1648$ ; high-IQ females:  $0.3629 \pm 0.1510$ ) ( $F = 5.8233$ ,  $p = 0.0181$ ).

**Table 3.7.** Statistical analysis results per female IQ group for the main network metrics.

Metric	Low-IQ Females	High-IQ Females	F	p-values
	Mean±SD	Mean±SD		
avg. clustering coefficient	1.2092±0.0923	1.1720±0.0657	4.2866	<b>0.0416</b>
characteristic pathlength	0.9562±0.0997	0.9781±0.0466	2.1312	0.1482
small-worldness	1.2821±0.1994	1.2002±0.0783	4.8060	<b>0.0313</b>
connectivity	0.1629±0.0689	0.2014±0.0856	5.8085	<b>0.0182</b>
diameter	0.4291±0.1654	0.3450±0.1263	6.8101	<b>0.0108</b>
radius	0.4394±0.1648	0.3629±0.1510	5.8233	<b>0.0181</b>
leaf fraction	0.5935±0.1034	0.6063±0.0940	0.4147	0.5214
tree-hierarchy	0.2968±0.0517	0.3031±0.0470	0.4147	0.5214
kappa	2.2465±0.2827	2.3164±0.2666	1.4271	0.2358
degree correlation	-0.3474±0.1338	-0.3766±0.1264	1.6282	0.2056

with **bold** highlight: statistical significant results ( $p < 0.05$ ).

▪ **Results for Low-IQ males/females**

Four global metrics indicated significant differences between males and females in the low-IQ group (**Table 3.8**), specifically for average clustering coefficient (low-IQ males:  $1.1671 \pm 0.0661$ ; low-IQ females:  $1.2092 \pm 0.0923$ ) ( $F = 4.1227$ ,  $p = 0.0463$ ), connectivity (low-IQ males:  $0.2058 \pm 0.0822$ ; low-IQ females:  $0.1629 \pm 0.0689$ ) ( $F = 4.7494$ ,  $p = 0.0328$ ), diameter (low-IQ males:  $0.3493 \pm 0.1491$ ; low-IQ females:  $0.4291 \pm 0.1654$ ) ( $F = 5.1985$ ,  $p = 0.0258$ ) and radius (low-IQ males:  $0.3584 \pm 0.1524$ ; low-IQ females:  $0.4394 \pm 0.1648$ ) ( $F = 5.3445$ ,  $p = 0.0239$ ).

**Table 3.8.** Statistical analysis results per low-IQ males and females for the main network metrics.

Metric	Low-IQ Males	Low-IQ Females	<i>F</i>	p-values
	Mean±SD	Mean±SD		
avg. clustering coefficient	1.1671±0.0661	1.2092±0.0923	4.1227	<b>0.0463</b>
characteristic path length	0.9523±0.0774	0.9562±0.0997	0.0055	0.9412
small-worldness	1.2334±0.1243	1.2821±0.1994	0.9492	0.3334
connectivity	0.2058±0.0822	0.1629±0.0689	4.7494	<b>0.0328</b>
diameter	0.3493±0.1491	0.4291±0.1654	5.1985	<b>0.0258</b>
radius	0.3584±0.1524	0.4394±0.1648	5.3445	<b>0.0239</b>
leaf fraction	0.5892±0.0775	0.5935±0.1034	0.0001	0.9907
tree-hierarchy	0.2946±0.0387	0.2968±0.0517	0.0001	0.9907
kappa	2.3391±0.4098	2.2465±0.2827	0.7141	0.4011
degree correlation	-0.3374±0.1138	-0.3474±0.1338	0.0033	0.9544

with **bold** highlight: statistical significant results ( $p < 0.05$ ).

▪ **Results for High-IQ males/females**

One significant difference was found between high-IQ males and females (**Table 3.9**) in characteristic path length (high-IQ males:  $0.9454 \pm 0.0878$ ; high-IQ females:  $0.9781 \pm 0.046$ ) ( $F = 4.5376$ ,  $p = 0.0369$ ).

**Table 3.9.** Statistical analysis results between high-IQ males and females for the main network metrics.

Metric	High-IQ Males	High-IQ Females	<i>F</i>	p-values
	Mean±SD	Mean±SD		
avg. clustering coefficient	1.1520±0.0396	1.1720±0.0657	1.9689	0.1653
characteristic path length	0.9454±0.0878	0.9781±0.0466	4.5376	<b>0.0369</b>
small-worldness	1.2287±0.1243	1.2002±0.0783	1.0741	0.3039
connectivity	0.2151±0.0916	0.2014±0.0856	0.4643	0.4980
diameter	0.5494±0.1948	0.5781±0.2116	0.2142	0.6450
radius	0.3937±0.1446	0.4174±0.1736	0.2158	0.6438

leaf fraction	0.6313±0.0766	0.6063±0.0940	1.6029	0.2100
tree-hierarchy	0.3156±0.0383	0.3031±0.0470	1.6029	0.2100
kappa	2.3229±0.3085	2.3164±0.2666	0.0002	0.9877
degree correlation	-0.3709±0.1213	-0.3766±0.1264	0.0516	0.8210
with <b>bold</b> highlight: statistical significant results ( $p < 0.05$ ).				

In summary, all three local MST metrics (DEG, BC, ECC) did not exhibit any significant differences among low/high-IQ groups as well as between the four possible gender-based group combinations (low/high-IQ males, low/high-IQ females, low-IQ males/females, high-IQ males/females). On the other hand, four global metrics (average clustering coefficient, connectivity, diameter and radius) revealed significant differences between low and high-IQ groups as well as between low-IQ male and female populations. The same conclusion stands for low/high-IQ females, with the addition of the small-world metric as well. Characteristic path length was the only metric that exhibited significant difference between high-IQ males and females. As far as the low/high-IQ males are concerned, no significant differences were identified. Our findings in men are in a similar direction with respect to the IQ level, but appear not significant. Both sexes have the characteristics of small-world networks with differences in females indicative of higher cerebellar neural efficiency, especially in higher-IQ females. In relation to the activities of the lobules, the metrics of DEG, BC, and ECC showed no differences between low and high-IQ individuals, or between men and women. The ECC values showed a relative homogeneous diffuse distribution, indicative of a rather compact organization of the activity of the cerebellar lobules.

### 3.9. Acknowledgements

The dataset for this part of the thesis was provided [in part] by the Human Connectome Project, WU-Minn Consortium (Principal Investigators: David Van Essen and Kamil Ugurbil; 1U54MH091657) funded by the 16 NIH Institutes and Centers that support the NIH Blueprint for Neuroscience Research; and by the McDonnell Center for Systems Neuroscience at Washington University.

The methods and results of this chapter along with the corresponding discussion section presented on **Chapter 5** later on, have been published in the *Frontiers in Human Neuroscience* journal: [Pezoulas VC, Zervakis M, Micheloqiannis S and Klados MA \(2017\) Resting-State Functional Connectivity and Network Analysis of Cerebellum with Respect to Crystallized IQ and Gender. \*Front. Hum. Neurosci.\* 11:189. doi: 10.3389/fnhum.2017.00189.](#)

## 4. Voxel-wise analysis of cerebellum

---

### 4.1. Overview

In this chapter, we examine the whole cerebellum in a voxel-wise manner instead of diving it into anatomical lobules as in the previous chapter. Although this initiative may result to a much more computationally complex problem, we expect that the innovation it offers is crucial for providing a straightforward and accurate interpretation of cerebellum's interaction networks. The main goal of this procedure is to cluster the cerebellar voxels that tend to exhibit similar correlation (functional activation) patterns into the same group. A modern clustering approach that overcomes the aforementioned computational burdens, through its ability to work directly on graphs, is based on Spectral Graph Theory concepts. In the current work, a spatially constrained algorithm based on the spectral clustering scheme is proposed and compared with the standard spectral clustering algorithms of the existing literature, first on simulated data and finally on cerebellum's voxel-wise BOLD time-series. Cross-validation is a necessary step in order to evaluate the coherence of the optimal number of clusters among the examined population. Several clustering evaluation measures such as the average silhouette and Davies-Bouldin indices have been also computed for this purpose. The result of the clustering procedure is a resting-state network atlas of cerebellum which is further combined with the corresponding anatomical atlas to provide a final functional atlas of cerebellum's activation distribution. An important issue that needs to be addressed after the clustering application, is to quantify the regional homogeneity of each derived atlas. This can be accomplished using a simple proposed measure based on the voxel-wise computation of Shannon's entropy through a pre-specified window. Another method often employed in several fMRI studies that is able to provide an accurate regional homogeneity evaluation is based on Kendall's coefficient of concordance. Using this concept, a final clustering method is also proposed based on the average Kendall map across all subjects. Finally, a gender-based functional connectivity analysis of cerebellum's network is performed on the basis of **Chapter 3**, using the functional atlas instead of the anatomical one.

The work presented in this chapter is an extended part of the research proposal entitled "*Cerebellum voxel-wise clustering and gender-based functional connectivity analysis: a resting-state fMRI study*" which was funded by the Pancretan Endowment Fund in the form of a scholarship of excellence given to the author (see [here](#) for further information).

## 4.2. Population of interest

Resting-state fMRI data were obtained once more from the HCP database (see **Section 1.2** for information about the HCP consortium, its pioneers as well as the fundamental HCP pre-processing pipelines). We select 50 males and 50 females (**Table 4.1**) in order to form an equally numbered population of interest. Recall from **Section 1.2.3** that all subjects with psychiatric history, extensive substance use and hard alcohol history have been removed since the cerebellum is heavily impacted by alcohol abuse/dependence (Sullivan et al., 2010) and there is also evidence to suggest that the cerebellum is impacted by marijuana as well (Block et al., 2000; Lopez-Larson et al., 2011; Solowij et al., 2011). Furthermore, the existing population has been already restricted to only one member of a sibling/twin pair in order to overcome shared variance issues.

Age interval	Males	Females	Total
22-25	10	9	19
26-30	19	23	41
31-35	21	18	39
<b>Total</b>	50	50	-

## 4.3. BOLD time-series extraction from the cerebellar voxels

We recruit the cerebellum anatomical atlas (Diedrichsen et al., 2009; Diedrichsen et al., 2011; Diedrichsen and Zotow, 2015) that was already presented in **Section 3.3** and apply the parcellation procedure in a partially similar way with the one described in the same section, without however taking into consideration the anatomical regional boundaries in order to define each single voxel as a region of interest (or unit). The total number of cerebellum voxels is equal to 21522 and the number of samples is 1200 per voxel. As a matter of fact, a 21522x1200 matrix is formed where the BOLD signal of the  $i$ -th voxel is placed in the  $i$ -th row for each individual.

## 4.4. Further pre-processing

Each voxel's time-course was further bandpass filtered using a higher order finite impulse response (FIR) bandpass filter applied in zero phase mode (bandwidth 0.01-0.1 Hz) in order to eliminate low frequency noise not implicated in resting state functional connectivity (i.e., slow scanner drifts and influences of higher frequencies reflecting possible cardiac or respiratory oscillations) (van den Heuvel et al., 2008b; Craddock et al., 2012). The filter was constructed based on the constrained least squares method with the following specifications:

cut-off frequency #1 = 0.01 Hz; cut-off frequency #2 = 0.1 Hz; stopband attenuation #1 & #2 = 60 dB; passband ripple = 1 dB; sample rate =  $1/f_s$ , where  $f_s$  is the sampling frequency of the fMRI scanner and is equal to  $1/TR$ , where  $TR$  is the scanner's repetition time parameter and is equal to 720 ms. As a result,  $f_s \approx 1.38$  Hz. In general, the sampling frequency of an fMRI scanner is very small due to the latency that is introduced between the neural firing and the blood oxygenation increase in that area. An indicative example of the filtering outcome is presented in **Fig 4.1**, for the time-course of a random voxel selected from a random subject.

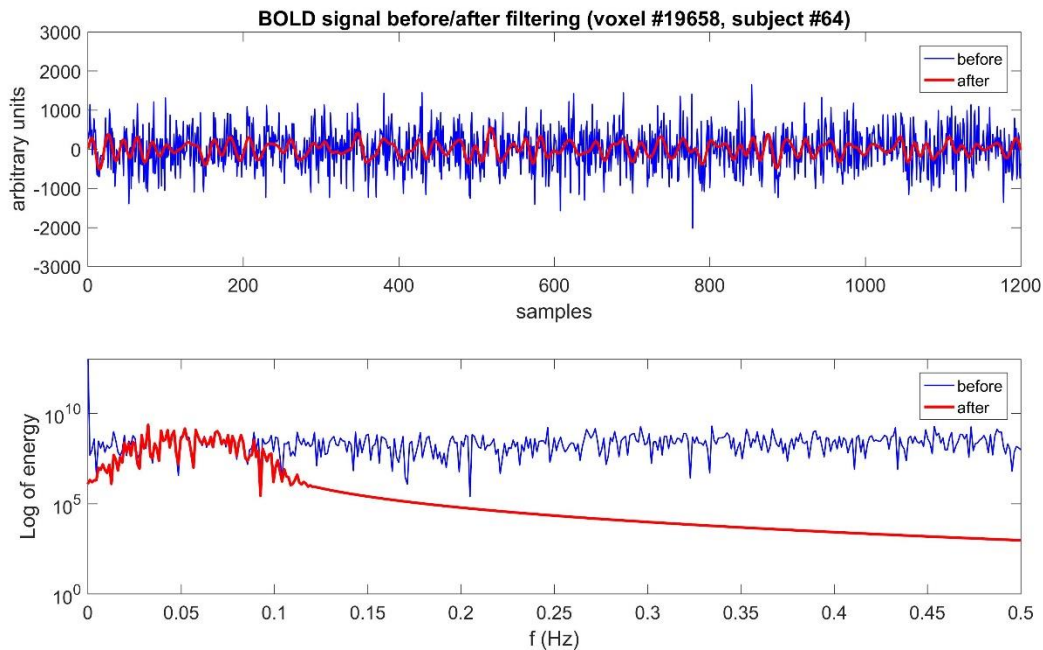


**Figure 4.1.** Application of a 50<sup>th</sup> order FIR filter on the BOLD signal of voxel #19658 of subject 64 in both time (upper panel) and frequency (lower panel) domains.

#### 4.5. Voxel-wise functional graphs construction

Pearson's product moment temporal correlation coefficient is once more employed as a functional connectivity quantifier and is computed between each possible pair of voxel's time-series. The result of this procedure is a 21522x21522 adjacency (correlation) matrix where 21522 is the number of nodes (each voxel is considered as a node/region of interest since it is a voxel-wise analysis) and the element  $(i, j)$  represents the correlation between the BOLD time-series of voxels  $i$  and  $j$ . In fact, each correlation matrix is modelled as a weighted and undirected graph  $G = (V, E)$  where  $V$  is the set of 21522 nodes and  $E$  is the set of edges, with a maximum number of approximately 232 million edges, where the negative correlations (i.e., weights) are usually discarded. The computational complexity of such a graph as well as the required memory space is large. In order to overcome these issues, we gained access to a remote Linux server provided by the computer room at the Technical University of Crete. With the following specifications: 16 GB free memory space with the ability to increase to 32 GB; 8

processing cores @ 2.1 GHz; 350 GB of free disk space; Linux OS; Linux distributor: Ubuntu 14.04.3 LTS. The whole analysis procedure was executed on that server. Please note that the voxel-wise functional graphs construction was executed individually per subject. Finally, the average correlation matrix across all 100 subjects was computed for further analysis.

## 4.6. Spectral graph theory concepts for clustering

### 4.6.1. Fundamental basis

Our main goal is to seek for ways to identify the cerebellar resting-state networks (RSNs) for extracting the Regions of Interest later on. Towards this direction, all cerebellar voxels need to be assigned in clusters based on the similarity of their correlation patterns. In addition, the core of the clustering idea is to employ a method that will work directly on the correlation graphs computed in previous section, using linear algebra and matrix theory concepts. A modern method that combines both of these factors is given by spectral graph theory, which is based on the eigenvectors of the Laplacian representation of a matrix, say  $\mathbf{X}$ , for finding partitions of that matrix (Shi and Malik, 2000). In fact, it is mathematically proven that the optimal partitioning of  $\mathbf{X}$  can be found by solving the generalized eigen-problem of its Laplacian matrix, assume  $\mathbf{L}$ , using linear algebra.

### 4.6.2. Eigenvalue decomposition (EVD)

An eigenvalue and an eigenvector of a square matrix, assume  $\mathbf{T}$ , is a scalar  $\lambda$  and a non-zero vector  $\mathbf{v}$ , respectively, so that the following equation is fulfilled:

$$\mathbf{T}\mathbf{v} = \lambda\mathbf{v} \quad (4.1)$$

and can be also written as,

$$(\mathbf{T} - \lambda\mathbf{I}) \cdot \mathbf{v} = 0, \quad \mathbf{v} \neq \mathbf{0} \quad (4.2)$$

which in turn implies that the matrix  $(\mathbf{T} - \lambda\mathbf{I})$  is singular and therefore:

$$\det(\mathbf{T} - \lambda\mathbf{I}) = 0 \quad (4.3)$$

The definition of an eigenvalue is connected with the characteristic equation (also known as characteristic polynomial) of matrix  $\mathbf{T}$ . The degree of the polynomial is the rank of  $\mathbf{T}$ . This denotes that an  $n \times n$  matrix has  $n$ -eigenvalues (including repeated eigenvalues). Assume that  $\lambda_1, \lambda_2, \dots, \lambda_n$  and  $\mathbf{v}_1, \mathbf{v}_2, \dots, \mathbf{v}_n$  are the corresponding eigenvalues and eigenvectors of  $\mathbf{T}$ . Then, the following stands:

$$\mathbf{T}\mathbf{E} = \mathbf{D}\mathbf{E} \quad (4.4)$$

where  $\mathbf{D}$  is an  $n \times n$  diagonal matrix, with the eigenvalues  $\lambda_j$  on the diagonal and  $\mathbf{E}$  is an  $n \times n$  orthogonal matrix, the  $j$ -th column of which is  $\mathbf{v}_j$ . Assuming that the eigenvectors are linearly independent, then matrix  $\mathbf{E}$  is non-singular and as a result its inverse,  $\mathbf{E}^{-1}$ , can be defined. Therefore, (4.4) can be re-written as follows:

$$\mathbf{T} = \mathbf{E}\mathbf{D}\mathbf{E}^{-1} \quad (4.5)$$

and by taking into consideration the fact that  $\mathbf{E}$  is orthogonal:

$$\mathbf{E}^T \mathbf{E} = \mathbf{E}\mathbf{E}^T = \mathbf{I} \quad (4.6)$$

then,

$$\mathbf{E}^T = \mathbf{E}^{-1} \quad (4.7)$$

and finally, the EVD of  $\mathbf{T}$  is given by:

$$\mathbf{T} = \mathbf{E}\mathbf{D}\mathbf{E}^T \quad (4.8)$$

### 4.6.3. The Laplacian of a graph

Assume a weighted and undirected graph  $\mathbf{G} = (\mathbf{V}, \mathbf{E})$  where  $\mathbf{V}$  is a set of  $n$ -nodes and  $\mathbf{E}$  is a set of edges. For a vector  $\mathbf{f} \in \mathbf{R}^V$  the Laplacian quadratic form of  $\mathbf{G}$  is defined as (Luxburg, 2007; Spielman, 2012):

$$\mathbf{f}^T \mathbf{L} \mathbf{f} = \sum_{i,j=1}^n w_{i,j} \cdot |(\mathbf{f}(i) - \mathbf{f}(j))|^2 \quad (4.9)$$

where  $w_{i,j}$  is the weight of the edge  $(i,j) \in \mathbf{E}$  that connects nodes  $i$  and  $j$ . In fact (4.9) denotes that the Laplacian provides a measure of the smoothness of  $\mathbf{f}$  over the edges in  $\mathbf{G}$ . This means that the Laplacian form of a graph defines a discrete operator that measures the smoothness of any function  $\mathbf{f}$  over a graph node  $u \in \mathbf{V}$ ,  $\mathbf{f}(u)$ . The function  $\mathbf{f}$  can be any function that assigns a value to  $u$ .

In order to define a matrix representation of the Laplacian matrix, it is first important to define the adjacency matrix  $\mathbf{X} \in \mathbf{R}^{n \times n}$  of the graph  $\mathbf{G}$  as follows:

$$\mathbf{X} = (X_{ij}) = \begin{cases} w_{ij}, & (i,j) \in \mathbf{E} \\ 0, & \text{otherwise} \end{cases} \quad (4.10)$$

Then, the matrix form of the (un-normalized) Laplacian of a graph  $\mathbf{G}$ , assume  $\mathbf{L}$ , is defined as:

$$\mathbf{L} = \mathbf{D} - \mathbf{X} \quad (4.11)$$

where  $\mathbf{D}$  is an  $n \times n$  diagonal matrix whose diagonal contains the weighted degrees of each node (vertex)  $u \in \mathbf{V}$  (i.e., the number of outgoing edges from a node):

$$d(u_i) = d_i = \sum_{j=1}^n w_{ij} \quad (4.12)$$

Therefore, an alternative and more complete form of (4.11) is the following:

$$\mathbf{L} = (L_{ij}) = \begin{cases} d_i, & i = j \\ -1, & i \neq j \\ 0, & o/w \end{cases} \quad (4.13)$$

The Laplacian matrix,  $\mathbf{L}$ , satisfies the following properties:

- $\mathbf{L}$  is symmetric and positive semi-definite.
- The smallest eigenvalue of  $\mathbf{L}$  is 0 and the corresponding eigenvector is the constant one vector,  $\mathbf{1}$ .
- $\mathbf{L}$  has non-negative, real-valued eigenvalues,  $0 = \lambda_1 \leq \lambda_2 \leq \dots \leq \lambda_n$ .

The Laplacian of the graph gives us the proper quadratic form that can help us solve the spectral clustering problem. The eigenvectors of the Laplacian solve the clustering problem by being smooth in the nodes that define the corresponding cluster and presenting large fluctuations in the rest of the nodes. What the Laplacian does is that it evaluates the difference of the function  $f$  on node  $i$  over its' neighbors. Then the smoothness of the function can be evaluated by the quadratic form of  $f^T \mathbf{L} f$ . A function  $f$  which has a low value of  $f^T \mathbf{L} f$  has the property that it varies only "a little bit" in regions where the data points lie dense (i.e., the graph is tightly connected), whereas it is allowed to vary more (e.g., to change the sign) in regions of low data density (Luxburg, 2007). In this sense, a small value of  $f^T \mathbf{L} f$  encodes the so called "cluster assumption" in semi-supervised learning, which requests that the decision boundary of a classifier should lie in a region of low density (Luxburg, 2007). Below follows an example of how the Laplacian of a graph is computed based on (4.11).

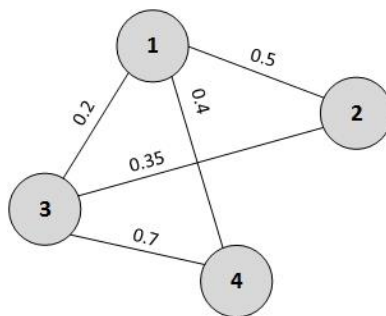


**Figure 4.2.** Example of a simple weighted and undirected graph with normalized weights.

The Laplacian of the graph in **Fig. 4.2** is equal to:

$$\mathbf{L} = \mathbf{D} - \mathbf{X} = \begin{bmatrix} 3 & 0 & 0 & 0 \\ 0 & 2 & 0 & 0 \\ 0 & 0 & 3 & 0 \\ 0 & 0 & 0 & 2 \end{bmatrix} - \begin{bmatrix} 0 & 0.5 & 0.2 & 0.4 \\ 0.5 & 0 & 0.35 & 0.4 \\ 0.2 & 0.35 & 0 & 0.7 \\ 0.4 & 0.4 & 0.7 & 0 \end{bmatrix} = \begin{bmatrix} 3 & -0.5 & -0.2 & -0.4 \\ -0.5 & 2 & -0.35 & -0.4 \\ -0.2 & -0.35 & 3 & -0.7 \\ -0.4 & -0.4 & -0.7 & 2 \end{bmatrix}$$

It is often convenient to use the (symmetric) normalized Laplacian of a graph,  $L_{sym}$ , instead of the un-normalized Laplacian:

$$L_{sym} = D^{-1/2}LD^{-1/2} = I - D^{-1/2}XD^{-1/2} \quad (4.14)$$

where  $I$  is an  $m \times m$  identity matrix and

$$D^{-1/2} = (D^{-1/2}_{i,j}) = \begin{cases} 1/\sqrt{d_i} & , \quad i = j \\ 0 & , \quad o/w \end{cases} . \quad (4.15)$$

An alternative and complete form of (4.14) is the following:

$$L^{sym} = (L^{sym}_{ij}) = \begin{cases} 1, & i = j \text{ and } d_i \neq d_j \\ -1/\sqrt{d_i \cdot d_j}, & i \neq j \text{ and } v_i \text{ is adjacent to } v_j \\ 0, & o/w \end{cases} \quad (4.16)$$

The symmetric Laplacian matrix,  $L^{sym}$ , satisfies the following properties:

- The smallest eigenvalue of  $L^{sym}$  is 0 and the corresponding eigenvector is the constant one vector,  $D^{1/2}\mathbf{1}$ .
- $L^{sym}$  is positive semi-definite with  $n$ - non-negative and real-valued eigenvalues,  $0 = \lambda_1 \leq \lambda_2 \leq \dots \leq \lambda_n$ .

The usefulness of the Laplacian of a graph will be made clearer on **Sections 4.6.4** and **4.6.5**.

#### 4.6.4. Spectral clustering

Given an  $m \times m$  similarity matrix  $X$ , the goal is to partition  $X$  into  $k$ -subsets. First, its Laplacian matrix is defined according to **Section 4.6.3**. In fact, it is mathematically proven that the optimal partitioning of  $X$  can be found by solving the generalized eigen-problem of its Laplacian matrix:

$$UL = AL \quad (4.17)$$

where  $A$  is an  $k \times k$  diagonal matrix with the eigenvalues on the main diagonal (sorted in descending order) and  $U$  is an  $m \times k$  square matrix with the largest  $k$ -eigenvectors stacked in columns. After the computation of the eigenvectors matrix  $U$ , a  $k$ -means approach is applied in order to cluster the first (largest)  $k$ -eigenvectors  $\mathbf{u}_1, \mathbf{u}_2, \dots, \mathbf{u}_k$  of  $U$  into clusters  $C_1, C_2, \dots, C_k$ . Then, each voxel (i.e., point in 3D space), assume  $x_i, i = 1, 2, \dots, m$ , is assigned to cluster  $Y_j$  if the corresponding row of  $U$ , assume  $\mathbf{y}_i$ , belongs to cluster  $C_j$ :

$$Y_j = \{x_i \mid \mathbf{y}_i \in C_j\} , \quad i = 1, 2, \dots, m \text{ and } j = 1, 2, \dots, k \quad (4.18)$$

The goal of the spectral clustering (SC) procedure is to solve an optimization problem which aims to separate the input data points into a pre-specified number of subsets (clusters) that are correctly separated by minimizing the similarity between the subsets and maximize the similarity within the clusters. In order to do so, spectral clustering uses the eigenvectors of the Laplacian matrix in order to project the original data onto a low dimensional space where data separation is easier for  $k$ -means to succeed (**Fig. 4.3**). A directly applied  $k$ -means on the original input space is not able to identify the concentric pattern shown in **Fig. 4.4** since the Euclidean distance space cannot be easily re-arranged so as to provide a concrete solution to the optimization problem.

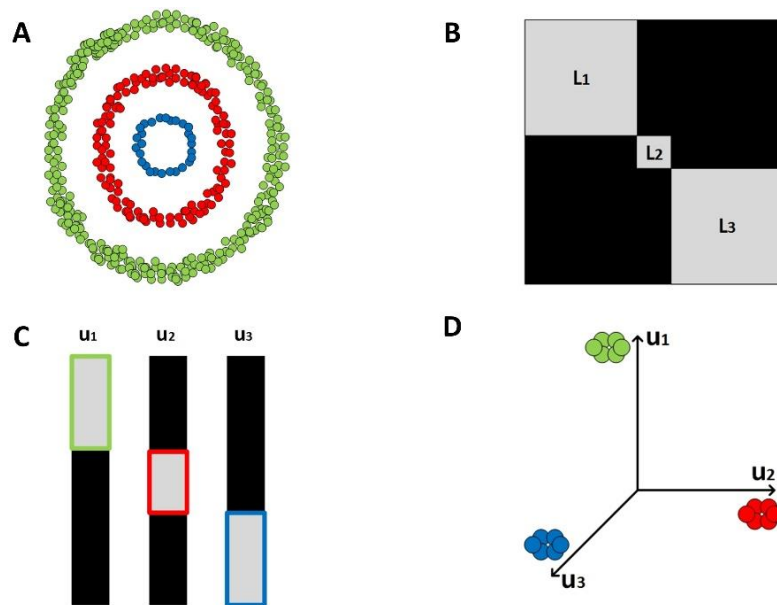


**Figure 4.3.** A simple visual representation of the spectral clustering steps. **(A)** A concentric distribution of data points on the input space where the data points with the same color have higher similarity (i.e., data points are separated into 3 groups/clusters). **(B)** The Laplacian matrix of the adjacency matrix that corresponds to **(A)**. **(C)** The first (largest) 3 eigenvectors of the Laplacian matrix. **(D)** The first 3 eigenvectors are used to project the original data points onto the eigen-space, where the data separation is much easier for  $k$ -means.

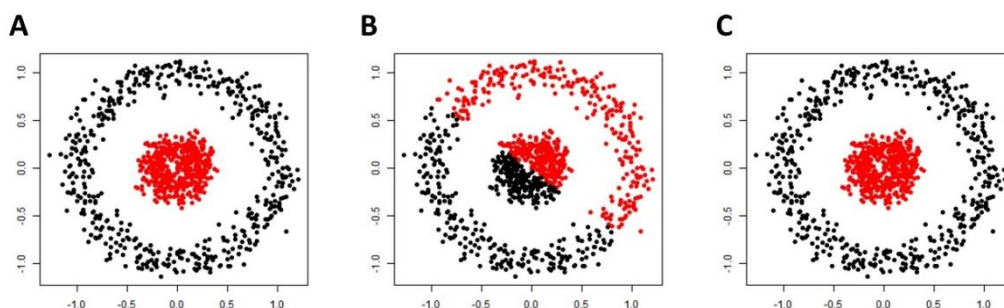


**Figure 4.4.** A simple demonstration of the superiority of spectral clustering. **(A)** The original pattern. **(B)** Spectral clustering successfully separates the data points based on the concentric formation. **(C)** The direct application of the  $k$ -means procedure on the input space is not able to distinguish the pattern. (Adapted and adjusted from [rpubs.com/sandipan/199446](https://rpubs.com/sandipan/199446)).

#### 4.6.5. The Normalized cut (N-cut) algorithm

A similar approach, which is also based on spectral graph theory, is the Normalized cut (N-cut) algorithm which was originally introduced by Shi and Malik (Shi and Malik, 2000). The goal of the N-cut algorithm is to partition a graph  $G$  into a pre-specified number of N-subsets (clusters) by cutting the edges that connect these subsets so that the similarity between the voxels of each cluster is smaller than the similarity within the voxels of different subsets. Assume that we want to partition  $G$  into two disjoint sets  $A$  and  $B$ , where  $A \cup B = V$ . In order to do so, the algorithm aims to minimize the following cut cost function:

$$cut(A, B) = \sum_{x_i \in A, x_j \in B} w_{ij} \quad (4.19)$$

where  $x_i, x_j$  are voxels in clusters  $A, B$ , respectively and  $w_{ij}$  is the similarity between voxels with indices  $i$  and  $j$  (i.e., correlation coefficient).

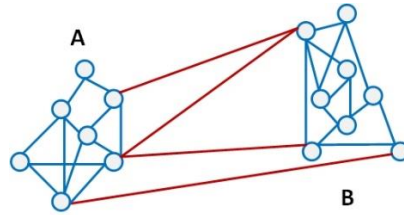


**Figure 4.5.** A simple undirected graph which can be partitioned into two disjoint subsets  $A$  and  $B$  by minimizing the cut cost (removing edges with red color).

A common problem related with the cost function in (4.19) however is that it may result to single voxel clusters (Fig. 4.6) and therefore the Normalized cut (Ncut) cost is defined:

$$\begin{aligned} Ncut(A, B) &= \frac{cut(A, B)}{\sum_{x_i \in A, x_k \in V} w_{ik}} + \frac{cut(A, B)}{\sum_{x_j \in B, x_k \in V} w_{jk}} \\ &= \frac{cut(A, B)}{assoc(A, V)} + \frac{cut(A, B)}{assoc(B, V)} \end{aligned} \quad (4.20)$$

The normalization factor that the N-cut algorithm introduces is able to minimize the similarity between clusters and at the same time maximize the similarity within the clusters. In fact, the optimal partitioning of  $X$  can be found by solving the generalized eigen-problem of its Laplacian matrix,  $L$ . It is proven that the minimization of (4.20) is equivalent to the Rayleigh quotient (Shi and Malik, 2000):

$$\min_x Ncut(x) = \min_y \frac{y^T (D - X) y}{y^T D y} \quad (4.21)$$

where  $\mathbf{x}$  is a  $|\mathbf{V}|$ -dimensional indicator vector ( $x_i = 1$  if node  $i$  belongs to  $\mathbf{A}$  and  $-1$  otherwise),  $\mathbf{y} = (1 + \mathbf{x}) - b(1 - \mathbf{x})$  where  $b = k/(1 - k)$  and  $k$  is the total normalized degree of all nodes in  $\mathbf{A}$  (i.e., sum of each node's degree in  $\mathbf{A}$  with the rest of the nodes in  $\mathbf{A}$  divided by the sum of each node's degree in  $\mathbf{V}$ ). It is obvious that the minimization of (4.21) can be accomplished by setting:

$$(\mathbf{D} - \mathbf{X})\mathbf{y} = \lambda \mathbf{D}\mathbf{y} \Leftrightarrow \mathbf{L}\mathbf{y} = \lambda \mathbf{D}\mathbf{y} \quad (4.22)$$

which is the solution to the general eigen-problem of  $\mathbf{L}$ . As a matter of fact, the N-cut and spectral clustering procedures are both eigenvector-based algorithms which are strongly related with each other since they solve the same eigen-problem (Shi and Malik, 2000).

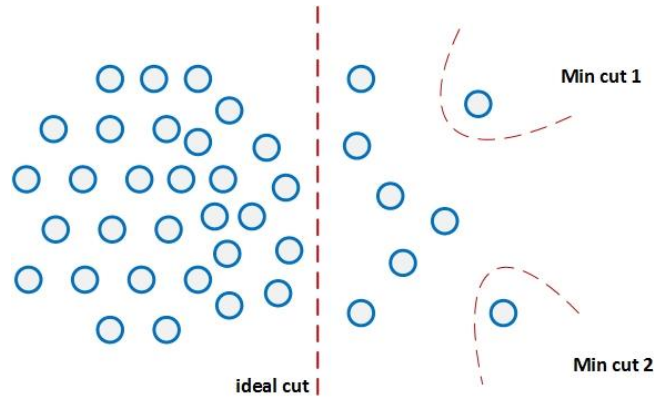


**Figure 4.6.** An example which demonstrates that minimizing a simple cut cost function is not able to provide an ideal segmentation and apparently results to single-voxel clusters. On the other hand, minimizing the Ncut cost can provide an ideal cut by making sure to provide a “balanced” number of data points per segment.

#### 4.6.6. Spatially constrained spectral clustering

A common problem with the spectral clustering methods though is the fact that they may create non-contiguous clusters, i.e., clusters with its voxels being spatially distributed. A solution to this problem can be offered by introducing a spatial constraint in the algorithmic procedure. More specifically, instead of applying the spectral clustering procedure on the original correlation matrix, the idea is to multiply it with a distance matrix, assume  $\mathbf{S} = (s_{ij})_{i,j=1,2,\dots,m}$ , that can be computed using a distance function (i.e., the Euclidean distance). For two voxels lying in the 3-D space with coordinates  $\mathbf{x}, \mathbf{y} \in \mathbf{R}^3$ , the Euclidean distance is defined as follows:

$$\mathbf{S}(\mathbf{x}, \mathbf{y}) = \sqrt{(x_1 - y_1)^2 + (x_2 - y_2)^2 + (x_3 - y_3)^2} \quad (4.23)$$

In order to examine the effect of the spatial constraint in the clustering procedure, different thresholds can be applied on  $\mathbf{S}$ :

$$\mathbf{S} = \begin{cases} 1, & s_{ij} \leq rc \\ 0, & s_{ij} > rc \end{cases} \quad (4.24)$$

where  $rc$  is the threshold parameter (value). This step results to a binary version of the original distance matrix. Finally, we define:

$$\mathbf{W} = \mathbf{S} \circ \mathbf{X} \quad (4.25)$$

where  $\circ$  denotes element-wise multiplication and  $\mathbf{X}$  is a non-negative similarity matrix (i.e.,  $x_{ij} \geq 0, \forall i, j = 1, 2, \dots, m$ ). By applying the spectral clustering concept on  $\mathbf{W}$  instead of  $\mathbf{X}$ , and testing for various thresholds on  $\mathbf{S}$  under a complete cross-validation procedure (proposed algorithm) we can constrain the number of neighboring voxels per cluster and thus perform a spatially constrained version of the original spectral clustering algorithm.

## 4.7. Clustering evaluation

In this study, the average silhouette and Davies-Bouldin indices are recruited as clustering evaluation measures.

### 4.7.1. Silhouette index

The silhouette index (width) of the  $i$ -th voxel,  $SI(i)$ , is a measure that quantifies the similarity of that voxel with the other voxels in its own cluster, assume  $A$ , when compared to the voxels in all the other clusters, assume  $C \neq A$  (Rousseeuw et al., 1987), and is defined as:

$$SI(i) = \frac{b(i) - a(i)}{\max\{a(i), b(i)\}} = \frac{[\min\{d(i, C)\}] - a(i)}{\max(a(i), b(i))} \quad (4.26)$$

where  $a(i)$  is the average Euclidean distance (dissimilarity) from the  $i$ -th voxel to all the other voxels in  $A$  and  $b(i)$  is the minimum average Euclidean distance (dissimilarity) from the  $i$ -th voxel to all the other voxels in  $C$ , denoted as  $d(i, C)$ , minimized over clusters. An alternative definition is the following:

$$SI(i) = \begin{cases} 1 - a(i)/b(i), & a(i) < b(i) \\ 0, & a(i) = b(i) \\ b(i)/a(i) - 1, & a(i) > b(i) \end{cases} \quad (4.27)$$

From (4.27) it is obvious that  $SI(i)$  ranges between -1 and 1 with high silhouette values denoting that the  $i$ -th voxel is well matched to the voxels in  $A$  and poorly matched to the voxels in the rest of the clusters. Finally, the average silhouette index is computed across the voxels of a cluster under evaluation and employed as a clustering evaluation metric.

#### 4.7.2. Davies-Bouldin index

The Davies-Bouldin index (Davies and Bouldin, 1979) is another well-known clustering evaluation metric which is based on the evaluation of the appropriateness of various divisions or partitions of the data by using features inherent to the data and is defined as:

$$DB = \frac{1}{K} \cdot \sum_{k=1}^K DB(k) = \frac{1}{K} \cdot \sum_{k=1}^K \max_{j \neq k} R_{j,k} = \frac{1}{K} \cdot \sum_{k=1}^K \max_{j \neq k} \left( \frac{S_j + S_k}{M_{j,k}} \right) \quad (4.28)$$

where:

- $K$  is the total number of clusters under evaluation
- $DB(k)$  is an intermediate Davies-Bouldin index for the  $k$ -th cluster
- $R_{j,k}$  measures how good the clustering scheme is
- $S_k$  measures the scatter within the cluster  $C_k$  and is defined as follows:

$$S_k = \left( \frac{1}{T_k} \cdot \sum_{j=1}^{T_k} |X_j - A_k|^p \right)^{1/p} \quad (4.29)$$

where  $X_j$  is an  $n$ -dimensional feature vector assigned to cluster  $C_k$ ,  $n$  is the number of voxels in cluster  $C_k$ ,  $A_k$  is the centroid of cluster  $C_k$ ,  $T_k$  is the size of cluster  $C_k$  and  $p$  is a distance function parameter which is usually set to 2 (i.e., the Euclidean distance).

- $S_j$  measures the scatter within the cluster  $C_j$
- $M_{j,k}$  measures the separation between clusters  $C_j$  and  $C_k$  and is defined as follows:

$$M_{j,k} = \|A_j - A_k\|_p = \left( \sum_{i=1}^n |a_{i,k} - a_{j,k}|^p \right)^{1/p} \quad (4.30)$$

where  $a_{i,k}$  and  $a_{j,k}$  are elements of  $A_k$ . Finally, the following properties are being conserved:

- $R_{j,k} \geq 0$
- $R_{j,k} = R_{k,j}$
- $R_{k,j} > R_{k,i}$  when  $S_j \geq S_i$  and  $M_{k,j} = M_{k,i}$
- $R_{k,j} > R_{k,i}$  when  $S_j = S_i$  and  $M_{k,j} \leq M_{k,i}$

A good clustering scheme is characterized by a large separation between clusters  $C_j$  and  $C_k$ ,  $M_{j,k}$  and a small within-cluster scatter,  $S_k$ . Therefore, the optimal number of clusters is the one that achieves the smallest Davies-Bouldin index.

## 4.8. Clustering homogeneity evaluation

After the construction of a clustermap (or atlas) it is important to seek for a way to evaluate each cluster's (or region's) coherence in terms of homogeneity. A proposed measure that is able to quantify the regional homogeneity of a clustermap is by computing the Shannon Entropy of a voxel with its neighbors that lie within a sphere with specific radius. For a given clustermap, we first select for each voxel its neighboring voxels' clustering indices that lie within a pre-specified sphere and afterwards store them in a vector, assume  $\mathbf{y}$ . Then, we estimate the probability distribution of  $\mathbf{y}$ ,  $\mathbf{p}_y$ , and compute Shannon's entropy as follows:

$$E(\mathbf{p}_y) = - \sum_{j=1}^n p_y(j) \cdot \log(p_y(j)) \quad (4.31)$$

where  $n$  is the number of different clustering indices in  $\mathbf{y}$ . Voxels with small entropy values indicate better cohesion of the region they belong to. Here, we plot the entropy distributions across all voxels in order to examine the clustering homogeneity per clustering approach.

## 4.9. Application on synthetic time-series

The main purpose of this simulation is to present the main weakness that the standard spectral clustering algorithms exhibit under realistic noisy environments and at the same time highlight the superiority of the spatially constrained version under the same circumstances. In order to do so, synthetic BOLD time-series (signals) with random superimposed noise were generated to investigate the accuracy of each clustering procedure. A compact 128x128 block containing  $k$ -randomly distributed patterns was generated. Each pattern has a representative or seed signal which is a sinus wave with random superimposed noise and a unique random frequency varying on the interval  $(0, f_N)$ , where  $f_N$  is the Nyquist frequency and is equal to  $f_s/2$ . The rest of the signals in a pattern have the same frequency as the pattern's (noisy) seed signal with random superimposed noise. For realistic purposes,  $f_s$  was set to 1.388 Hz which is equal to the fMRI scanner's ratio  $1/TR$  (i.e.,  $1/0.72$ ). The number of square blocks was set to  $k = 4, 6$  and  $8$  and the number of samples was set to 100 per time-course. In each case, after generating the synthetic BOLD time-series, Pearson's correlation coefficient was computed between each pair of synthetic time-series, leading to a **16384x16384** adjacency matrix, where the where the element  $(i, j)$  is the correlation between the time-series of points  $i$  and  $j$  in the 128x128 block. Then, the SC, N-cut and SCSC clustering approaches were applied on the corresponding correlation matrices. An extra distance matrix is necessary for the application of the SCSC with  $rc = 2$  (covering 12 points), where the element  $(i, j)$  is the Euclidean distance between points  $i$  and  $j$ . Finally, Shannon's entropy was computed on each clustermap using various sphere's radius values, i.e.,  $r = 2$  (12 points);  $r = 3$  (28 points);  $r = 4$  (48 points);  $r = 5$  (80 points);  $r = 6$  (112 points), to evaluate each clustermap's homogeneity.

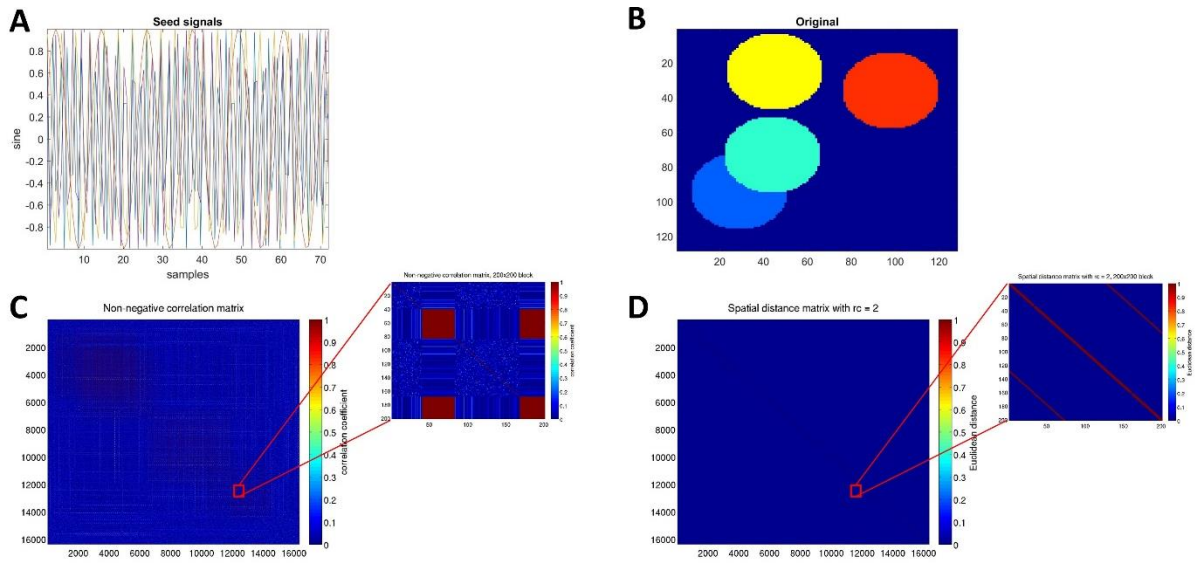


**Figure 4.7.** The 1<sup>st</sup> run of the simulation experiment using  $k = 4$  patterns. **(A)** The generated seed signals for each pattern. **(B)** The 4 randomly placed patterns on a 128x128 noisy block. Recall that each point in **(B)** is a synthetic time-course. **(C)** The 16534x16534 non-negative correlation matrix with a 200x200 block for zooming purposes. **(D)** The 16534x16534 distance matrix using  $rc = 2$ , with a 200x200 block for zooming purposes.

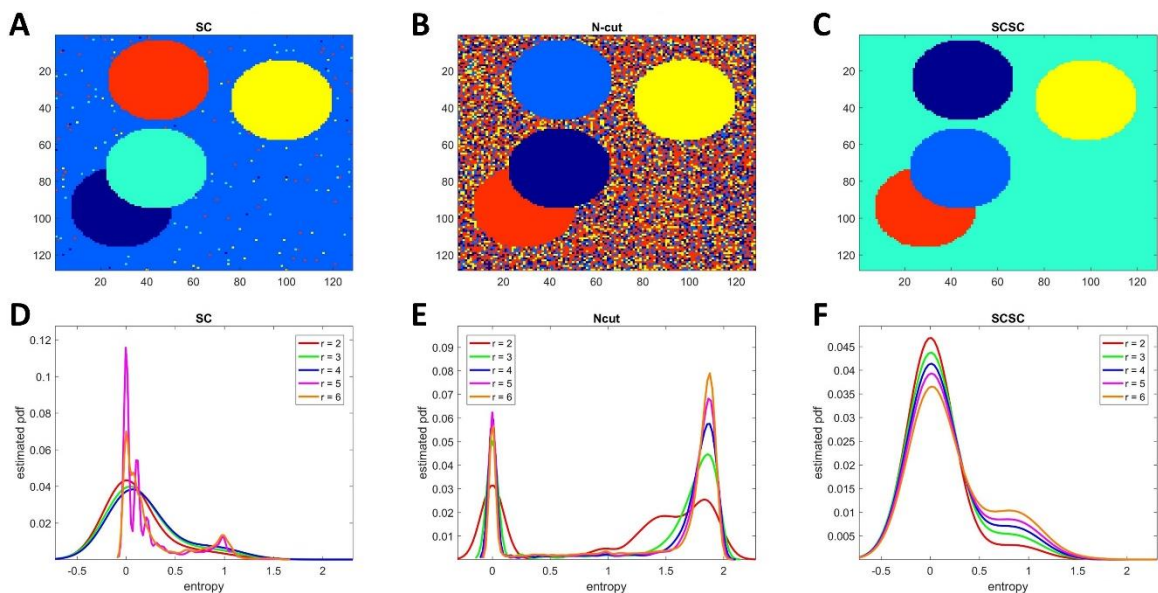


**Figure 4.8.** Simulation results for the 1<sup>st</sup> run after the application of the **(A)** Spectral, **(B)** N-cut and **(C)** Spatially Constrained Spectral clustering procedures, respectively, alongside with the corresponding clustermap's entropy distributions **(D)**, **(E)**, **(F)**, using various radius values.

- Moving on to the 2<sup>nd</sup> run of the simulation, using six randomly distributed patterns.

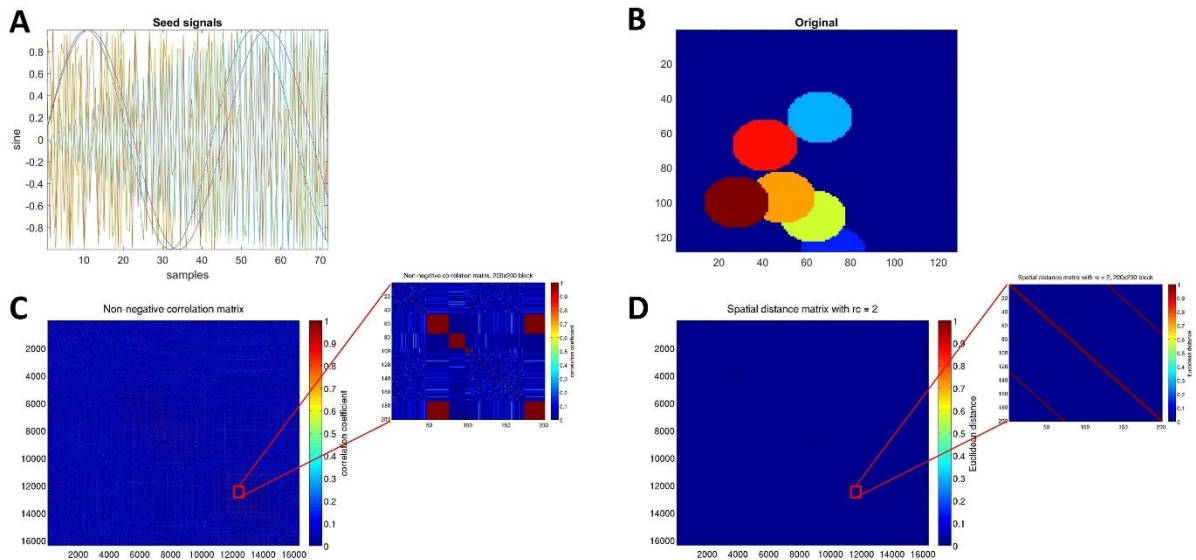


**Figure 4.9.** The 2<sup>nd</sup> run of the simulation experiment using  $k = 6$  patterns. **(A)** The generated seed signals for each pattern. **(B)** The 6 randomly placed patterns on a 128x128 noisy block. Recall that each point in **(B)** is a synthetic time-course. **(C)** The 16534x16534 non-negative correlation matrix with a 200x200 block for zooming purposes. **(D)** The 16534x16534 distance matrix using  $rc = 2$ , with a 200x200 block for zooming purposes.

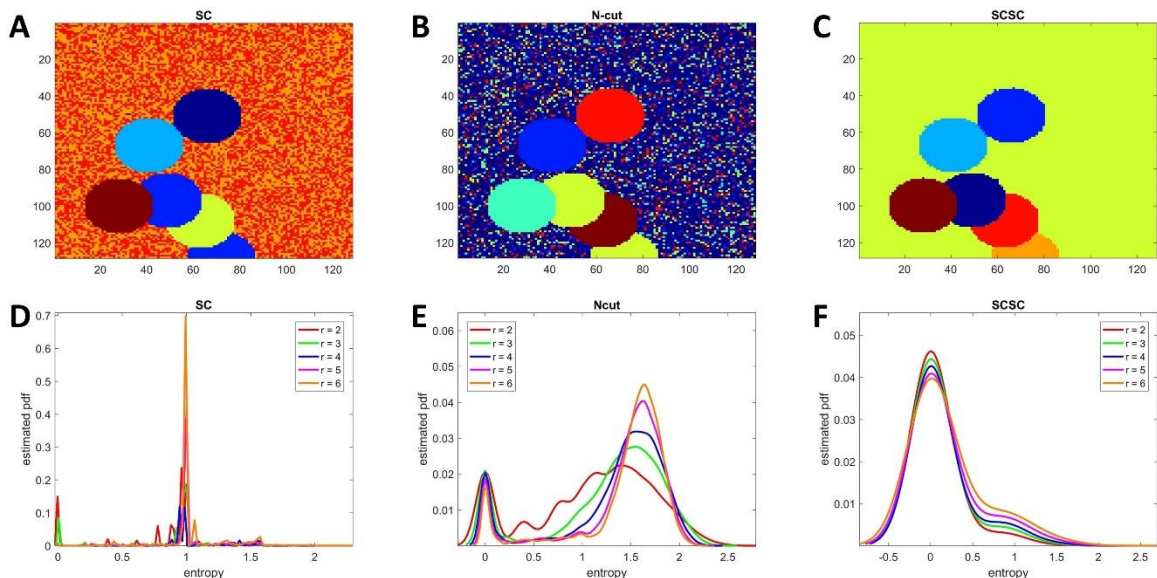


**Figure 4.10.** Simulation results for the 2<sup>nd</sup> run after the application of the **(A)** Spectral, **(B)** N-cut and **(C)** Spatially Constrained Spectral clustering procedures, respectively, alongside with the corresponding clustermap's entropy distributions **(D)**, **(E)**, **(F)**, using various radius values.

-And finally to the 3<sup>rd</sup> run, using eight randomly distributed patterns.

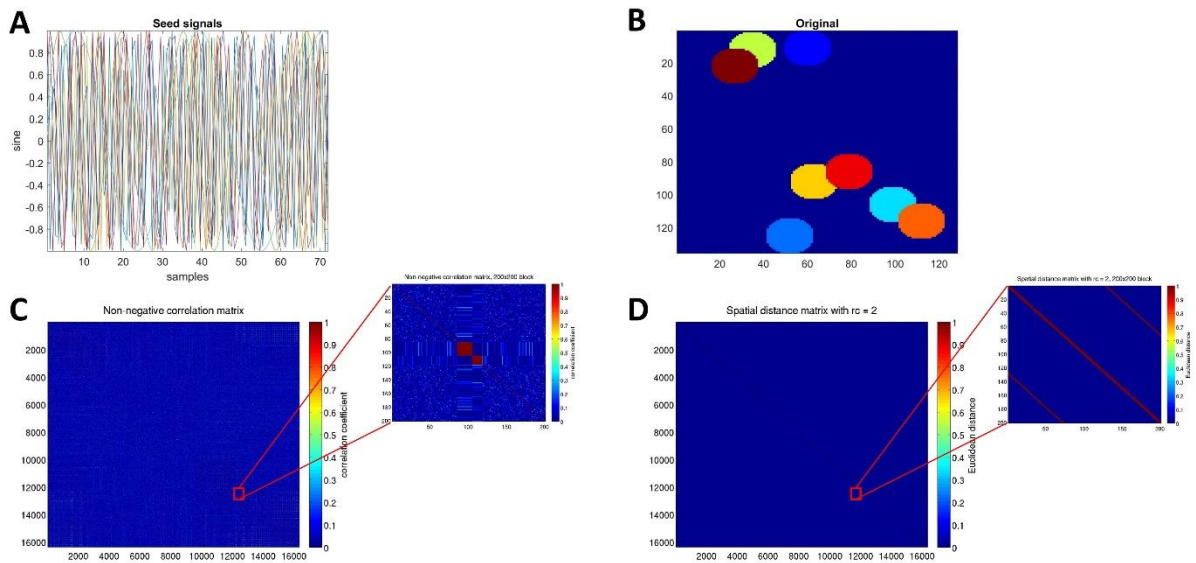


**Figure 4.11.** The 3<sup>rd</sup> run of the simulation experiment using  $k = 8$  patterns. **(A)** The generated seed signals for each pattern. **(B)** The 8 randomly placed patterns on a 128x128 noisy block. Recall that each point in **(B)** is a synthetic time-course. **(C)** The 16534x16534 non-negative correlation matrix with a 200x200 block for zooming purposes. **(D)** The 16534x16534 distance matrix using  $rc = 2$ , with a 200x200 block for zooming purposes.

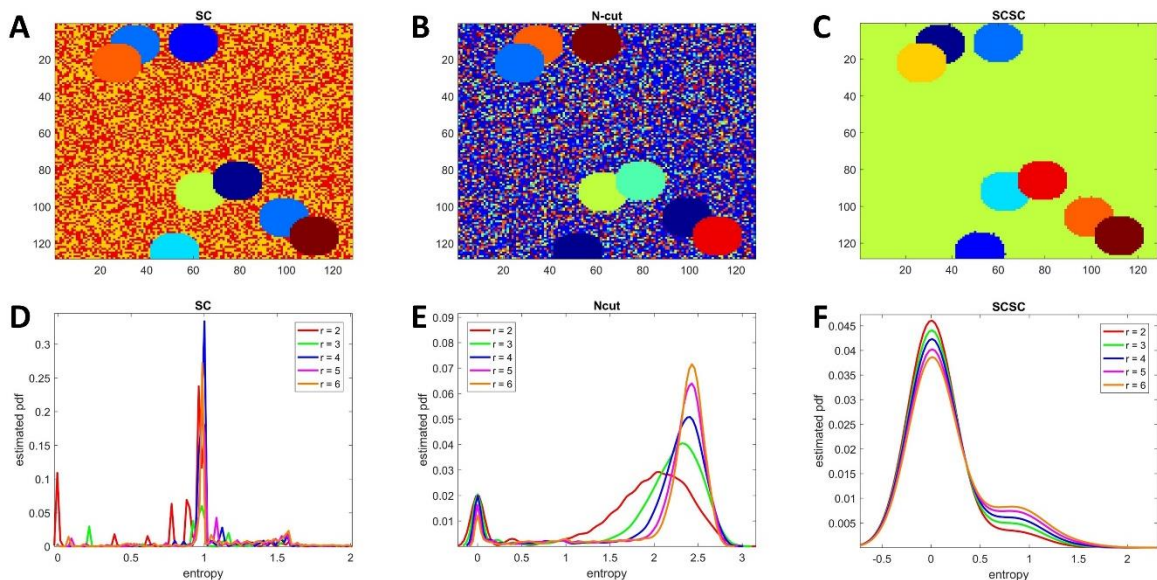


**Figure 4.12.** Simulation results for the 3<sup>rd</sup> run after the application of the **(A)** Spectral, **(B)** N-cut and **(C)** Spatially Constrained Spectral clustering procedures, respectively, alongside with the corresponding clustermap's entropy distributions **(D)**, **(E)**, **(F)**, using various radius values.

According to **Figs 4.8, 4.10** and **4.12** it is obvious that the SC and N-cut algorithms are not able to distinguish the patterns from the noisy background across all three runs, a fact that is also validated from their corresponding entropy distributions which tend to exhibit very high entropy values (i.e., large uncertainty with non-uniform distributions) and as a result the homogeneity of the resulted clustermaps is too small. On the other hand, the SCSC algorithm correctly discriminates the patterns from the background noise due to the spatial constraint that introduces in order to restrict the number of neighbors and reduce the noise levels to a large extent. As a matter of fact, the resulted clusters are non-spatially distributed (i.e., contiguous). This outcome can be also verified from the related entropy distributions which tend to be smooth and uniform, with the entropy values approximating zero (very small uncertainty) which results to a much better and desirable clustermap homogeneity. Note that in all cases, the estimated probability density of the entropy values is small which is normal because entropy is a continuous variable and the probability of an entropy value being equal to  $X+\epsilon$  is small, where  $X$  is a continuous random variable and  $\epsilon$  is a small interval.

#### 4.10. Application on cerebellum's data

Each subject's correlation coefficient (adjacency) matrix is computed according to the procedure described in **Section 4.5**, without discarding the negative correlations for avoiding biases introduced during the averaging procedure. The average correlation matrix across 100 subjects is finally computed and on the latter the negative correlations are discarded. This matrix is a 21522x21522 double matrix. The memory of the Linux-based remote server was able to successfully handle this process and thus no sparse matrix approaches were needed for better data handling. Afterwards, the spatial (Euclidean) distance matrix  $\mathbf{S}$  was computed only once since it is common for all subjects because it is exclusively based on the voxels coordinates. This matrix is a 21522x21522 matrix, where the element  $(i, j)$  represents the Euclidean distance between voxels  $i$  and  $j$ . Different thresholds ( $rc$  values) are then applied on  $\mathbf{S}$  in order to examine the effect of the distance on the SCSC procedure and how this affects the optimal number of clusters. These thresholds correspond to a sphere's radius since the voxels lie on the 3D space. For example, a sphere with  $rc$  (radius) value of 2 covers 33 voxels;  $rc = 3$  (123 voxels),  $rc = 5$  (515 voxels),  $rc = 8$  (1947 voxels),  $rc = 10$  (3589 voxels),  $rc = 12$  (5763 voxels). For each threshold under evaluation, the resulting binary version of the distance matrix  $\mathbf{S}$  is (elementwise) multiplied with the average correlation matrix in order to define the 21522x21522 spatially constrained correlation matrix  $\mathbf{W}$  (**Fig. 4.13**).

This matrix is given as input into the SC procedure and the clustering evaluation measures described in **Section 4.7** were computed for 30 clusters under evaluation (**Fig. 4.14**). A number of 30 clusters under evaluation is more than enough since after the 30<sup>th</sup> eigenvalue the magnitude becomes too low or remains stable, based on the corresponding  $rc$  value (**Fig. 4.14(A)**). This denotes that the eigenvalue plots are highly affected by the  $rc$  values. In order to determine the appropriate number of clusters, we seek for the largest gap between two

consecutive clustering indices on the average silhouette plots. This indicates a breakdown of a cluster, as presented in the work of Sato et al., 2013, which suggests that when the largest gap in an average silhouette plot is located between the  $k^{\text{th}}$  and the  $(k+1)^{\text{th}}$  cluster, the optimal number of clusters should be set to  $k$ . The largest gap after the  $k^{\text{th}}$  cluster denotes an immediate clustering breakdown and thus the proposed number of clusters is  $k$ . The same thing is expected to stand for the Davies-Bouldin index. According to **Fig. 4.14**, the distribution of the evaluation measures (**Fig. 4.14(B), (C)**) is similar, with the optimal number of cluster however being different, according to the largest gap criterion. Therefore, a cross-validation procedure is necessary to seek for the  $rc$  value that exhibits the most stable performance.

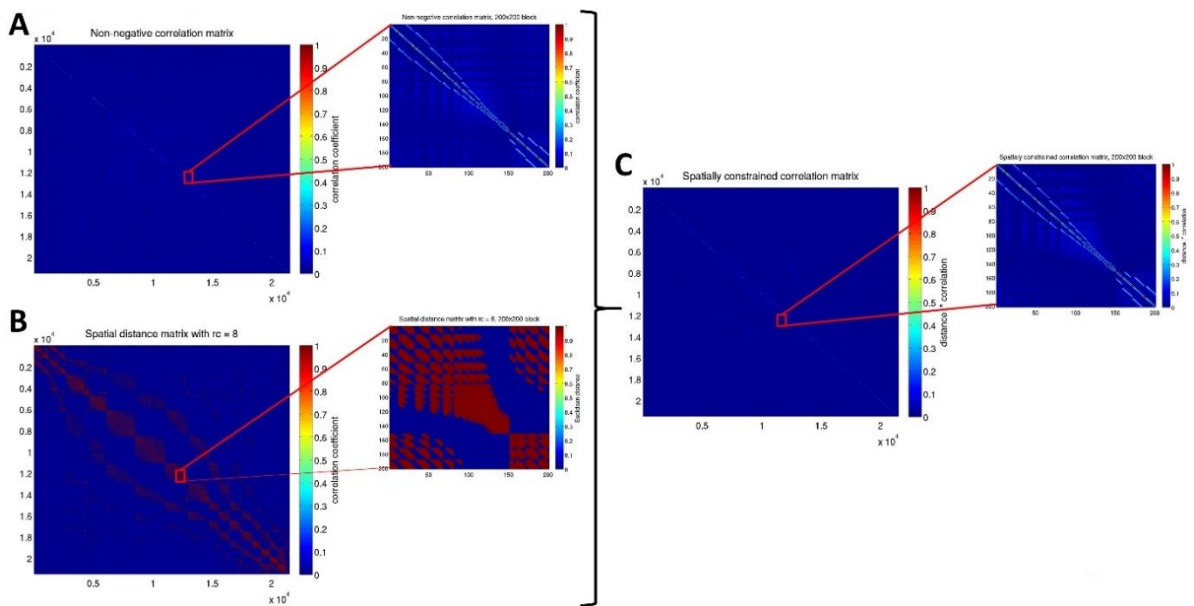


**Figure 4.13.** The formation of the spatially constrained correlation matrix. **(A)** The average 21522x21522 non-negative correlation (adjacency) matrix with an additional 200x200 block for zooming purposes. **(B)** The average 21522x21522 Euclidean distance matrix with an additional 200x200 block for zooming purposes. **(C)** The spatially constrained correlation matrix which is the result of the element-wise multiplication between matrices in **(A)** and **(B)**.

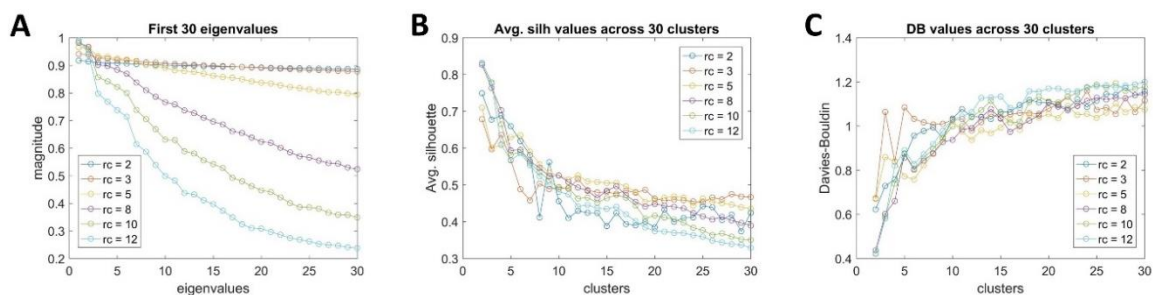


**Figure 4.14.** Clustering evaluation results for 30 clusters under examination, on the average correlation matrix. **(A)** The first 30 eigenvalues. **(B)** The average silhouette and **(C)** Davies-Bouldin values computed across 30 clusters for various thresholds (i.e.,  $rc = 2, 3, 5, 8, 10,$  and  $12$ ) on the distance matrix  $S$ .

#### 4.11. Cross-validation for performance evaluation

In order to validate the consistency of the number of clusters across the total population, a repeated cross-validation procedure is executed by first computing the average correlation matrices across 10 randomly selected subjects for 10 times (runs) in total, i.e., 10 average correlation matrices across 10 random subjects per run and finally by re-applying the proposed clustering procedure on each individual run. The goal of this step is to search for the  $rc$  value that exhibits the most stable performance (same  $k$  across each run).

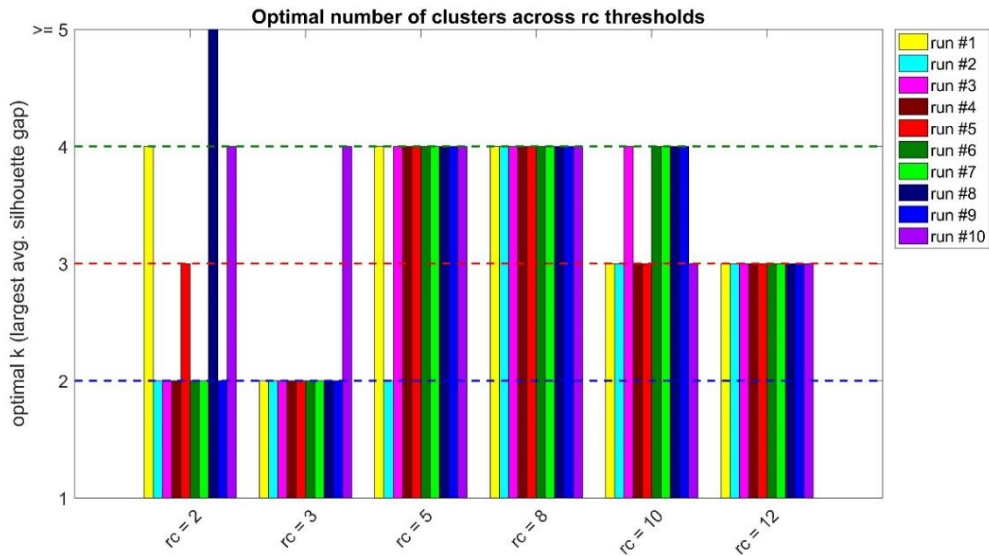


**Figure 4.15.** The optimal number of clusters across each  $rc$  value for all validation runs, as indicated by the largest gap on each run's average silhouette plot across 30 clusters.

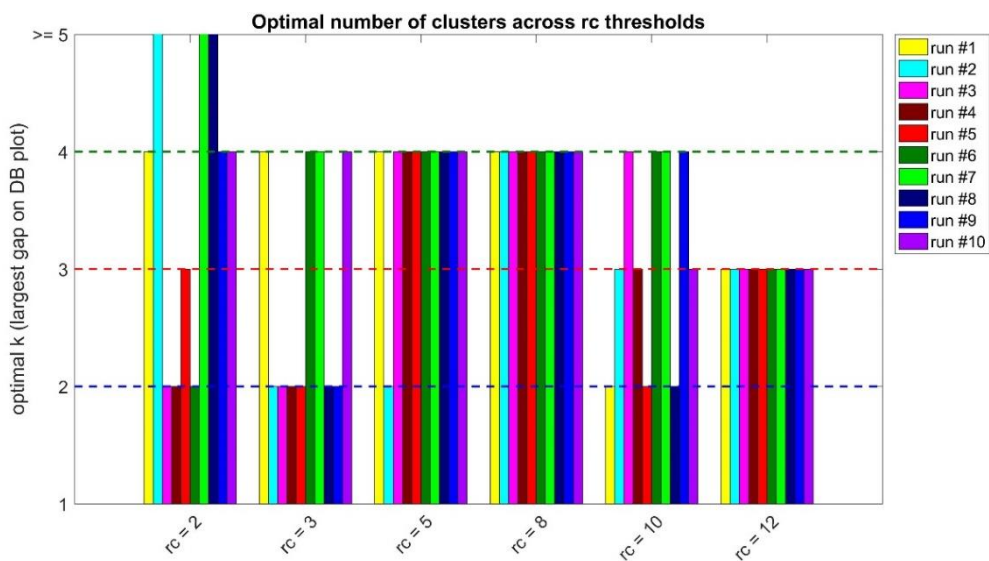


**Figure 4.16.** The optimal number of clusters across each  $rc$  value for all validation runs, as indicated by the largest gap on each run's Davies-Bouldin plot across 30 clusters.

According to **Figs 4.15** and **4.16**, the SCSC procedure for  $rc = 8$  on  $\mathcal{S}$  was stable at  $k = 4$  clusters across all runs. The same stands for  $rc = 12$  but at  $k = 3$  clusters. In addition, the case for  $rc = 5$  is interesting since it is stable at  $k = 4$  clusters across 9 out of 10 runs. The rest of the thresholding values do not exhibit any consistency at all. An  $rc$  value of 8 covers 1947 voxels instead of  $rc = 12$  which is a threshold that covers an area of 5763 voxels and thus is too large. The fact that  $rc = 5$  has the second best performance at  $k = 4$  reassures that fact that the number of clusters should be set to 4. The evidence so far suggest that the threshold  $rc = 8$  on  $\mathcal{S}$  with a pre-defined number of  $k = 4$  clusters is dominant, however it is important to evaluate the consistency of the resulting clustermaps for us to reach to a final decision.

With the purpose of quantifying the consistency between each pair of clustermaps (i.e., 3D matrices with clustering labels or atlases) among all runs, the Dice similarity coefficient was computed in order to measure the similarity between a pair of clustermaps (Craddock et al., 2012). For two clustermaps, assume  $A$  and  $B$ , the Dice similarity coefficient is defined as the ratio of twice the number of voxels common to both clustermaps divided by the total number of voxels in both clustermaps (Dice, 1945):

$$Dice = \frac{2 \cdot |A \cap B|}{|A| + |B|} \quad (4.32)$$

which results to numbers between 0 and 1, where the latter value corresponds to a perfect correspondence between two clustermaps. In this work, the Dice similarity coefficient was evaluated individually for each pair of 10 clustermaps (recall that there are 21522 voxels per clustermap) which were obtained through the SCSC procedure using  $k = 4$  with an  $rc$  on  $\mathcal{S}$  equal to 8. A common problem though with the computation of **(4.32)** lies in the fact that each voxel's clustering label, within each clustermap, is randomly assigned to a label after the application of the SCSC algorithm and therefore the clusters should be correctly matched prior to the computation of **(4.32)**. This problem is known in the literature as the assignment (or matching) problem and one widely used solution to this problem is given by the Hungarian algorithm (also known as Kuhn-Munkres algorithm or Munkres assignment algorithm).

Since the problem in our case is less complex due to the small number of clusters (i.e., 4), a simpler solution was developed. More specifically, for a pair of clustermaps, assume  $A$  and  $B$ , four assignments are performed for each cluster in  $B$ , using clustermap  $A$  as the reference clustermap. For example, for a cluster on  $A$ , say  $x$ , four clustermaps are created, i.e.,  $B_1$ ,  $B_2$ ,  $B_3$  and  $B_4$  one for each possible assignment. Then the clustermap that owns the cluster, say  $y$ , which achieves the maximum Dice coefficient value with  $x$ , is chosen as its similar one. Of course  $x$  might be already assigned to  $y$  and thus the number of assignments should be four per cluster (16 assignments for each clustermap in total). Moreover, if there are more than one candidate clusters with the maximum Dice value, the next one is chosen. Finally, for each pair of correctly matched clustermaps, four Dice values are returned (where each Dice value is in fact the maximum across all possible assignments; one Dice value per cluster) and the

average Dice similarity coefficient is then employed as a clustering consistency quantifier. The consistency evaluation results are presented, for each cluster individually, on the sequel.

**- Consistency evaluation for cluster 1**

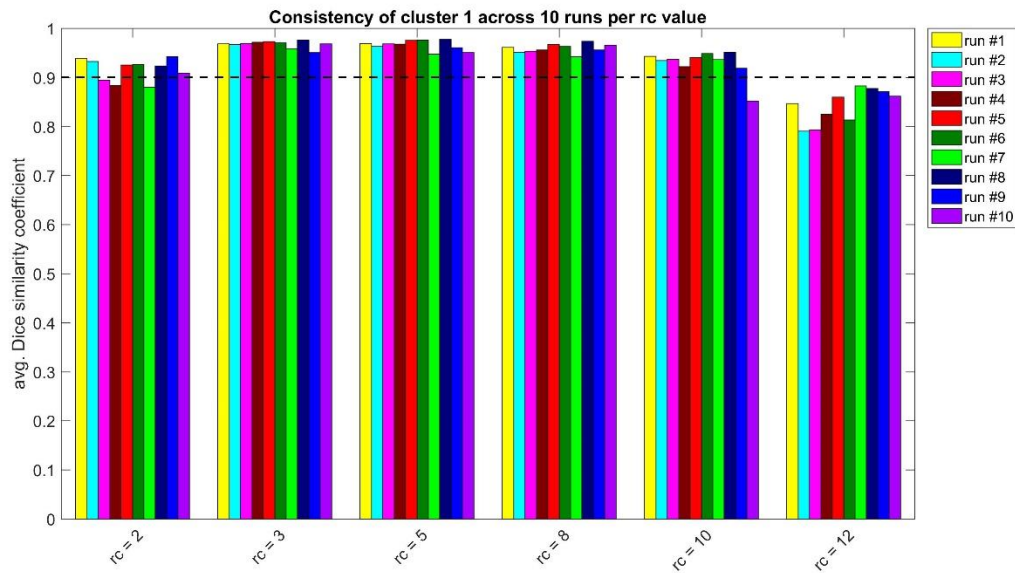


**Figure 4.17.** Consistency evaluation results for each  $rc$  value across all runs for cluster 1. The black dashed line indicates a clustering consistency of 0.9 (90%).

**- Consistency evaluation for cluster 2**

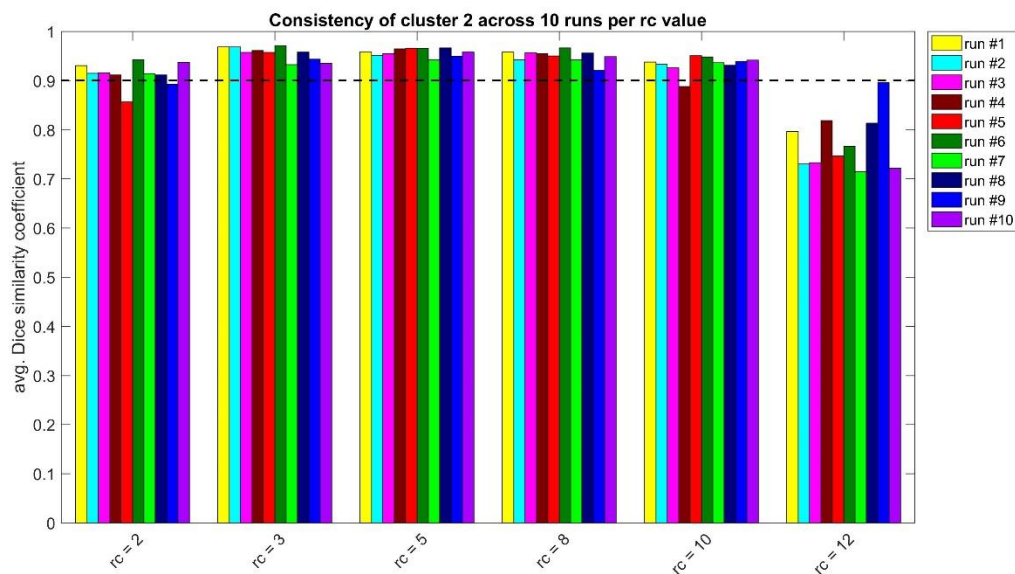


**Figure 4.18.** Consistency evaluation results for each  $rc$  value across all runs for cluster 2. The black dashed line indicates a clustering consistency of 0.9 (90%).

- Consistency evaluation for cluster 3

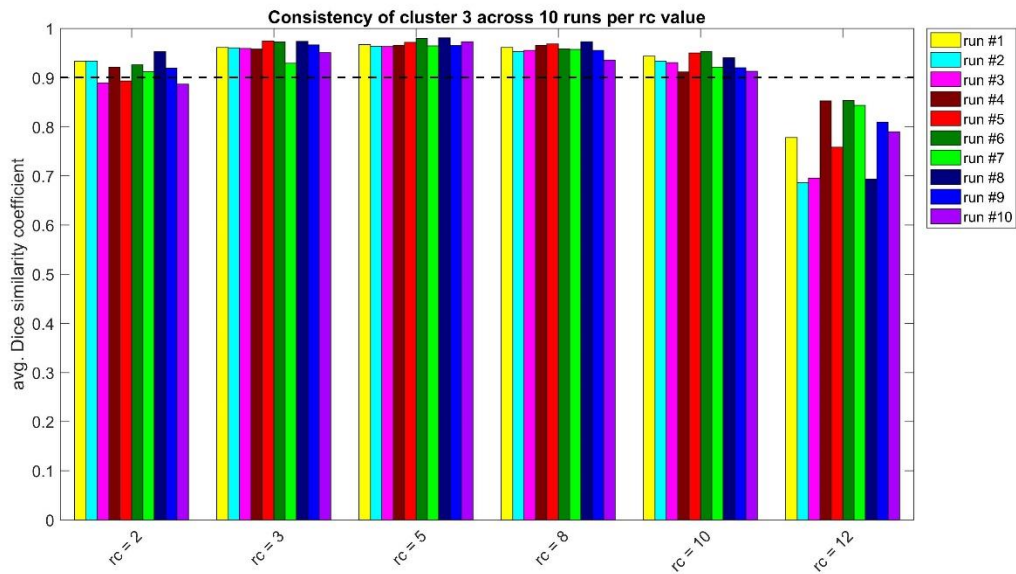


**Figure 4.19.** Consistency evaluation results for each  $rc$  value across all runs for cluster 3. The black dashed line indicates a clustering consistency of 0.9 (90%).

- Consistency evaluation for cluster 4

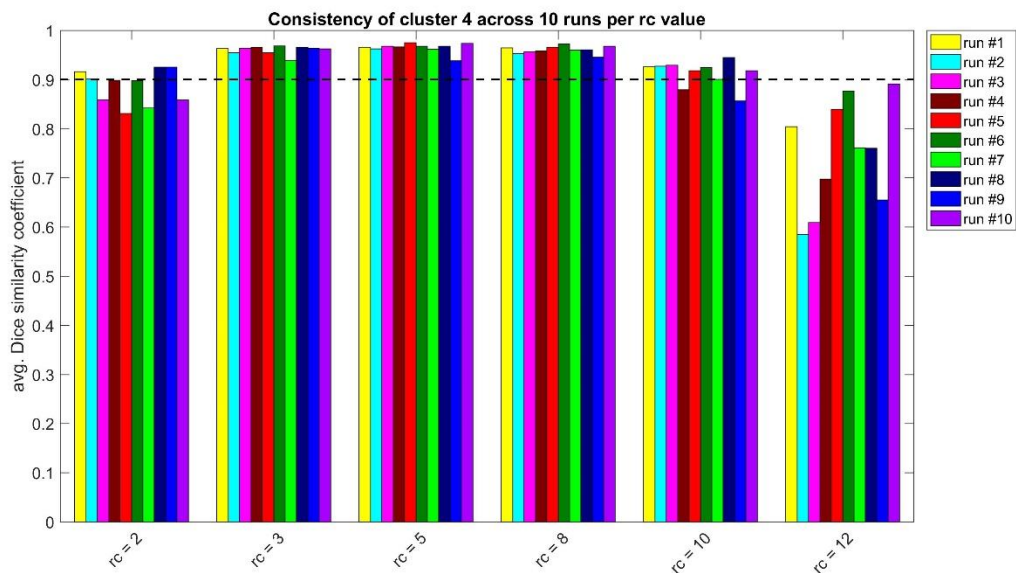


**Figure 4.20.** Consistency evaluation results for each  $rc$  value across all runs for cluster 4. The black dashed line indicates a clustering consistency of 0.9 (90%).

In general, the average Dice coefficient values were very high for all  $rc$  values across all runs and for all four clusters under evaluation except from the case for  $rc = 12$  which produces the least consistent clustermaps than all the other cases. The case for  $rc = 2$  appears with less

than 90% consistency (but not less than 85%), specifically for clusters 1 (3/10 runs), 2 (2/10 runs), 3 (3/10 runs), 4 (4/10 runs). A similar behavior stands for  $rc = 10$  but to a smaller extent since it appears with not less than 85% consistency for clusters 1 (1/10 runs), 2 (1/10 runs) and 4 (2/10 runs). The remaining  $rc$  values, i.e, 3, 5, 8, are the “elite” values since they achieve more than 90% consistency across all runs, for all four clusters, which sometimes exceeds 95% specifically for the cases of  $rc = 5$  and 8.

By taking into consideration the fact that  $rc = 8$  (with  $k = 4$  clusters) was the most stable threshold across all 10 runs of the proposed cross-validation procedure (Figs 4.15-4.16) and that it is able to produce clustermaps with each cluster having at least 95% consistency across 10 runs (Figs 4.17-4.20), it is chosen as the default parameter of the SCSC procedure. From now on, the SCSC will be applied on the original data using  $rc = 8$  on  $\mathcal{S}$  ( $k = 4$  clusters). At this point it is important to note that the cross-validation procedure was the most time consuming process due to the repeated clustering evaluation procedures.

#### 4.12. Resting-state network atlas

In order to create a resting-state network (RSN) atlas, the SCSC algorithm was applied on the average correlation matrix computed across all 100 subjects, with the number of clusters being set to  $k = 4$  with an  $rc = 8$  on  $\mathcal{S}$ . The result is a clustermap or atlas (a 3D matrix with clustering labels assigned per voxel) which has been already registered in the MNI coordinate space (template) and represents the four identified cerebellar resting-state networks (Fig. 4.19). These four clusters are well-separated and consistent. For the sake of completeness, and for comparison purposes only, the SC and Ncut algorithms have been also applied on the same matrix for  $k = 4$  (Figs 4.20-4.21, respectively), along with complete 3D versions of the clustermaps and the corresponding Shannon’s entropy distributions, across all voxels, for various sphere’s radius values (i.e.,  $r = 2$  (33 voxels);  $r = 3$  (123 voxels);  $r = 4$  (257 voxels);  $r = 5$  (515 voxels);  $r = 6$  (924 voxels)) in order to compare the clustering homogeneity of the resulting clustermaps with the one obtained from the SCSC procedure (Fig. 4.21).

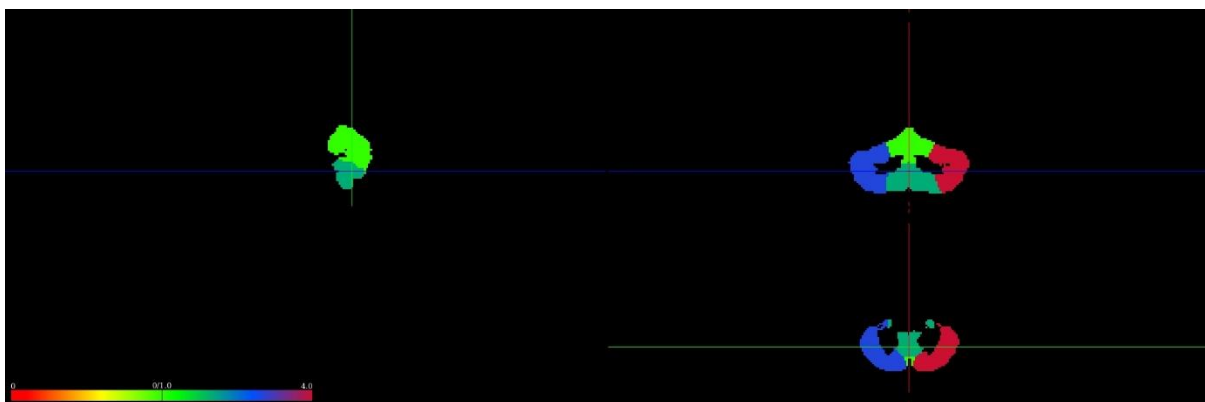


**Figure 4.21.** The resulting clustermap after the application of the SCSC approach for  $k = 4$ , in 2D form with slice indices  $P = 46$ ,  $C = 31$ ,  $A = 15$ .

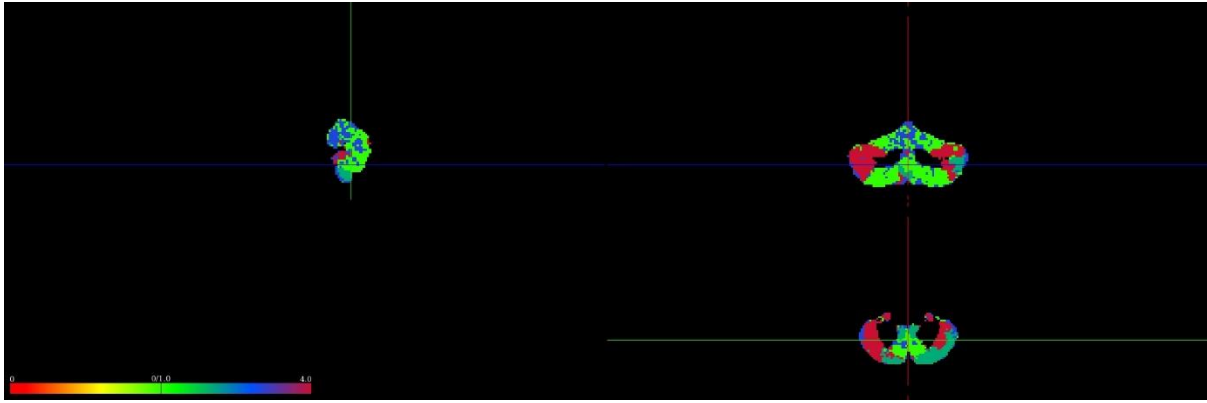


**Figure 4.22.** The resulting clustermap after the application of the SC approach for  $k = 4$ , in 2D form with slice indices  $P = 46$ ,  $C = 31$ ,  $A = 15$ .

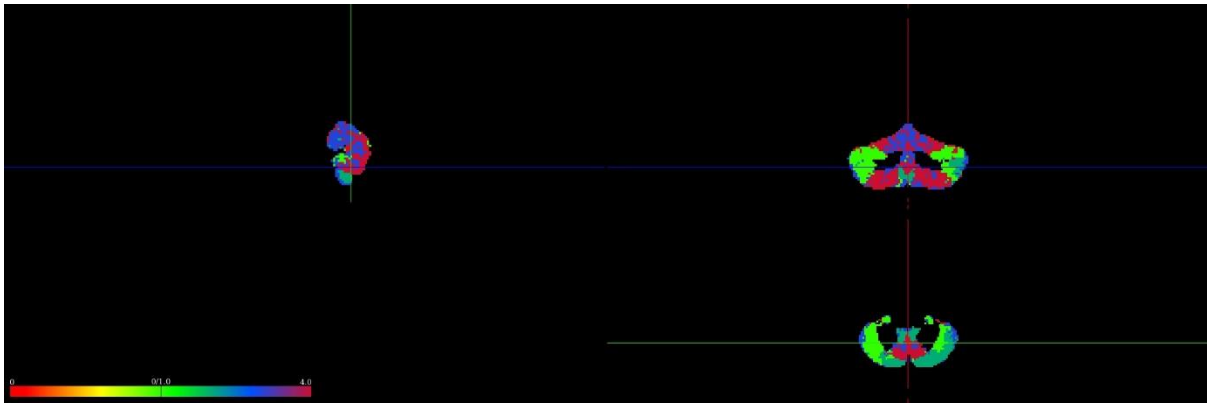


**Figure 4.23.** The resulting clustermap after the application of the Ncut approach for  $k = 4$ , in 2D form with slice indices  $P = 46$ ,  $C = 31$ ,  $A = 15$ .

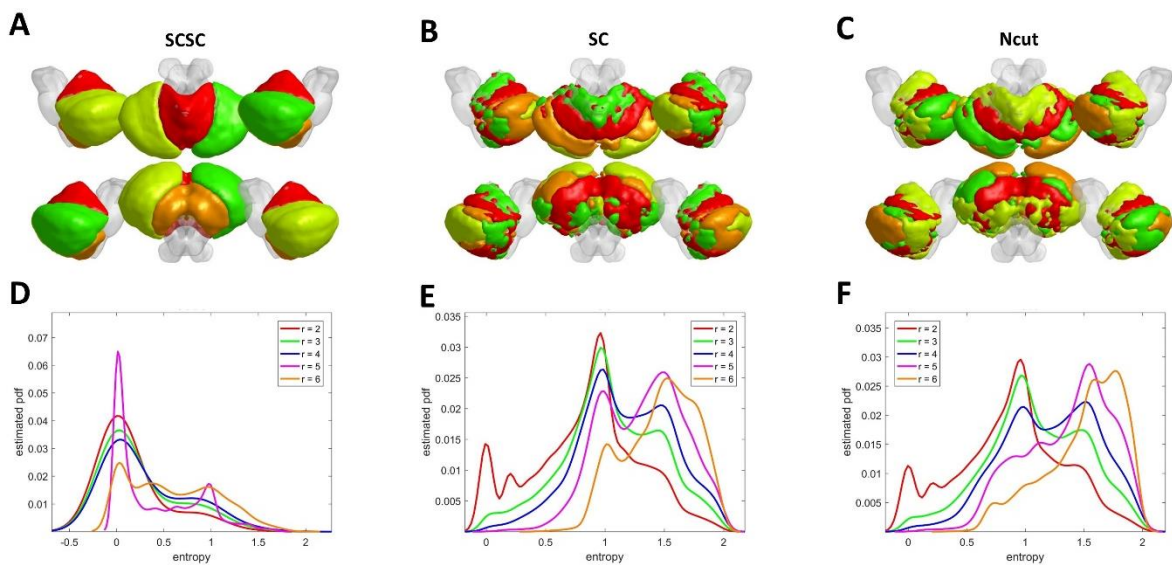


**Figure 4.24.** The resulting clustermaps along with the corresponding voxel-wise entropy distributions for each clustering approach.

Notice that the clusters derived from the SCSC algorithm are spatially contiguous and homogeneous whereas the clusters obtained from the SC algorithm are spatially distributed. In addition, the entropy distributions for each atlas are also presented on **Fig. 4.22**, for different sphere's radius values. It is now obvious that the SCSC algorithm appears to achieve small entropy values and thus consistent ROIs with better cohesion. *At this point, it is important to note that the color of the clusters in each atlas should not be used for comparing the clustermaps. Each clustermap is the result of a different clustering procedure that yields different clustering label assignments per voxel.*

### 4.13. Final cerebellar atlas

In order to extract a much more detailed atlas, the RSN atlas obtained from the SCSC approach is combined with the anatomical atlas of cerebellum which was already obtained from the SUIT toolbox (Diedrichsen et al., 2009; Diedrichsen et al., 2011; Diedrichsen and Zotow, 2015) which is presented in **Fig. 4.25(A)** using BrainNet Viewer (Xia et al., 2013). After projecting the RSN atlas (**Fig. 4.25(B)**) onto the anatomical atlas, the resulting overlaid regions can be treated as functional ROIs. Regions that contain less than 10 voxels are ignored from further analysis. As a result, the final number of extracted ROIs is equal to 46 (**Fig. 4.25 (C)**). In fact, this procedure aims to extract a large number of functional ROIs in order to provide a much more detailed and data-driven (accurate) network analysis of cerebellum. The projection is valid since the voxel coordinates of the anatomical atlas lie on the same space (i.e., MNI space) with the coordinates of the RSN atlas.

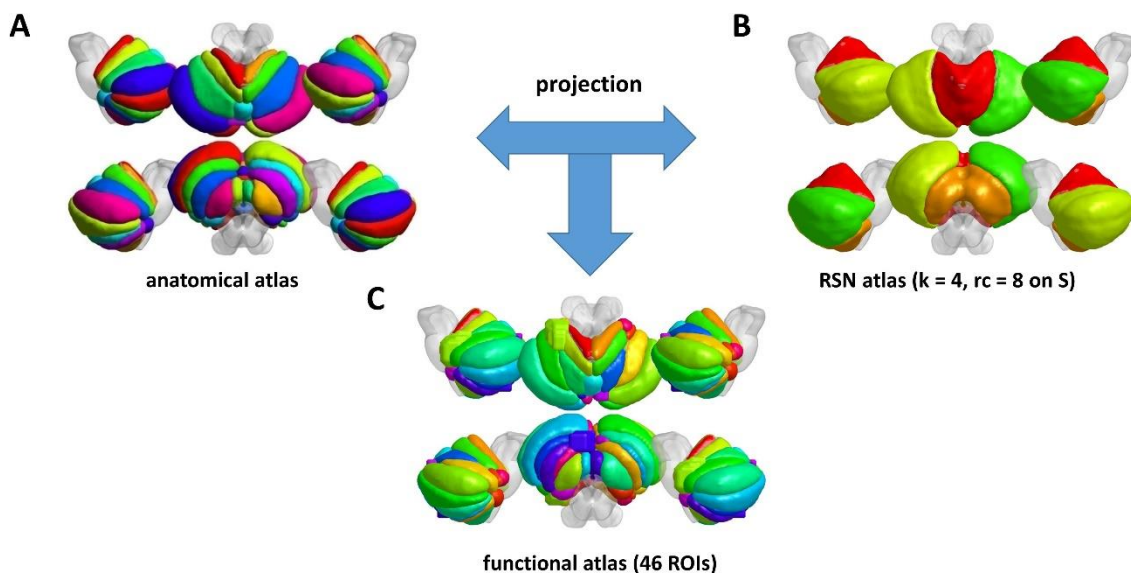


**Figure 4.25.** The construction steps of cerebellum's functional atlas. **(A)** The anatomical atlas is projected on **(B)** the RSN atlas leading to a new **(C)** functional atlas with 46 functional ROIs.

**Table 4.2.** Number of anatomically overlaid voxels for each functional ROI.

Anatomical ROIs	# of voxels covered per cluster for each anatomical ROI			
	C1 (light green)	C2 (green)	C3 (blue)	C4 (purple)
Left I-IV	601	0	21	0
Right I-IV	604	6	0	42
Left V	585	0	139	0
Right V	580	2	0	94
Left VI	533	0	1049	0
Vermis VI	380	0	0	0
Right VI	517	5	0	976
Left Crus I	32	0	2360	0
Vermis Crus I	1	0	0	0
Right Crus I	23	0	0	2478
Left Crus II	105	0	1761	0
Vermis Crus II	81	0	0	0
Right Crus II	107	0	0	1658
Left VIIb	31	23	794	0
Vermis VIIb	27	0	0	0
Right VIIb	31	65	0	782
Left VIIIa	2	228	582	0
Vermis VIIIa	117	104	0	0
Right VIIIa	4	598	0	251
Left VIIIb	0	656	1	0
Vermis VIIIb	1	109	0	0
Right VIIIb	0	719	0	0
Left IX	1	554	0	0
Vermis IX	17	113	0	0
Right IX	2	650	0	0
Left X	0	107	26	0
Vermis X	2	45	0	0
Right X	0	140	0	0

\* regions filled with grey color are ignored due to the small number of assigned voxels (<10).

**Table 4.3.** Percentage of anatomically overlaid voxels for each functional ROI.

Anatomical ROIs	% of voxels covered per cluster for each anatomical ROI			
	C1 (light green)	C2 (green)	C3 (blue)	C4 (purple)
Left I-IV	96.62	0.00	3.38	0.00
Right I-IV	92.64	0.92	0.00	6.44
Left V	80.80	0.00	19.20	0.00
Right V	85.80	0.30	0.00	13.91
Left VI	33.69	0.00	66.31	0.00
Vermis VI	100.00	0.00	0.00	0.00
Right VI	34.51	0.33	0.00	65.15
Left Crus I	1.34	0.00	98.66	0.00
Vermis Crus I	100.00	0.00	0.00	0.00
Right Crus I	0.92	0.00	0.00	99.08
Left Crus II	5.63	0.00	94.37	0.00
Vermis Crus II	100.00	0.00	0.00	0.00
Right Crus II	6.06	0.00	0.00	93.94
Left VIIb	3.66	2.71	93.63	0.00
Vermis VIIb	100.00	0.00	0.00	0.00
Right VIIb	3.53	7.40	0.00	89.07
Left VIIIa	0.25	28.08	71.67	0.00
Vermis VIIIa	52.94	47.06	0.00	0.00
Right VIIIa	0.47	70.11	0.00	29.43
Left VIIIb	0.00	99.85	0.15	0.00
Vermis VIIIb	0.91	99.09	0.00	0.00
Right VIIIb	0.00	100.00	0.00	0.00
Left IX	0.18	99.82	0.00	0.00
Vermis IX	13.08	86.92	0.00	0.00
Right IX	0.31	99.69	0.00	0.00
Left X	0.00	80.45	19.55	0.00
Vermis X	4.26	95.74	0.00	0.00
Right X	0.00	100.00	0.00	0.00

**Table 4.4.** The anatomical locations of the identified functional regions.

Anatomical ROIs	Functional region number (number of voxels)		
Left I-IV	8 (21)	30 (601)	
Right I-IV	1 (42)	31 (604)	
Left V	9 (139)	32 (585)	
Right V	2 (94)	33 (380)	
Left VI	10 (1049)	34 (533)	
Vermis VI	35 (380)		
Right VI	3 (976)	36 (517)	
Left Crus I	11 (2360)	37 (32)	
Vermis Crus I			
Right Crus I	4 (2478)	38 (23)	
Left Crus II	12 (1761)	39 (105)	
Vermis Crus II	40 (81)		
Right Crus II	5 (1658)	41 (107)	
Left VIIb	13 (794)	16 (23)	42 (31)
Vermis VIIb	43 (27)		
Right VIIb	6 (782)	17 (65)	44 (31)
Left VIIIa	14 (582)	18 (228)	
Vermis VIIIa	19 (104)	45 (117)	
Right VIIIa	7 (251)	20 (598)	
Left VIIIb	21 (656)		
Vermis VIIIb	22 (109)		
Right VIIIb	23 (719)		
Left IX	24 (554)		
Vermis IX	25 (113)	46 (17)	
Right IX	26 (650)		
Left X	15 (26)	27 (107)	
Vermis X	28 (45)		
Right X	29 (140)		

It is worth mentioning that large anatomical lobules of cerebellum such as Left/Right VI, Left/Right Crus I & II, Left/Right VIIb (**Tables 4.3-4.4**) have been “divided” into more than one functional regions (nodes), a fact that can lead to a deeper investigation of each anatomical lobule’s implication in cerebellum’s inner functional connectivity. Notice that no functional regions have been formed for lobule Vermis Crus I since it contains only one voxel.

According to the literature, the node of a ROI is defined as the center of mass of that ROI. This is used only for network visualization purposes. In order to do so, the node of each ROI is placed on its most centered voxel coordinates (in the MNI space). Here, the centered voxel of a region is defined as the one with the smallest total distance from any other voxel within that region (see **Table 4.5**). This procedure is repeated for all 46 functional regions with the final locations of the nodes being presented later on **Figs 4.26-4.27**.

**Table 4.5.** MNI coordinates of each functional region's node.

Functional region	MNI coordinates		
	X	Y	Z
1	24	-32	-32
2	28	-36	-30
3	30	-54	-28
4	38	-68	-32
5	26	-78	-42
6	32	-66	-52
7	32	-58	-54
8	-20	-32	-30
9	-26	-36	-30
10	-28	-56	-26
11	-38	-68	-32
12	-26	-76	-42
13	-28	-66	-52
14	-28	-56	-54
15	-26	-36	-42
16	-6	-72	-46
17	10	-72	-48
18	-16	-64	-52
19	0	-68	-42
20	24	-58	-54
21	-18	-50	-54
22	0	-64	-42
23	18	-50	-54
24	-6	-54	-48
25	0	-56	-38
26	6	-54	-48
27	-20	-36	-46
28	0	-48	-36
29	22	-36	-46
30	-6	-46	-16
31	8	-44	-18
32	-10	-54	-16
33	12	-54	-16
34	-12	-66	-20
35	0	-70	-20
36	14	-66	-20
37	-8	-78	-26
38	8	-76	-26
39	-4	-80	-34
40	0	-74	-32
41	6	-80	-34
42	-6	-72	-38
43	0	-68	-32
44	8	-70	-36
45	0	-66	-34
46	0	-54	-30

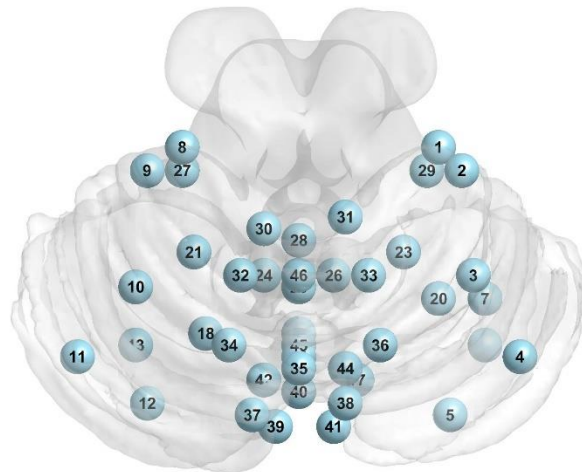


**Figure 4.26.** The location of the 46 functional nodes in 3D coronal view using BrainNet Viewer (Xia et al., 2013).

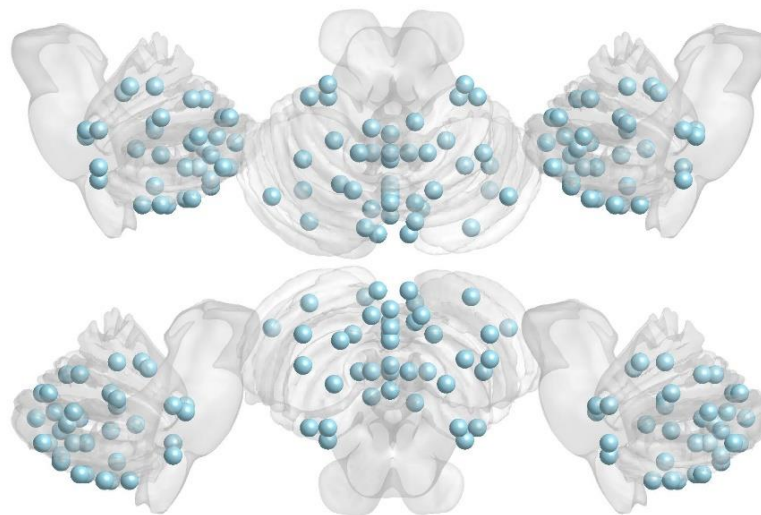


**Figure 4.27.** The location of the 46 functional nodes in 3D complete view (without labels for better visualization) using BrainNet Viewer (Xia et al., 2013).

#### 4.14. Gender-based functional connectivity analysis

In this final section, a gender-based functional connectivity and network analysis of cerebellum is executed based on the functional atlas that was constructed in **Section 4.13**. The goal of this scheme is **(a)** to test for significant differences between male and female functional cerebellar networks and **(b)** identify the functional regions that achieve the highest average degree and/or betweenness centrality among each population known as hubs. This procedure is similar to the one described in **Chapter 3** but with the difference that this time the functional cerebellar atlas is used for a gender-based network analysis only.

#### 4.14.1. Functional parcellation of cerebellum

A functional parcellation of cerebellum is performed for each subject separately using the final functional atlas of cerebellum (**Section 4.13**) which was constructed through the combination of Diedrichsen's anatomical atlas (Diedrichsen et al., 2009; Diedrichsen et al., 2011; Diedrichsen and Zotow, 2015) with the RSN atlas that was obtained from the SCSC procedure using  $rc = 8$  ( $k = 4$  clusters) on the distance matrix  $\mathcal{S}$ . The result of the parcellation procedure is a 46x1200 BOLD signals matrix, where the  $i$ -th row represents the average (pre-processed) BOLD signal across the voxels of the  $i$ -th functional ROI.

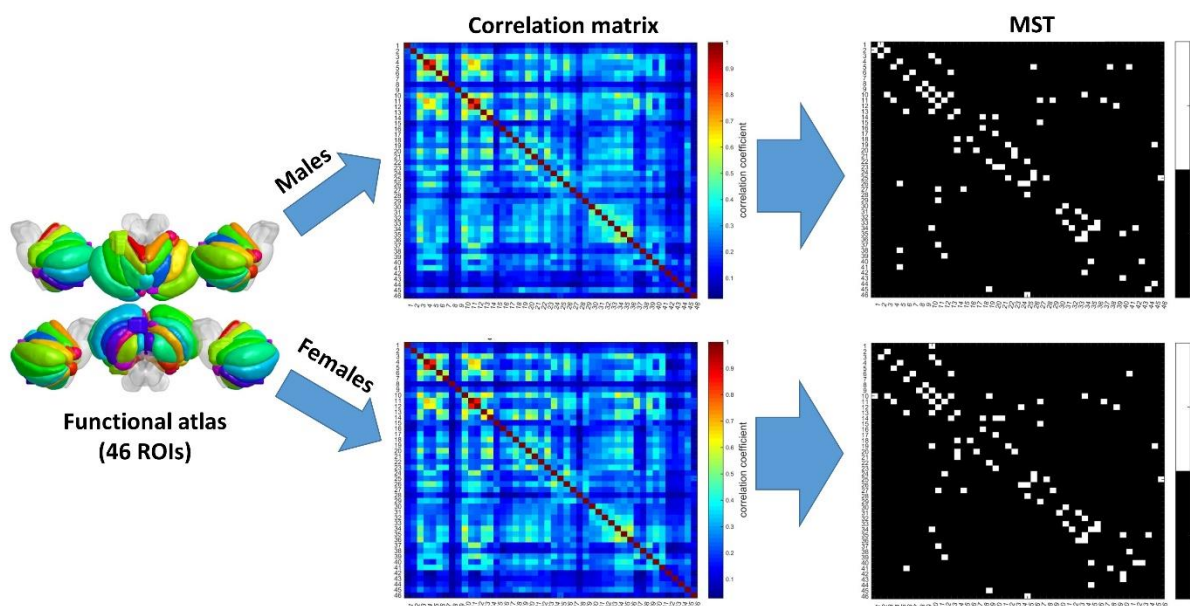


**Figure 4.28.** Network analysis strategy using the functional atlas of cerebellum. The 46x46 correlation matrices are first constructed after parcellating the functional atlas individually for both genders and then the corresponding Minimum Spanning Trees (MSTs) are formed. On the latter, various local and global metrics are extracted for statistical and hub analysis.

#### 4.14.2. Network construction and Minimum Spanning Trees formation

Cerebellum's functional connectivity was assessed by computing Pearson's correlation coefficients between each pair of the 46 ROIs inside the cerebellum, leading to a  $46 \times 46$  correlation (adjacency) matrix per subject in both IQ groups. Negative correlations have been excluded from further analysis (Bohr et al., 2013), with the elimination of the corresponding edge. The average correlation networks across males and females are presented on **Fig 4.29**. Afterwards, the corresponding MSTs were computed for each population based on Kruskal's algorithmic scheme and various local and global metrics were computed for each MST. The average MSTs for both males and females are presented on **Fig. 4.30**. For detailed information about the MSTs construction method as well as the computed set of local and global network metrics, see **Section 3.5**.

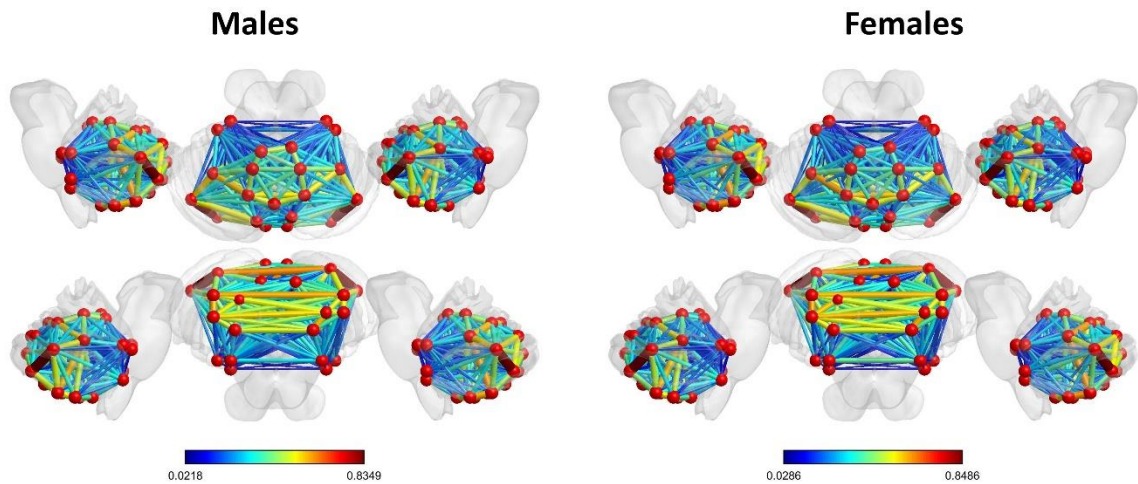


**Figure 4.29.** The average correlation networks of both males and females projected on cerebellum's surface using BrainNet Viewer (Xia et al., 2013).

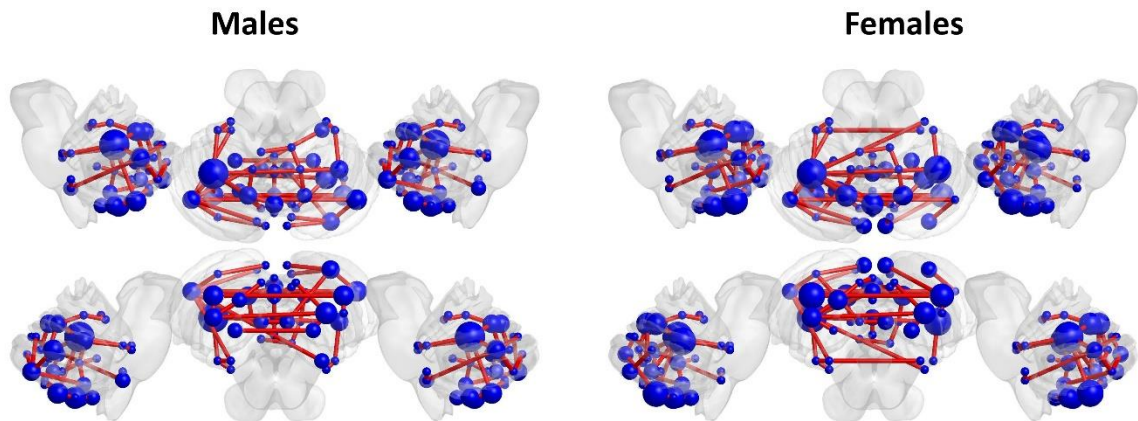


**Figure 4.30.** The MSTs of the corresponding average correlation networks for both males and females projected on cerebellum's surface using BrainNet Viewer (Xia et al., 2013). Each node's size linearly depends on its corresponding average BC value across each population.

#### 4.14.3. Statistical analysis and hubs

Three local (BC, ECC, DEG) and six global (diameter, degree correlation, radius, kappa, leaf fraction, tree hierarchy) metrics were computed in order to examine the topological and functional characteristics of every MST. Several global weighted graph metrics, including average weighted clustering coefficient, characteristic path length, and connectivity, were also examined in our procedure. The feature datasets are, in general, non-normal so that natural log-transformation was applied in order to approximate normal distribution properties, with the addition of a very small constant ( $1 \cdot e^{-24}$ ) for avoiding zero-value transforms. Statistical analysis was performed using 1-way balanced ANOVA in order to test for differences males and females (males/females; 50/50). All p-values were corrected based on False Discovery Rate (FDR) using the Benjamini-Hochberg procedure (Benjamini and Hochberg, 1995) with the significance level set to 0.05.

As far as the local MST measures are concerned, no significant differences were found between males and females (see **Appendix; Tables A4, A5 and A6**). At this point, it is worth mentioning that the significant difference that was found (only) in functional region 10, by the metric of eccentricity (**Table A6**), is not considered accurate but rather an FDR correction overfit. On the other hand, it is interesting the fact that tree-hierarchy was the only global measure that exhibited a statistical significant difference among males and females (males:  $0.3807 \pm 0.0463$ ; females:  $0.3999 \pm 0.0466$ ) ( $F = 4.3938$ ,  $p = 0.0386$ ) with values close to 0.4 for both populations (**Table 4.6**), which indicates that the tree topologies of both males and females are close to the optimal tree configuration (i.e., values around 0.5), with significant differences between these (close-to-optimal) tree configurations.

**Table 4.6.** Statistical analysis results based on gender for the main network metrics.

Metric	Males	Females	<i>F</i>	p-values
	Mean±SD	Mean±SD		
avg. clustering coefficient	0.2641±0.1168	0.2559±0.0874	0.0000	0.9999
characteristic path length	4.8376±0.4128	4.6283±1.1273	0.1972	0.6580
connectivity	0.2543±0.1189	0.2499±0.0887	0.0650	0.7992
diameter	0.3298±0.1323	0.3096±0.0782	0.2803	0.5977
radius	0.2042±0.1269	0.1834±0.0471	0.5030	0.4799
leaf fraction	0.5298±0.0572	0.5333±0.0500	0.1592	0.6908
tree-hierarchy	0.3807±0.0463	0.3999±0.0466	4.3938	<b>0.0386</b>
kappa	15.3239±1.8603	15.5915±1.0772	1.1942	0.2772
degree correlation	-0.2163±0.1045	-0.2472±0.1008	2.5079	0.1165

with **bold** highlight: statistical significant results ( $p < 0.05$ ).

In addition, a hub analysis was conducted by computing the regions with the highest DEG, BC values (hubs) across both males and females, respectively.

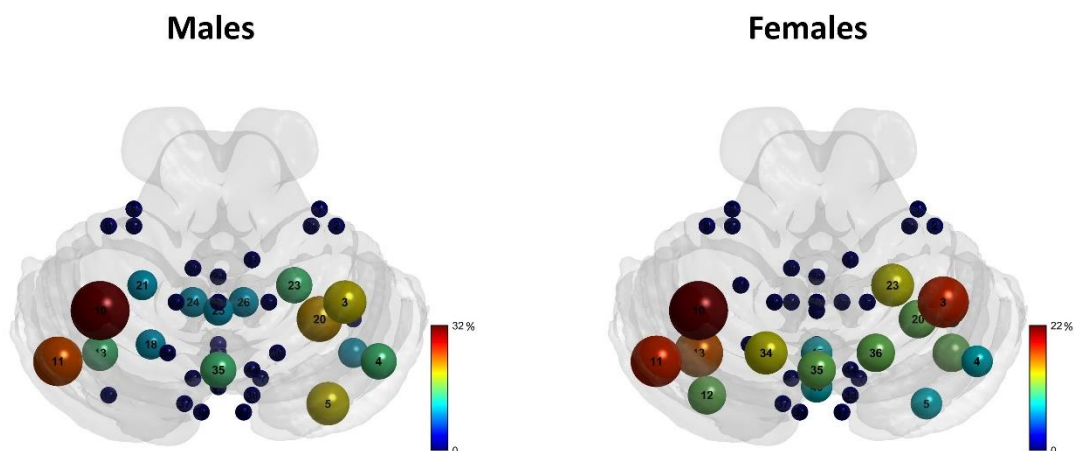


**Figure 4.31.** Nodes with the highest DEG across males and females.

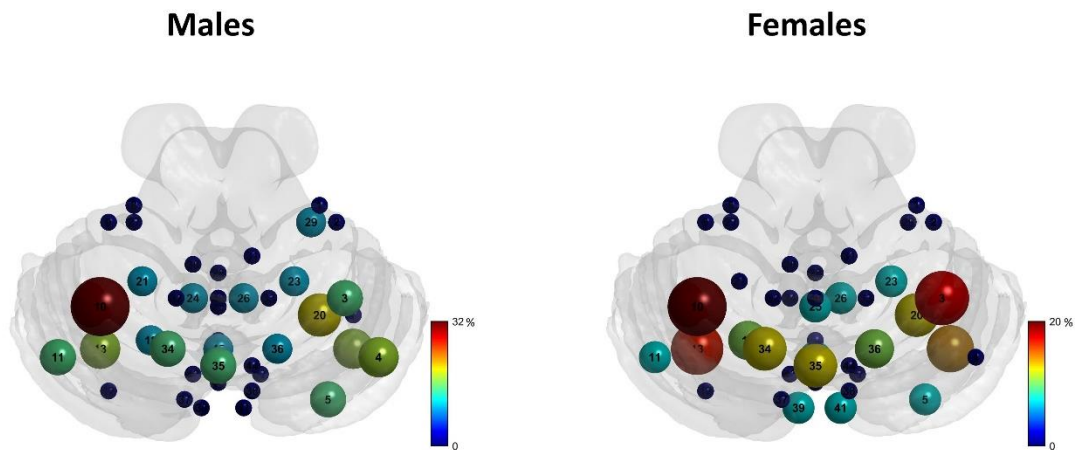


**Figure 4.32.** Nodes with the highest BC across males and females.

According to **Figs 4.31-4.32**, functional node 10, which is located in lobule Left VI, is a critical node for both genders with an observed male dominance since it exhibits the highest DEG in 32% of males and 22% of females as well as the highest BC in 32% of males and 20% of females. This is concordance with the left cerebellar hemispheric dominance as well as with Left VI's importance during information transfer within cerebellum's network (Pezoulas et al., 2017). Moreover, there are additional nodes that can be characterized as hubs but to a lower extent, such as functional node 3 which is located in lobule Right VI and is mostly a hub for the female population due to the fact that it exhibits the highest DEG in 8% of males and 12% of females and the highest BC in 4% of males and 14% of females. The same thing stands for functional node 13 (located in lobule Left VIIb) which appears to have the highest DEG in 10% of females and the highest BC in 12% of females. Finally, functional node 11 (located in lobule Left Crus I) exhibits the highest DEG in 14% of males and 12% of females without however any worth mentioned hub percentages for the BC metric.

#### 4.15. Acknowledgements

The dataset for the final part of this thesis was again provided [in part] by the Human Connectome Project, WU-Minn Consortium (Principal Investigators: David Van Essen and Kamil Ugurbil; 1U54MH091657) funded by the 16 NIH Institutes and Centers that support the NIH Blueprint for Neuroscience Research; and by the McDonnell Center for Systems Neuroscience at Washington University.

This chapter is part of the research proposal which was funded by the **Pancretan Endowment Fund (PEF)** in the form of a scholarship of excellence that the author received in December 2016, for conducting research at the Technical University of Crete, Chania, Greece. The methodological basis of this chapter with the addition of the corresponding discussion section presented on **Chapters 5** later on, have been submitted for publication in the form of a full paper at the [Journal of Biomedical and Health Informatics](#), an IEEE EMB society journal.

## 5. Discussion and future work

---

### 5.1. Discussion

In the first part of this thesis, a lobular functional connectivity and network analysis of cerebellum was performed using Graph Theory aspects on resting-state fMRI data, by taking into consideration the factors of crystallized IQ and gender (Pezoulas et al., 2017). The small-world network structure, characterized by high global and local efficiency, is a property of anatomical and functional brain networks. This configuration maximizes the efficiency and minimizes the costs of information processing. It implies high clustering of nodes (compatible with segregated or modular processing) and short path length (compatible with distributed or integrated processing) (Watts and Strogatz, 1998; Bassett and Bullmore, 2006) and has been extensively reported in EEG, MEG, Tractography and fMRI studies (Stam, 2004; Tewarie et al., 2014; Stam et al., 2016). Focusing on cerebellum, the examination of low and high-IQ individuals suggest that both sexes have the characteristics of small-world networks with differences in females indicative of higher neural efficiency of the cerebellum, especially in higher-IQ females. The more efficient network organization in women reflects the different hemispheric organization between genders. The considerations of three global metrics in women support this conclusion. Our findings in men are in a similar direction with respect to the IQ level, but appear not significant. The lower small-worldness in high-IQ females, compared to low-IQ females and to men counterparts, forms an interesting finding of our study. The higher small-world organization, with higher clustering coefficient and lower path length in low-IQ females, is indicative of a more optimum functionally organized segregation and integration. In contrast, in high IQ females, the segregation and integration of the functional networks at rest can be explained as the idle state of more efficient reactivity in cognitive tasks, in accordance to the neural efficiency hypothesis. The same stands for the male population but without any significance. It is known that the neural efficiency hypothesis becomes relevant during brain activations, where more efficient individuals show lower (weak) brain activation as they functionally react easier. In agreement to these results, an earlier study which was conducted by Dr. Sifis Micheloyannis revealed that highly educated individuals showed less prominent small-world structure than their less educated and lower IQ counterparts (Micheloyannis et al., 2006).

Five global network metrics (i.e., average clustering coefficient, small-worldness, connectivity, diameter, radius) revealed statistically significant differences between low and high-IQ individuals (**Table 3.5** for low/high-IQ population, **Table 3.7** for low/high-IQ females), as well as within males and females for both low and high-IQ groups (**Table 3.8** for low-IQ males/females, **Table 3.9** for high-IQ males/females). Three cerebellar lobules (i.e., Left Crus II, Left X, and Vermis VIII) in low-IQ individuals (in both genders) showed maximum correlation with the median response time, implying increased effort dedicated locally by this population in cognitive tasks. Since the intrinsic organization of cerebellar functions at rest follows the functional organization of the cerebrum, a similar co-activation with the brain structures is expected (Liao et al., 2010; Kelly et al., 2012). Thus, differences between men and women, as well as between low and high-IQ individuals, which appear intrinsically in the cerebellar network organization at rest, are expected to reflect differences in cognitive functions in association with intelligence. It is interesting that our study supports these assumptions at a statistically significant level only in women. There is a trend toward the same direction in men, but without significant differences between low and high-IQ individuals. This differentiation between men and women is indicative of gender differences in cognitive functions which are associated with intelligence. The network connectivity was higher in high-IQ women than low-IQ women, with smaller diameter and radius values (**Table 3.7**). These findings show that the network organization in women with high-IQ at rest is more efficient. In combination with the findings of small-world organization, it may also signify the expression of neuronal-network efficiency in this sub-population. Male groups exhibit similar trends, but without any significance. The increased readiness and efficiency of network organization, as well as the lower small-worldness in high-IQ females, compared to low-IQ females and to men counterparts, forms an interesting finding of our study. According to the intrinsic cerebellar connections, these findings could be related to the fact that the cerebellar-cerebral coordination differs among individuals, with known language dominance in women, which is more effective in highly intelligent individuals.

In addition, the lobules with the highest DEG, BC values can be related mainly with cognitive functions, where a left cerebellar dominance is observed. It is further known that these lobules are related to motor and cognitive functions (Koziol et al., 2014). In terms of DEG and BC metrics, many lobules exhibited higher values on the left side whereas some other lobules express right activation related to motor and cognitive functions but to a smaller extent; i.e., IV, V, VI and parts of HVIIb and HVIII related to motor function (Stoodley et al., 2012), while Crus I, Crus II, lobule VI, VIIa and VIIb related to cognitive function (Bernard et al., 2012). The dominance of DEG and BC on left lobules was exhibited in both sexes, but the stronger Left VI hub indication in high-IQ women is a novel finding and goes in parallel with other higher-level organizations in this group. The aforementioned hubs are related to frontal, pre-frontal, temporal, parietal lobes (lobule VI), frontal gyrus, precuneus, angular gyrus, interior parietal lobe (Crus I) (Bernard et al., 2012; Koziol et al., 2014). An additional finding related to nodes of the cerebellum is that regions Left Crus II, Left X, and Vermis VIII in low-IQ individuals (both men and women) showed maximum correlation with the median

response time, implying that these lobules become more important only in low-IQ individuals (**Table 3.4**).

In the second part of this thesis, a voxel-wise clustering approach was developed in order to perform a more detailed, accurate and data-driven analysis of cerebellum's functional connectivity network so as to reveal the underlying resting-state and functional cerebellar activity as well as execute a gender-based network analysis. For this purpose, spectral graph theory concepts were applied in order to cluster the voxels that exhibit similar correlation patterns by partitioning the average correlation matrix across the population of interest. The main problem with these clustering approaches though is that they do not provide spatially contiguous clusters but spatially distributed clusters, a fact that is connected with background noise. In cerebellum for example, this noise may be interpreted by voxels which might not be activated and are usually located in the white matter of the cerebellum's deep nuclei. In order to overcome this issue, a spatially constrained version of the original spectral clustering approach (i.e., Spatially Constrained Spectral Clustering - SCSC) along with various thresholds on the distance matrix and a repeated cross-validation was proposed and tested on synthetic BOLD time-series prior to any application on the original data. All the three versions of the simulation (**Figs 4.7-4.12**) were able to highlight the weakness of the conventional spectral clustering approach in providing spatially contiguous clusters under noisy environments. The corresponding entropy densities confirm this weakness with high concentration around 1 (complete uncertainty). On the other hand, the SCSC approach tends to be much smoother, with high entropy concentration around 0 (which implies no uncertainty at all).

The SCSC algorithm was then applied on the original data across 30 clusters under evaluation by testing the effects of various thresholds ( $rc$  values) on the distance matrix (i.e., 3, 5, 8, 10, and 12). According to the average silhouette and Davies-Bouldin plots, all thresholds tend to have a similar behavior (**Fig. 4.14**). However, according to the largest gap criterion, the appropriate number of clusters is slightly different across the thresholds (usually 4 or 5). In addition, the eigenvalue plots are highly affected by the threshold values due to the spatial constraint they introduce. The repeated cross-validation procedure was able to provide a clearer view. In fact, it revealed that the most stable threshold on the distance matrix, across all runs, was 8 with the appropriate number of clusters being  $k = 4$  across 100% of the runs (**Figs 4.15-4.16**). Moreover, these parameters were able to generate clustermaps (atlases) with more than 90% consistency per cluster which confirms this selection (**Figs 4.17-4.20**). As a result, the SCSC procedure was applied on the original data using  $rc = 8$  on the distance matrix and  $k = 4$  clusters. The result is a resting-state network (RSN) atlas of cerebellum with 4 identified spatially-contiguous clusters (**Fig. 4.21**). This atlas was compared with those of the conventional spectral clustering and N-cut procedures, highlighting once more the problem of the spatially distributed clusters (**Fig. 4.24**). This fact is also confirmed by the corresponding entropy distributions which are similar as in the simulation case.

The RSN atlas was finally combined with the anatomical atlas, in the same coordinate space, in order to create a functional atlas with more regions for executing a more accurate

gender-based network analysis. This functional atlas of cerebellum contains 46 spatially contiguous regions (**Figs 4.26-4.27**) and is used to parcellate the cerebellum in a similar way like the one described in **Chapter 3**, for constructing functional connectivity networks and MSTs for both males and females (**Fig. 4.28**). The statistical analysis procedure on the extracted local and global network/MST descriptors indicated only one statistical significant difference and specifically for the tree-hierarchy measure. This difference is important since it denotes that there is an alteration in the optimal tree configuration of the cerebellar network of males and females. Moreover, the tree-hierarchy values are close to 0.5 which corresponds to an optimal tree organization. Therefore, both males and females have a close to optimal cerebellar network organization with significant differences among them. Hub analysis revealed another important outcome of the network analysis. More specifically, a left cerebellar dominance is observed in both males and females which is in concordance with the results presented in **Chapter 3**. Functional node 10 is a dominant hub (**Figs 4.31-4.32**) and belongs to the Left VI lobule of cerebellum which was identified as a dominant hub in the lobular analysis of **Chapter 3**. This outcome enhances Left VI's dominance in cerebellum's functional connectivity and highlights the importance of further studies that will focus on the association of this cerebellar region with cerebrum. Additional hub nodes are functional nodes 3 (located in lobule Right VI) mostly for the female population, 13 (located in lobule Left VIIb) which appears with higher hub indications again in females and 11 (located in lobule Left Crus I) mostly in males. From existing studies (Stoodley and Schmahmann, 2009; Bernard et al., 2012; Stoodley et al., 2012), these hubs have the following main connections to cerebral hemispheres: lobule VI has functional connectivity to frontal, pre-frontal, temporal, parietal lobes, while Crus I to frontal gyrus, precuneus, angular gyrus, inferior parietal lobule. These highly active lobules have certain functional implications and this is in concordance with the left dominance in functions related to cognition and working memory (Fabbro, 2000; Manto et al., 2012; Stoodley et al., 2012). The rest of the hub nodes located in the right part of the cerebellar hemisphere are mainly related with motor functions and in part with emotion.

One reported difference between men and women is related to the dominance of the women hemispheres in language (van Dun et al., 2016). Additional anatomical differences between men and women have been demonstrated in several studies. In particular, although there is no difference in intelligence ability, the neural substrates of general intelligence are different between the sexes (Stam, 2004; Malpas et al., 2016). Moreover, the cerebellar functional connections depend on the IQ level, which is in accordance to the neural efficiency hypothesis. The global network organization of the cerebellum, in coordination with cortical regions, is known from numerous studies and various analytic methods (Buckner et al., 2011; Manto et al., 2012; Koziol et al., 2014; Ramnani, 2014). Our findings support and enhance such information related to the importance of the cerebellar lobules at rest, as well as their inter-connectivity. As known, regions that are co-activated during a function tend to show co-activation at rest, as well. The lobules reflecting high betweenness centrality and degree at rest are indicative of more information load at rest. Furthermore, it is expected that they

attain increased activation during function, in coordination with the co-activated regions of the cerebrum hemispheres and with other regions of the cerebellum.

All in all, our results from the first part of this study suggest that both sexes have the characteristics of small-world networks with differences in females indicative of higher neural efficiency of the cerebellum, especially in higher-IQ females. The more efficient network organization in women reflects the different hemispheric organization between genders. The considerations of three global metrics in women support this conclusion. Our findings in men are in a similar direction with respect to the IQ level, but appear not significant. The lower small-worldness in high-IQ females, compared to low-IQ females and to men counterparts, forms an interesting finding of our study. In addition, five global metrics (i.e., average clustering coefficient, small-worldness, connectivity, diameter and radius) revealed significant differences between low and high-IQ individuals, as well as within females in low and high-IQ groups. The dominance of DEG and BC on left lobules was exhibited in both sexes, but the stronger Left VI hub indication in high-IQ women is a novel finding and goes in parallel with other higher-level organizations in this group. Three cerebellar lobules (i.e., Left Crus II, Left X, and Vermis VIIIb) in low-IQ individuals (both genders) showed maximum correlation with the median response time, implying increased effort dedicated locally by this population in cognitive tasks. The second part of this thesis provides a functional atlas of the human cerebellum based on a voxel-wise spatially constrained spectral clustering approach. The extracted atlas provides the first complete functional atlas of cerebellum's network at rest, based on rs-fMRI data obtained from the Human Connectome Project. A gender-based cerebellar network analysis based on this atlas reveals significant differences in the optimal tree configurations of males and females. Our hub analysis findings support the left hemispheric dominance in cerebellum's functional connectivity, highlighting the importance of lobule Left VI during information transfer.

## **5.2. Future work**

Brain network analysis using Graph Theory aspects is a straightforward approach for modeling brain's functional connectivity in the form of a graph (i.e., a network) where the regions of interest (ROIs) or channels (in the case of EEG/MEG studies) represent the nodes and the similarities between each possible pair of channels or regions represent the edges. Moreover, the application of spectral graph clustering approaches based on voxel-wise connectivity networks is a modern network analysis approach since it not only combines direct application on the graph but also results to a lesser computational complexity through the combination of matrix theory and linear algebra concepts.

The aforementioned approaches can be also applied on a variety of EEG or MEG data obtained from healthy or impaired subjects. The application of MSTs can provide information about the backbone of the original brain network and therefore reveal useful structural and

functional properties of the network. The concept of spectral clustering can be able to identify the underlying sub-networks of brain's functional connectivity and therefore be combined with statistical analysis in order to signify differences in the functional activation patterns of brain among healthy and pathological groups. It is also crucial to combine the present findings with future studies in order to shed light into the disturbances of cerebellar-cerebrum connections with respect to intelligence in both sexes. It is well-known that the prefrontal and posterior parietal lobes, which are mostly related to intelligence, have many connections to cerebellum. Therefore, a cerebellar-cerebrum connectivity study could reveal common cortex patterns of brain activations related to intelligence and gender. Finally, it would be interesting to examine the relation of cerebellum with other demographic factors such as lifespan development.

The Affinity propagation clustering (APC) procedure (Frey and Dueck, 2007) is another completely data-driven clustering approach which initially considers all data points as possible exemplars (i.e., members of the input set that are representative of clusters) and through the minimization of an energy function and message-passing architecture, obtains the optimal set of exemplars and their corresponding clusters. APC has been used lately in fMRI data analysis (Zhang et al., 2011) for detecting brain's functional activations. An interesting future work would be to apply the APC method in cerebellum and compare the clustering performance of the APC and SCSC algorithms. A similar work has not yet been reported in the current literature and would be a straightforward one. Affinity propagation has been recently combined with the Adaptive Sparse Representation (ASR) method (Wang et al., 2014), an alternative approach of Pearson's pairwise correlation that takes into consideration the linear relationship of one node with every other node within the network (Li and Wang, 2015). This can provide more accurate information about brain activation patterns.

Cerebellum's regional homogeneity (ReHo) can be assessed using Kendall's coefficient of concordance (KCC), a measure that quantifies the similarity of a voxel's time-series by taking into consideration its neighboring voxels time-series that lie within a sphere of pre-specified radius. KCC has been used in several fMRI studies (Baumgartner, 1999; Zang et al., 2004) to reveal the complexity of the human brain. KCC can be also used as a dimensionality reduction approach, by preserving only the voxels with high KCC values (i.e.,  $> 0.8$ ). In contrast, voxels with very small KCC values correspond to regions with small homogeneity, usually in areas with high white matter concentration - note that gray matter usually contains the neurons used for information processing and it is mostly located on the surface (e.g., in the cerebellar cortex). The remaining voxels can then be clustered using the SCSC approach in order to obtain a gray matter atlas of cerebellum.

Future studies need to be addressed in order to clarify the outcomes of this thesis in cerebellum-cerebral connections. The present findings combined with future studies could practically contribute to the examination of disturbances in cerebellum and/or cerebellar-cerebrum connections with respect to intelligence in both sexes. Moreover, the atlases that were constructed in this thesis can be used for the investigation of significant differences in

the cerebellum's functional connectivity between normal subjects and subjects with various pathologies (i.e., Alzheimer's disease, ADHD, ASD, etc.).

### **5.3. Cerebellum's atlases availability**

The resting-state and functional cerebellar atlases which were created in **Chapter 4** will be uploaded on the following github repository ([github.com/vpz4/Functional-connectivity-analysis-of-cerebellum](https://github.com/vpz4/Functional-connectivity-analysis-of-cerebellum)) as soon as the second part of this thesis will be accepted publication. This will be done so as to promote neuroscientific exploratory studies based on cerebellum's network in order to shed light into the relation of cerebellum's functional connectivity with the rest of the brain's activation patterns in healthy as well as pathological populations.

## 6. References

---

- Allen, E. A., Erhardt, E. B., Damaraju, E., Gruner, W., Segall, J. M., Silva, R. F., et al. (2011). A baseline for the multivariate comparison of resting-state networks. *Front. Syst. Neurosci.* 5, 2. doi: 10.3389/fnsys.2011.00002
- Andersen, B. B., Korbo, L., and Pakkenberg, B. (1992). A quantitative study of the human cerebellum with unbiased stereological techniques. *J. Comp. Neurol.* 326, 549-560. doi: 10.1002/cne.903260405
- Apps, R., and Hawkes, R. (2009). Cerebellar cortical organization: a one-map hypothesis. *Nat. Rev. Neurosci.* 10, 670-681. doi:10.1038/nrn2698
- Aguirre, G. K., Zarahn, E., and D'esposito, M. (1998). The variability of human, BOLD hemodynamic responses. *Neuroimage* 8, 360-369. doi: 10.1006/nimg.1998.0369
- Barabási, A. L., Réka A. (1999). Emergence of scaling in random networks. *Science* 286, 509-512. doi: 10.1126/science.286.5439.509
- Barch, D. M., Burgess, G. C., Harms, M. P., Petersen, S. E., Schlaggar, B. L., Corbetta, M., et al. (2013). Function in the human connectome: task-fMRI and individual differences in behavior. *Neuroimage* 80, 169-189. doi: 10.1016/j.neuroimage.2013.05.033
- Barnes, J. (2013). Essential biological psychology; Chapter 1, Neurons, Neurotransmission and Communication. SAGE publications.
- Bassett, D. S., and Bullmore, E. (2006). Small-world brain networks. *The Neuroscientist* 12, 512-523. doi: 10.1177/1073858406293182
- Basten, U., Hilger, K., and Fiebach, C. J. (2015). Where smart brains are different: a quantitative meta-analysis of functional and structural brain imaging studies on intelligence. *Intelligence* 51, 10-27. doi: 10.1016/j.intell.2015.04.009
- Baumgartner, R., Somorjai, R., Summers, R., and Richter, W. (1999). Assessment of cluster homogeneity in fMRI data using Kendall's coefficient of concordance. *J. Magn. Reson. Imag.* 17, 1525-1532. doi: 10.1016/S0730-725X(99)00101-0
- Beckmann, C. F., and Smith, S. M. (2004). Probabilistic independent component analysis for functional magnetic resonance imaging. *IEEE Trans. Med. Imaging* 23, 137-152. doi: 10.1109/TMI.2003.822821

- Belliveau, J. W., Kennedy, D. N. Jr., McKinstry, R. C., Buchbinder, B. R., Weisskoff, R. M., Cohen, M. S., et al. (1991). Functional mapping of the human visual cortex by magnetic resonance imaging. *Science* 254, 716-719. doi: 10.1126/science.1948051
- Benjamini, Y., and Hochberg, Y. (1995). Controlling the false discovery rate: a practical and powerful approach to multiple testing. *J. R. Stat. Soc. B* 57, 289-300. doi: 10.2307/2346101
- Bernard, J. A., Seidler, R. D., Hassevoort, K. M., Benson, B. L., Welsh, R. C., Wiggins, J. L., et al. (2012). Resting state cortico-cerebellar functional connectivity networks: a comparison of anatomical and self-organizing map approaches. *Front. Neuroanat.* 6, 31. doi: 10.3389/fnana.2012.00031
- Bilker, W. B., Hansen, J. A., Brensinger, C. M., Richard J., Gur, R. E., and Gur, R. C. (2012). Development of abbreviated nine-item forms of the Raven's standard progressive matrices test. *Assessment* 19, 354-369. doi: 10.1177/1073191112446655
- Biswal, B., Yetkin, F. Z., Haughton, V. M., Hyde, J. S., 1995. Functional connectivity in the motor cortex of resting human brain using echo-planar MRI. *Magn. Reson. Med.* 34, 537-541. doi: 10.1002/mrm.1910340409
- Block, R., O'Leary, D. S., Hichwa, R. D., Augustinack, J. C., Ponto, L. L., Ghoneim, M. M., et al. (2000). Cerebellar hypoactivity in frequent marijuana users. *Neuroreport* 11, 749-753. doi: 10.1097/00001756-200003200-00019
- Boccaletti, S., Latora, V., Moreno, Y., Chavez, M., Hwang, D.U. (2006). Complex networks: structure and dynamics. *Phys. Rep.* 424, 175-308. doi: 10.1016/j.physrep.2005.10.009
- Boersma, M., Smit, D. J. A., Boomsma, D. I., De Geus, E. J. C., Delemarre-van de Waal, H. A., and Stam, C. J. (2013). Growing trees in child brains: graph theoretical analysis of electroencephalography-derived minimum spanning tree in 5- and 7-year-old children reflects brain maturation. *Brain Connect.* 3, 50-60. doi: 10.1089/brain.2012.0106
- Bohr, I. J., Kenny, E., Blamire, A., O'Brien, J. T., Thomas, A. J., Richardson, J., et al. (2013). Resting-state functional connectivity in late-life depression: higher global connectivity and more long distance connections. *Front. Psych.* 3, 116. doi: 10.3389/fpsy.2012.00116
- Brooks, J. (1937). The action of nitrite on haemoglobin in the absence of oxygen. *Proc. R. Soc. Lond. B* 123, 368-382. doi: 10.1098/rspb.1937.0057
- Buckner, R. L., Krienen, F. M., Castellanos, A., Diaz, J. C., Yeo, B. T. T. (2011). The organization of the human cerebellum estimated by intrinsic functional connectivity. *J. Neurophysiol.* 106, 2322-2345. doi: 10.1152/jn.00339.2011
- Bullmore, E., Sporns, O. (2009). Complex brain networks: graph theoretical analysis of structural and functional systems. *Nat. Rev. Neurosci.* 10, 186-198. doi/10.1038/nrn2575
- Caldwell, J. H. (2009). Action Potential Initiation and Conduction in Axons. Elsevier.
- Carr, D. H., Brown, J., Bydder, G. M., Steiner, R. E., Weinmann, H. J., Speck, U., et al. (1984). Gadolinium-DTPA as a contrast agent in MRI: initial clinical experience in 20 patients. *Am. J. Roentgenol.* 143, 215-224. doi: 10.2214/ajr.143.2.215

- Chen, S., and Li, X. (2012). Functional magnetic resonance imaging for imaging neural activity in the human brain: the annual progress. *Comput. Math. Methods Med.* 2012: 613465. doi: 10.1155/2012/613465
- Chiang, M. C., Barysheva, M., Shattuck, D. W., Lee, A. D., Madsen, S. K., Avedissian, C., et al. (2009). Genetics of brain fiber architecture and intellectual performance. *J. Neurosci.* 29, 2212-2224. doi: 10.1523/JNEUROSCI.4184-08.2009
- Choi, Y. Y., Shamosh, N. A., Cho, S. H., DeYoung, C. G., Lee, M. J., Lee, J. M., et al. (2008). Multiple bases of human intelligence revealed by cortical thickness and neural activation. *J. Neurosci.* 28, 10323-10329. doi: 10.1523/JNEUROSCI.3259-08.2008
- Craddock, R. C., James, G. A., Holtzheimer, P. E., Hu, X. P., and Mayberg, H. S. (2012). A whole brain fMRI atlas generated via spatially constrained spectral clustering. *Hum. Brain Mapp.* 33, 1914-1928. doi: 10.1002/hbm.21333
- D'Mello, A. M., and Stoodley, C. J. (2015). Cerebro-cerebellar circuits in autism spectrum disorder. *Front. Neurosci.* 9: 408. doi: 10.3389/fnins.2015.00408
- Davies, D. L., and Bouldin, D. W. (1979). A cluster separation measure. *IEEE Trans Pattern Anal Mach Intell.* 1, 224-227. doi: 10.1109/TPAMI.1979.4766909
- da Silva, F. L. (2010). EEG - fMRI: Physiological Basis, Technique, and Applications; Chapter 2, EEG: Origin and Measurement. Springer.
- Deary, I. J., Penke, L., and Johnson, W. (2010). The neuroscience of human intelligence differences. *Nat. Rev. Neurosci.* 11, 201-211. doi: 10.1038/nrn2793
- Dice, L. R. (1945). Measures of the amount of ecologic association between species. *Ecology* 26, 297-302. doi: 10.2307/1932409
- Diedrichsen, J., Balsters, J. H., Flavell, J., Cussans, E., and Ramnani, N. (2009). A probabilistic MR atlas of the human cerebellum. *Neuroimage* 46, 39-46. doi: 10.1016/j.neuroimage.2009.01.045
- Diedrichsen, J., Maderwald, S., Küper, M., Thürling, M., Rabe, K., Gizewski, E. R., et al. (2011). Imaging the deep cerebellar nuclei: a probabilistic atlas and normalization procedure. *Neuroimage* 54, 1786-1794. doi: 10.1016/j.neuroimage.2010.10.035
- Diedrichsen, J., and Zotow, E. (2015). Surface-based display of volume-averaged cerebellar imaging data. *PLoS ONE* 10: e0133402. doi: 10.1371/journal.pone.0133402
- Douw, L., Schoonheim, M. M., Landi, D., van der Meer M. L., Geurts, J. J. G., Reijneveld, J. C., et al. (2011). Cognition is related to resting-state small-world network topology: an magnetoencephalographic study. *Neuroscience* 175, 169-177. doi: 10.1016/j.neuroscience.2010.11.039
- Duncan, J. (1995). Attention, intelligence, and the frontal lobes. In M.S. Gazzaniga, M. (Ed.), *The cognitive neurosciences* 721-733, Cambridge, MA US: The MIT Press.
- Duncan, J., Seitz, R. J., Kolodny, J., Bor, D., Herzog, H., Ahmed, A., et al. (2000). A neural basis for general intelligence. *Science* 289, 457-460. doi: 10.1126/science.289.5478.457

- E, K. H., Chen, S. H. A., Ho, M. H. R., and Desmond, J. E. (2014). A meta-analysis of cerebellar contributions to higher cognition from PET and fMRI studies. *Hum. Brain Mapp.* 35, 593-615. doi: 10.1002/hbm.22194
- Elster, A.D. (2017). What is the difference between T2 and T2\*?. [Questions and answers in MRI](#).
- Engels, M. M. A., Stam, C. J., van der Flier, W. M., Scheltens, P., de Waal, H., van Straaten, E. C. W. (2015). Declining functional connectivity and changing hub locations in Alzheimer's disease: an EEG study. *BMC Neurol.* 15, 145. doi: 10.1186/s12883-015-0400-7
- Erdős, P., and Rényi, A. (1960). On the evolution of random graphs. *Bull. Inst. Internat. Statist.* 38, 343-347.
- Fabbro, F. (2000). Introduction to language and cerebellum. *J. Neurolinguistics* 13, 83-94. doi: 10.1016/S0911-6044(00)00005-1
- Feldman, R. S. (2011). *Understanding Psychology*, 10<sup>th</sup> edition; Chapter 3, Neuroscience and Behavior. The McGraw Hill Companies.
- Fletcher, T. F. (2016). Lecture on cerebellum. [Minnesota Veterinary Anatomy Courseware Web Site](#), College of Veterinary Medicine, University of Minnesota.
- Fornito, A., Zalesky, A., and Breakspear, M. (2013). Graph analysis of the human connectome: promise, progress, and pitfalls. *Neuroimage* 80, 426-444. doi: 10.1016/j.neuroimage.2013.04.087
- Frey, B. J., and Dueck, D. (2007). Clustering by passing messages between data points. *Science* 315, 972-976. doi: 10.1126/science.1136800
- Glasser, M. F., Sotiropoulos, S. N., Wilson, J. A., Coalson, T. S., Fischl, B., Andersson, J. L., et al. (2013). The minimal processing pipelines of the Human Connectome Project. *Neuroimage* 80, 105-124. doi: 10.1016/j.neuroimage.2013.04.127
- Glickstein, M. (2007). What does the cerebellum really do? *Curr. Biol.* 17, 824–827. doi: 10.1016/j.cub.2007.08.009
- Glover, G.H. (2011). Overview of functional magnetic resonance imaging. *Neurosurg. Clin. N. Am.* 22, 133-139. doi: 10.1016/j.nec.2010.11.001
- Golby, A., Silverberg, G., Race, E., Gabrieli, S., O'Shea, J., Knierim, K., et al. (2005). Memory encoding in Alzheimer's disease: an fMRI study of explicit and implicit memory. *Brain* 128, 773-787. doi: 10.1093/brain/awh400
- Goulas, A., Schaefer, A., Margulies, D. S. (2015). The strength of weak connections in the macaque cortico-cortical network. *Brain Struct. Funct.* 220, 2939-2951. doi: 10.1007/s00429-014-0836-3
- Guyton and Hall. *Textbook of Medical Physiology*, 12<sup>th</sup> edition. Saunders, 2012.
- Haier, R. J., Jung, R. E., Yeo, R. A., Head, K., and Alkire, M. T. (2005). The neuroanatomy of general intelligence: sex matters. *Neuroimage* 25, 320-327. doi: 10.1016/j.neuroimage.2004.11.019
- Hampson, D. R, and Blatt, G. J. (2015). Autism spectrum disorders and neuropathology of the cerebellum. *Front. Neurosci.* 9:420. doi: 10.3389/fnins.2015.00420

- Hosseini, S. M. H., and Kesler, S. R. (2013). Influence of choice of null network on small-world parameters of structural correlation networks. *PLoS One* 8, e67354. doi: 10.1371/journal.pone.0067354
- Hulshoff Pol, H. E., Schnack, H. G., Posthuma, D., Mandl, R. C. W., Baaré, W. F., van Oel, C., et al. (2006). Genetic contributions to human brain morphology and intelligence. *J. Neurosci.* 26, 10235-10242. doi: 10.1523/JNEUROSCI.1312-06.2006
- Johnsrude, I., and Hauk, O. (2005). Neuroimaging: Techniques for examining human brain function. In: Braisby N, editor. Cognitive psychology: a methods companion. New York: Oxford University Press.
- Jung, R. E., Brooks, W. M., Yeo, R. A., Chiulli, S. J., Weers, D. C., and Sibbitt, W. L. Jr. (1999). Biochemical markers of intelligence: a proton MR spectroscopy study of normal human brain. *Proc. Biol. Sci.* 266, 1375-1379. doi: 10.1098/rspb.1999.0790
- Jung, R. E., and Haier, R. J. (2007). The Parieto-Frontal Integration Theory (P-FIT) of intelligence: converging neuroimaging evidence. *Behav. Brain Sci.* 30, 135-154. doi: 10.1017/S0140525X07001185
- Kelly, C., Biswal, B. B., Craddock, R. C., Castellanos, F. X., and Milham, M. P. (2012). Characterizing variation in the functional connectome: promise and pitfalls. *Trends Cogn. Sci.* 16, 181-188. doi: 10.1016/j.tics.2012.02.001
- Kim, D. J., Davis, E. P., Sandman, C. A., Sporns, O., O'Donnell, B. F., Buss, C., et al. (2016). Children's intellectual ability is associated with structural network integrity. *Neuroimage* 124, 550-556. doi: 10.1016/j.neuroimage.2015.09.012
- Klados, M. A., Styliadis, C., Frantzidis, C. A., Paraskevopoulos, E., and Bamidis, P.D. (2016). Beta-band functional connectivity is reorganized in mild cognitive impairment after combined computerized physical and cognitive training. *Front. Neurosci.* 10, 55. doi: 10.3389/fnins.2016.00055
- Koziol, L. F., Budding, D., Andreasen, N., D'Arrigo, S., Bulgheroni S., Imamizu, H., et al. (2014). Consensus paper: the cerebellum's role in movement and cognition. *Cerebellum* 13, 151-177. doi: 10.1007/s12311-013-0511-x
- Kruskal, J. B. (1956). On the shortest spanning subtree of a graph and the traveling salesman problem. *Proc. Am. Math. Soc.* 7, 48-50. doi: 10.1090/S0002-9939-1956-0078686-7
- Laird, A. R., Robinson, J. L., McMillan, K. M., Tordesillas-Gutiérrez, D., Moran, S. T., Gonzales, S. M., et al. (2010). Comparison of the disparity between Talairach and MNI coordinates in functional neuroimaging data: validation of the Lancaster transform. *Neuroimage* 51, 677-683. doi: 10.1016/j.neuroimage.2010.02.048
- Laskaris, N. A., and Ioannides, A. A. (2001). Exploratory data analysis of evoked response single trials based on minimal spanning tree. *Clin. Neurophysiol.* 112, 698-712. doi: 10.1016/S1388-2457(00)00560-5
- Li, S. C., Lindenberger, U., Hommel, B., Aschersleben, G., Prinz, W., and Baltes, P. B. (2004). Transformations in the couplings among intellectual abilities and constituent cognitive processes across the life span. *Psychol. Sci.* 15, 155-163. doi: 10.1111/j.0956-7976.2004.01503003.x

- Li, Y., Liu, Y., Li, J., Qin, W., Li, K., Yu, C., and Jiang, T. (2009). Brain anatomical network and intelligence. *PLoS Comput. Biol.* 5: e1000395. doi: 10.1371/journal.pcbi.1000395
- Li, X., and Wang, H. (2015). Identification of functional networks in resting state fMRI data using adaptive sparse representation and affinity propagation clustering. *Front. Neurosci.* 9: 383. doi: 10.3389/fnins.2015.00383
- Liao, W., Mantini, D., Zhang, Z., Pan, Z., Ding, J., Gong, Q., et al. (2010). Evaluating the effective connectivity of resting state networks using conditional Granger causality. *Biol. Cybern.* 102, 57-69. doi: 10.1007/s00422-009-0350-5
- Lindquist, M. A. (2008). The statistical analysis of fMRI data. *Statist. Sci.* 23, 439-464. doi: 10.1214/09-STS282
- Logothetis, N. K. (2002). The neural basis of the blood-oxygen-level-dependent functional magnetic resonance imaging signal. *Phil. Trans. R. Soc. Lond. B.* 357, 1003-1037. doi: 10.1098/rstb.2002.1114
- Logothetis, N. K., and Wandell, B. A. (2004). Interpreting the BOLD signal. *Annu. Rev. Physiol.* 66, 735-769. doi: 10.1146/annurev.physiol.66.082602.092845
- Logothetis, N. K. (2008). What we can do and what we cannot do with fMRI. *Nature* 453, 869-878. doi: 10.1038/nature06976
- Lopez-Larson, M. P., Bogorodskid, P., Rogowskæ, J., McGladea, E., Kinga, J. B., Terrya, J., et al. (2011). Altered prefrontal and insular cortical thickness in adolescent marijuana users. *Behav. Brain Res.* 220, 164-172. doi: 10.1016/j.bbr.2011.02.001
- Luxburg U. V., 2007. A tutorial on spectral clustering. *Stat. Comput.* 17, 395-416. doi: 10.1007/s11222-007-9033-z
- Malonek, D., and Grinvald, A. (1996). Interactions between electrical activity and cortical microcirculation revealed by imaging spectroscopy: implications for functional brain mapping. *Science* 272, 551-554. doi: 10.1126/science.272.5261.551
- Malpas, C. B., Genc, S., Saling, M. M., Velakoulis, D., Desmond, P. M., and O'Brien, T. J. (2016). MRI correlates of general intelligence in neurotypical adults. *J. Clin. Neurosci.* 24, 128-134. doi: 10.1016/j.jocn.2015.07.012
- Manto, M., Bower, J.M., Conforto, A.B., Delgado-Garcia, J.M., da Guarda, S.N., Gerwig, M., et al. (2012). Consensus paper: roles of the cerebellum in motor control-the diversity of ideas on cerebellar involvement in movement. *Cerebellum* 11, 457-487. doi: 10.1007/s12311-011-0331-9
- Matthews, P.M., and Jezzard, P. (2004). Functional magnetic resonance imaging. *J. Neurol. Psychiatry* 75, 6-12. PMID: PMC1757457.
- McDaniel, M. A. (2005). Big-brained people are smarter: a meta-analysis of the relationship between in vivo brain volume and intelligence. *Intelligence* 33, 337-346. doi: 10.1016/j.intell.2004.11.005
- Mechelli, A., Price, C. J., Friston, K. J., and Ashburner, J. (2005). Voxel-based morphometry of the human brain: methods and applications. *Curr. Med. Imaging Rev.* 1, 105-113. doi: 10.2174/1573405054038726

- Menon, R. S., Ogawa, S., Hu, X., Strupp, J. P., Anderson, P., and Uğurbil, K. (1995). BOLD based functional MRI at 4 Tesla includes a capillary bed contribution: echo-planar imaging correlates with previous optical imaging using intrinsic signals. *Magn. Reson. Med.* 33, 453-459. doi: 10.1002/mrm.1910330323
- Messé, A., Marrelec, G., Bellec, P., Perlberg, V., Doyon, J., Pélégrini-Issac, M., et al. (2012). Comparing structural and functional graph theory features in the human brain using multimodal MRI. *IRBM* 33, 244-253. doi: 10.1016/j.irbm.2012.04.005
- Micheloyannis, S., Pachou, E., Stam, C. J., Vourkas, M., Erimaki, S., and Tsirka, V. (2006). Using graph theoretical analysis of multi channel EEG to evaluate the neural efficiency hypothesis. *Neurosci. Lett.* 402, 273-277. doi: 10.1016/j.neulet.2006.04.006
- Miraglia, F., Vecchio, F., Bramanti, P., and Rossini, P. M. (2016). EEG characteristics in “eyes open” vs “eyes closed” conditions: small world network architecture in healthy aging and age-related brain degeneration. *Clin. Neurophysiol.* 127, 1261-1268. doi: 10.1016/j.clinph.2015.07.040
- Muller, L., Destexhe, A., and Rudolph-Lilith, M. (2014). Brain networks: small-worlds, after all? *New J. Phys.* 16. doi: 10.1088/1367-2630/16/10/105004
- Nicolas-Alonso, L. F., and Gomez-Gil, J. (2012). Brain computer interfaces, a review. *Sensors* 12, 1211-1279. doi: 10.3390/s120201211
- Ogawa, S., and Lee, T. M. (1990). Magnetic resonance imaging of blood vessels at high fields: in vivo and in vitro measurements and image stimulation. *Magn. Reson. Med.* 16, 9-18. doi: 10.1002/mrm.1910160103
- Ogawa, S., Lee, T. M., Kay, A. R., and Tank, D. W. (1990). Brain magnetic resonance imaging with contrast dependent on blood oxygenation. *Proc. Natl. Acad. Sci. USA.* 87, 9868-9872. doi: 10.1073/pnas.87.24.9868
- Olde Dubbelink, K. T. E., Hillebrand, A., Stoffers, D., Deijen, J. B., Twisk, J. W. R., Stam, C. J., et al. (2014). Disrupted brain network topology in Parkinson’s disease: a longitudinal magnetoencephalography study. *Brain* 137, 197-207. doi: 10.1093/brain/awt316
- Onnela, J. P., Saramäki, J., Kertész, J., and Kaski, K. (2005). Intensity and coherence of motifs in weighted complex networks. *Phys. Rev. E* 71, 065103. doi: 10.1103/PhysRevE.71.065103
- O’Reilly, J. X., Beckmann, C. F., Tomassini, V., Ramnani, N., and Johansen-Berg, H. (2010). Distinct and overlapping functional zones in the cerebellum defined by resting state functional connectivity. *Cereb. Cortex* 20, 953-965. doi: 10.1093/cercor/bhp157
- Orringer, D., Vago, D. R., and Golby, A. J. (2012). Clinical applications and future directions of functional MRI. *Semin. Neurol.* 32, 466-475. doi: 10.1055/s-0032-1331816
- Otte, W. M., van Diessen, E., Paul, S., Ramaswamy, R., Subramanyam Rallabandi, V. P., Stam, C. J., et al. (2015). Aging alterations in whole-brain networks during adulthood mapped with the minimum spanning tree indices: the interplay of density, connectivity cost and life-time trajectory. *Neuroimage* 109, 171-189. doi: 10.1016/j.neuroimage.2015.01.011

- Paschal, C. B., and Morris, H. D. (2004). K-space in the clinic. *J. Magn. Reson. Imaging* 19, 145-159. doi: 10.1002/jmri.10451
- Paul, E. J., Larsen, R. J., Nikolaidis, A., Ward, N., Hillman, C. H., Cohen, N. J., et al. (2016). Dissociable brain biomarkers of fluid intelligence. *Neuroimage* 137, 201-211. doi: 10.1016/j.neuroimage.2016.05.037
- Pelvig, D. P., Pakkenberg, H., Stark, A. K., and Pakkenberg B. (2008). Neocortical glial cell numbers in human brains. *Neurobiol. Aging*. 29, 1754-1762. doi: 10.1016/j.neurobiolaging.2007.04.013
- Perrachione, T. K., and Ghosh, S. S. (2013). Optimized design and analysis of sparse-sampling fMRI experiments. *Front. Neurosci.* 7, 55. doi: 10.3389/fnins.2013.00055
- Pezoulas, V. C., Zervakis, M., Michelogiannis, S., Klados, M. A. (2017). Resting-State Functional Connectivity and Network Analysis of Cerebellum with Respect to Crystallized IQ and Gender. *Front. Hum. Neurosci.* 11, 189. doi: 10.3389/fnhum.2017.00189
- Ramnani, N. (2014). Automatic and controlled processing in the corticocerebellar system. *Prog. Brain Res.* 210, 255-285. doi: 10.1016/B978-0-444-63356-9.00010-8
- Reijneveld, J. C., Ponten, S. C., Berendse, H. W., and Stam, C. J. (2007). The application of graph theoretical analysis to complex networks in the brain. *Clin. Neurophysiol.* 118, 2317-2331. doi: 10.1016/j.clinph.2007.08.010
- Riedel, M. C., Ray, K. L., Dick, A. S., Sutherland, M. T., Hernandez, Z., Fox, P. M., Eickhoff, S. B., Fox, P. T., Laird, A. R. (2015). Meta-analytic connectivity and behavioral parcellation of the human cerebellum. *Neuroimage* 117, 327-342. doi: 10.1016/j.neuroimage.2015.05.008
- Roostaei, T. (2014). The human cerebellum: a review of physiological neuroanatomy. *Neurol. Clin.* 32, 859-869. doi: 10.1016/j.ncl.2014.07.013
- Rousseeuw, P. J. (1987). Silhouettes: a graphical aid to the interpretation and validation of cluster analysis. *Comput. Appl. Math.* 20, 53-65. doi: 10.1016/0377-0427(87)90125-7
- Rubinov, M., and Sporns, O. (2010). Complex network measures of brain connectivity: uses and interpretations. *Neuroimage* 52, 1059-1069. doi: 10.1016/j.neuroimage.2009.10.003
- Ryman, S. G., Yeo, R. A, Witkiewitz, K., Vakhtin, A. A., van den Heuvel, M., de Reus, M., et al. (2016). Fronto-Parietal gray matter and white matter efficiency differentially predict intelligence in males and females. *Hum. Brain Mapp.* 37, 4006-4016. doi: 10.1002/hbm.23291
- Sabsevitz, D. S., Swanson, S. J., Hammeke, T. A., Spanaki, M. V., Possing, E. T., Morris, G. L., et al. (2003). Use of preoperative functional neuroimaging to predict language deficits from epilepsy surgery. *Neurology* 60, 1788-1792. doi: 10.1212/01.WNL.0000068022.05644.01
- Saka, M., Berwick, J., and Jones, M. (2010). Linear superposition of sensory-evoked and ongoing cortical hemodynamics. *Front. Neuroenerg.* 2, 23. doi: 10.3389/fnene.2010.00023
- Salimi-Khorshidi, G., Douaud, G., Beckmann, C. F., Glasser, M. F., Griffanti, L., Smith, S. M. (2014). Automatic denoising of functional MRI data: combining independent component analysis and hierarchical fusion of classifiers. *Neuroimage* 90, 449-468. doi: 10.1016/j.neuroimage.2013.11.046

- Sato, J. R., Takahashi, D. Y., Hoexter, M. Q., Massirer, K. B., and Fujita, A. (2013). Measuring network's entropy in ADHD: a new approach to investigate neuropsychiatric disorders. *Neuroimage* 77, 44-51. doi: 10.1016/j.neuroimage.2013.03.035
- Schipolowski, S., Wilhelm, O., and Schroeders, U. (2014). On the nature of crystallized intelligence: the relationship between verbal ability and factual knowledge. *Intelligence* 46, 156-168. doi: 10.1016/j.intell.2014.05.014
- Schmahmann, J. D. (1991). An emerging concept: the cerebellar contribution to higher function. *Arch. Neurol.* 48, 1178-1187. 10.1001/archneur.1991.00530230086029
- Schmahmann, J.D., and Sherman, J.C. (1998). The cerebellar cognitive affective syndrome. *Brain* 121, 561-579. doi: 10.1093/brain/121.4.561
- Schmahmann, J.D., Doyon, J., McDonald, D., Holmes, C., Lavoie, K., Hurwitz, A. S., Kabani, N., Toga, A., Evans, A., Petrides, M., 1999. Three-dimensional MRI atlas of the human cerebellum in proportional stereotaxic space. *Neuroimage* 10, 233-260. doi: 10.1006/nimg.1999.0459
- Schmahmann, J. D. (2004). Disorders of the cerebellum: ataxia, dysmetria of thought, and the cerebellar cognitive affective syndrome. *J. Neuropsychiatry Clin. Neurosci.* 16, 367-78. doi: 10.1176/jnp.16.3.367
- Shaw, P., Greenstein, D., Lerch, J., Clasen, L., Lenroot, R., Gogtay, N., et al. (2006). Intellectual ability and cortical development in children and adolescents. *Nature* 440, 676-679. doi: 10.1038/nature04513
- Shi, J., and Malik, J. (2000). Normalized cuts and image segmentation. *IEEE Trans on PAMI* 22, 888-905. doi: 10.1109/34.868688
- Signorelli, F., Guyotat, J., Isnard, J., Schneider, F., Mohammedi, R., and Bret, P. (2001). The value of cortical stimulation applied to the surgery of malignant gliomas in language areas. *Neurol. Sci.* 22, 3-10. doi: 10.1007/s100720100000
- Signorelli, F., Guyotat, J., Schneider, F., Isnard, J., and Bret, P. (2003). Technical refinements for validating functional MRI-based neuronavigation data by electrical stimulation during cortical language mapping. *Minim. Invasive Neurosurg.* 46, 265-268. doi: 10.1055/s-2003-44454
- Smith, S.M., Miller, K.L., Salimi-Khorshidi, G., Webster, M., Beckmann, C.F., Nichols, T.E., et al. (2011). Network modelling methods for FMRI. *Neuroimage* 54, 875-891. doi: 10.1016/j.neuroimage.2010.08.063
- Smith, S. M., Nichols, T. E., Vidaurre, D., Winkler, A. M., Behrens, T. E. J., Glasser, M. F., et al. (2015). A positive-negative mode of population covariation links brain connectivity, demographics and behavior. *Nature Neurosci.* 18, 1565-1567. doi: 10.1038/nn.4125
- Sokolov, A. A., Erb, M., Grodd, W., and Pavlova, M. A. (2014). Structural loop between the cerebellum and the superior temporal sulcus: evidence from diffusion tensor imaging. *Cereb. Cortex* 24, 626-632. doi: 10.1093/cercor/bhs346

- Solowij, N., Jones, K. A., Rozman, M. E., Davis, S. M., Ciarrochi, J., Heaven, P. C. L., et al. (2011). Verbal learning and memory in adolescent cannabis users, alcohol users and non-users. *Psychopharmacology* 216, 131-144. doi: 10.1007/s00213-011-2203-x
- Song, M., Zhou, Y., Li, J., Liu, Y., Tian, L., Yu, C., et al. (2008). Brain spontaneous functional connectivity and intelligence. *Neuroimage* 41, 1168-1176. doi: 10.1016/j.neuroimage.2008.02.036
- Song, J., Nair, V. A., Gaggli, W., and Prabhakaran, V. (2015). Disrupted brain functional organization in epilepsy revealed by graph theory analysis. *Brain. Connect.* 5, 276-283. doi: 10.1089/brain.2014.0308
- Sperling, R., Chua, E., Cocchiarella, A., Rand-Giovannetti, E., Poldrack, R., Schacter, D. L., et al. (2003). Putting names to faces: successful encoding of associative memories activates the anterior hippocampal formation. *Neuroimage* 20, 1400-1410. doi: 10.1016/S1053-8119(03)00391-4
- Spielman, D. A. (2012). Algorithms, Graph Theory, and the Solution of Laplacian Linear Equations. In: Czumaj A., Mehlhorn K., Pitts A., Wattenhofer R. (eds) Automata, Languages, and Programming. *ICALP, Lecture Notes in Computer Science*, 7392. Springer, Berlin, Heidelberg. doi: 10.1007/978-3-642-31585-5\_5
- Sporns, O. (2006). Small-world connectivity, motif composition, and complexity of fractal neuronal connections. *BioSystems* 85, 55-64. doi: 10.1016/j.biosystems.2006.02.008
- Stam, C. J. (2004). Functional connectivity patterns of human magnetoencephalographic recordings: a 'small-world' network? *Neurosci. Lett.* 355, 25-28. doi: 10.1016/j.neulet.2003.10.063
- Stam, C. J., De Haan, W., Daffertshofer, A., Jones, B. F., Manshanden, I., vanCappellen van Walsum, A. M., et al. (2009). Graph theoretical analysis of magnetoencephalographic functional connectivity in Alzheimer's disease. *Brain* 132, 213-224. doi: 10.1093/brain/awn262
- Stam, C. J., and van Straaten, E. C. W. (2012). The organization of physiological brain networks. *Clin. Neurophysiol.* 123, 1067-1087. doi: 10.1016/j.clinph.2012.01.011
- Stam, C. J., Tewarie, P., Van Dellen, E., van Straaten, E. C. W., Hillebrand, A., and Van Mieghem, P. (2014a). The trees and the forest: characterization of complex brain networks with minimum spanning trees. *Int. J. Psychophysiol.* 92, 129-138. doi: 10.1016/j.ijpsycho.2014.04.001
- Stam, C.J. (2014b). Modern network science of neurological disorders. *Nat. Rev. Neurosci.* 15, 683-695. doi:/10.1038/nrn3801
- Stam, C. J., van Straaten, E. C. W., Van Dellen, E., Tewarie, P., Gong G, Hillebrand, A., et al. (2016). The relation between structural and functional connectivity patterns in complex brain networks. *Int. J. Psychophysiol.* 103, 149-160. doi: 10.1016/j.ijpsycho.2015.02.011
- Sternberg, R. J., and Sternberg, K. (2012). *Cognitive Psychology*, 6<sup>th</sup> edition. Australia: Cengage Learning/Wadsworth.
- Stoodley, C. J., and Schmahmann, J. D. (2009). Functional topography in the human cerebellum: a meta-analysis of neuroimaging studies. *Neuroimage* 44, 489-501. doi: 10.1016/j.neuroimage.2008.08.039

- Stoodley, C. J., and Schmahmann, J. D., (2010). Evidence for topographic organization in the cerebellum of motor control versus cognitive and affective processing. *Cortex* 46, 831-844. doi: 10.1016/j.cortex.2009.11.008
- Stoodley, C. J., Valera, E. M., and Schmahmann, J. D. (2012). Functional topography of the cerebellum for motor and cognitive tasks: an fMRI study. *Neuroimage* 59, 1560-1570. doi: 10.1016/j.neuroimage.2011.08.065
- Stoodley, C. J. (2014). Distinct regions of the cerebellum show gray matter decreases in autism, ADHD, and developmental dyslexia. *Front. Syst. Neurosci.* 8, 92. doi: 10.3389/fnsys.2014.00092
- Stoodley, C.J., and Limperopoulos, C. (2016). Structure-function relationships in the developing cerebellum: evidence from early-life cerebellar injury and neurodevelopmental disorders. *Semin. Fetal. Neonatal. Med.* 21, 356-364. doi: 10.1016/j.siny.2016.04.010
- Styliadis, C., Ioannides, A. A., Bamidis, P. D., and Papadelis, C. (2015). Distinct cerebellar lobules process arousal, valence and their interaction in parallel following a temporal hierarchy. *Neuroimage* 110, 149-161. doi: 10.1016/j.neuroimage.2015.02.006
- Sullivan, E. V., Harris, R. A., and Pfefferbaum A. (2010). Alcohol's effects on brain and behavior. *Alcohol Res. Health* 33, 127-143. PMID: PMC3625995
- Suzuki, L., Coulon, P., Sabel-Goedknecht, E. H., and Ruigrok, T. J. H. (2012). Organization of cerebral projections to identified cerebellar zones in the posterior cerebellum of the rat. *J. Neurosci.* 32, 10854-10869. doi: 10.1523/JNEUROSCI.0857-12.2012
- Szalkai, B., Varga, B., and Grolmusz, V. (2015). Graph theoretical analysis reveals: women's brain are better connected than men's. *PLoS ONE* 10, e0130045. doi: 10.1371/journal.pone.0130045
- Tewarie, P., Hillebrand, A., van Dellen, E., Schoonheim, M. M., Barkhof, F., Polman, C. H., et al. (2014). Structural degree predicts functional network connectivity: a multimodal resting-state fMRI and MEG study. *Neuroimage* 97, 296-307. doi: 10.1016/j.neuroimage.2014.04.038
- Tewarie, P., Schoonheim, M. M., Schouten, D. I., Polman, C. H., Balk, L. J., Uitdehaag, B. M. J., et al. (2015a). Functional brain networks: Linking thalamic atrophy to clinical disability in multiple sclerosis, a multimodal fMRI and MEG Study. *Hum. Brain Mapp.* 36, 603-618. doi: 10.1002/hbm.22650
- Tewarie, P., van Dellen, E., Hillebrand, A., and Stam, C. J. (2015b). The minimum spanning tree: an unbiased method for brain network analysis. *Neuroimage* 104, 177-188. doi: 10.1016/j.neuroimage.2014.10.015
- Tomasi, D., and Volkow, N. D. (2012). Gender differences in brain functional connectivity density. *Hum. Brain Mapp.* 33, 849-860. doi: 10.1002/hbm.21252
- Tsvetanov, K. A., Henson, R. N. A., Tyler, L. K., Razi, A., Geerligs, L., Ham, T. E., et al. (2016). Extrinsic and intrinsic brain network connectivity maintains cognition across the lifespan despite accelerated decay of regional brain activation. *J. Neurosci.* 36, 3115-3126. doi: 10.1523/JNEUROSCI.2733-15.2016

- Van den Heuvel, M. P., Stam, C. J., Boersma, M., and Hulshoff Pol, H. E. (2008a). Small-world and scale-free organization of voxel-based resting-state functional connectivity in the human brain. *Neuroimage* 43, 528-539. doi: 10.1016/j.neuroimage.2008.08.010
- Van den Heuvel, M.P, Mandl, R., and Hulshoff Pol H. (2008b). Normalized Cut Group Clustering of Resting-State fMRI Data. *PLoS ONE* 3: e2001. doi: 10.1371/journal.pone.0002001
- Van den Heuvel, M. P., Stam, C. J., Kahn, R. S., and Hulshoff Pol, H. E. (2009). Efficiency of functional brain networks and intellectual performance. *J. Neurosci.* 29, 7619-7624. doi: 10.1523/JNEUROSCI.1443-09.2009
- Van Dellen, E., de Waal, H., van der Flier, W. M., Lemstra, A. W., Slooter, A. J. C., Smits, L. L., et al. (2015). Loss of EEG network efficiency is related to cognitive impairment in dementia with lewy bodies. *Mov. Disord.* 30, 1785-1793. doi: 10.1002/mds.26309
- Van Diessen, E., Otte, W. M., Braun, K. P. J., Stam, C. J., and Jansen, F. E. (2014). Does sleep deprivation alter functional EEG networks in children with focal epilepsy? *Front. Syst. Neurosci.* 8, 67. doi: 10.3389/fnsys.2014.00067
- Van Diessen, E., Numan, T., van Dellen, E., van der Kooi, A. W., Boersma, M., Hofman, D., et al. (2015). Opportunities and methodological challenges in EEG and MEG resting state functional brain network research. *Clin. Neurophysiol.* 126, 1468-1481. doi: 10.1016/j.clinph.2014.11.018
- Van Dun, K., Manto, M., and Mariën, P. (2016). The language of the cerebellum. *Aphasiology* 0, 1-21. doi: 10.1080/02687038.2015.1132297
- Van Essen, D. C., Ugurbil, K., Auerbach, E., Barch, D., Behrens, T. E. J., Bucholz, R., et al. (2012). The Human Connectome Project: a data acquisition perspective. *Neuroimage* 62, 2222-2231. doi: 10.1016/j.neuroimage.2012.02.018
- Van Essen, D. C., Smith, S. M., Barch, D. M., Behrens, T. E. J., Yacoub, E., and Ugurbil, K. (2013). The WU-Minn Human Connectome Project: an overview. *Neuroimage* 80, 62-79. doi: 10.1016/j.neuroimage.2013.05.041
- Van Overwalle, F., D'aes, T., and Mariën, P. (2015). Social cognition and the cerebellum: a meta-analytic connectivity analysis. *Hum. Brain Mapp.* 36, 5137-5154. doi: 10.1002/hbm.23002
- Van Overwalle, F., and Mariën, P. (2016). Functional connectivity between the cerebrum and cerebellum in social cognition: a multi-study analysis. *Neuroimage* 124, 248-255. doi: 10.1016/j.neuroimage.2015.09.001
- Voogd, J. (2003). The human cerebellum. *J. Chem. Neuroanat.* 26, 243-252. doi: 10.1016/j.jchemneu.2003.07.005
- Vuksanović, V., and Hövel, P. (2015). Dynamic changes in network synchrony reveal resting-state functional networks. *Chaos* 25, 023116. doi: 10.1063/1.4913526
- Wang, J., Zuo, X., and He, Y. (2010). Graph-based network analysis of resting-state functional MRI. *Front. Syst. Neurosci.* 4, 16. doi: dx.doi.org/10.3389/fnsys.2010.00016
- Wang, J., Lu, C., and Wang, M. (2014). Robust face recognition via adaptive sparse representation. *IEEE Trans. Cybern.* 44, 2368-2378. doi: 10.1109/TCYB.2014.2307067

- Watts, D. J., and Strogatz, S. H. (1998). Collective dynamics of 'small-world' networks. *Nature* 393, 440-442. doi: 10.1038/30918
- Xia, M., Wang, J., and He, Y. (2013). BrainNet viewer: a network visualization tool for human brain connectomics. *PLoS ONE* 8: e68910. doi: 10.1371/journal.pone.0068910
- Ye, M., Yang, T., Qing, P., Lei, X., Qiu, J., and Liu, G. (2015). Changes of functional brain networks in major depressive disorder: a graph theoretical analysis of resting-state fMRI. *PLoS One* 10, e0133775. doi: 10.1371/journal.pone.0133775
- Yeo, R. A., Ryman, S. G., van den Heuvel, M. P., de Reus, M. A., Jung, R. E., Pommy, J., et al. (2016). Graph metrics of structural brain networks in individuals with schizophrenia and healthy controls: group differences, relationships with intelligence, and genetics. *J. Int. Neuropsychol. Soc.* 22, 240-249. doi: 10.1017/S1355617715000867
- Yi, L. Y., Liang, X., Liu, D. M., Sun, B., Ying, S., Yang, D. B., et al. (2015). Disrupted topological organization of resting-state functional brain network in subcortical vascular mild cognitive impairment. *CNS Neurosci. Ther.* 21, 846–854. doi: 10.1111/cns.12424
- Yu, Y., Zhou, X., Wang, H., Hu, X., Zhu, X., Xu, L., et al. (2015). Small-world brain network and dynamic functional distribution in patients with subcortical vascular cognitive impairment. *PLoS One* 10, e0131893. doi: 10.1371/journal.pone.0131893
- Zang, Y., Jiang, T., Lu, Y., He, Y., and Tian, L. (2004). Regional homogeneity approach to fMRI data analysis. *Neuroimage* 22, 394-400. doi: 394-400. 10.1016/j.neuroimage.2003.12.030
- Zhang, J., Li, D., Chen, H., and Fang, F. (2011). Analysis of activity in fMRI data using affinity propagation clustering. *Comput. Methods Biomech. Biomed. Engin.* 14, 271-281. doi: 10.1080/10255841003766829
- Zhang, Z., Chen, G., Diao, Z., and Hemmer, P. R. (2009). *Advances in Applied Mathematics and Global Optimization*; Chapter 14, NMR Quantum Computing. Springer International Publishing.

## Ethics Statement

*We requested and received access to data collected by the Human Connectome Project (HCP) for the purpose of scientific investigation and agreed to their open access terms of use. The HCP consent procedure was approved by the Washington University institutional review board. For more information, see Van Essen et al. (2013).*

## Acknowledgements

*Data were provided [in part] by the Human Connectome Project, WU-Minn Consortium (Principal Investigators: David Van Essen and Kamil Ugurbil; 1U54MH091657) funded by the 16 NIH Institutes and Centers that support the NIH Blueprint for Neuroscience Research; and by the McDonnell Center for Systems Neuroscience at Washington University.*

*The results of the first part of this study were based on the crystallized IQ scores provided by the HCP database which were used as an IQ measure. Separation based on the crystallized IQ level, into two groups, was executed through the valuable guidance of Professor Sifis Micheloyannis (passed away - Director of Neurophysiological Research Laboratory (L. Widén), School of Medicine, University of Crete, Heraklion, Greece). The methodology as well as the results of this part of the study were published under the *Frontiers in Human Neuroscience* journal which is a well-known open-access neuroscientific journal.*

*Access on subjects sensitive data (known as Level 2 access) was granted by our team member Dr. Manousos A. Klados who is currently a Lecturer in Biomedical Engineering at the School of Life & Health Sciences, Aston University, Birmingham, UK.*

## Publications

[Pezoulas VC, Zervakis M, Michelogiannis S and Klados MA \(2017\). Resting-State Functional Connectivity and Network Analysis of Cerebellum with Respect to Crystallized IQ and Gender. Front. Hum. Neurosci. 11:189. doi: 10.3389/fnhum.2017.00189](#)

[Pezoulas V, Zervakis M, Micheloyannis S and Klados MA \(2016\). Investigating the correlation between crystallized IQ and network metrics in cerebellum using resting-state fMRI. Front. Hum. Neurosci. Conference Abstract: SAN2016 Meeting. doi: 10.3389/conf.fnhum.2016.220.00013](#)

**Pezoulas VC, Michalopoulos K, Klados MA, Micheloyannis S, Bourbakis N, Zervakis M (2017). Cerebellum voxel-wise clustering and gender-based functional connectivity analysis using resting-state fMRI. Prepared for submission in the IEEE Biomedical Health and Informatics (BHI) Journal.**

# Appendix

**Table A1.** Mean±SD values based on IQ, for the normalized degree.

ROI	Location (Name)	Low-IQ	High-IQ	Low-IQ Males	High-IQ Males	Low-IQ Females	High-IQ Females
		Mean±SD	Mean±SD	Mean±SD	Mean±SD	Mean±SD	Mean±SD
1	Left I-IV	0.1837±0.1029	0.1813±0.0967	0.1851±0.1005	0.1663±0.0774	0.1829±0.1054	0.1927±0.1088
2	Left V	0.1951±0.1002	0.1704±0.1256	0.2147±0.1274	0.1505±0.0556	0.1839±0.0805	0.1856±0.1589
3	Left VI	0.6859±0.3066	0.7566±0.3007	0.6738±0.3511	0.7733±0.2837	0.6928±0.2823	0.7439±0.3162
4	Left Crus I	0.5616±0.2928	0.5477±0.2716	0.5497±0.3324	0.5838±0.2948	0.5683±0.2715	0.5202±0.2530
5	Left Crus II	0.3543±0.2488	0.3487±0.2391	0.3580±0.2425	0.3219±0.2225	0.3522±0.2550	0.3691±0.2520
6	Left VIIb	0.3652±0.2874	0.3183±0.2355	0.2835±0.2250	0.3188±0.2417	0.4116±0.3103	0.3179±0.2338
7	Left VIIIa	0.3176±0.2200	0.2837±0.1853	0.3228±0.2420	0.2320±0.1253	0.3147±0.2094	0.3232±0.2138
8	Left VIIIb	0.1718±0.0895	0.1472±0.0762	0.1552±0.0637	0.1353±0.0452	0.1813±0.1007	0.1562±0.0929
9	Left IX	0.1791±0.1043	0.1897±0.1291	0.1930±0.1373	0.1898±0.1248	0.1712±0.0808	0.1896±0.1340
10	Left X	0.1579±0.0715	0.1456±0.0590	0.1427±0.0544	0.1528±0.0635	0.1665±0.0789	0.1402±0.0555
11	Vermis VI	0.2037±0.1334	0.1763±0.1427	0.1819±0.1376	0.1976±0.1936	0.2161±0.1309	0.1601±0.0858
12	Vermis Crus II	0.2056±0.1251	0.1832±0.0958	0.1827±0.0876	0.1896±0.0965	0.2186±0.1414	0.1784±0.0963
13	Vermis VIIb	0.1481±0.0639	0.1378±0.0496	0.1539±0.0911	0.1373±0.0599	0.1447±0.0424	0.1382±0.0408
14	Vermis VIIIa	0.2550±0.2053	0.1972±0.1200	0.2493±0.2217	0.1923±0.1267	0.2582±0.1979	0.2009±0.1163
15	Vermis VIIIb	0.2215±0.1864	0.1730±0.1019	0.2117±0.1948	0.1642±0.0808	0.2271±0.1835	0.1797±0.1161
16	Vermis IX	0.2406±0.1565	0.2188±0.1484	0.2208±0.1516	0.2172±0.1661	0.2519±0.1598	0.2201±0.1357
17	Vermis X	0.1551±0.0755	0.1367±0.0407	0.1522±0.0869	0.1347±0.0412	0.1567±0.0692	0.1382±0.0408
18	Right I-IV	0.2176±0.1693	0.1731±0.0767	0.2467±0.2286	0.1761±0.0780	0.2011±0.1240	0.1708±0.0767
19	Right V	0.2046±0.1500	0.1664±0.0941	0.1987±0.1869	0.1520±0.0628	0.2079±0.1267	0.1774±0.1119
20	Right VI	0.4341±0.3026	0.4681±0.2960	0.3848±0.3069	0.4095±0.2826	0.4621±0.3001	0.5128±0.3018
21	Right Crus I	0.4310±0.2554	0.3970±0.2338	0.3644±0.2501	0.4780±0.2655	0.4688±0.2534	0.3352±0.1875
22	Right Crus II	0.3338±0.2621	0.3227±0.2529	0.2929±0.2571	0.3371±0.2813	0.3570±0.2650	0.3116±0.2322
23	Right VIIb	0.2567±0.1945	0.2269±0.1729	0.2572±0.2067	0.2384±0.2195	0.2565±0.1897	0.2180±0.1292
24	Right VIIIa	0.2775±0.2046	0.2833±0.2037	0.3061±0.2083	0.2250±0.1420	0.2612±0.2031	0.3278±0.2325
25	Right VIIIb	0.1921±0.1728	0.2109±0.2203	0.2538±0.2621	0.1727±0.1679	0.1570±0.0734	0.2400±0.2514
26	Right IX	0.3009±0.2348	0.2095±0.1398	0.3147±0.2445	0.1995±0.1515	0.2931±0.2316	0.2170±0.1317
27	Right X	0.1532±0.0727	0.1436±0.0479	0.1382±0.0522	0.1342±0.0385	0.1618±0.0814	0.1507±0.0534

**Table A2.** Mean±SD values based on IQ, for the normalized betweenness centrality.

ROI	Location (Name)	Low-IQ	High-IQ	Low-IQ Males	High-IQ Males	Low-IQ Females	High-IQ Females
		Mean±SD	Mean±SD	Mean±SD	Mean±SD	Mean±SD	Mean±SD
1	Left I-IV	0.0354±0.0758	0.0391±0.0640	0.0382±0.0610	0.0322±0.0554	0.0338±0.0837	0.0444±0.0702
2	Left V	0.0523±0.0823	0.0401±0.1071	0.0736±0.0910	0.0230±0.0593	0.0402±0.0753	0.0530±0.1320
3	Left VI	0.6693±0.3542	0.7198±0.3628	0.6835±0.3673	0.7387±0.3587	0.6613±0.3506	0.7054±0.3700
4	Left Crus I	0.6002±0.3346	0.5808±0.3230	0.5613±0.3855	0.6504±0.3275	0.6223±0.3045	0.5278±0.3135
5	Left Crus II	0.3147±0.3198	0.3242±0.3063	0.3045±0.3013	0.3081±0.3276	0.3205±0.3331	0.3364±0.2928
6	Left VIIb	0.2989±0.3353	0.2775±0.3358	0.2105±0.2753	0.2482±0.3078	0.3492±0.3582	0.3000±0.3582
7	Left VIIIa	0.2084±0.2553	0.1722±0.2192	0.2226±0.2594	0.1060±0.1527	0.2003±0.2556	0.2228±0.2490
8	Left VIIIb	0.0403±0.1259	0.0143±0.0714	0.0214±0.0714	0.0039±0.0208	0.0511±0.1480	0.0223±0.0928
9	Left IX	0.0413±0.0893	0.0647±0.1459	0.0695±0.1228	0.0619±0.1528	0.0253±0.0589	0.0669±0.1425
10	Left X	0.0184±0.0594	0.0180±0.0712	0.0044±0.0218	0.0375±0.1038	0.0263±0.0717	0.0031±0.0189
11	Vermis VI	0.0784±0.1598	0.0529±0.1699	0.0727±0.1858	0.0774±0.2120	0.0816±0.1453	0.0342±0.1290
12	Vermis Crus II	0.0569±0.1318	0.0383±0.0571	0.0358±0.0557	0.0462±0.0609	0.0689±0.1592	0.0322±0.0541
13	Vermis VIIb	0.0033±0.0191	0.0031±0.0176	0.0090±0.0313	0.0036±0.0193	0±0	0.0027±0.0164
14	Vermis VIIIa	0.1016±0.1695	0.0620±0.1033	0.0974±0.1742	0.0731±0.1238	0.1039±0.1687	0.0535±0.0852
15	Vermis VIIIb	0.0744±0.1537	0.0412±0.0851	0.0716±0.1604	0.0339±0.0638	0.0759±0.1516	0.0467±0.0988
16	Vermis IX	0.0891±0.1293	0.0723±0.1088	0.0919±0.1616	0.0689±0.1118	0.0875±0.1088	0.0748±0.1079
17	Vermis X	0.0167±0.0750	0.0032±0.0185	0.0251±0.1065	0.0040±0.0213	0.0119±0.0500	0.0027±0.0164
18	Right I-IV	0.0626±0.1178	0.0404±0.0747	0.0883±0.1634	0.0381±0.0612	0.0479±0.0801	0.0421±0.0844
19	Right V	0.0652±0.1619	0.0355±0.0877	0.0637±0.1718	0.0199±0.0460	0.0661±0.1580	0.0475±0.1086
20	Right VI	0.3834±0.3767	0.3863±0.3631	0.3321±0.3785	0.3111±0.3262	0.4126±0.3768	0.4437±0.3832
21	Right Crus I	0.3979±0.3166	0.3820±0.2797	0.3026±0.2970	0.4589±0.2971	0.4521±0.3178	0.3234±0.2542
22	Right Crus II	0.2789±0.3339	0.2405±0.2795	0.1991±0.2776	0.2228±0.2722	0.3242±0.3571	0.2540±0.2878
23	Right VIIb	0.1880±0.2807	0.1696±0.2706	0.1811±0.2332	0.1492±0.2568	0.1920±0.3069	0.1851±0.2831
24	Right VIIIa	0.1618±0.2700	0.1920±0.2653	0.2106±0.2965	0.0952±0.1775	0.1340±0.2530	0.2658±0.2980
25	Right VIIIb	0.0509±0.1721	0.0725±0.2041	0.1211±0.2647	0.0306±0.1091	0.0110±0.0569	0.1044±0.2507
26	Right IX	0.1540±0.2148	0.0726±0.1333	0.1984±0.2233	0.0707±0.1525	0.1288±0.2082	0.0741±0.1187
27	Right X	0.0071±0.0287	0.0128±0.0447	0±0	0.0032±0.0175	0.0111±0.0355	0.0200±0.0567

**Table A3.** Mean±SD values based on IQ, for the normalized eccentricity.

ROI	Location (Name)	Low-IQ	High-IQ	Low-IQ Males	High-IQ Males	Low-IQ Females	High-IQ Females
		Mean±SD	Mean±SD	Mean±SD	Mean±SD	Mean±SD	Mean±SD
1	Left I-IV	0.8062±0.1066	0.7970±0.0971	0.8062±0.1066	0.7970±0.0971	0.8128±0.1090	0.7889±0.0928
2	Left V	0.7509±0.1173	0.7650±0.1225	0.7509±0.1173	0.7650±0.1225	0.7545±0.1164	0.7493±0.1204
3	Left VI	0.6315±0.1008	0.6349±0.1039	0.6315±0.1008	0.6349±0.1039	0.6312±0.0996	0.6340±0.1162
4	Left Crus I	0.6444±0.1191	0.6586±0.1023	0.6444±0.1191	0.6586±0.1023	0.6324±0.1129	0.6802±0.1108
5	Left Crus II	0.6668±0.1134	0.6777±0.0984	0.6668±0.1134	0.6777±0.0984	0.6516±0.1020	0.6912±0.1079
6	Left VIIb	0.6873±0.0893	0.6860±0.0999	0.6873±0.0893	0.6860±0.0999	0.6714±0.0948	0.6765±0.1091
7	Left VIIIa	0.7198±0.0967	0.7135±0.0967	0.7198±0.0967	0.7135±0.0967	0.7158±0.0977	0.6885±0.0992
8	Left VIIIb	0.7863±0.1085	0.7872±0.1185	0.7863±0.1085	0.7872±0.1185	0.7906±0.1093	0.7620±0.1183
9	Left IX	0.7657±0.1169	0.7721±0.1259	0.7657±0.1169	0.7721±0.1259	0.7619±0.1126	0.7981±0.1340
10	Left X	0.7958±0.1280	0.7869±0.1225	0.7958±0.1280	0.7869±0.1225	0.7875±0.1340	0.7926±0.1083
11	Vermis VI	0.7245±0.1106	0.7577±0.1146	0.7245±0.1106	0.7577±0.1146	0.7192±0.1092	0.7592±0.1171
12	Vermis Crus II	0.7952±0.1220	0.7844±0.1117	0.7952±0.1220	0.7844±0.1117	0.7967±0.1126	0.7773±0.1199
13	Vermis VIIb	0.9276±0.0881	0.9327±0.0841	0.9276±0.0881	0.9327±0.0841	0.9294±0.0970	0.9188±0.0946
14	Vermis VIIIa	0.7640±0.1184	0.7847±0.1217	0.7640±0.1184	0.7847±0.1217	0.7716±0.1258	0.7873±0.1088
15	Vermis VIIIb	0.8405±0.1239	0.8392±0.1157	0.8405±0.1239	0.8392±0.1157	0.8414±0.1233	0.8384±0.1255
16	Vermis IX	0.8039±0.1264	0.8116±0.1156	0.8039±0.1264	0.8116±0.1156	0.8036±0.1214	0.8031±0.1182
17	Vermis X	0.8956±0.1198	0.9371±0.0843	0.8956±0.1198	0.9371±0.0843	0.9064±0.1096	0.9356±0.0816
18	Right I-IV	0.8099±0.1129	0.8003±0.1182	0.8099±0.1129	0.8003±0.1182	0.8114±0.1050	0.8078±0.1300
19	Right V	0.7646±0.1153	0.7665±0.1174	0.7646±0.1153	0.7665±0.1174	0.7645±0.1140	0.7555±0.1241
20	Right VI	0.6665±0.1017	0.6677±0.1006	0.6665±0.1017	0.6677±0.1006	0.6690±0.1019	0.6674±0.1109
21	Right Crus I	0.6663±0.1005	0.6803±0.1029	0.6663±0.1005	0.6803±0.1029	0.6593±0.1054	0.7071±0.1028
22	Right Crus II	0.6818±0.1049	0.7081±0.0980	0.6818±0.1049	0.7081±0.0980	0.6782±0.1104	0.7292±0.0988
23	Right VIIb	0.7056±0.0951	0.7112±0.1105	0.7056±0.0951	0.7112±0.1105	0.7043±0.0991	0.7051±0.1136
24	Right VIIIa	0.7266±0.1035	0.7140±0.1019	0.7266±0.1035	0.7140±0.1019	0.7189±0.0769	0.6947±0.1105
25	Right VIIIb	0.7770±0.1202	0.7763±0.0987	0.7770±0.1202	0.7763±0.0987	0.7642±0.1097	0.7839±0.1076
26	Right IX	0.7378±0.1057	0.7739±0.1030	0.7378±0.1057	0.7739±0.1030	0.7487±0.1121	0.7880±0.0936
27	Right X	0.8061±0.1106	0.7831±0.0996	0.8061±0.1106	0.7831±0.0996	0.7945±0.1081	0.7713±0.1066

**Table A4.** Statistical analysis results based on gender, for degree.

Functional region	Males	Females	<i>F</i>	p-values
	Mean±SD	Mean±SD		
1	0.0253±0.0078	0.0284±0.0110	2.5233	0.5842
2	0.0253±0.0090	0.0267±0.0110	0.4096	0.8306
3	0.0756±0.0477	0.0742±0.0408	0.0310	0.9648
4	0.0653±0.0316	0.0684±0.0276	0.8756	0.7024
5	0.0578±0.0330	0.0467±0.0234	2.8407	0.5842
6	0.0564±0.0351	0.0551±0.0274	0.0001	1.0000
7	0.0284±0.0127	0.0338±0.0192	2.2027	0.5842
8	0.0236±0.0053	0.0240±0.0061	0.1508	0.8846
9	0.0271±0.0103	0.0284±0.0127	0.2736	0.8393
10	0.1156±0.0670	0.0880±0.0451	5.4527	0.4963
11	0.0827±0.0404	0.0831±0.0378	0.0407	0.9648
12	0.0529±0.0257	0.0609±0.0232	3.6808	0.5842
13	0.0640±0.0323	0.0707±0.0446	0.1376	0.8846
14	0.0538±0.0266	0.0644±0.0328	2.7156	0.5842
15	0.0280±0.0108	0.0258±0.0082	1.2073	0.7024
16	0.0276±0.0115	0.0284±0.0156	0.0226	0.9648
17	0.0302±0.0125	0.0271±0.0113	2.0803	0.5842
18	0.0458±0.0282	0.0458±0.0267	0.0050	1.0000
19	0.0373±0.0226	0.0338±0.0192	0.9630	0.7024
20	0.0636±0.0404	0.0582±0.0347	0.2098	0.8516
21	0.0382±0.0220	0.0360±0.0210	0.2823	0.8393
22	0.0347±0.0186	0.0333±0.0169	0.0979	0.9140
23	0.0538±0.0359	0.0604±0.0407	0.8876	0.7024
24	0.0467±0.0340	0.0404±0.0228	0.8232	0.7024
25	0.0427±0.0233	0.0484±0.0316	0.4316	0.8306
26	0.0542±0.0333	0.0489±0.0229	0.3092	0.8393
27	0.0333±0.0186	0.0369±0.0218	0.5909	0.7824
28	0.0289±0.0103	0.0253±0.0078	3.7966	0.5842
29	0.0329±0.0207	0.0382±0.0229	2.2213	0.5842
30	0.0400±0.0215	0.0360±0.0219	1.5007	0.6425
31	0.0440±0.0271	0.0360±0.0179	1.6821	0.6166
32	0.0378±0.0202	0.0409±0.0203	0.9454	0.7024
33	0.0436±0.0233	0.0369±0.0183	2.3325	0.5842
34	0.0556±0.0274	0.0702±0.0431	1.7988	0.6166
35	0.0533±0.0348	0.0591±0.0369	0.9369	0.7024
36	0.0533±0.0301	0.0582±0.0375	0.3008	0.8393
37	0.0329±0.0163	0.0342±0.0169	0.2163	0.8516
38	0.0249±0.0073	0.0276±0.0115	1.6569	0.6166
39	0.0369±0.0199	0.0378±0.0234	0.0007	1.0000
40	0.0400±0.0224	0.0458±0.0303	0.6664	0.7660
41	0.0387±0.0210	0.0391±0.0260	0.0607	0.9505
42	0.0258±0.0094	0.0258±0.0094	0	1.0000
43	0.0307±0.0173	0.0244±0.0067	5.6562	0.4963
44	0.0258±0.0094	0.0244±0.0067	0.5521	0.7824
45	0.0409±0.0271	0.0364±0.0245	0.9242	0.7024
46	0.0244±0.0067	0.0271±0.0103	2.2197	0.5842

**Table A5.** Statistical analysis results based on gender, for betweenness centrality.

Functional region	Males	Females	<i>F</i>	p-values
	Mean±SD	Mean±SD		
1	0.0071±0.0186	0.0165±0.0333	2.2772	0.6545
2	0.0062±0.0179	0.0138±0.0362	0.3447	0.9141
3	0.2730±0.2304	0.3074±0.2446	1.1454	0.6952
4	0.2317±0.2029	0.2543±0.1798	2.2151	0.6545
5	0.1611±0.1830	0.1354±0.1670	1.1730	0.6952
6	0.1696±0.2187	0.2034±0.2230	0.1631	0.9141
7	0.0320±0.0884	0.0533±0.1193	1.2758	0.6952
8	0.0027±0.0107	0.0044±0.0160	0.1541	0.9141
9	0.0157±0.0510	0.0181±0.0412	0.2332	0.9141
10	0.4548±0.2483	0.3930±0.2471	1.4608	0.6952
11	0.3026±0.2124	0.3404±0.1768	0.0097	0.9994
12	0.1446±0.1355	0.1912±0.1603	2.0404	0.6545
13	0.2123±0.2007	0.2975±0.2600	0.0330	0.9606
14	0.1858±0.2156	0.2543±0.2171	1.5255	0.6952
15	0.0124±0.0236	0.0104±0.0291	0.9774	0.7481
16	0.0240±0.0777	0.0156±0.0383	0.0001	0.9994
17	0.0318±0.0598	0.0207±0.0753	2.6410	0.6545
18	0.1037±0.1710	0.1207±0.1898	0.0425	0.9606
19	0.0633±0.1326	0.0645±0.1427	1.9735	0.6545
20	0.2110±0.2281	0.1817±0.2037	0.0390	0.9606
21	0.0871±0.1786	0.0524±0.1068	0.1772	0.9141
22	0.0631±0.1299	0.0410±0.0971	0.0520	0.9606
23	0.1464±0.1861	0.1600±0.1817	0.7637	0.8418
24	0.0935±0.1420	0.0731±0.1033	0.6296	0.8588
25	0.0674±0.1001	0.0966±0.1563	0.0005	0.9994
26	0.1240±0.1604	0.1073±0.1250	0.0000	0.9994
27	0.0268±0.0515	0.0437±0.0881	0.1884	0.9141
28	0.0297±0.0693	0.0062±0.0156	3.8854	0.6545
29	0.0431±0.1155	0.0505±0.0872	3.5571	0.6545
30	0.0807±0.1374	0.0407±0.0849	2.6490	0.6545
31	0.0718±0.1064	0.0315±0.0428	0.2022	0.9141
32	0.0607±0.1042	0.0594±0.0740	1.9043	0.6545
33	0.0779±0.1147	0.0435±0.0601	2.0050	0.6545
34	0.1852±0.1937	0.2137±0.2130	0.0409	0.9606
35	0.1526±0.2134	0.1521±0.1962	1.6006	0.6952
36	0.1298±0.1491	0.1889±0.2064	0.2258	0.9141
37	0.0376±0.0787	0.0452±0.0985	0.3669	0.9141
38	0.0095±0.0291	0.0253±0.0797	1.1937	0.6952
39	0.0462±0.0828	0.0895±0.1617	0.1229	0.9285
40	0.0648±0.1120	0.0882±0.1388	0.1739	0.9141
41	0.0825±0.1417	0.0972±0.1815	0.3391	0.9141
42	0.0096±0.0266	0.0088±0.0249	0.0000	0.9994
43	0.0217±0.0451	0.0044±0.0135	4.5188	0.6545
44	0.0142±0.0458	0.0069±0.0236	0.3833	0.9141
45	0.0627±0.1226	0.0394±0.0802	0.6853	0.8568
46	0.0076±0.0306	0.0146±0.0369	1.9627	0.6545

<b>Table A6. Statistical analysis results based on gender, for eccentricity.</b>				
<b>Functional region</b>	<b>Males</b>	<b>Females</b>	<b>F</b>	<b>p-values</b>
	Mean±SD	Mean±SD		
1	0.8399±0.1221	0.8133±0.1173	1.1702	0.9525
2	0.8046±0.1297	0.8233±0.1130	0.7500	0.9525
3	0.6639±0.1008	0.6420±0.1085	1.3582	0.9525
4	0.6910±0.1098	0.6977±0.1088	0.1093	0.9525
5	0.7085±0.1095	0.7215±0.0993	0.4924	0.9525
6	0.7090±0.1040	0.6834±0.1267	1.6624	0.9525
7	0.7586±0.1164	0.7269±0.1305	1.9638	0.9525
8	0.8520±0.1079	0.8521±0.1011	0.0015	0.9895
9	0.7902±0.1154	0.7923±0.1093	0.0189	0.9844
10	0.6357±0.0838	0.6269±0.0903	0.3525	0.9525
11	0.6810±0.1083	0.6710±0.1013	0.1836	0.9525
12	0.6997±0.1080	0.6927±0.1002	0.0833	0.9525
13	0.6921±0.0999	0.6613±0.1143	2.5408	0.9525
14	0.6978±0.1136	0.6866±0.1074	0.2390	0.9525
15	0.8193±0.1012	0.8126±0.1197	0.1702	0.9525
16	0.7743±0.1282	0.7893±0.1246	0.3798	0.9525
17	0.7607±0.1047	0.7551±0.1047	0.0801	0.9525
18	0.7163±0.1143	0.7276±0.1181	0.2261	0.9525
19	0.7752±0.1296	0.7808±0.1255	0.0616	0.9525
20	0.6997±0.1059	0.6936±0.0988	0.0596	0.9525
21	0.7136±0.1026	0.7397±0.1059	1.5577	0.9525
22	0.7803±0.1256	0.7785±0.1183	0.0002	0.9895
23	0.7043±0.0986	0.7112±0.0950	0.1502	0.9525
24	0.7405±0.1212	0.7579±0.1001	0.8511	0.9525
25	0.7747±0.1259	0.7765±0.1247	0.0054	0.9844
26	0.7280±0.1093	0.7358±0.1035	0.1545	0.9525
27	0.7785±0.1137	0.7624±0.0940	0.4415	0.9525
28	0.7835±0.1263	0.8268±0.1246	3.0531	0.9525
29	0.7557±0.1215	0.7638±0.1239	0.0997	0.9525
30	0.7204±0.1134	0.8234±0.1114	21.0082	<b>0.0006</b>
31	0.7572±0.1102	0.7909±0.1093	2.3463	0.9525
32	0.7371±0.1019	0.7417±0.1019	0.0427	0.9623
33	0.7363±0.1052	0.7567±0.1044	0.9440	0.9525
34	0.6658±0.1048	0.6698±0.0867	0.1037	0.9525
35	0.7171±0.1142	0.6822±0.0799	2.4159	0.9525
36	0.7006±0.1131	0.6927±0.0924	0.0678	0.9525
37	0.7632±0.1164	0.7462±0.0936	0.4464	0.9525
38	0.8027±0.1158	0.7972±0.1241	0.0786	0.9525
39	0.7425±0.1304	0.7360±0.0976	0.0061	0.9844
40	0.7638±0.1255	0.7484±0.1186	0.3437	0.9525
41	0.7462±0.1121	0.7268±0.1174	0.7848	0.9525
42	0.8233±0.1189	0.8062±0.1185	0.5242	0.9525
43	0.8168±0.1189	0.8345±0.1147	0.6098	0.9525
44	0.8522±0.1076	0.8269±0.1159	1.3860	0.9525
45	0.7767±0.1147	0.7777±0.1003	0.0146	0.9844
46	0.8744±0.1102	0.8345±0.1041	3.2345	0.9525

